FACULTAD DE CIENCIAS
Departamento de Química Física Aplicada

Estructura y reactividad de metales y sulfuros metálicos en reacciones de desoxigenación

Memoria para aspirar al grado de
DOCTOR

Cristina Valero Loricera

Instituto de Catálisis y Petroleoquímica
Consejo Superior de Investigaciones Científicas

Madrid, 2014

FACULTAD DE CIENCIAS
Departamento de Química Física Aplicada

Memoria para aspirar al grado de
DOCTOR

Cristina Valero Loricera

Estructura y reactividad de metales y sulfuros metálicos en reacciones de desoxigenación

Directora:

Dra. Bárbara García Pawelec
Científico Titular

Instituto de Catálisis y Petroleoquímica (CSIC)
Madrid, 2014

Agradecimientos

Desde pequeña me enseñaron que uno tiene que ser agradecido con lo que la vida le regala, esta tesis me regala muchos conocimientos, experiencias, momentos y muchas personas que hacen de esta memoria algo más que un libro.

En primer lugar quiero agradecer a la Dra. Bárbara García Pawelec, por la dirección de esta tesis, por su confianza en mi trabajo, por sus comentarios, su ilusión y su completa dedicación a la ciencia. Gracias por el estímulo final que necesitaba para que esta tesis viera la luz.

Quisiera agradecer especialmente al Prof. José Luis García Fierro, por su apoyo, ánimo y dedicación durante todos estos años. Gracias por dejarme formar parte de este grupo de trabajo donde he crecido científica y personalmente.

Agradecer al Ministerio de Ciencia e Innovación por la ayuda BES-2008-006914 de Formación de Personal Investigador (FPI) asociada al proyecto ENE2007-67533-C02-01 que me ha permitido desarrollar esta Tesis Doctoral.

Quisiera agradecer sinceramente a todos los servicios del Instituto de Catálisis y Petroleoquímica, a todo el personal de la Unidad de Apoyo siempre dispuesto a ayudar y orientar, a Nuria y Alberto que me han ayudado siempre con el papeleo, al Sevicio de limpieza, en especial a Amparo, Gema y Pilar, al Servicio de Mantenimiento, Informática y Almacén por la amabilidad con la siempre me han atendido. Mención especial a Paco Chacón, lo dije desde el momento en que empecé a "pegarme" con mi equipo, a Paco le debo media tesis, sin él las medidas de actividad recogidas en esta memoria no hubieran sido posibles, ¡muchas gracias!

Gracias al Doctor Christophe Geantet del Institut de recherches sur la catalyse et l'environnement de Lyon (IRCELYON) por aceptarme en su laboratorio y sobre todo por cuidarme. Gracias a Lis, Adriana, David, Álex y Elodie por hacerme sentir como en casa.

Gracias al personal investigador del grupo de Energía y Química Sostenibles al que seguro que en algún momento he acudido para pedirles opinión o consejo: Pilar, Miguel, José Miguel, Rufino, Mariví, Manolo, Rafa, Sergio, Consuelo. A los excatalíticos que me aconsejaron y ayudaron en los inicios Patri H., Cruz, José Ángel, Inés, Sara, Mª Elena, Desi, Nikos, Cristina A., Manuel M., María B., David, Aitor, Javi. A los que vinieron de estancia y dejaron su esencia: Andresito, Cristian, Thaisa, María de Bilbao.

Gracias a mi grupo de la comida con los que he compartido muchas risas e historias Carlota, Fernando, Aldossary, María José (Wapis), Noelia A., Gema, Mayka, José Luis. Gracias a Mª Carmen por ayudarme con reactivos, columnas de croma y citas del TEM, a Gofu por ser tan "especial" en todos los sentidos, a Paco por ser ejemplo de serenidad, paciencia y buena persona. Gracias a Rut por todos sus consejos en mi última etapa de la tesis y por los chocolates con los que repoblaba el XPS, a Vanesa por tener siempre una palabra bonita y de ánimo para mí. Gracias a Silvia y a Horacio por ser tan buenos vecinos de búnker, por prestarme las llaves de GC, por ayudarme a apretar las balas y por preguntar siempre con tanto cariño ¿cómo va esa tesis?. A Patri P. por mostrarme que todavía quedan personas buenas y humildes de las de verdad, por enseñarme a contar partículas en el TEM y por aconsejarme siempre positivamente. Mención especial a Sergio G. porque un simple gracias se queda pequeño, gracias por compartir tus conocimientos, por enseñarme la cinta de grafito que ha salvado algún que otro experimento y por estar disponible siempre que he necesitado ayuda. Gracias a

Lola porque a pesar de no coincidir en el ICP, crea tan buen ambiente que hace que dé gusto pasar tiempo con ella fuera de él.

Gracias a Antonio, Jaime, Patricia, Laura G., Mario, Ana I., Manuel y Reich por acogerme a la hora del café y por hacerme sentir como una más. A Reich un gracias especial por ser tan detallista, por acordarse de mí fuera y traerme siempre regalos que me alegraban el día. Gracias a Ana Carolina e Irantzu que pese a estar lejos, para mí siguen estando cerca, gracias por todos los ratos juntas, por hacerme reír, por quererme y por formar parte de mi vida. Gracias a Bea por ayudarme en cuestiones burocráticas incluso cuando ya no era su cometido, gracias por poner siempre la nota de color. Gracias a mi prima MJ Valero, con la que tantas veces me han confundido en los papeleos en secretaría, por lo vivido y por lo que queda por vivir. A Fran por nuestras largas conversaciones sobre casi cualquier cosa, por no cansarte de nosotras, por los consejos y por el apoyo. A Noe punto Mota, por ser tan parecida a mí, por entendernos con la mirada, por su humor y por la tienda de rosquillas que vamos a montar en cuanto acabe la tesis. A Laura Barrio por el apoyo incondicional, por los consejos, por soportar mis conversaciones con el ordenador y mis cantos con los cascos, porque me deja reírme de ella aunque siempre me pregunte: ¿te estás riendo de mí? Gracias a Inmi, porque siempre sabe ponerle una sonrisa y un toque de humor a cualquier historia por deprimente que sea, porque me parece una valiente (aunque tenga miedo de ir sola a casa por la noche) y porque ha entrado en mi vida para quedarse.

Gracias a los agrícolos y exagrícolos con los que empecé en esto de la investigación, Edu y Diego por sus conocimientos, por las toli preguntas y los buenos ratos que pasamos; a Marcos por su buen humor y la felicidad desprendida; Diana, Sandra, Palomi y Patri tan diferentes y tan mujeres hechas y derechas las cuatro, de ellas aprendí a hacerme mayor tanto en ciencia como en la

vida, ya que cuando entré era de las "pequeñitas"; Rebe y Ana por compartir estreses del máster, se cierra el círculo, soy la última en leer la tesis, Berre, la barriada cuenta con una nueva doctora; y por los agrícolas que quedan Tere y Carlos por transmitirme paz y tranquilidad ambos dos, a vosotros ya no os queda nada, ¡ánimo!.

Al Centro Juvenil Savio ese que me ha visto crecer y convertirme en lo que hoy soy. Un gracias enorme a todos se empapan y se mojan en él, por alumbrar y salar al mundo. Una mención especial a Juan Sánchez, por ser referente, por su trabajo y su humildad, las cosas pequeñas son las que nos hacen grandes y eso está claro que lo he aprendido de él. Gracias a los animadores por su entrega a los demás y la alegría que los caracteriza, a mí me alegran la vida. Gracias por lo compartido, gracias porque "lo que no se da se pierde". No me olvido de la gente con la que comparto campamentos y vida de Centro Juvenil Naranjoven, Centro Juvenil Atocha y Citycentro, porque en vuestra entrega a los demás hacéis que la vida tenga un poco más de sentido, en especial gracias a Santi por estar pendiente de mí y disponible cuando le he necesitado. Gracias porque "con vosotros me hallo a gusto". A mis "old managers" aunque sólo sea porque estoy en todas las cosas metida con ellos y me encanta, por las conversaciones de casi todo y por el compartir. A mi amigo Néstor por estar siempre, porque sé que si le digo que necesito ayuda estará (a no ser que tenga clase de teatro, inglés o tenis). Finalmente a mi amiga Covi, mitad de esta tesis es suya, gracias por ser mi Pepito Grillo, por acompañarme en todas las etapas de la vida, porque no hay nadie que me entienda más que tú sin la necesidad de tener que contarlo, gracias por creer y confiar en mí más de lo que yo nunca haré.

Dicen que nací con estrella y es algo de lo que nunca he dudado, por eso creo que caí en el búnker 2. Gracias a mis compañeros de búnker, si me pusiera a

enumerar seguramente escribiría otra tesis con tantas cosas vividas, habladas y sentidas. Gracias a Juanma por ser ejemplo de organización (gracias por aquella agenda), por acogerme desde el primer día, por darme consejos y por tirarme de las orejas cuando lo necesitaba, gracias por ser mi amigo. Gracias a Rosa, mi Chop, la chica rara que tenía una foto con Cayetano se convirtió en mi compañera de palmas, de visitas al baño, de historias, en mi amiga del alma. Sin duda una de las mejores cosas que me llevo del ICP sois vosotros dos.

Gracias a mis abuelos, porque si yo estoy aquí es por ellos. Gracias a mi abuela Tanis por sus consejos y sus reflexiones de vida, que aunque a veces da bastante rodeo si escuchas lo que dice tiene sentido y a mi abuela Maruja por ser mi fan número uno y partirse de risa con todas las tonterías que puedo llegar a decir. A los que se fueron, gracias por cuidarme desde ahí arriba, estoy segura que tenéis revolucionado el cielo y seguro que mi abuelo Jacinto está echándose un baile con "el tractor amarillo" de fondo mientras mi abuelo Luis está cantando a pleno pulmón "eres alta y delgada como tu madre".

A mi hermana Yazmina por su sensibilidad, su forma de amar y porque creo que no hay persona en la faz de la tierra que presuma de mí como ella. Por último gracias a mis padres, por acompañarme en el camino dejándome elegirlo libremente. Gracias a mi padre por su humildad y lealtad con sus principios, por quererme hasta límites insospechados. Gracias a mi madre por mimarme, cuidarme, gracias por su entrega y amor incondicional. Gracias papás por educarme y por quererme tanto.

La vida la entiendo como un regalo, una donación al mundo. Aquí os dejo un trozo de la mía, porque estoy convencida que lo que no se da, se pierde.

Cristina Valero Loricera

A mis abuelos

A mis padres

Contenido

Resumen- Summary

Resumen

La búsqueda de nuevos combustibles más sostenibles y seguros ha fomentado el desarrollo de nuevas fuentes de energía y procesos que hagan frente a los desafíos del mundo actual. En este sentido los biocombustibles juegan un papel cada vez más importante para satisfacer la demanda de combustibles líquidos, ya que los combustibles actuales se producen principalmente a partir de petróleo y las reservas se están agotando.

Los biocombustibles derivados de la biomasa tienen un alto contenido de oxígeno y un bajo poder calorífico, por tanto es deseable y necesario eliminar el oxígeno y de este modo hacer que se asemeje al petróleo crudo. Por tanto, se requiere mejorar la calidad del biocombustible mediante el proceso de hidrotratamiento catalítico. Mediante este proceso se inyecta hidrógeno y se reducen los compuestos oxigenados a estructuras hidrocarbonadas que mejoran la calidad del combustible.

Esta tesis se centró en el diseño de cinco series de nuevos catalizadores eficientes en la hidrodesoxigenación de biomasa incidiendo en las funcionalidades soporte y naturaleza de las fases activas. Incluyendo el estudio de la actividad de los catalizadores sintetizados frente a alimentaciones modelo, así como su caracterización físico-química exhaustiva con el fin de conseguir el conocimiento detallado de estos sistemas catalíticos que permita fijar los desarrollos de la presente línea de investigación.

La primera serie estudiada fue la de los catalizadores binarios Co-Mo soportados en sílices mesoporosas de diferente morfología (HMS, SBA-15, SBA-16 y DMS-1) presentados en el **Capítulo 4**. Los resultados de actividad confirmaron la importancia de la morfología del soporte en la reacción de hidrodesoxigenación (HDO): los catalizadores sulfurados CoMo/SBA-16 y CoMo/SBA-15 presentaron mayor actividad y selectividad que sus homólogos soportados en DMS-1 y HMS. De la caracterización físico-química exhaustiva tanto de los precursores calcinados como de los catalizadores frescos sulfurados y usados en reacción se concluyó que el aumento de la actividad catalítica está relacionado con una mejora en la exposición superficial de las fases activas y un aumento de la acidez de los catalizadores soportados en SBA-16 y SBA-15.

Teniendo en cuenta estos resultados, la investigación propuesta para el **Capítulo 5** se centró en la optimización de los catalizadores ternarios Co-Mo-W soportados en los materiales SBA-15 y SBA-16 modificados con una cantidad variable de fósforo. El catalizador CoMoW/SBA-16 modificado con la cantidad optimizada de fósforo (0.5 % en peso) resultó más activo en la reacción modelo de HDO de anisol. Los resultados obtenidos de caracterización de los mismos permitieron establecer una correlación entre el número de centros ácidos fuertes y la actividad catalítica. Además, los resultados XPS demostraron que la actividad catalítica está relacionada con el enriquecimiento superficial de la fase activa.

Para un tercer capítulo (**Capítulo 6**) de resultados se propusieron estudios sobre una serie de catalizadores ZnNi soportado sobre TiO_2, SiO_2-$2TiO_2$, TiO_2/SBA-15 y SBA-15 para estudiar el comportamiento del efecto del soporte en la reacción. El catalizador bifuncional ZnNi/Ti-SBA-15 resultó ser el catalizador más prometedor para la eliminación de oxígeno en biolíquidos. Los dos soportes SBA-

15 y Ti-SBA 15 fueron más eficaces que $2TiO_2$-SiO_2 y TiO_2 debido a su mayor área superficial BET y su acidez. La actividad del catalizador, la selectividad y la estabilidad están estrechamente relacionados con la cantidad de Ni accesible, NiO y centros ácidos del catalizador.

Durante la estancia en el Institut de Recherches sur la Catalyse et l'Environnement de Lyon (IRCELYON) se optó por el estudio de una serie de catalizadores de Pt-Ir soportados sobre materiales zeolíticos (HY y ZSM-5), resultados mostrados en el **Capítulo 7** de la memoria de tesis. Se obtuvo una mayor actividad catalítica para la reacción de HDO de fenol en los catalizadores de Pt (mono y bimetálico) soportados sobre HY. Este comportamiento se deba quizás a que la zeolita HY tiene un tamaño de poro mayor que ZSM-5 que beneficia la reacción HDO, además tiene mayor número de Al alrededor de los grupos silanol, que inducen una fuerte transferencia de grupos OH generando un gran número de centros ácidos.

Finalmente en el **Capítulo 8** se hizo un estudio sobre catalizadores de Pd soportados sobre Al_2O_3 y zeolita HY y mezcla de ambos. El catalizador que presentó una mayor actividad fue el Pd/20% HY-Al esto se explica con una mayor dispersión de la fase activa en la superficie del soporte. Se observó una disminución de la actividad del catalizador Pd/20% HY-Al al Pd / HY, indicando que una alta acidez del catalizador daría lugar a la desactivación del mismo.

Summary

The research for new sustainable and safe fuels has encouraged the development of new energy sources and processes that address the challenges of today's world. Thus biofuels play an increasingly important role in meeting the demand for liquid fuels paper, since the current fuel is mainly produced from oil and reserves are running low.

Biofuels derived from biomass have a high oxygen content and low calorific value, so it is desirable and necessary to remove oxygen and thus make resembles crude oil. Therefore, it is necessary to improve the quality of biofuel by catalytic hydrotreating process. Through this process, hydrogen is injected and oxygenates compounds are reduced to hydrocarbon structures that improve the quality of the fuel.

This thesis focused on the design of five series of new efficient catalysts in biomass hydrodeoxygenation influencing support functionality and nature of the active phases. Including the study of catalyst activity versus feeds synthesized model and its physicochemical characterization exhaustively in order to obtain detailed knowledge of these catalyst systems to enable the establishment of developments of this line of investigation.

The study was the first series of binary Co-Mo catalysts supported on mesoporous silicas of different morphology (HMS, SBA-15, SBA-16 and DMS-1)

presented in **Chapter 4**. Activity results confirmed the importance of morphology of the support in the reaction hydrodeoxygenation (HDO), sulfide CoMo/SBA-15 and CoMo/SBA-16 catalysts showed higher activity and selectivity than their counterparts supported on HMS and DMS-1. From the physicochemical thoroughly both precursors calcined, sulfurized fresh and used catalysts in reaction characterization was concluded that the increase of the catalytic activity is related to an improvement in surface exposure of the active phases and increased acidity catalysts supported on SBA-16 and SBA-15.

Given these results, the proposed research to **Chapter 5** focused on the optimization of the ternary catalysts Co-Mo-W supported on SBA-15 and SBA-16 materials modified with a variable amount of phosphorus. The modified with optimized amount of phosphorus (0.5 wt%) was more active with CoMoW/SBA-16 catalyst in the model reaction of anisole HDO. The results of characterization thereof are allowed to establish a correlation between the number of strong acid sites and the catalytic activity. Furthermore, XPS results showed that the catalytic activity is related to the surface enrichment of the active phase.

For a third chapter (**Chapter 6**) results of studies on a series ZnNi catalysts supported on TiO_2, SiO_2-$2TiO_2$, TiO_2/SBA-15 and SBA-15 to study the behavior of the effect of the support on the reaction is proposed. The bifunctional catalyst ZnNi/Ti-SBA-15 proved to be the most promising for the removal of oxygen in bioliquids catalyst. The two supports SBA-15 and Ti-SBA-15 were more effective than TiO_2-SiO_2 and $2TiO_2$ due to the higher BET surface area and acidity. The catalyst activity, selectivity and stability are closely related to the amount of accessible Ni, NiO and acid centers of the catalyst.

During the stay at the Institut de Recherches sur la Catalyse et l'Environnement de Lyon (IRCELYON) we chose to study a series of Pt-Ir catalysts supported on zeolite materials (HY and ZSM-5), the results shown in **Chapter 7** of the PhD dissertation. A higher catalytic activity for the reaction of phenol HDO catalysts Pt (mono and bimetallic) supported on HY was obtained. This behavior may be because the HY zeolite has a pore size greater than ZSM-5 benefiting HDO reaction, also has a greater number of Al around the silanol groups, which induce a strong transfer of OH groups to generate a number of acid sites.

Finally in **Chapter 8** a study Pd catalysts supported on Al_2O_3 and zeolite HY and mixture thereof was made. Pd/20% HY-Al catalyst had a higher activity, this is explained for greater dispersion of the active phase on the support surface. A decrease in catalyst activity Pd/20%HY-Al to Pd/HY, suggesting that high acidity of the catalyst would result in deactivation of the same.

Capítulo 1

Introducción

1. Introducción

Capítulo 1
Introducción

1.1. Situación energética actual

El consumo de energía se ha incrementado de forma considerable en los últimos años debido al aumento de la población mundial y a que nuestra forma de vida resulta cada vez más dependiente de la energía (1) (2). Debido al aumento progresivo del parque automovilístico en los países desarrollados y también en los emergentes, cabe esperar que los combustibles de transporte experimenten una demanda igualmente creciente (3). Resulta importante señalar el hecho de que el consumo de combustibles a gran escala lleva asociados importantes problemas económicos, políticos y medioambientales. En primer lugar, la disponibilidad de estos recursos naturales es limitada. En la actualidad el ritmo de consumo de los combustibles fósiles, que cada día resulta más elevado para cubrir las necesidades de los países industrializados y los países emergentes, es varios órdenes de magnitud superior al ritmo de regeneración de su generación. Esta descompensación entre las velocidades de consumo y de generación va a conducir necesariamente a su agotamiento en las próximas décadas (4). De entre todos los combustibles fósiles, el petróleo es el que tiene un umbral de agotamiento más

cercano (30-40 años). El consumo de combustibles fósiles para la generación de energía supone la emisión de grandes cantidades de CO_2 (un gas con un potente efecto invernadero) lo que contribuye de manera decisiva al calentamiento global y a problemas climáticos relacionados con este fenómeno (5). Por último, el tercer gran problema de los combustibles fósiles es su desigual distribución geográfica (los países del Medio-Este monopolizan un 60% de las reservas mundiales de petróleo) lo que causa importantes conflictos internacionales y obliga a transportar el combustible largas distancias para suministrarlos a los países no productores.

Ante esta situación los biocombustibles están experimentando una demanda creciente. La razones son varias. La primera es que es un recurso renovable y posee una huella de carbono bastante reducida, es decir una parte del CO_2 emitido a la atmósfera durante la combustión lo fijan de nuevo las plantas mediante la función clorofílica, lo que contrasta con los combustibles fósiles. La segunda es que, mientras que la electricidad y el calor pueden generarse a partir de un amplio espectro de alternativas (energías solar, eólica, hidroeléctrica, geotérmica, calor, etc.), la producción de combustibles líquidos para el transporte cuenta casi exclusivamente con el uso de biomasa como única fuente de carbono alternativa a los combustibles fósiles. Finalmente, las regulaciones medioambientales son cada vez más estrictas e imponen una producción de biocombustibles de forma creciente. *The Renewable Energy Directive* (RED) de la Unión Europea ha señalado que el combustible automoción incorporará un 10% de biocombustibles del total de combustible de automoción para el año 2020 (6). Con la nueva directiva, los biocombustibles deben contribuir a la reducción de CO_2 del 35%, y se plantea el objetivo de alcanzar el 50% de reducción de CO_2 para el año 2017 (60% para las nuevas plantas de producción). Por tanto, los combustibles derivados de la biomasa podrían ser los combustibles del futuro, ya que pueden

producirse dentro de un ciclo relativamente corto y se consideran benignos para el medio ambiente (3) (7).

1.2. Importancia de los hidrotratamientos

En los últimos años, se está llevando a cabo un gran esfuerzo en el campo de la investigación para encontrar combustibles alternativos y equivalentes a los tradicionales (gasolina y diesel) (8). A tal efecto, se están explorando nuevas vías de obtención de combustibles no convencionales, los cuales cabe esperar que jueguen un papel cada vez más importante para satisfacer dicha demanda. Se ha estimado que el 12.6% del suministro mundial de combustibles en 2030 provendrá de fuentes no convencionales (renovables). Se trata de aprovechar recursos naturales que no se agotan y a los que se puede recurrir de manera permanente. Pero en la actualidad, estas nuevas fuentes de energía no cubren una fracción muy pequeña de la demanda energética de los países ya sea porque se encuentran en una etapa de desarrollo tecnológico muy temprana o porque existen dificultades para su captación y concentración. Entre las energías no convencionales se pueden mencionar: la energía solar, la energía eólica, la energía química, la energía nuclear, la energía geotérmica y la energía de la biomasa. Estas energías renovables representan una parte importante de los suministros no convencionales, con una contribución cada vez más en valor absoluto y como porcentaje con respecto a las otras fuentes renovables.

1.3. Descripción de procesos

En la industria, el hidrotratamiento comprende un conjunto de reacciones que eliminan los heteroátomos no deseados (O, S, N) y se saturan de hidrógeno algunas moléculas insaturadas. Estas reacciones implican la hidrogenólisis del enlace C-M (M = S, O, N) y se clasifican según el heteroátomo que se va a eliminar. Las reacciones de mayor interés son la hidrodesulfuración (HDS) e hidrodesnitrogenación (HDN) para la mejora de la calidad de los combustibles fósiles y la hidrodesoxigenación (HDO) para la mejora de los biocombustibles. En las reacciones de HDS, HDN y HDO se eliminan los átomos S, N y O, respectivamente.

La transformación de la biomasa en productos aptos para su uso como combustible tiene lugar en diversas etapas. En primer lugar, la biomasa se somete a un proceso de pirólisis en atmósfera inerte a temperaturas moderadas (400-600 °C) obteniéndose una serie de productos gaseosos que posteriormente condensan produciendo un líquido oscuro y viscoso, denominado de forma genérica *bio-oil*. Este *bio-oil* está formado por una mezcla compleja de más de 400 compuestos oxigenados que incluyen ácidos, alcoholes, aldehídos, ésteres, cetonas y compuestos aromáticos (9) (10). Los *bio-oils* normalmente contienen un 25-30% en peso de agua y un 10% de partículas sólidas (coque). Dado que una gran parte de la energía de la lignocelulosa se retiene en el bio-oil (hasta un 70%), la pirólisis permite acumular la energía de la biomasa sólida en un líquido de menor volumen y, por tanto, más manejable (11). Una ventaja importante de la pirolisis, en comparación con otros métodos, es la simplicidad ya que requiere un solo reactor para producir el *bio-oil*.

Los *bio-oils* no pueden usarse directamente como combustibles ya que poseen un alto contenido en oxígeno lo que da lugar a una estabilidad baja y una elevada corrosividad del líquido. Para que los *bio-oils* puedan usarse como biocombustibles necesitan ser tratados catalíticamente para eliminar una parte del oxígeno y adecuar sus propiedades a las de los hidrocarburos líquidos (HL) (derivados del petróleo). Se han desarrollado varios procesos catalíticos para reducir el contenido en oxígeno de los *bio-oils*. Una de las rutas más simples es la **hidrodesoxigenación (HDO)**. En este proceso el *bio-oil* se trata bajo presión parcial de hidrógeno elevada sobre catalizadores de sulfuros de Co(Ni)-Mo(W) (12) (13). La reacción HDO elimina una parte importante del contenido de oxígeno presente en el *bio-oil* (en forma de H_2O) y mejora las propiedades del líquido hasta el punto que puede usarse como combustible o para ser mezclado con combustibles procedentes del petróleo.

En esta memoria se describe la preparación, caracterización y estudio de la actividad catalítica de varias series de catalizadores en la reacción de hidrodesoxigenación (HDO) de *bio-oil* o en su defecto de moléculas modelo oxigenadas, tales como anisol y fenol, con el objetivo de diseñar nuevos catalizadores para los procesos de HDO de *bio-oils*.

1.4. Biocombustibles

El término biocombustible se refiere a los combustibles líquidos o gaseosos para el sector de transporte, producidos principalmente a partir de la biomasa (14). A continuación se muestran los biocombustibles de primera y de segunda

generación, distinguidos por la materia prima utilizada y los avances tecnológicos necesarios para obtenerlos (15).

1.4.1. Biocombustibles de primera generación

Los biocombustibles de primera generación se producen a partir de azúcares como la caña de azúcar y del almidón de algunos cereales para fabricar bioetanol, así como de semillas (colza, soja, palma) de las que se extraen aceites que son susceptibles de procesos v esterificación para fabricar biodiesel. El bio-etanol se produce a partir de la fermentación de azúcar o el almidón y el biodiesel se produce mediante esterificación de aceites vegetales (16) (17) (18). Estos biocombustibles se han producido en muchos países (4) (19), pero han sufrido fuertes críticas debido a que requieren de biomasa de calidad alimentaria para su producción, necesitan tierras de cultivo y agua, cuando en realidad hay pobreza y hambre en varios países, y especialmente en el continente africano. Además, su eficiencia energética por unidad de tierra cultivada es relativamente baja (en comparación con los cultivos energéticos) (20), incrementan el precio de los alimentos, y producen un impacto negativo en la biodiversidad. Se señala además que la reducción en la emisión de gases de efecto invernadero resulta limitada al mismo tiempo que los costes de producción son relativamente altos (21).

1.4.2. Biocombustibles de segunda generación

Actualmente se están llevando a cabo numerosos estudios sobre biocombustibles de segunda generación para optimizar la eficiencia de transformación de biomasa a hidrocarburos líquidos (HL) mediante procesos que

transforman el material ligno-celulósico primero en gas de síntesis (CO+H2) y después su conversión en hidrocarburos o alcoholes (11) (22) (23) (24). El proceso para la producción de combustibles líquidos empleando como materia prima carbón, gas natural o biomasa tiene tres fases fundamentales. La primera es la gasificación de estos sustratos para producir el gas de síntesis mediante dosificación controlada del oxígeno o el aire. El gas de síntesis, con las especificaciones requeridas, se convierte en hidrocarburos/alcoholes mediante el proceso *Fisher-Tropsch.* El H_2 y el CO se recombinan en la superficie de catalizadores apropiados bajo presión y temperaturas elevadas. Finalmente, el producto resultante pasa a una fase de refino tradicional. También se han desarrollado los procesos de síntesis de alcoholes superiores a partir del gas de síntesis o hidrocarburos a partir de metanol (11) (25) (26) (27) (28) (29).

La elección del proceso de conversión depende del tipo y cantidad de biomasa disponible y de la forma deseada de la energía, es decir, de las necesidades de uso final, de las normas ambientales, de factores económicos y otros factores específicos de proyecto.

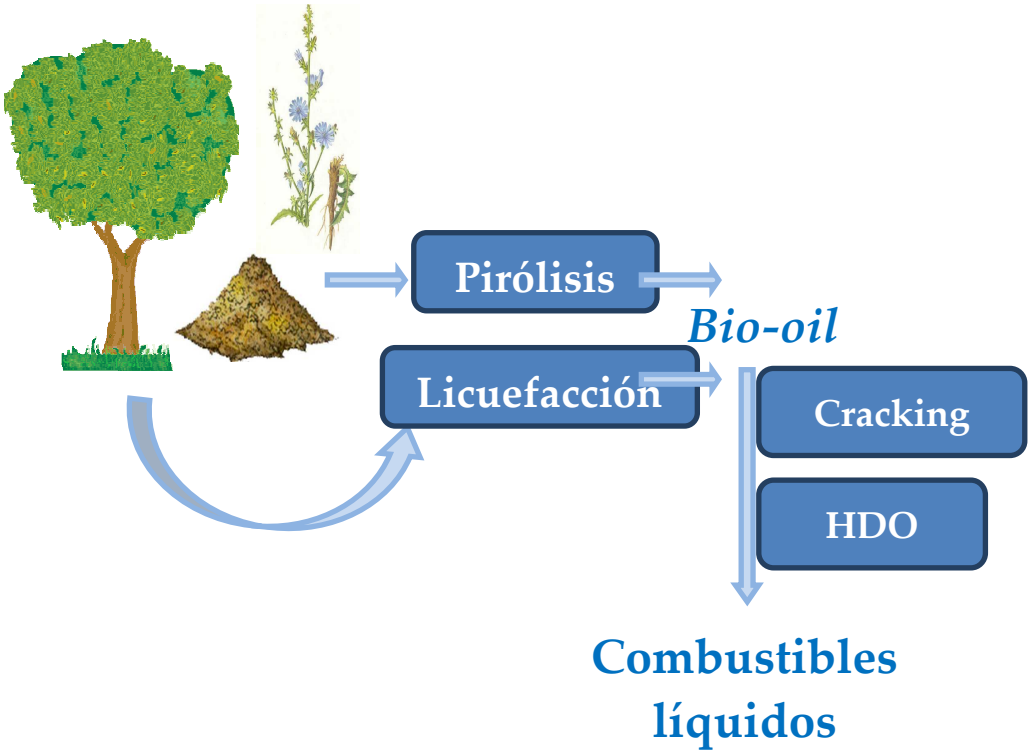

Figura 1.1. Procesos termoquímicos para elaboración de biocombustibles a partir de biomasa.

Un método prometedor consiste en la transformación de biomasa en lo que se conoce como *bio-oil* mediante licuefacción o pirolisis. Posteriormente, las propiedades de este *bio-oil* se mejoran mediante tratamiento catalítico. La gasificación de la biomasa y su conversión en hidrocarburos se realiza mediante la ***pirólisis flash*** a alta temperatura, seguida por la licuefacción de la biomasa (**licuefacción** a alta presión). A continuación se describen estos procesos en cierto detalle.

1.4.2.1. Pirólisis *flash* y licuefacción de la biomasa para la producción de *bio-oils*

La **pirólisis *flash*** es la primera etapa de transformación de biomasa lignocelulósica en *bio-oil* (11) (12) (30). La *pirólisis flash* es una técnica de densificación donde se incrementa tanto la densidad de masa como la de energía. La biomasa se trata a temperaturas intermedias (300-600 °C) con velocidades de calentamiento elevadas (10^3-10^4 K/s) y tiempos de residencia cortos (1-2 s) (31) (32) (33). De este modo, la densidad energética puede aumentar en un factor de 7-8 (34) (35). En la biomasa se identifican más de 300 compuestos diferentes, donde la composición específica de los productos depende del origen de ésta y de las condiciones de proceso usadas (31). Prácticamente cualquier tipo de biomasa, desde las fuentes más tradicionales como el bálago del cereal, residuos agro-forestales, lodos de aguas residuales y los residuos avícolas (33) (36) (37), puede procesarse mediante *pirólisis flash*.

La segunda ruta de conversión de biomasa en biocombustible es la licuefacción de la misma. La **licuefacción** directa consiste en el tratamiento de la biomasa con hidrógeno y/o monóxido de carbono bajo la presencia de un catalizador para obtener una fracción gaseosa, constituida fundamentalmente por CO_2 y metano, y una fracción líquida que puede considerarse como un combustible sintético. El proceso se lleva a cabo en un reactor a presión donde se introduce el material con un disolvente adecuado en presencia de un catalizador. El rango recomendado de temperatura varía entre 300 y 370 °C, dependiendo del tipo y de la composición de la biomasa. A temperaturas más elevadas, p. ej. 350 °C, se producen principalmente gases que inhiben la producción de *bio-oil*. A

temperaturas más bajas, del orden de 280 °C, la conversión de biomasa es muy reducida (38). Dado que los precursores de biomasa son residuos, se reducen notablemente las emisiones netas de dióxido de carbono (compensación de CO_2). En términos de rendimiento, no se puede comparar la licuefacción con la pirolisis. Sin embargo, la licuefacción tiene otras ventajas fundamentales, tales como la producción de un *bio-oil* estable y un medio de reacción acuoso, que no requiere secado, proceso que consume bastante energia (39).

Tabla 1.1. Composición del *bio-oil* (% en peso) en función del tipo de biomasa utilizado para su producción.

	Mazorcas de maíz	Rastrojos de maíz	Pino	Madera blanda	Madera dura
Ref.	(40)	(40)	(41) (32)	(42)	(42)
T [°C]	500	500	520	500	-
Reactor	lecho fluidizado	lecho fluidizado	flujo	rotatorio	flujo
Agua	25	9	24	29-32	20-21
Aldehídos	1	4	7	1-17	0-5
Ácidos	6	6	4	3-10	5-7
Carbohidratos	5	12	34	3-7	3-4
Fenólicos	4	2	15	2-3	2-3
Furanos, etc.	2	1	3	0-2	0-1
Alcoholes	0	0	2	0-1	0-4
Cetonas	11	7	4	2-4	7-8
Inclasificado	46	57	5	24-57	47-58

Fuente de tabla: (8)

Como se puede observar en la **Tabla 1.1**, el principal producto es agua, constituyendo entre un 10-30% en peso, pero también contiene: hidroxialdehídos, hidroxiacetonas, azúcares, ácidos carboxílicos, ésteres, furanos, guaiacoles y compuestos fenólicos, donde muchos de estos compuestos fenólicos se presentan como olígomeros (31) (43) (44) (45). El *bio-oil* que proviene de este tipo de biomasa

se caracteriza por presentar mejores balances energéticos, menores emisiones de gases de efecto invernadero, además de no requerir de tierras de cultivo y agua para su producción.

En la **Tabla 1.2** se comparan las propiedades del *bio-oil* con las del petróleo crudo en términos de contenido en agua, pH, densidad, viscosidad, poder calorífico y composición elemental (C, O, H, S y N). La principal diferencia radica en la composición elemental: el biocombustible procedente de la biomasa contiene entre un 10-40 % de oxígeno en peso (31) (32) (40). Esto afecta a la homogeneidad, polaridad, poder calorífico, viscosidad y acidez del aceite.

Tabla 1.2. Comparación entre *bio-oil* y petróleo crudo (16) (17) (31).

	Bio-oil	**Petróleo crudo**
Agua (% en peso)	15-30	0.1
pH	2.8-3.8	-
δ [kg/l]	1.05-1.25	0.86
$\mu_{50^{o}C}$[cP]	40-100	180
Poder calorífico [MJ/kg]	16-19	44
C [% en peso]	55-65	83-86
O [% en peso]	28-40	<1
H [% en peso]	5-7	11-14
S [% en peso]	<0.05	<4
N [% en peso]	<0.4	<1

Fuente de tabla: (8)

Las moléculas de bajo peso molecular que contienen oxígeno, especialmente alcoholes y aldehídos, actúan como una especie de agente tensoactivo para los compuestos de mayor peso molecular, que normalmente se consideran apolares e inmiscibles en agua y promueven la apariencia homogénea del aceite (46). Esto significa que los *bio-oils* procedentes de la biomasa tienen una

naturaleza polar debido al alto contenido de agua y, por lo tanto, son inmiscibles con el petróleo crudo. El alto contenido de agua y el alto contenido de oxígeno, producen una disminución en el poder calorífico del *bio-oil*, llegando a ser la mitad que el petróleo crudo (31) (32) (43) (47).

El pH del *bio-oil* está por lo general en el intervalo de 2 a 4, que está relacionado principalmente con el contenido de ácido acético y ácido fórmico (48). Su naturaleza ácida constituye un problema, ya que requiere de condiciones muy severas en los equipos de almacenamiento, transporte y procesado. Los materiales comunes de construcción tales como acero inoxidable y aluminio han demostrado ser inadecuados cuando se trabaja con *bio-oils* debido al problema de la corrosión (31) (47). Además, presentan cierta inestabilidad durante el almacenamiento, donde la viscosidad, el poder calorífico y la densidad se ven afectadas, debido a la presencia de compuestos orgánicos altamente reactivos. Se asume que las olefinas son activas en la repolimerización en presencia de aire. Además, las cetonas, aldehídos y ácidos orgánicos pueden reaccionar para formar éteres, acetales y hemiacetales, respectivamente. Este tipo de reacciones efectivamente aumentan el peso molecular medio del *bio-oil*, la viscosidad y el contenido de agua. La disminución global de la calidad del aceite puede considerarse como una función del tiempo de almacenamiento, resultado de la separación de fases (49) (50) (41).

1.4.2.2. HDO y *cracking* de *bio-oil*

Sobre la base de lo expuesto anteriormente resulta evidente que los grupos que contienen oxígeno son los responsables de algunas propiedades que causan el deterioro del combustible: alta viscosidad, menor volatilidad, corrosividad, inmiscibilidad con combustibles fósiles, inestabilidad térmica y tendencia a

polimerizar durante el almacenamiento y transporte (13). Además, producen depósitos carbonosos indeseados en la zona de combustión de los motores utilizados en automoción. Los ácidos carboxílicos, cetonas, aldehídos son los compuestos más agresivos presentes en los *bio-oils.*

La mejora del *bio-oil* a escala comercial, en términos de costes e infraestructuras, está todavía en fase de estudio. Una solución ideal de esa mejora del *bio-oil* sería el empleo de la infraestructura actual de las refinerías de petróleo, capaz de reducir las emisiones de CO_2 y así reducir el impacto ambiental (51). Los procesos principales desarrollados para la mejora del *bio-oil* son: **hidrodesoxigenación (HDO)** y ***cracking***. Sin embargo, el proceso de HDO parece ser el más factible puesto que en la infraestructura actual presente en las refinerías, las unidades de hidrotratamiento tradicionales se pueden utilizar para llevar a cabo reacciones de HDO, donde el oxígeno se elimina bajo presión de hidrógeno y en presencia de un catalizador adecuado. Los compuestos que contienen oxígeno se reducen a estructuras hidrocarbonadas cuyo contenido calorífico se incrementa notablemente con respecto al compuesto oxigenado.

En la **Tabla 1.3** se resumen diferentes vías de producción de biocombustibles así como los costes de producción estimados. Los precios se basan en el poder calorífico inferior (LHV). La biomasa como alimento implica una gran flexibilidad con respecto a la fuente de alimentación.

Tabla 1.3. Información general de las rutas potenciales para la producción de combustibles derivados de la biomasa

Tecnología	Alimentación	Plataforma química	Precio [$/top[a]]	Ref.
HDO	Biomasa	*Bio-oil*	740	(52)
craqueo sobre zeolitas	Biomasa	*Bio-oil*	-	
Fischer-Tropsch	Biomasa	Gas de síntesis	840-1134	(53)
H_2	Biomasa	Gas de síntesis	378-714	(28) (53)
Metanol	Biomasa	Gas de síntesis	546-588	(53)
Alcoholes pesados	Biomasa	Gas de síntesis	1302-1512	(53)
Bioetanol	Caña de azúcar	-	369-922	(54)
Bioetanol	Maíz	-	1107-1475	(54)
Bioetanol	Biomasa	-	1475-2029	(54)
Biodiesel	Aceite de canola	-	586-1171	(54)
Biodiesel	Aceite de palma	-	586-937	(54)
Gasolina	Aceite crudo	-	1046	(55) (56)

[a]tep: tonelada equivalente de petróleo, 1 top = 42 GJ. Fuente de tabla: (8)

Los precios de producción estimados (**Tabla 1.3**) indican que la HDO constituye una solución factible para la producción de combustibles sintéticos (16) (57)(58)(59)

En los últimos años ha habido un creciente interés con relación a la investigación científica en reacciones de HDO y se han investigado intensamente la mejora de los biocumbustibles provenientes de la biomasa (31) (32) (43) (60), y los mecanismos de reacción así como la cinética de la reacción de HDO (10) (12) (13) (8).

1.5. Mejora de la calidad del *bio-oil*. Eliminación de oxígeno (HDO)

El procesado catalítico de mejora del *bio-oil* es complicado debido a la gran diversidad de compuestos presentes. Como se observa en la **Figura 1.2** en la unidad de hidrotratamiento pueden ocurrir de forma simultánea, reacciones de c*racking*, descarbonilación, descarboxilación, hidrocraqueo, hidrodesoxigenación, hidrogenación y polimerización (61) (62) (63).

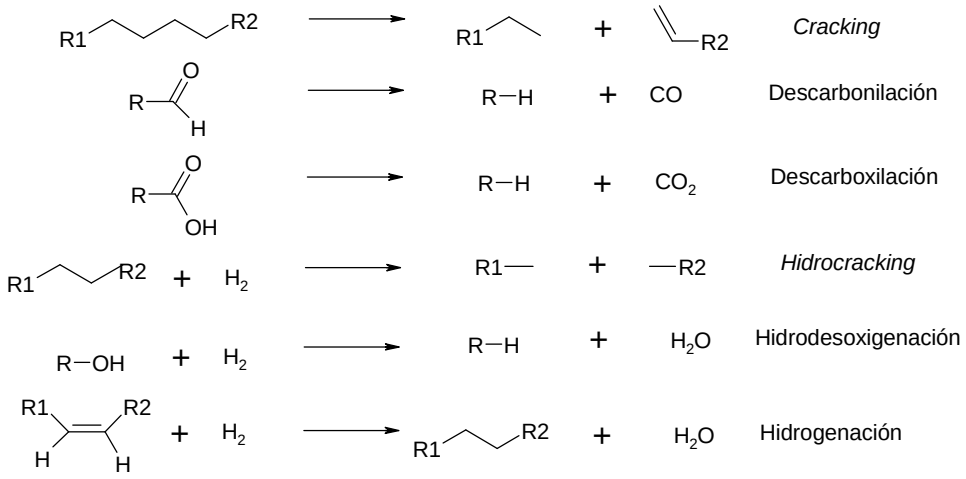

Figura 1.2. Reacciones asociadas a la mejora de la calidad del *bio-oil*. (8)

La gran variedad de compuestos presentes en el *bio-oil*, originada por la diversidad de las materias primas utilizadas (biomasa), hace que exista un número elevado de factores que influencian el proceso de HDO. Para obtener una visión general de la termodinámica del proceso, Barin (64) ha partido de un modelo sencillo como es la reacción del fenol con hidrógeno:

$$fenol + H_2 \leftrightarrow benceno + H_2O \quad \text{(Ec. 1.1)}$$

$$fenol + 4H_2 \leftrightarrow ciclohexano + H_2O \quad \text{(Ec. 1.2)}$$

Las reacciones de transformación del fenol (**Ecuación 1.1** y **Ecuación 1.2**) han sido propuestas por Massoth y col. (65) y Yunquan y col. (66). El cálculo de equilibrio termodinámico para las dos reacciones muestra que para conseguir la conversión completa de fenol se necesitan temperaturas de al menos 600 ºC a presión atmosférica y en condiciones estequiométricas. El aumento de la presión o el exceso de hidrógeno desplazarán el equilibrio hacia la conversión completa. Se han hecho cálculos similares con furfural, pero los resultados fueron similares. De esta manera, la termodinámica no parece constituir un obstáculo para los procesos, cuando se evalúan las reacciones más simples de las moléculas modelo.

En la práctica es difícil evaluar la conversión de cada componente individual del biocombustible. Por eso dos parámetros importantes son el rendimiento (R) (**Ecuación 1.3**) y el grado de desoxigenación (HDO) (**Ecuación 1.4**):

$$R_{biocombustible} = \left(\frac{m_{biocombustible}}{m_{alimentación}} \right) \cdot 100 \quad \text{(Ec. 1.3)}$$

$$Grado_{HDO} = \left(1 - \frac{\%\, peso_{o-producto}}{\%\, peso_{o-alimentación}} \right) \cdot 100 \quad \text{(Ec. 1.4)}$$

donde $R_{biocombustible}$ es el rendimiento de biocombustible, $m_{biocombustible}$ es la masa del biocombustible producido, $m_{alimentación}$ es la masa de la alimentación, $Grado_{HDO}$ es el grado de hidrodesoxigenación y $\%peso_o$ es el tanto por ciento de oxígeno en el biocombustible. Los dos parámetros juntos puedan dar una visión general de la efectividad del proceso, debido a que el rendimiento de biocombustible describe la selectividad hacia el producto deseado y el grado de desoxigenación describe cual

ha sido la eficacia en la eliminación de oxígeno, o lo que es lo mismo la calidad del biocombustible producido. Sin embargo, por separado los parámetros son menos descriptivos ya que para ninguna reacción no se suele lograr un rendimiento del 100%. Además, ninguno de los parámetros se refiere a la eliminación de especies específicas perjudiciales y éstas tienen que ser analizadas en detalle.

La reacción de HDO puede escribirse tal como ha propuesto Bridgwater (44) (67):

$$CH_{1.4}O_{0.4} + 0.7H_2 \leftrightarrow 1^n CH_2^{\ n} + 0.4H_2O \qquad \text{(Ec. 1.5)}$$

Aquí "CH_2" representa un producto de hidrocarburos no especificado. Esta reacción es exotérmica y cálculos sencillos han mostrado un calor global promedio de reacción del orden de 2.4 MJ/kg cuando se usan biocombustibles (68). Se forma agua como producto de la reacción, por lo que se observan dos fases: una orgánica y otra acuosa. Sin embargo, también se ha observado la aparición de dos fases orgánicas debido a la producción de compuestos orgánicos con densidades inferiores y superiores que el agua. En el caso que se formen aceites ligeros, éstos se separan en la parte superior del agua, mientras que la fase pesada continúa bajo la fase acuosa. Las dos fases orgánicas formadas se observan generalmente en los casos con diferentes grados de desoxigenación, dándose un alto grado de fraccionamiento de la alimentación (17).

En el caso de la eliminación completa de oxígeno de los compuestos oxigenados la estequiometría de la **Ecuación 1.5**, predice un máximo de rendimiento de un 56-58% (44). Sin embargo, la desoxigenación completa indicada por la **Ecuación 1.5** rara vez se consigue debido al alto número de reacciones que

tienen lugar. En su lugar se forma un producto con oxígeno residual. En este sentido, un trabajo de Venderbosch y col. (17) describe la estequiometría de HDO según la **Ecuación 1.6** (excluyendo la fase gaseosa):

$$CH_{1.47}O_{0.56} + 0.39H_2 \leftrightarrow 0.74CH_{1.47}O_{0.11} + 0.19CH_{3.02}O_{1.09} + 0.29H_2O \quad \text{(Ec. 1.6)}$$

Donde el compuesto $CH_{1.47}O_{0.11}$ es de la fase orgánica y $CH_{3.02}O_{1.09}$ es el compuesto orgánico más ligero que se sitúa sobre la fase acuosa. En la fase orgánica resultante, la relación O/C es significativamente menor (0.11) que la proveniente del *bio-oil* de partida (0.56). Sin embargo, en la fase acuosa se observa una mayor relación O/C (1.09) que en el *bio-oil* de origen (17).

1.5.1. Condiciones que afectan a la reacción de HDO

Como se ha descrito con anterioridad, la hidrodesoxigenación (HDO) aprovecha las instalaciones ya usadas en la industria de refinería para el proceso de hidrodesulfuración (HDS) (44) (69).

En cuanto a las condiciones de reacción de HDO, se usa generalmente alta presión, en el rango de 7.5 a 30 MPa (32) (70) (71). La bibliografía de patentes describe un intervalo de presiones de operación entre 1.0 -12 MPa (72) (73). El trabajar a presión elevada favorece la solubilidad del hidrógeno en el *bio-oil* y por lo tanto una mayor disponibilidad de hidrógeno en la vecindad del catalizador. Esto aumenta la velocidad de reacción y disminuye aún más la coquización en el reactor (17) (74).

Además, el tiempo de residencia juega un papel clave, pues a mayores tiempos de residencia mejor es el grado de desoxigenación obtenido (32). En un

reactor de flujo continuo, Elliott y col. (71) mostraron que el contenido de oxígeno de un *bio-oil* mejorado disminuyó desde el 21% al 10% en peso al disminuir la LHSV (velocidad espacial de líquidos) de 0.70 h^{-1} a 0.25 h^{-1} con un catalizador de Pd/C y unas condiciones de reacción de 14 MPa y 340°C. En general la LHSV debería ser del orden de 0.1-1.5 h^{-1} (73). Este tiempo de permanencia es válido tanto para los reactores de flujo continuo como para autoclaves, que por lo general se llevan a cabo en períodos de tiempo de 3-4 horas (63) (75) (76).

Con relación a la temperatura de reacción, en general, las reacciones de HDO se llevan a cabo a temperaturas entre 250-450 °C (17) (69). Como la reacción es exotérmica y los cálculos de equilibrio predicen una conversión potencial completa de compuestos modelo a temperaturas por encima de 600 °C, parece que la elección de la temperatura de funcionamiento debe estar basada principalmente en aspectos cinéticos. El efecto de la temperatura fue investigado por Elliott y Hart (71) con un catalizador de Pd/C en un reactor de lecho fijo a 140 bar. Se encontró que el rendimiento de aceite se redujo del 75% al 56% cuando se aumenta la temperatura desde 310 °C a 360 °C. Además, se observó un aumento en el rendimiento de los productos gaseosos por un factor de 3. El grado de desoxigenación se incrementó de un 65% a 310 °C a un 70% a 340 °C. Por encima de 340 °C el grado de desoxigenación no aumentó, en su lugar se produjo cracking. Las observaciones de Elliot y col. (71) se refieren a la reactividad de los diferentes grupos funcionales presentes en el biocombustible derivado de la biomasa (57) (77).

La **Tabla 1.4** resume las energías de activación, las temperaturas requeridas para que una reacción tenga lugar y el consumo de hidrógeno para HDO de diferentes compuestos modelo sobre un catalizador Co-MoS_2/Al_2O_3.

Tabla 1.4. Energía de activación (E_A), temperatura de reactividad (Tr), y el consumo de hidrógeno para la desoxigenación de diferentes grupos funcionales o moléculas sobre un catalizador $CoMoS_2/Al_2O_3$. Datos: (57)

Molécula	E_A [kJ/mol]	Tr [°C]	Consumo de H_2
Cetona	50	203	$2H_2$/molécula
Ácido carboxílico	109	283	$3H_2$/molécula
Metoxi-fenol	113	301	$\approx 6H_2$/molécula
4-Metil fenol	141	340	$\approx 4H_2$/molécula
2-Etil fenol	150	367	$\approx 4H_2$/molécula
Dibenzofurano	143	417	$\approx 8H_2$/molécula

Fuente de tabla: (8)

En este catalizador la energía de activación para la reacción de hidrodesoxigenación de cetonas es relativamente baja, por lo que estas moléculas pueden ser desoxigenadas a temperaturas cercanas a 200 °C. Sin embargo, para los enlaces más complejos o impedidos estéricamente por el oxígeno, como es el caso de los furanos o fenoles orto sustituidos, es necesaria una temperatura significativamente más alta para que la reacción proceda. Sobre esta base, la reactividad aparente de diferentes compuestos se ha resumido como (13):

alcohol > cetona > alquiléter > ácido carboxílico ≈ m-/p- fenol ≈ naftol > diariléter ≈ o- fenol ≈ alquilfurano > benzofurano > dibenzofurano (Ec. 1.7)

Un aspecto importante de la reacción HDO es el consumo de hidrógeno. En un trabajo de Venderbosch y col. (17) se investigó el consumo de hidrógeno necesario para producir biocombustible en función de la tasa de desoxigenación sobre un catalizador de Ru/C en un reactor de lecho fijo. El consumo de hidrógeno sufre un gran incremento a medida que aumenta el grado de hidrodesoxigenación de la biomasa. Los compuestos oxigenados altamente reactivos, como cetonas, se

convierten fácilmente con bajo consumo de hidrógeno, pero una pequeña parte del oxígeno se une a los compuestos más estables. Así, las moléculas más complejas sufren una hidrogenación inicial/saturación de la molécula y por lo tanto, el consumo de hidrógeno supera la predicción estequiométrica (13). Obviamente, el consumo de hidrógeno para HDO de una cetona es significativamente menor que para un furano. En general esto significa que con el fin de alcanzar el 50% de hidrodesoxigenación (aprox. 25% en peso de oxígeno en el *bio-oil*) se necesitan 8 moles de H_2 por kg de biocombustible producido. Por el contrario, la hidrodesoxigenación completa (y por consiguiente la saturación) tiene un consumo de hidrógeno de aproximadamente 25 mol H_2/kg, es decir, tres veces más.

El uso de hidrógeno para mejorar los *bio-oils* tiene dos efectos con respecto al mecanismo de reacción: la eliminación de oxígeno y la saturación de los enlaces dobles. Esto se traduce en la disminución de la relación O/C y el aumento de la relación H/C, los cuales incrementan el poder calorífico (HV) del combustible. Mercader y col. (70) encontraron que el poder calorífico superior del producto final era aproximadamente proporcional al hidrógeno consumido en el proceso, con un aumento en el HV de 1 MJ/kg por cada mol/kg H_2 consumido.

En la **Tabla 1.5** se resumen los intervalos ideales de trabajo de los distintos parámetros experimentales que influyen en la reacción de HDO.

Tabla 1.5. Resumen de los parámetros experimentales que influyen en la producción de biocombustibles

Parámetros experimentales que influyen en HDO	Intervalo de trabajo	Referencias
Presión (P°)	Generalmente: 7.5-30 MPa Patentes: 1.0-12 MPa	(32) (70) (71) (72) (73)
Velocidad espacial (LHSV)	0.1-1.5 h^{-1}	(73)
Tiempo de reacción (t)	3-4 horas	(63) (75) (76)
Temperatura (T°)	250- 450 °C	(17) (69)
Consumo de H_2	50% HDO: 8 moles H_2/Kg biocombustible producido 100% HDO: 25 moles H_2/Kg biocombustible producido	(13)

1.6. Catalizadores usados en reacciones de HDO

En los últimos años, se ha dedicado un gran esfuerzo al estudio de sistemas catalíticos capaces de mejorar la calidad del *bio-oil* en términos de contenido de oxígeno, es decir, catalizadores activos y estables en reacciones de HDO. A continuación, se describen algunos de los resultados más relevantes encontrados en bibliografía.

1.6.1. Sulfuros/óxidos

Los sulfuros tradicionalmente utilizados en los procesos de hidrotratamiento convencionales, Co-MoS_2 y Ni-MoS_2 se han estudiado

ampliamente en la reacción de HDO (12) (13) (74) (77) (78) (79) (80) (81) (82) (83) (84) (85) (86) (87) (88) (89) (90) (91) (92).

Samolada y col. (78) utilizaron un catalizador $CoMoS_2/Al_2O_3$ en reacciones de HDO y observaron que la producción de biocombustible depende del grado de hidrodesoxigenación. El rendimiento de biocombustible disminuye con el grado de hidrodesoxigenación, debido al aumento de producción de agua y de productos gaseosos. Esto demuestra que cuando se utilizan condiciones severas para eliminar el oxígeno, se produce una disminución significativa en el rendimiento de biocombustible; éste cae desde el 55% al 30% mientras que el grado de hidrodesoxigenación aumenta del 78% al 100%. Por consiguiente, un aspecto importante a evaluar es la cantidad de oxígeno que debe ser eliminada (93).

En estos catalizadores, el Co y el Ni se utilizan como promotores. El efecto del promotor es donar electrones a los átomos de molibdeno. Esto debilita el enlace entre el molibdeno y el azufre y favorece la formación de sitios vacantes de azufre (CUS- *coordinatively unsaturated sites*) que son los sitios activos, tanto en HDS como en reacciones HDO (65) (90) (94) (95) (96).

Romero y col. (95) estudiaron catalizadores de MoS_2 en la reacción de HDO de 2-etilfenol, propusieron el siguiente mecanismo de reacción (**Figura 1.3**).

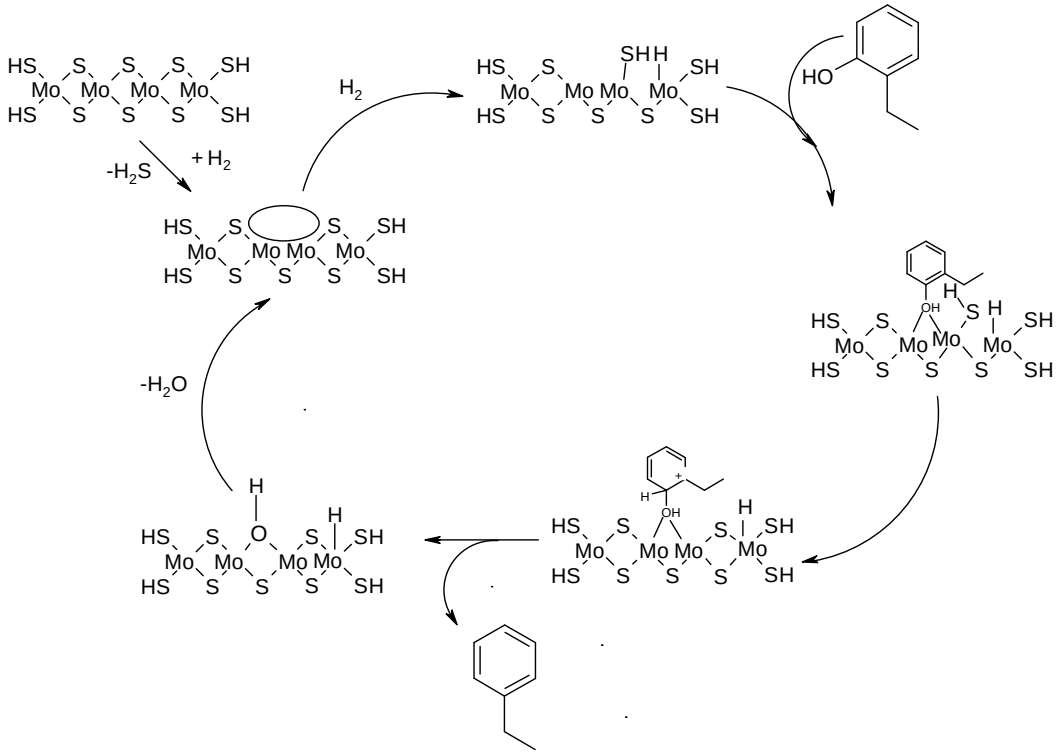

Figura 1.3. Mecanismo propuesto para HDO de 2-etilfenol sobre un catalizador Co–MoS_2. Fuente imagen: Romero y col. (95)

El oxígeno de la molécula se adsorbe sobre una vacante localizada en el borde de la lámina de MoS_2, activando el compuesto. Las especies SH también estarán presentes a lo largo del borde del catalizador ya que éstos se generan a partir del H_2 alimentado. Esto permite la donación de protón del azufre a la molécula adjunta, que forma un carbocatión, dando lugar a la rotura directa del enlace C-O y formando el compuesto desoxigenado. El oxígeno se elimina después formando la molécula de agua. Para que el mecanismo funcione, es necesario que el oxígeno del grupo formado se adsorba sobre el metal y se elimine como agua. Durante el transcurso de la reacción estos autores observaron una disminución de la actividad como consecuencia de la pérdida de fase activa, sulfuro. Para evitar

esto, otros autores han propuesto la co-alimentación de H_2S en el sistema regenerando los sitios sulfuros favoreciendo de este modo una mayor estabilidad del catalizador (89) (94) (97) (98). Además, Senol y col. (97) (98) observaron que parte del azufre que se pierde de la fase activa da lugar a la formación de pequeñas cantidades de tioles y sulfuros durante la reacción de HDO, concluyendo que estos catalizadores contaminan el biocombustible con azufre. Una solución interesante sería el uso de un catalizador industrial tipo Co-MoS_2/Al_2O_3 utilizado en las reacciones de HDS, que es activo en la eliminación de azufre del biocombustible a un nivel de unas pocas ppm (99).

En base a estudios teóricos mediante DFT- *Density functional theory*, Moberg y col. (100) propusieron la fase MoO_3 como fase activa en catalizadores de HDO. Estos cálculos muestran que la reacción de HDO sobre catalizadores oxídicos es posible asumiendo la adsorción de moléculas que contienen oxígeno sobre un metal coordinativamente insaturado, seguido de donación de protones y por último produciéndose la desorción. Por tanto, la actividad de catalizadores de tipo óxido y sulfuro se basa principalmente en la presencia de sitios ácidos. El paso inicial de la quimisorción es la interacción con un sitio ácido de Lewis, donde se atrae el par solitario del oxígeno de la molécula hacia los sitios insaturados del metal. Por esta razón se puede especular que la reactividad del sistema en parte se debe a la disponibilidad y la fuerza de los sitios ácidos de Lewis en el catalizador. Gervasini y Auroux (101) propusieron que la acidez de diferentes óxidos de metales de transición sigue la siguiente tendencia:

$$Cr_2O_3 > WO_3 > Nb_2O_5 > Ta_2O_5 > V_2O_5 \approx MoO_3$$

Esta información sobre la acidez debe compararse con la fuerza relativa de los sitios ácidos de Lewis de los diferentes óxidos. Esto fue investigado por Li y Dixon (102), quienes mostraron que la fuerza relativa de los sitios ácidos de Lewis sigue el siguiente orden:

$WO_3 > MoO_3 > Cr_2O_3$

El paso siguiente del mecanismo de reacción de HDO es la donación del protón, es decir, hidrógeno disponible en la superficie del catalizador, que para los óxidos estará presente como grupos hidroxilo (ácidos de Brønsted). En este sentido, Busca y col. (103) mostraron que la acidez de Brønsted de diferentes óxidos sigue el orden (100):

$WO_3 > MoO_3 > V_2O_5 > Nb_2O_5$

Los datos de actividad en la reacción de hidrodesoxigenación revelan que MoO_3 funciona como un catalizador debido a la presencia de sitios ácidos fuertes de Lewis y sitios ácidos fuertes hidroxilo tipo Brønsted. Sin embargo, Whiffen y Smith (104) investigaron HDO de 4-metilfenol sobre catalizadores másicos MoO_3 y MoS_2 en un reactor discontinuo y encontraron que la actividad de MoO_3 era menor que la de MoS_2 para esta reacción. Así, la fase MoO_3 parece que no es la mejor fase activa para un catalizador de tipo óxido. Otros óxidos interesantes para HDO es el WO_3 por su alta disponibilidad de sitios ácidos. Echeandía y col. (105) investigaron óxidos de W y Ni-W sobre carbón activo en la reacción de HDO de fenol. Estos catalizadores presentaron buena actividad para la reacción de HDO y especialmente el sistema de Ni-W que presentó un gran potencial para la conversión completa de la molécula modelo. Además, estos autores apenas

observaron desactivación por coque después de 6 h de reacción y lo adscribieron a la baja acidez del soporte.

1.6.2. Metales nobles

El mecanismo de HDO sobre catalizadores basados en metales nobles soportados todavía no está claro. Generalmente se reconoce que los metales son donadores de hidrógeno, pero la adsorción de los compuestos oxigenados puede tener lugar en el metal (106) (107) (108) o en la interfase metal-soporte (**Figura 1.4**) (106) (109) (110). Esto indica que estos sistemas catalíticos pueden ser activos en las diferentes reacciones, ya que muchos de los catalizadores de metales nobles son activos para HDO.

Gutiérrez y col. (76) estudiaron la actividad de metales nobles tales como Rh, Pd y Pt soportados sobre ZrO_2 en la reacción de HDO de guaiacol. Estos autores observaron que la tendencia de actividad fue:

$Rh/ZrO_2 > Co\text{-}MoS_2/Al_2O_3 > Pd/ZrO_2 > Pt/ZrO_2$

Wildschut y col. (63) (111) estudiaron sistemas Ru/C, Pd/C y Pt/C para la reacción de HDO de *bio-oil* procedente de *pirólisis flash*. Ru/C y Pd/C resultaron buenos catalizadores para el proceso pues mostraron un alto grado de desoxigenación y altos rendimientos de *bio-oil*, con relación a los catalizadores de referencia $Co\text{-}MoS_2/Al_2O_3$ y $Ni\text{-}MoS_2/Al_2O_3$.

A través de experimentos en un reactor discontinuo (autoclave) con una mezcla de compuestos representativos de un *bio-oil* procedente de una biomasa

real, Fiesk y col. (112) encontraron unos resultados positivos para el catalizador Pt/Al_2O_3 tanto para HDO como para reformado con vapor, sugiriendo que se podría producir H_2 *in situ*. Este enfoque es atractivo para el gasto que se produce al tener que suministrar hidrógeno, ya que es una de las principales desventajas de la tecnología HDO. Sin embargo, el catalizador sufría una desactivación significativa debido a la formación de carbón.

En resumen, los catalizadores basados en metales nobles Ru, Rh, Pd y posiblemente Pt, también parecen ser catalizadores potenciales para la reacción de HDO, pero el alto precio de los metales los hace poco atractivos.

1.6.3. Metales de transición

Como alternativa a los catalizadores de metales nobles se estudió el uso de los catalizadores de metales de transición que tienen precios significativamente más bajos (113). Yankovlev y col. (114) investigaron catalizadores basados en níquel para la reacción de HDO de anisol en un reactor de lecho fijo a temperaturas en el rango de 250 a 400 °C y presiones en el intervalo de 5 a 20 bares. La actividad de estos catalizadores sigue el orden:

$Ni\text{-}Cu/CeO_2 > Ni\text{-}Cu/Al_2O_3 > Ni/Al_2O_3 >> Ni/ZrO_2 > Ni\text{-}Cu/ZrO_2$

A partir de estos resultados se demostró que la fase Ni-Cu tiene un potencial para eliminar completamente el contenido de oxígeno de anisol. En genera,l se puede decir que los catalizadores basados en Ni soportados son una alternativa a otros metales debido tanto al precio como a sus propiedades hidrogenantes. En este sentido, se encontró que los catalizadores de Ni-Cu

soportados exhiben una alta actividad para hidrodesoxigenación de guaiacol debido a la formación de nanopartículas de Ni pequeñas (115). En el trabajo de Echeandía y col. (105) se estudió el efecto de diferentes catalizadores de óxido de Ni-W soportados sobre carbón activo para la reacción de HDO de fenol. Con el carbón activo se obtuvo una menor formación de coque sobre la superficie de los catalizadores que usando alúmina. Sitthisa y Resasco (116) estudiaron la reacción de HDO de furfural sobre catalizadores de Cu, Pd y Ni soportados sobre sílice, obteniendo altos valores de conversión con los catalizadores basados en Pd y Ni. La adición de Zn a Ni tiene un efecto positivo sobre éste en términos de dispersión de Ni (117) y en rendimiento catalítico (118) (119) (120). El uso de óxidos metálicos parcialmente reducidos también ha sido propuesto, siendo eficaces en la mejora de los *bio-oil* (114) (121) (122). Así, la forma de óxido activa los grupos oxo y el metal reducido activa el hidrógeno.

Se han propuesto diferentes mecanismos de reacción para estos sistemas, indicando que los catalizadores deben ser bifuncionales. La bifuncionalidad del catalizador implica dos aspectos. Por un lado, la necesaria **activación de los compuestos oxigenados**, que probablemente se podría lograr mediante un catión expuesto, a menudo asociada con el soporte del catalizador. Esto se debe combinar con la facilidad para la **donación de hidrógeno** a los compuestos oxigenados, que podría tener lugar en los metales de transición, ya que tienen potencial suficiente para activar el H_2 (123) (124) (125) (114). El mecanismo combinado se presenta en la **Figura 1.4**, donde la adsorción y la activación de los compuestos oxigenados tienen lugar sobre el soporte.

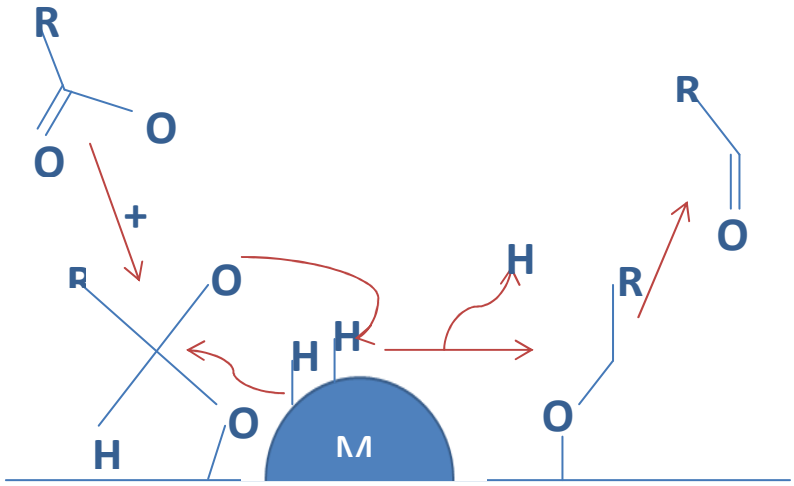

Figura 1.4. Mecanismo de reacción HDO sobre catalizadores soportados sobre metales nobles y de transición. (123) (124).

Un enfoque diferente de catalizadores de metales de transición para HDO fue publicado por Zhao y col. (126) (127) (128). En estos estudios se vio que los fenoles podrían hidrogenarse mediante un sistema acuoso heterogéneo: catalizador metálico mezclado con un ácido mineral en una solución fenol/agua. En estos sistemas hidrogenados la desoxigenación puede llevarse a cabo por la extracción de agua con el ácido mineral, en este caso la donación procede del metal (127). Tanto Pd/C como Ni Raney (aleación Níquel- alúmina) resultaron efectivos cuando se combinaron con Nafion/SiO_2 como ácido mineral (128). Sin embargo, este concepto se ha realizado solamente en reactor tipo autoclave. Además la influencia del uso de altas concentraciones de fenol debería evaluarse para determinar el potencial del sistema.

1.6.4. Fosfuros de metales de transición

Otras fases activas estudiadas en reacciones de HDO han sido los fosfuros de metales de transición. Estas fases activas han presentado una elevada actividad en la reacción de HDS, superando incluso a los sulfuros tradicionales. Zhao y col. (129) estudiaron la actividad en la reacción de HDO de guaiacol en un reactor de lecho fijo donde una corriente de gas H_2/N_2 se saturó con otra de guaicol gaseoso (H_2/guaiacol = 33) sobre catalizadores fosfuro soportados sobre SiO_2. El orden de actividad que se encontró fue el siguiente:

$$Ni_2P/SiO_2 > Co_2P/SiO_2 > Fe_2P/SiO_2 > WP/SiO_2 > MoP/SiO_2$$

Se observó que estos catalizadores eran menos activos que Pd/Al_2O_3, pero más estables que $Co\text{-}MoS_2/Al_2O_3$. Así, las ventajas de estos catalizadores son su gran disponibilidad y bajo precio, comparado con los catalizadores de metales nobles y su alta capacidad para activar el hidrógeno.

De todo lo expuesto con anterioridad se deduce que son muchas las fases activas que se pueden utilizar en reacciones de HDO, pero estos sistemas catalíticos requieren investigaciones adicionales para poder evaluar su potencial en este tipo de reacciones.

1.7. Soportes usados en reacciones de HDO

La selección del soporte de la fase activa es esencial para la formulación de un catalizador y, por supuesto, para las reacciones de HDO (114).

1.7.1. Alúmina

El soporte comercial más ampliamente utilizado en unidades de hidrotratamiento es Al_2O_3, sin embargo este soporte no ha resultado adecuado para reacciones de HDO, ya que en presencia de grandes cantidades de agua se convierte a bohemita (AlO (OH)) (12) (17) (130). El trabajo de Laurent y Delmon (130) con Ni-MoS_2/γ-Al_2O_3 demostró que la formación de bohemita daba lugar a la oxidación del níquel en el catalizador. Estos óxidos de níquel eran inactivos con respecto a la reacción de HDO y además podrían bloquear otros sitios de Mo o Ni en el catalizador. Al tratar el catalizador con una mezcla de dodecano y agua durante 60 h, se observó una disminución en dos tercios de la actividad con relación al mismo catalizador tratado sólo con dodecano (12) (130).

Además, Popov y col. (131) encontraron que 2/3 de la alúmina se recubre de especies fenólicas cuando se satura a 400 °C en un flujo de fenol/Ar. Las especies observadas en la superficie, parece que son precursoras de la formación de carbono, lo que indica que hay gran probabilidad de que se forme coque en este tipo de soportes. Esto se debe a la presencia de sitios ácidos de tipo Lewis en el soporte que favorecen la acumulación no deseada de depósitos de coque (132). Como alternativa a Al_2O_3, el carbón parece ser un soporte bastante prometedor (63) (105) (133) (134) (135). La naturaleza neutra del carbón es beneficiosa, ya que la tendencia a formar carbón se reduce en comparación con Al_2O_3 (105) (134).

1.7.2. Sílice

También el SiO_2 se ha considerado como un soporte adecuado para HDO ya que al igual que el carbón tiene un carácter neutro y por lo tanto tiene una afinidad relativamente baja para la formación de coque (129). Propov y col. (131) mostraron que la concentración de especies de fenol adsorbidas en el SiO_2 es solamente de 12% respecto a la concentración que se encuentra en Al_2O_3 a 400 °C. El SiO_2 sólo interactua con el fenol a través de enlaces de hidrógeno, pero en el caso de la Al_2O_3 se observó que las especies se adsorben más fuertemente en los sitios ácidos de la superficie para inducir la disociación del fenol (136) y así favorecer la formación de coque (92).

1.7.3. Zeolitas

En estudios relativamente recientes se ha puesto de manifiesto que las ***zeolitas*** son mejores soportes que la alúmina o sílice para la reacción de hidrodesoxigenación de fenol ya que poseen un sistema regular de poros y centros ácidos fuertes (137). El término zeolita se usa para denotar aluminosilicatos cristalinos microporosos (poros de menos de 2 nm de diámetro) de origen natural o sintético. Estructuralmente, las zeolitas son complejas y pueden considerarse polímeros inorgánicos cristalinos basados en una red tridimensional de tetraedros (T) de SiO_4 y AlO_4 enlazados entre sí a través de los oxígenos de los vértices. Estas redes dan lugar a una serie de canales y cavidades de dimensiones moleculares. Además, como consecuencia de la sustitución isomórfica de una proporción de iones Si^{4+} por iones Al^{3+}, se introduce una cierta carga negativa en la estructura que

se compensa con protones (ácidos de Brønsted) u otro tipo de cationes (ácidos de Lewis) que se sitúan en el interior de los poros (138).

Aunque la aplicación de las zeolitas está a veces limitada por sus pequeñas aperturas de poro, son los catalizadores más ampliamente aplicados en la industria, especialmente en el área del refino del petróleo. La importancia de las zeolitas en diferentes procesos catalíticos se atribuye a sus propiedades singulares en comparación con otros materiales. Estas propiedades son: (i) Elevada superficie específica y capacidad de adsorción. (ii) Posibilidad de controlar sus propiedades de adsorción ajustando la hidrofobia o la hidrofilia de los materiales. (iii) Posibilidad de incorporar en la estructura zeolítica diferentes especies metálicas. (iv) Los tamaños de los canales y las cavidades están en el intervalo de dimensiones de muchas moléculas de interés (5-12 Å). (v) La especificidad de la estructura porosa hace que estos materiales puedan reconocer moléculas. El éxito considerable de las zeolitas se debe especialmente a la última propiedad señalada: la selectividad de forma (selectividad hacia el reactivo, hacia el producto y en el estado de transición). Su capacidad de acomodar sólo moléculas de una forma particular y tamaño dentro de los poros de su estructura ha conducido a desarrollos significativos. Por esta razón, se estudió el efecto de diferentes zeolitas con el fin de estudiar el efecto sobre la reacción de HDO de fenol.

1.7.4. Aluminosilicatos y silicatos mesoporosos

Los ***materiales mesoporosos*** abren un amplio abanico de posibilidades, debido principalmente a su elevada superficie específica lo que favorece la dispersión de la fase activa. Además, poseen tamaño de poros uniforme,

propiedades ácidas modulables mediante la incorporación de heteroátomos dentro de la mesoestructura así como estabilidad térmica.

1.7.4.1. **MCM-41**

A **B** **C**

Figura 1.5. Estructuras de: A) MCM-41; B) MCM-48 y C) MCM-50. (139).

Los primeros materiales de este tipo (M41S) se descubrieron en la empresa Mobil en 1992 (**Figura 1.5**). Presentan tres estructuras principalmente: la hexagonal, MCM-41; cúbica, MCM-48; y la laminar, MCM-50. El sistema MCM-41 se ha estudiado ampliamente y aplicado en la preparación de catalizadores activos en reacciones de hidrotratamiento (140) (141) (142) (143). Los sistemas MCM-41 se caracterizan por poseer poros uniformes y tamaño de poro ajustable en el rango de 16 a 100 Å mediante elección de un tensoactivo adecuado y condiciones de reacción y químicas auxiliares. Además, la distribución de tamaños de poro es tan estrecha como la de las zeolitas convencionales. Una vez sintetizados, se calcinan a 500 °C para eliminar las moléculas de tensoactivo, y así se obtiene un material con superficie específica elevada. Normalmente, se usan iones de amonio cuaternario de cadena larga [$C_nH_{2n+1}(CH_3)_3N^+$ (n=8-16)] como tensoactivos, los cuales son

conocidos por formar micelas o fases de cristal líquido en disoluciones acuosas. Las especies de silicato y aluminosilicato condensan y polimerizan alrededor de las partes hidrofílicas de los agregados de tensoactivos para formar las paredes de los sólidos porosos al mismo tiempo que rodean a las moléculas de tensoactivo (139).

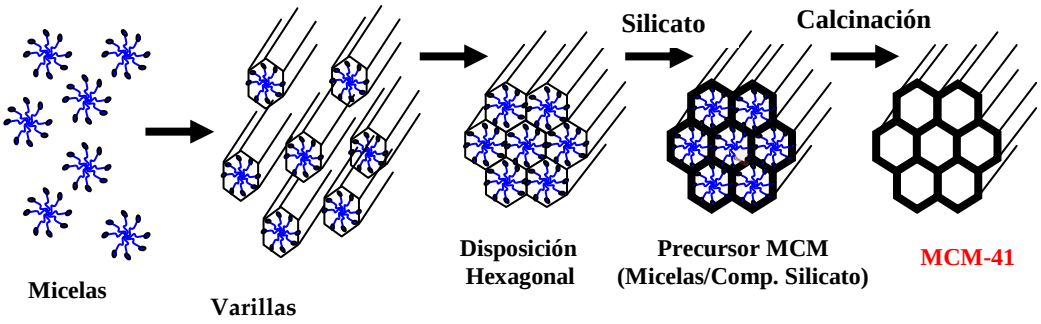

Figura 1.6. Modelo esquemático de la síntesis del MCM-41 siguiendo una estructuración tipo cristal líquido. (139).

Antes de la incorporación del precursor inorgánico las moléculas de tensoactivo están en equilibrio dinámico de diferentes formas de micelas y moléculas simples. El primer paso, conducido por interacciones electrostáticas, es la formación de pares iónicos entre las especies iónicas polidentadas y policargadas y las especies de tensoactivo. El par iónico se autoorganiza posteriormente dando lugar a una mesofase teniendo normalmente estructura de cristal líquido, esto es, hexagonal, cúbica o laminar. La estructura de la mesofase depende de la composición de la mezcla, del pH y de la temperatura (144). El último paso es la condensación de las especies inorgánicas dando lugar a una estructura rígida.

Se conoce con cierto detalle que parámetros tales como el tipo de tensoactivo, la relación molar silicio/tensoactivo, el pH, la temperatura de reacción

y el uso de condiciones hidrotermales afectan al diámetro de poro, al espesor de la pared y a la estructura resultante. La influencia de estos y otros parámetros de síntesis se han discutido de forma muy extensa en la bibliografía (145) (146) (147).

El éxito obtenido en la preparación de sílice mesoporosa, que a menudo no se usa como catalizador tal cual, fue el punto de partida para la preparación de sistemas con aplicación potencial en catálisis. Normalmente se añaden funciones catalíticas al incorporar sitios activos en las paredes de la sílice o por deposición de especies activas en la superficie interior del material. La incorporación de heteroátomos en la red de materiales micro o mesoporosos ha abierto nuevas oportunidades en el campo de la catálisis heterogénea. Esto es especialmente importante ya que la sustitución de la sílice permite un ajuste de la acidez o creación de las propiedades redox, similar a lo observado en aluminosilicatos amorfos y zeolitas. La modificación de la composición de la red es posible por síntesis directa, es decir, a partir de mezclas que contienen tanto sílice como el heteroátomo a incorporar, o por post-tratamiento de un material mesoporoso de sílice inicialmente preparado. Mediante el primer método se consigue que el heteroelemento esté homogéneamente incorporado, mientras que por el segundo, se modifica principalmente la superficie de las paredes (139).

Una de las características interesantes de los sólidos mesoporosos para su uso en catálisis es la multitud de posibilidades para modificarlos. Las modificaciones se pueden usar para ajustar la funcionalidad superficial, para incorporar funciones catalíticas o para cambiar las propiedades texturales. Las ventajas de usar sólidos mesoporosos en catálisis se deben a sus tamaños de poro relativamente elevados que facilitan la transferencia de masa y a la elevada área

superficial que permite una elevada concentración de sitios activos por unidad de masa del material.

En este sentido, los aluminosilicatos mesoporosos modificados con Al (Al-MCM-41), resultaron muy activos en el craqueo catalítico de aceite de palma para producir combustibles líquidos (148) (149) y también para tratar vapores procedentes de la *pirólisis flash* de biomasa (150) (151). La sílice mesoporosa MCM-41 posee propiedades texturales muy interesantes (alta superficie específica, en el rango de 600-1000 m^2/g y una distribución uniforme de diámetros de poro comprendidos entre 1.5 a 10 nm) (152), que son necesarias para procesar moléculas más voluminosos. Además, su elevada área superficial favorece la dispersión de la fase activa, y una menor resistencia a los grupos ácidos OH que los de las zeolitas, por lo que reduce la formación de coque.

En las rutas sintéticas que utilizan tensoactivos iónicos como agentes directores de la estructura (S), éstos se unen con un precursor inorgánico (I) de carga opuesta mediante interacciones coulombianas (S^+I^- , S^-I^+) (153). Otra ruta, en la que el tensoactivo y las especies inorgánicas tienen la misma carga, la formación de la mesoestructura implica el uso de contraiones (X^- o M^+) que deben estar presentes en cantidades estequiométricas, ($S^+ X^- I^+$, $S^- M^+ I^-$) (139).

Tanev y Pinnavaia (154) (155) desarrollaron una ruta neutra para la preparación de materiales mesoporosos usando tensoactivos no iónicos. La formación de materiales mesoporosos, en este caso, se basa en un enlace de hidrógeno entre el precursor inorgánico neutro (I°) y el tensoactivo no iónico. El tensoactivo no iónico podría ser una amina primaria neutra (S°) o un tensoactivo tipo polioxietileno (N°). El uso de tensoactivos no iónicos es triple: intentar inducir la precipitación, limitar o controlar el tamaño de partícula o el tamaño de partícula

de agregado y formar poros (156). Las ventajas más interesantes al utilizar tensoactivos no iónicos en relación a los iónicos son: (i) son más baratos, no tóxicos y biodegradables; (ii) originan mayores espesores de pared mejorando la estabilidad hidrotermal de los óxidos mesoporosos; (iii) mayor facilidad para ajustar el diámetro de poro medio al variar tanto el tipo como la concentración de tensoactivo; (iv) la eliminación del disolvente resulta más fácil pues la unión entre el tensoactivo y la red inorgánica es más fácil de disociar; (v) tendencia a producir materiales con paredes más gruesas y tamaños de partículas más pequeños. De todo esto se puede inferir, que estos tensoactivos son prometedores agentes directores de estructura para la síntesis de nuevos materiales porosos (139).

1.7.4.2. HMS

Uno de los materiales mesoporosos preparados a partir de una ruta sintética neutra fue el HMS (*Hexagonal Mesoporous Silica*) y ha sido usado en numerosas reacciones de hidrotratamiento (157) (158) (159) (160). El HMS se preparó por la ruta (S°I°), en la que se favorece el enlaces de hidrógeno y autounión entre el tensoactivo amino neutro y el precursor inorgánico neutro. En comparación con la sílice MCM-41 estructurada electrostáticamente, los materiales HMS muestran un mayor espesor de pared de la red (1.7-3.0 nm), mayor estabilidad térmica y tamaños cristalinos más pequeños, pero un menor ordenamiento a largo alcance (161) (162).

1.7.4.3. SBA-15

Zhao y col. (163) llevaron a cabo un gran progreso en la preparación de sílice mesoporosa al usar copolímeros triblock-polioxialquileno (Pluronic) para la síntesis de materiales de gran tamaño de poro: con forma hexagonal bidimensional SBA-15 (*S*anta *BA*rbara No. 15) y con estructura cúbica SBA-16, así como otras estructuras. El mecanismo propuesto es $S^+X^-I^+$, puesto que el copolímero está positivamente cargado bajo las condiciones de reacción. El material SBA-15 puede prepararse con tamaños de poro entre 4.6 y 30.0 nm (164) y espesores de pared de 3.1 y 6.4 nm cambiando tanto la temperatura como el tiempo de reacción, además presenta mejores propiedades hidrotermales que los materiales MCM-41 (debido a la formación de paredes más gruesas) (163). SBA-15 tiene poros hexagonales en una matriz de dos dimensiones con canales largos en una dimensión (grupo *P6mm*) (165). Además ofrece ventajas tales como elevada superficie específica, composición variable y alta estabilidad térmica. La modificación de SBA- 15 con Ti aumenta la dispersión de los metales activos sobre el catalizador (166), y también aumenta el rendimiento catalítico (167). Sin embargo, en algunas condiciones las nanopartículas de Ti tienden a sinterizar con el consiguiente bloqueo de la accesibilidad de los reactivos a los centros activos (168).

1.7.4.4. SBA-16

Otro material mesoporoso es el SBA-16. Este material fue sintetizado inicialmente por Zhao et al. (163) en presencia de copolímero triblock Pluronic F127. Al contrario que el SBA-15, éste tiene una estructura cúbica (*Im3m*) de sílice mesoporosa (SBA-16). Se utiliza menos como soporte de catalizadores de hidrotratamiento, aunque ambos materiales SBA-15 y SBA-16 se mantienen

estables en agua hirviendo durante 48 h (169). En el material SBA-16 cada uno de sus mesoporos está conectado a sus ocho vecinos más cercanos (170). Esto permite una mejor difusión de las moléculas grandes en los poros. De esta manera sería interesante comparar las propiedades mesoporosas con DMS-1 (*Disordered mesoporous silica*) que tiene la disposición desordenada de sus microporos con alta área superficial (en el 600-1000 m^2/g), mientras que la disposición atómica es desordenada en una manera similar a la sílice mesoporosa (171).

El efecto de la funcionalización de los materiales mesoporosos con los grupos–PO_3H_2 se estudió previamente en la reacción de hidrodesulfuración de dibenzotiofeno y 4,6-dimetildibenzotiofeno sobre los catalizadores binarios Co-Mo soportados en HMS (157) (172) o SBA-15 (173). Por esta razón, en esta Tesis resulta interesante el estudio de estos materiales en las reacciones HDO.

1.7.5. Óxidos metálicos

Otros óxidos metálicos como el ZrO_2 y CeO_2 se han considerado como soportes adecuados para la síntesis de catalizadores. El ZrO_2 tiene acidez débil, significativamente inferior a la de Al_2O_3 (174). Tanto el ZrO_2 como el CeO_2 pueden activar los compuestos oxigenados en su superficie, como se muestra en la **Figura 1.4** y con ello aumentar la actividad. Así, se presentan como una fórmula atractiva para el diseño de nuevos catalizadores (76) (114) (174) (175).

En resumen, se deben considerar dos aspectos en la elección del soporte para la reacción de HDO. Por un lado, su afinidad para la **formación de coque debe ser baja**, lo que requiere una baja acidez. Por otra parte, el soporte debe tener

la **capacidad de activar los compuestos oxigenados**. El último es especialmente importante cuando se trata de catalizadores de metales de transición.

1.8. Desactivación

El principal problema en las reacciones de HDO es la desactivación. Esto puede ocurrir por envenenamiento de los centros activos por especies oxigenadas o agua, sinterización del catalizador, deposición de los metales (específicamente metales alcalinos), o coque (68). La extensión de estos fenómenos depende del catalizador, pero la deposición de coque parece ser un problema general y la vía principal de desactivación del catalizador (176).

El carbón se forma principalmente a través de la polimerización y reacciones de policondensación en la superficie catalítica, formando especies poliaromáticas. Esto tiene como consecuencia el bloqueo de los centros activos de los catalizadores (176). Específicamente para el catalizador Co-MoS_2/Al_2O_3, se ha demostrado que el coque se acumula rápidamente debido a la fuerte adsorción de especies poliaromáticas. Estas especies llenan el volumen de poros del catalizador durante la puesta en marcha del sistema. En un estudio de Fonseca et al. (177) se puso de relieve que aproximadamente un tercio del volumen total de poros de un catalizador Co-MoS_2/Al_2O_3 queda ocupado por el coque durante la etapa de deposición inicial de carbono, a partir de ese momento se alcanza el estado estacionario en el que se limita la deposición de carbono adicional (176).

La velocidad de reacción para formar coque está en gran medida controlada por la alimentación, si bien las condiciones del proceso también juegan un papel importante. Con respecto a la alimentación de hidrocarburos, los

alquenos y aromáticos tienen una mayor afinidad para formar coque, debido a una interacción mucho más fuerte con la superficie catalítica que la que tienen los hidrocarburos saturados. Esta unión más fuerte a la superficie hace más probable que el hidrocarburo deposite coque. Para los hidrocarburos que contienen oxígeno se ha identificado que los compuestos con un átomo de carbono tienen mayor afinidad hacia la formación de coque por reacciones poliméricas en la superficie del catalizador (176).

En general, se observa un aumento del grado de coquización con el aumento de la acidez del catalizador influenciado por los sitios ácidos Lewis y Brønsted. La función principal de los sitios ácidos Lewis es la de unir las especies a la superficie del catalizador. Los sitios ácidos de Brønsted funcionan donando protones a los compuestos de relevancia, formando carbocationes que se cree que son los responsables de la coquización (176). Esto constituye un problema ya que también se requieren sitios ácidos en el mecanismo de HDO. Además se ha encontrado que la presencia de ácidos orgánicos (como ácido acético) en la alimentación incrementaría la afinidad para la formación de carbono, ya que cataliza la ruta de degradación térmica (111).

Con todo lo expuesto con anterioridad, esta Memoria se centra en la síntesis de catalizadores basados en diferentes metales y sustratos con el fin de obtener sistemas catalíticos activos para la hidrodesoxigenación de compuestos oxigenados provenientes de la biomasa.

1.9. Bibliografía

1. United Nations Department of Economic and Social Affairs. *http://www.un.org/esa/population/*. 2010.

2. U.S. Energy Information Administration Independent Statistics and Analysis. *http://www.eia.doe.gov/*. 2010.

3. *Production of bioethanol from lignocellulosic materials via the biochemical pathway: A review.* **Balat, M.** s.l. : Energy Conversion and Management , 2011, Vols. (52) 858-875.

4. BP Statistical Review of World Energy. *bp.com/statiscalreview.* 2010.

5. **progress, Worldwatch institute center for american.** *American energy: the renewable path to energy security.* 2006.

6. **Comission, European.** *COMMUNICATION FROM THE COMMISSION TO THE EUROPEAN PARLIAMENT, THE COUNCIL, THE EUROPEAN ECONOMIC AND SOCIAL COMMITTEE AND THE COMMITTEE OF THE REGIONS Renewable Energy: a major player in the European energy market.* Bruselas : s.n., 2012.

7. *Production and energetic utilization of wood from short.* **Roedl, A.** s.l. : The International Journal of Life Cycle Assessment, 2010, Vols. (15) 567-578.

8. *A review of catalytic upgrading of bio-oil to engine fuels.* **P.M. Mortensen, J.D. Grunwaldta, P.A. Jensena, K.G. Knudsenc, A.D. Jensena.** s.l. : Applied Catalysis A: General, 2011, Vols. (407) 1-19.

9. *Developments in direct thermochemical liquefaction of biomass: 1983-1990.* **D.C. Elliott, D. Beckman, A.V. Bridgwater, J.P. Diebold, S.B. Gevert, Y. Solantausta.** s.l. : Energy & Fuels, 1991, Vols. (5) 399-410.

10. *Pyrolysis of Wood/Biomass for Bio-oil: A Critical Review.* **D. Mohan, C.U. Pittman Jr., P.H. Steele.** s.l. : Energy & Fuels, 2006, Vols. (20) 848-889.

11. *Synthesis of transportation fuels from biomass: Chemistry, catalysts, and engineering.* **G.W. Huber, S. Iborra, A. Corma.** s.l. : Chemical Reviews, 2006, Vols. (106) 4044-4098.

12. *Historical Developments in Hydroprocessing Bio-oils.* **Elliott, D.C.** s.l. : Energy & Fuels, 2007, Vols. (21) 1792-1815.

13. *Catalytic hydrodeoxygenation.* **Furimsky, E.** s.l. : Applied Catalysis A: General, 2000, Vols. (199) 147-190.

14. *Biofuels sources, biofuel policy, biofuel economy and global biofuel projections.* **Demirbas, A.** s.l. : Energy Conversion and Management, 2008, Vols. (49) 2106-2116.

15. **C.M.M., Machado.** *Situación de los Biocombustibles de 2da y 3era Generación en América Latina y Caribe.* s.l. : Organización Latinoamericana de Energía y el Instituto Interamericano de Cooperación para la Agricultura, 2010.

16. *Consider upgrading pyrolysis oils into renewable fuels.* **J. Holmgren, R. Marinageli, P. Nair, D.C. Elliiott, R. Bain.** s.l. : Hydrocarbon Processing, 2008, Vols. 95-103.

17. *Stabilization of biomass-derived pyrolysis oils.* **R.H. Venderbosch, A.R. Ardiyanti, J. Wildschut, A. Oasmaa, H.J. Heeres.** s.l. : Journal of Chemical Technology and Biotechnology, 2010, Vols. (85) 674-686.

18. **Wenzel, H.** *Breaking the biomass bottleneck of the fossil free society.* Concito : Technical report, 2010.

19. *Competitive liquid biofuels from biomass.* **Demirbas, M.F.** s.l. : Applied Energy, Vols. (88) 17-28.

20. *Energy production from biomass (part 1): overview of biomass.* **McKendry, P.** s.l. : Bioresource Technology, 2002, Vols. (83) 37-46.

21. *Production of first and second generation biofuels: A comprehensive review.* **S.N. Naik, V.V. Goud, P.K. Rout, A.K. Dalai.** 578-597, s.l. : Renewable and Sustainable Energy Reviews, 2010, Vol. (14).

22. *Thermochemical conversion of biomass to second generation biofuels through.* **T. Damartzis, A. Zabaniotou.** s.l. : Renewable and Sustainable Energy Reviews, 2011, Vols. (15) 366-378.

23. *Review of syngas production via biomass DFBGs.* **K. Göransson, U. Söderlind, J. He, W. Zhang.** s.l. : Renewable and Sustainable Energy Reviews, 2011, Vols. (15) 482-492.

24. *Exploration of the possibilities for production of Fischer.* **M.J.A. Tijmensen, A.P.C. Faaij, C.N. Hamelinck, M.R.M. van Hardeveld.** s.l. : Biomass and Energy, 2002, Vols. (23) 129-152.

25. *Coupling of Alcohols over Alkali-Promoted Cobalt–Molybdenum Sulfide.* **J.M. Christensen, P.A. Jensen, N.C. Schiødt, A.D. Jensen.** s.l. : ChemCatChem, 2010, Vols. (2) 523-526.

26. *Effects of H2S and process conditions in the synthesis of mixed alcohols from syngas over alkali promoted cobalt-molybdenum sulfide.* **J.M. Christensen, P.M. Mortensen, R. Trane, P.A. Jensen, A.D. Jensen.** s.l. : Applied Catalysis A: General, 2009, Vols. (366) 29-43.

27. *Methanol-to-hydrocarbons: process technology.* **Keil, F.J.** s.l. : Microporous and Mesoporous Materials, 1999, Vols. (29) 49-66.

28. **P.L. Spath, M.K. Mann, W.A. Amos.** *Update of hydrogen from biomass-determination of the delivered cost of hydrogen.* s.l. : Technical report, U.S. Department of Energy's Hydrogen Program, 2003.

29. *Methanol-to-hydrocarbons: catalytic materials and their behavior.* **Stöcker, M.** s.l. : Microporous and Mesoporous Materials, 1999, Vols. (29) 3-48.

30. *Technoeconomic Assessment of Direct Biomass Liquefaction to Transportation Fuels.* **D.C. Elliot, E.G. Baker, D. Beckman, Y. Solantausta, V. Tolenhiemo, S. Gevert, C. Hörnell, A. Östman, B. Kjellström.** s.l. : Biomass, 1990, Vols. (22) 251-269.

31. *Review of biomass pyrolysis oil properties and upgrading research.* **Q. Zhang, J. Chang, T. Wang, Y. Xu.** s.l. : Energy Conversion and Management, 2007, Vols. (48) 87-92.

32. *Fast pyrolysis technology development.* **R.H. Venderbosch, W. Prins.** s.l. : Biofuels, Bioproducts and Biorefining, 2010, Vols. (4) 178-208.

33. *Review Biomass for energy.* **Bridgwater, T.** s.l. : Journal of the Science of Food and Agriculture, 2006, Vols. (86) 1755-1768.

34. *Use of mobile fast pyrolysis plants to densify biomass and reduce biomass handling costs—A preliminary assessment.* **P.C. Badger, P. Fransham.** s.l. : Biomass & Bioenergy, 2006, Vols. (86) 1755-1768.

35. *The BTL2 Process of Biomass Utilization Entrained-Flow Gasification of Pyrolyzed Biomass Slurries.* **K. Raffelt, E. Henrich, A. Koegel, R. Stahl, J. Steinhardt, F. Weirich.** s.l. : Applied Biochemistry and Biotechnology, 2006, Vols. (129) 153-164.

36. *Biowastes to biofuels.* **A. Demirbas, M. Balat, H. Balat.** s.l. : Energy Conversion and Management, 2011, Vols. (52) 1815-1828.

37. *Pyrolysis of biomass to produce fuels and chemical feedstocks.* **Yaman, S.** s.l. : Energy Conversion and Management, 2004, Vols. (45) 651-671.

38. *A review on process conditions for optimum bio-oil yield in hydrothermal liquefaction of biomass.* **J. Akhtar, N.A.S. Amin.** s.l. : Renewable and Sustainable Energy Reviews , 2011, Vols. (15) 1615-1624.

39. *Hydrothermal liquefaction of biomass: A review of subcritical water technologies.* **S.S. Toor, L. Rosendahl, A. Rudolf.** s.l. : Energy, 2011, Vols. (36) 2328-2342.

40. *Bio-oil and bio-char production from corn cobs and stover by fast pyrolysis.* **C.A. Mullen, A.A. Boateng, N.M. Goldberg, I.M. Lima, D.A. Laird, K.B. Hicks.** s.l. : Biomass and Bioenergy, 2010, Vols. (34) 67-74.

41. *Fast Pyrolysis of Forestry Residue. 3. Storage Stability of Liquid Fuel.* **A. Oasmaa, E. Juoppala.** s.l. : Energy & Fuels, 2003, Vols. (17) 1075-1084.

42. *Norms and standards for fast pyrolysis liquids 1. Round robin test.* **A. Oasmaa, D. Meier.** s.l. : Journal of Analytical and Applied Pyrolysis, 2005, Vols. (73) 323-334.

43. *Overview of Applications of Biomass Fast Pyrolysis Oil.* **S. Czernik, A.V. Brigwater.** s.l. : Energy & Fuels, 2004, Vols. (18) 590-598.

44. *Production of high grade fuels and chemicals from catalytic pyrolysis of biomass.* **Bridgwater, A.V.** s.l. : Catalysis Today, 1996, Vols. (29) 285-295.

45. *Bio-fuels from thermochemical conversion of renewable resources: A review.* **H.B. Goyal, D. Seal, R.C. Saxena.** s.l. : Renewable and Sustainable Energy Reviews, 2008, Vols. (12) 504-517.

46. **A.V. Bridgwater, S. Czernik, J. Piskorz.** *Progress Thermochemical Biomass Conversion.* s.l. : Blackwell Wissenschafts- Verlag 977-997, 2001.

47. *Overview of fuel properties of biomass fast pyrolysis oils.* **L. Qiang, L. Wen-Zhi, Z. Xi-Feng.** s.l. : Energy Conversion and Management, 2009, Vols. (50) 1376-1383.

48. *Acidity of Biomass Fast Pyrolysis Bio-oils.* **A. Oasmaa, D.C. Elliot, J. Korhonen.** s.l. : Energy & Fuels, 2010, Vols. (24) 6548-6554.

49. *Characterization and stability analysis of wood-derived bio-oil.* **J.D. Adjaye, R.K. Sharma, N.N. Bakhshi.** s.l. : Fuel Processing Technology, 1992, Vols. (31) 241-256.

50. *Bio-oils obtained by vacuum pyrolysis of softwood bark as a liquid fuel for gas turbines. Part II: Stability and ageing of bio-oil and its blends with methanol and a pyrolytic aqueous phase.* **M.E. Boucher, A. Chaala, H. Pakdel, C. Roy.** s.l. : Biomass & Bioenergy, 2000, Vols. (19) 351-361.

51. **R. Pachauri, A. Reisinger.** *Climate change 2007: synthesis report. Contribution of working groups I, II and III to the fourth assessment report of the intergovernmental panel on climate change.* Geneva, Switzerland : Technical report, IPCC, 2007.

52. **S.B. Jones, C. Valkenburg, C.W. Walton, D.C. Elliott, J.E. Holladay, D.J. Stevens, C. Kinchin, S. Czernik.** *Production of Gasoline and Diesel from Biomass via Fast Pyrolysis, Hydrotreating and Hydrocracking: A Design Case.* s.l. : U.S. Department of ENergy, 2009. PNNL- 18284.

53. **P.L. Spath, D.C. Dayton.** *Preliminary screening- technical and economic assessment of synthesis gas to fuels and chemicals with emphasis on the potential for biomass- derived syngas.* Golden, CO, USA : Technical report, National Renewable Energy Lab., 2003. www.osti.gov/bridge.

54. **B. Dawson, M. Spannagle.** *The Complete Guide to Climate Change.* s.l. : Routledge, 2009.

55. **Statistics, U.S. Energy Information Administration Independent.** http://www.eia.doe.gov/oog/info/gdu/gasdiesel.asp. 2011.

56. **Oil-Price-Net.** http://www.oil-price.net. 2011.

57. *Hydrotreatment of pyrolysis oils from biomass: reactivity of the various categories of oxygenated compounds and preliminary techno-economical study.* **P. Grange, E. Laurent, R. Maggi, A. Centeno, B. Delmon.** s.l. : Catalysis Today, 1996, Vols. (29) 297-301.

58. *Biomass to fuels: The role of zeolite and mesoporous materials .* **C. Perrego, A. Bosetti.** s.l. : Microporous and Mesoporous Materials, 2011, Vols. (144) 28-39.

59. *Analysis of transport costs for energy crops for use in biomass pyrolysis plant networks.* **J.G. Rogers, J.G. Brammer.** s.l. : Biomass and Bioenergy, 2009, Vols. (33) 1367-1375.

60. *Review of fast pyrolysis of biomass and product upgrading.* **Bridgwater, A.V.** s.l. : Biomass and Bioenergy, 2012, Vols. (38) 68-94.

61. *Catalytic conversion of a biomass-derived oil to fuels and chemicals I: Model compound studies and reaction pathways.* **J.D. Adjaye, N.N. Bakhshi.** s.l. : Biomass & Bioenergy, 1995, Vols. (8) 131-149.

62. *Production of hydrocarbons by catalytic upgrading of a fast pyrolysis bio-oil. Part I: Conversion over various catalysts.* **J.D. Adjaye, N.N. Bakhshi.** s.l. : Fuel Processing Technology, 1995, Vols. (45) 161-183.

63. *Hydrotreatment of Fast Pyrolysis Oil Using Heterogeneous Noble-Metal Catalysts.* **J. Wildschut, F.H. Mahfud, R.H. Venderbosch, H.J. Heeres.** s.l. : Industrial and Engineering Chemistry Research, 2009, Vols. (48) 10324-10334.

64. **Barin, I.** *Thermochemical Data of Pure Substances.* s.l. : VCH, 1989.

65. *Catalytic Hydrodeoxygenation of Methyl-Substituted Phenols: Correlations of Kinetic Parameters with Molecular Properties.* **F.E. Massoth, P. Politzer, M.C. Concha, J.S. Murray, J. Jakowski, J. Simons.** s.l. : The Journal of Physical Chemistry B, 2006, Vols. (110) 14283-14291.

66. *Hydrodeoxygenation of Phenolic Model Compounds over MoS2 Catalysts with Different Structures.* **Y. Yunquan, L. He'an, T. Gangsheng, K.J. Smith, T.C. Thian.** s.l. : Chinese Journal of Chemical Engineering, 2008, Vols. (16) 733-739.

67. *Catalysis in thermal biomass conversion.* **Bridgwater, A.V.** s.l. : Applied Catalysis A: General , 1994, Vols. (116) 5-47.

68. **Wildschut, J.** Pyrolisis oil upgrading to transportation fuels by catalytic hydrotreatment. Rijksuniversiteit Groningen : s.n., 2009.

69. *Synergies between Bio- and Oil Refineries for the Production of Fuels from Biomass.* **A. Corma, G.W.Huber.** s.l. : Angewandte Chemie International Edition, 2007, Vols. (46) 7184-7201.

70. *Production of advanced biofuels: Co-processing of upgraded pyrolysis oil in standard refinery units.* **F. de Miguel Mercader, M.J. Groeneveld, S.R.A. Kersten, N.W.J. Way, C.J. Schaverien, J.A. Hogendoorn.** s.l. : Applied Catalysis B: Environmental, 2010, Vols. (96) 57-68.

71. *Catalytic Hydroprocessing of Biomass Fast Pyrolysis Bio-oil to Produce Hydrocarbon Products.* **D.C. Elliott, T.R. Hart, G.G. Neuenshwander, L.J. Rotness, A.H. Zacher.** s.l. : Environmental Progress & Sustainable Energy, 2009, Vols. (28) 441-449.

72. **A. Daudin, L. Bournay, T. Chapus.** *Method for converting effluents of renewable origin into fuel of excellent quality by using a molybdenum- based catalyst. Us 2010/0163458 a1* 2010.

73. **M.J. McCall, T.A. Brandvold.** *Fuel and fuel blending components from biomass derived pryrolysis oil. Us 2009/0253948 a1* 2009.

74. *Catalytic deoxygenation of liquid biomass for hydrocarbon fuels.* **K.C. Kwon, H. Mayfield, T. Marolla, B. Nichols, M. Mashburn.** s.l. : Renewable Energy, 2011, Vols. (36) 907-915.

75. *Catalytic hydrotreatment of vacuum pyrolysis oils from wood.* **J. Gagnon, S. Kaliaguine.** s.l. : Industrial & Engineering Chemistry Research, 1988, Vols. (27) 1783-1788.

76. *Hydrodeoxygenation of guaiacol on noble metal catalysts.* **A. Gutierrez, R.K. Kaila, M.L. Honkela, R. Slioor, A.O.I. Krause.** s.l. : Catalysis Today, 2009, Vols. (147) 239-246.

77. *Study of Hydrodeoxygenation of Bio-Oil from the Fast Pyrolysis of Biomass.* **Z. Su-Ping, Y. Yong-Jie, R. Zhengwei, L. Tingchen.** s.l. : Energy Source, 2003, Vols. (25) 57-65.

78. *Production of a bio-gasoline by upgrading biomass flash pyrolysis liquids via hydrogen processing and catalytic cracking.* **M.C. Samolada, W. Baldauf, I.A. Vasalos.** s.l. : Fuel, 1998, Vols. (77) 1667-1675.

79. *Effect of water on the stability of Mo and CoMo hydrodeoxygenation catalysts: A combined experimental and DFT study.* **M. Badawi, J.F. Paul, S. Cristol, E. Payen, Y. Romero, F. Richard, S. Brunet, D. Lambert, X. Portier, A. Popov, E. Kondratieva,**

J.M. Goupil, J.E. Falah, J.P. Gilson, L. Mariey, A. Travert, F. Mauge. s.l. : Journal of Catalysis, 2011, Vols. (282) 155-164.

80. *Upgrading of flash pyrolysis oil and utilization in refineries.* **W. Baldauf, U. Balfanz, M. Rupp.** s.l. : Biomass Bioenergy, 1994, Vols. (7) 237-244.

81. *Hydrodeoxygenation of guaiacol Part II: Support effect for CoMoS catalysts on HDO activity and selectivity.* **V.N. Bui, D. Laurenti, B.P. Delichère, C. Geantet.** s.l. : Applied Catalysis B: Environmental , 2011, Vols. (101) 246- 255.

82. *Influence of the Support of CoMo Sulfide Catalysts and of the Addition of Potassium and Platinum on the Catalytic Performances for the Hydrodeoxygenation of Carbonyl, Carboxyl, and Guaiacol-Type Molecules.* **A. Centeno, E. Laurent, B. Delmon.** s.l. : Journal of Catalysis, 1995, Vols. (154) 288-298.

83. *Vapor-Phase Catalytic Hydrodeoxygenation of Benzofuran.* **M.C. Edelman, M.K. Maholland, R.M. Baldwin, S.W. Cowley.** s.l. : Journal of Catalysis, 1988, Vols. (111) 243-253.

84. *CoMo/carbon hydrodeoxygenation catalysts: influence of the hydrogen sulfide partial pressure and of the sulfidation temperature .* **M. Ferrari, S. Bosmans, R. Maggi, B. Delmon, P. Grange.** s.l. : Catalysis Today, 2001, Vols. (65) 257-264.

85. *Mild hydrotreating of biomass pyrolysis oils to produce a suitable refinery feedstock.* **R.J. French, J. Hrdlicka, R. Baldwin.** s.l. : Environmental Progress & Sustainable Energy, 2010, Vols. (29) 142-150.

86. *Mild Hydrotreating of Bio-Oil: Effect of Reaction Severity and Fate of Oxygenated Species.* **R.J. French, J. Stunkel, R.M. Baldwin.** s.l. : Energy & Fuels, 2011, Vols. (25) 3266-3274.

87. *From biomass to fuels: Hydrotreating of oxygenated compounds .* **I. Gandarias, V.L. Barrio, J. Requies, P.L. Arias, J.F. Cambra, M.B. Güemez.** s.l. : International Journal of Hydrogen Energy, 2008, Vols. (33) 3485-3488.

88. *Upgrading of bio-liquids on different mesoporous silica-supported CoMo catalysts.* **R. Nava, B. Pawelec, P. Castaño, M.C. Álvarez Galván, C.V. Loricera, J.L.G. Fierro.** s.l. : Applied Catalysis B: Environmental, 2009, Vols. (92) 154-167.

89. *Insight to sulfur species in the hydrodeoxygenation of aliphatic esters over sulfided NiMo/γ-Al2O3 catalyst.* **E.M. Ryymin, M.L. Honkela, T.R. Viljava, A.O.I. Krause.** s.l. : Applied Catalysis A: General, 2009, Vols. (358) 42-48.

90. *Competitive reactions and mechanisms in the simultaneous HDO of phenol and methyl heptanoate over sulphided NiMo/γ-Al2O3 .* **E.M. Ryymin, M.L. Honkela, T.R. Viljava, A.O.I. Krause.** s.l. : Applied Catalysis A: General , 2010, Vols. (389) 114-121.

91. *Effect of H2S on the stability of CoMo/Al2O3 catalysts during hydrodeoxygenation .* **T.R. Viljava, R.S. Komulainen, A.O.I. Krause.** s.l. : Catalysis Today , 2000, Vols. (60) 83-92.

92. **W. Zhang, Y. Zhan, L. Zhao, W. Wei.** s.l. : Energy & Fuels, 2010, Vols. (24) 2052-2059.

93. *Characterization of Hydrotreated Fast Pyrolysis Liquids.* **A. Oasmaa, E. Kuoppala, A.R. Ardiyanti, R.H. Venderbosch, H.J. Heeres.** s.l. : Energy & Fuels, 2010, Vols. (24) 5264-5272.

94. *DFT study of furan adsorption over stable molybdenum sulfide catalyst under HDO conditions.* **M. Badawi, S. Cristol, J.F. Paul, E. Payen.** s.l. : Comptes Rendus Chimie, 2009, Vols. (12) 754-761.

95. *Hydrodeoxygenation of 2-ethylphenol as a model compound of bio-crude over sulfided Mo-based catalysts: Promoting effect and reaction mechanism.* **Y. Romero, F. Richard, S. Brunet.** s.l. : Applied Catalysis B: Environmental, 2010, Vols. (98) 213-223.

96. **H. Topsøe, B.S. Clausen, F.E. Massoth.** *Hydrotreating Catalysis .* s.l. : Springer-Verlag, 1996.

97. *Effect of hydrogen sulphide on the hydrodeoxygenation of aromatic and aliphatic oxygenates on sulphided catalysts .* **O. Senol, E.M. Ryymin, T.R. Viljava, A. Krause.** s.l. : Journal of Molecular Catalysis A: Chemical, 2007, Vols. (277) 107-112.

98. *Effect of sulphiding agents on the hydrodeoxygenation of aliphatic esters on sulphided catalysts .* **O. Senol, T.R. Viljava, A. Krause.** s.l. : Applied Catalysis A: General, 2007, Vols. (326) 236-244.

99. **Prins, R.** *Handbook of Heterogeneous Catalysis.* s.l. : Wiley (chapter 13.2) 2695-2718, 2008.

100. *Mechanism of Hydrodeoxygenation of Acrolein on a Cluster Model of MoO3.* **D.R. Moberg, T.J. Thibodeau, F.G. Amar, B.G. Frederick.** s.l. : The Journal of Physical Chemistry C, 2010, Vols. (114) 13782-13795.

101. *Acidity and basicity of metal oxide surfaces II. Determination by catalytic decomposition of isopropanol .* **A. Gervasini, A. Auroux.** s.l. : Journal of Catalysis, 1991, Vols. (131) 190-198.

102. *Molecular and Electronic Structures, Brönsted Basicities, and Lewis Acidities of Group VIB Transition Metal Oxide Clusters.* **S. Li, D.A. Dixon.** s.l. : Journal of Physical Chemistry A, 2006, Vols. (110) 6231-6244.

103. **Busca, G.** *The Surface Acidity and Basicity of Solid Oxides and Zeolites. In Metal Oxides: chemistry and applications; .* s.l. : Fierro, J. L. G. CRC Taylor & Francis: Boca Raton, FL, 2006; pp 247.

104. *Hydrodeoxygenation of 4-Methylphenol over Unsupported MoP, MoS2, and MoOx Catalysts.* **V.M.L. Whiffen, K.J.Smith.** s.l. : Energy & Fuels, 2010, Vols. (24) 4728-4737.

105. *Synergy effect in the HDO of phenol over Ni–W catalysts supported on active carbon: Effect of tungsten precursors.* **S. Echeandia, P.L. Arias, V.L. Barrio, B.Pawelec, J.L.G. Fierro.** s.l. : Applied Catalysis B: Environmental, 2010, Vols. (101) 1-12.

106. *Selectivity enhancement in heterogeneous catalysis induced by reaction modifiers .* **T. Mallat, A. Baiker.** s.l. : Applied Catalysis A: General, 2000, Vols. (200) 3-22.

107. *Adsorption of activated ketones on platinum and their reactivity to hydrogenation: a DFT study .* **A. Vargas, T. Bürgi, A. Baiker.** s.l. : Journal of Catalysis, 2004, Vols. (222) 439-449.

108. *Adsorption modes of aromatic ketones on platinum and their reactivity towards hydrogenation .* **A. Vargas, S. Reimann, S. Diezi, T. Mallat, A. Baiker.** s.l. : Journal of Molecular Catalysis, 2008, Vols. (282) 1-8.

109. *Influence of metal-support effects on acetophenone hydrogenation over platinum .* **S.D. Lin, D.K. Sanders, M.A. Vannice.** s.l. : Applied Catalysis A: General, 1994, Vols. (113) 59-73.

110. *Hydrogenation of co and carbonyl functional groups.* **Vannice, M.A.** s.l. : Catalysis Today, 1992, Vols. (12) 255-267.

111. *Catalytic hydrotreatment of fast pyrolysis oil: Model studies on reaction pathways for the carbohydrate fraction.* **J. Wildschut, J. Arentz, C.B. Rasrendra, R.H. Venderbosch, H.J. Heeres.** s.l. : Environmental Progress, 2009, Vols. (28) 450-460.

112. *Bio-oil upgrading over platinum catalysts using in situ generated hydrogen.* **C.A. Fisk, T. Morgan, Y. Ji, M. Crocker, C. Crrofcheck, S.A. Lewis.** s.l. : Applied Catalysis A: General, 2009, Vols. (358) 150-156.

113. **Survey, U.S. Geological.** Mineral Commodity Summaries 2010. [En línea] 2010. http://minerals.usgs.gov/minerals/pubs/mcs/.

114. *Development of new catalytic systems for upgraded bio-fuels production from bio-crude-oil and biodiesel .* **V.A. Yakovlev, S.A. Khromova, O.V. Sherstyuk, V.O. Dundich, D.Y. Ermakov, C.M. Novopashina, M.Y. Lebedev, O. Bulavchenkko, V.N. Parmon.** s.l. : Catalysis Today, 2009, Vols. (144) 362-366.

115. *Guaiacol Hydrodeoxygenation in the Presence of Ni-Containing Catalysts.* **M.V. Bykova, O.A. Bulavchenko, D.Yu Ermanov, M.Yu Lebedev, V.A. Yakovlev, Y.N. Parmon.** s.l. : Catalysis in Industry , 2011, Vols. 3 (1) 15-22.

116. *Hydrodeoxygenation of Furfural Over Supported Metal Catalysts: A Comparative Study of Cu, Pd and Ni.* **S. Sitthisa, D.E. Resasco.** s.l. : Catalysis Letters, 2011, Vols. (141) 784-791.

117. *Reductive Deposition of Ni-Zn Nanoparticles Selectively on TiO2 Fine Particles in the Liquid Phase.* **H. Takahashi, Y. Sunagawa, S. Myagmarjav, K. Yamamoto, N. Sato, A. Muramatsu.** s.l. : Materials Transactions, 2003, Vols. (44) 2414-2416.

118. *Study on Cu-Ni-Zn Catalyst for Catalytic Amination of Fatty Alcohol .* **Q. Li, G. Zhang, S. Peng.** s.l. : Chinese Journal of Catalysis, 2001, Vols. (22) 7-10.

119. *Study of the Individual Reactions of Hydrodesulphurization of Dibenzothiophene and Hydrogenation of 2-Methylnaphthalene on ZnNiMo/γ-Alumina Catalysts.* **C.F. Linares, M. Fernández.** s.l. : Catalysis Letters, 2008, Vols. (126) 341-345.

120. *Enhancement of pyrolysis gasoline hydrogenation over Zn- and Mo-promoted Ni/γ-Al2O3 catalysts.* **Y. Qian, S. Liang, T. Wang, Z. Wang, W. Xie, X. Xu.** s.l. : Catalysis Communications, 2011, Vols. (12) 851-853.

121. *Influence of ultrasonic on the preparation of Ni–Mo–B amorphous catalyst and its performance in phenol hydrodeoxygenation.* **W.Y. Wang, Y.Q. Yang, J.G. Bao, C. Zhuo.** s.l. : Journal of Fuel Chemistry and Technology, 2009, Vols. (37) 701-706.

122. *Hydrodeoxygenation of 4-Methylphenol over Unsupported MoP, MoS2, and MoOx Catalysts.* **V.M.L. Whiffen, K.J. Smith.** s.l. : Energy & Fuels, 2010, Vols. (24) 4728-4737.

123. *Hydrogenation of oleic acid over ruthenium catalysts .* **M.J. Mendes, O.A.A. Santos, E Jordâo, A.M. Silva.** s.l. : Applied Catalysis A: General, 2001, Vols. (217) 253-262.

124. *Effects of the support on the morphology and electronic properties of supported metal clusters: modern concepts and progress in 1990s* . **A.Y. Stakheev, L.M. Kustov.** s.l. : Applied Catalysis A: General, 1999, Vols. (1889 3-35.

125. *Metal-support effects on the intramolecular selectivity of crotonaldehyde hydrogenation over platinum* . **M.A. Vannice, B. Sen.** s.l. : Journal of Catalysis, 1989, Vols. (115) 65-78.

126. *Aqueous-phase hydrodeoxygenation of bio-derived phenols to cycloalkanes* . **C. Zhao, J. He, A.A. Lemonidou, X. Li, J.A. Lercher.** s.l. : Journal of Catalysis, 2011, Vols. (280) 8-16.

127. *Highly selective catalytic conversion of phenolic bio-oil to alkanes.* **C. Zhao, Y. Kuo, A.A. Lemonidou, X. Li, J.A. Lercher.** s.l. : Angewandte Chemie International Edition, 2009, Vols. (48) 3987-3990.

128. *Hydrodeoxygenation of bio-derived phenols to hydrocarbons using RANEY® Ni and Nafion /SiO2 catalysts.* **C. Zhao, Y. Kuo, A.A. Lemonidou, X. Li, J.A. Lercher.** s.l. : Chemical Communications, 2010, Vols. (46) 412-414.

129. *Hydrodeoxygenation of guaiacol as model compound for pyrolysis oil on transition metal phosphide hydroprocessing catalysts* . **H.Y. Zhao, D. Li, P. Bui, S.T. Oyama.** s.l. : Applied Catalysis A: General, 2010, Vols. (391) 305-310.

130. *Influence of water in the deactivation of a sulfided NiMoγ-Al2O3 catalyst during hydrodeoxygenation* . **E. Laurent, B. Delmon.** s.l. : Journal of Catalysis, 1994, Vols. (146) 281-291.

131. *Bio-oils Hydrodeoxygenation: Adsorption of Phenolic Molecules on Oxidic Catalyst Supports.* **A. Popov, E. Kondratieva, J.M. Goupil, L. Mariey, P. Bazin, J.P. Gilson, A. Travert, F. Mauge.** s.l. : The Journal of Physical Chemistry C, 2010, Vols. (114) 15661-15670.

132. *Effects of Support Surface Chemistry in Hydrodeoxygenation Reactions over CoMo/Activated Carbon Sulfided Catalysts.* **G. de la Puente, A. Gil, J.J. Pis, P. Grange.** s.l. : Langmuir, 1999, Vols. (15) 5800-5806.

133. *The effect of molybdenum precursor on the dispersion and hydrodesulfurization activity of carbon-supported sulfide catalysts.* **K.V.R. Charry, H. Ramakrishna, G. Murali Dhar.** s.l. : Journal of Molecular Catalysis, 1991, Vols. (68) L25-L30.

134. *Catalytic Hydroprocessing of Chemical Models for Bio-oil.* **D.C. Elliott, T.R. Hart.** s.l. : Energy & Fuels, 2009, Vols. (23) 631-637.

135. *A review of catalytic hydrotreating processes for the upgrading of liquids produced by flash pyrolysis .* **R. Maggi, B. Delmon.** 1997, Vols. (106) 99-113.

136. *IR study of the interaction of phenol with oxides and sulfided CoMo catalysts for bio-fuel hydrodeoxygenation .* **A. Popov, E. Kondratieva, J.P. Gilson, L. Mariey, A. Travert, F. Mauge.** s.l. : Catalysis Today , 2011, Vols. (172) 132-135.

137. *Pt⌣IrAl2O3 catalysts—The effect of Pt⌣Ir interaction on Ir agglomeration and catalytic performance.* **Y.J. Huang, S.C. Fung, W.E. Gates, G.B. McVicker.** s.l. : Journal of Catalysis, 1989, Vols. (118) 192-202.

138. *State of the art and future challenges of zeolites as catalysts.* **Corma, A.** s.l. : Journal of Catalysis, 2003, Vols. (216) 298-312.

139. **Infantes-Molina, M.A.** Tesis: Catalizadores de cobalto soportados sobre sólidos mesoporosos para reacciones de hidrotratamiento. 2006.

140. *Influence of nitrogen compounds on deep hydrodesulfurization of 4,6-dimethyldibenzothiophene over Al2O3- and MCM-41-supported Co-Mo sulfide catalysts.* **U.T. Turaga, X. Ma, C. Song.** s.l. : Catalysis Today, 2003, Vols. (86) 265–275.

141. *New hydrotreating NiMo catalysts supported on MCM-41 modified with phosphorus.* **J.M. Herrera, J. Reyes, P. Roquero, T. Klimova.** s.l. : Microporous and Mesoporous Materials, 2005, Vols. (83) 283-291.

142. *MCM-41-supported Co-Mo catalysts for deep hydrodesulfurization of light cycle oil.* **U.T. Turaga, C. Song.** s.l. : Catalysis Today , 2003, Vols. (86) 129-140.

143. *Ni and Mo interaction with Al-containing MCM-41 support and its effect on the catalytic behavior in DBT hydrodesulfurization.* **T. Klimova, M. Calderón, J. Ramírez.** s.l. : Applied Catalysis A: General, 2003, Vols. (240) 29-40.

144. *Organization of Organic Molecules with Inorganic Molecular Species into Nanocomposite Biphase Arrays.* **Q. Huo, D.I. Margolese , U. Ciesla , D.G. Demuth , P. Feng , T.E. Gier , P. Sieger , A. Firouzi , B.F. Chmelka.** s.l. : Chemical Materials, 1994, Vols. (6)1176–1191.

145. *Well-Ordered Spherical Mesoporous Materials CMI-1 Synthesized via an Assembly of Decaoxyethylene Cetyl Ether and TMOS.* **J.L. Blin, A. Léonard, B.L. Su.** s.l. : Chemical Materials, 2001, Vols. (13) 3542-3553.

146. *Non-ionic surfactant (C13EOm, m=6, 12 and 18) for large pore mesoporous molecular sieves preparation .* **J.L Blin, A Becue, B Pauwels, G Van Tendeloo, B.L Su.** s.l. : Microporous and Mesoporous Materials, Vols. (44-45) 41-51.

147. *From Microporous to Mesoporous Molecular Sieve Materials and Their Use in Catalysis.* **Corma, A.** s.l. : Chemical Reviews, 1997, Vol. (97) 2373−2419.

148. *Liquid hydrocarbon fuels from palm oil by catalytic cracking over aluminosilicate mesoporous catalysts with various Si/Al ratios.* **F.A. Twaiq, R.A. Mohamed, S. Bhatia.** s.l. : Microporous and Mesoporous Materials, 2003, Vols. (64) 95-107.

149. *Performance of composite catalysts in palm oil cracking for the production of liquid fuels and chemicals .* **F.A. Twaiq, R.A. Mohamed, S. Bhatia.** s.l. : Fuel Processing Technology, 2004, Vols. (85) 1283-1300.

150. *In situ catalytic upgrading of biomass derived fast pyrolysis vapours in a fixed bed reactor using mesoporous materials .* **J. Adam, E. Antonakou, A. Lappas, M. Stöcker,**

M.H. Nilsen, A. Bouzga, J.E. Hustad, G. Øye. s.l. : Microporous and Mesoporous Materials, 2006, Vols. (96) 93-101.

151. *Pyrolysis of biomass in the presence of Al-MCM-41 type catalysts .* **J. Adam, M. Blazsó, E. Mészáros, M. Stöcker, M.H. Nilsen, A. Bouzga, J.E. Hustad, M. Grønli, G. Øye.** s.l. : Fuel, 2005, Vols. (84) 1494-1502.

152. *Ordered mesoporous molecular sieves synthesized by a liquid-crystal template mechanism.* **C.T. Kresge, M.E. Leonowicz, W.J. Roth, J.C. Vartuli, J.S. Beck.** s.l. : Nature, 1992, Vols. (359) 710-712.

153. *Surfactant controlled preparation of mesostructured transition-metal oxide compounds.* **U. Ciesla, D. Demuth, R. Leon, P. Petroff, G. Stucky, K. Unger, F. Schüth.** s.l. : Journal of the Chemical Society, Chemical Communications, 1994, Vols. (11) 1387-1388.

154. *A Neutral Templating Route to Mesoporous Molecular Sieves.* **P.T. Tanev, T.J. Pinnavaia.** s.l. : Science, 1995, Vols. (267) 865-867.

155. *Templating of Mesoporous Molecular Sieves by Nonionic Polyethylene Oxide Surfactants.* **S.A. Bagshaw, E. Prouzet, T.J. Pinnavaia.** s.l. : Science, 1995, Vols. (269) 1242-1244.

156. *Preparation of mesoporous silica by co-precipitation in the presence of non-ionic surfactant.* **L. Wang, Z. Wang, J. Zhao, Z. Yuan, H. Yang, M. Zhao.** 1999, Vols. (59) 171-174.

157. *Comparison of the morphology and reactivity in HDS of CoMo/HMS, CoMo/P/HMS and CoMo/SBA-15 catalysts.* **R. Nava, B. Pawelec, J. Morales, R.A. Ortega, J.L.G. Fierro.** s.l. : Microporous and Mesoporous Materials, 2009, Vols. (118) 189-201.

158. *Synthesis and Characterization of Ti-HMS and CoMo/Ti-HMS Oxide Materials with Varying Ti Content.* **T.A. Zepeda, T. Halachev, B. Pawelec, R. Nava, T. Klimova, G.A. Fuentes, J.L.G. Fierro.** s.l. : Chemical Materials, 2005, Vols. (17) 4062-4073.

159. *Hydrodesulfurization of dibenzothiophene over CoMo/HMS and CoMo/Ti-HMS catalysts.* **T.A. Zepeda, T. Halachev, B. Pawelec, R. Nava, T. Klimova, G.A. Fuentes, J.L.G. Fierro.** s.l. : Catalysis Communications, 2006, Vols. (7) 33-41.

160. *HDS of dibenzothiophene over polyphosphates supported on mesoporous silica.* **B. Pawelec, S. Damyanova, R. Mariscal, J.L.G. Fierro, I. Sobrados, J. Sanz, L. Petrov.** s.l. : Journal of Catalysis, 2004, Vols. (223) 86-97.

161. *Mesoporous Silica Molecular Sieves Prepared by Ionic and Neutral Surfactant Templating: A Comparison of Physical Properties.* **P.T. Tanev, T.J. Pinnavaia.** s.l. : Chemical Materials, 1996, Vols. (8) 2068–2079.

162. *Preparation of lamellar and hexagonal forms of mesoporous silica and zirconia by the neutral amine route: lamellar–hexagonal transformation in the solid state.* **N. Ulagappan, N. Battaram, V.N. Raju, C.N.R. Rao.** s.l. : Chemical Communications, 1996, Vols. (0) 2243-2244.

163. *Triblock Copolymer Syntheses of Mesoporous Silica with Periodic 50 to 300 Angstrom Pores.* **D. Zhao, J. Feng, Q. Huo, N. Melosh, G.H. Fredrickson, B.F. Chmelka, G.D. Stucky.** s.l. : Science, 1998, Vols. (279) 548-552.

164. *Oxyethylene/oxybutylene block copolymers as structure-directing agents in the preparation of mesoporous silica.* **C.E. Tattershall, N.P. Jerome, P.M. Budd.** s.l. : Journal of Materials Chemistry, 2001, Vols. (11) 2979-2984.

165. *Investigation of the Morphology of the Mesoporous SBA-16 and SBA-15 Materials.* **W.J.J. Stevens, K. Lebeau, M. Mertens, G. Van Tendeloo, P. Cool, E.F. Vansant.** s.l. : The Journal of Physical Chemistry B, 2006, Vols. (110) 9183-9187.

166. *Impact of Al and Ti ions on the dispersion and performance of supported NiMo(W)/SBA-15 catalysts in the HDS and HYD reactions.* **A. Olivas, T.A. Zepeda.** s.l. : Catalysis Today, 2009, Vols. (143) 120-125.

167. *CoMo/Ti-SBA-15 catalysts for dibenzothiophene desulfurization.* **R. Nava, R.A. Ortega, G. Alonso, C. Ornelas, B. Pawelec, J.L.G. Fierro.** s.l. : Catalysis Today, 2007, Vols. (127) 70-84.

168. *Enhancement of biphenyl hydrogenation over gold catalysts supported on Fe-, Ce- and Ti-modified mesoporous silica (HMS).* **P. Castano, T.A. Zepeda, B. Pawelec, M. Makkee, J.L.G. Fierro.** s.l. : Journal of Catalysis, 2009, Vols. (267) 30-39.

169. *Nonionic Triblock and Star Diblock Copolymer and Oligomeric Surfactant Syntheses of Highly Ordered, Hydrothermally Stable, Mesoporous Silica Structures.* **D. Zhao, Q. Huo, J. Feng, B.F. Chmelka, G.D. Stucky.** s.l. : Journal of the American Chemical Society, 1998, Vols. (120) 6024-6036.

170. *Direct imaging of the pores and cages of three-dimensional mesoporous materials.* **Y. Sakamoto, M. Kaneda, O. Teresaki, D. Zhao, J.M. Kim, G.D. Stucky, H.J. Shin, R. Ryoo.** s.l. : Nature, 2000, Vols. (408) 449-453.

171. *Highly active disordered extra large pore titanium silicate .* **A. Bahaumik, S. Samanta, N. Kishor Malet.** s.l. : Microporous and Mesoporous Materials, 2004, Vols. (68) 29-35.

172. *Influence of the preparation method on the activity of phosphate-containing CoMo/HMS catalysts in deep hydrodesulphurization .* **R. Nava, J. Morales, G. Alonso, C. Ornelas, B. Pawelec, J.L.G. Fierro.** s.l. : Applied Catalysis A: General, 2007, Vols. (321) 58-70.

173. *Comparison of the morphology and HDS activity of ternary Co-Mo-W catalysts supported on P-modified SBA-15 and SBA-16 substrates .* **R. Huirache-Acuña, B. Pawelec, J. Morales, E. Rivera-Muñoz, R. Nava, J. Espino, J.L.G. Fierro.** s.l. : Applied Catalysis B: Environmental, 2009, Vols. (92) 168-184.

174. *Simulated solar-light assisted photocatalytic ozonation of metoprolol over titania-coated magnetic activated carbon .* **V. Bui, D. Laurenti, P. Delichère, C. Geantet.** s.l. : Applied Catalysis B: Environmental, 2011, Vols. (111) 246-255.

175. *Nickel catalysts for the hydrodeoxygenation of biodiesel.* **V.O. Dundich, S.A. Khromova, D.Y. Ermakov, M.Y. Lebedev, V.M. Novopashina, V.G. Sister, A.I. Yakimchuck, V.A. Yakovlev.** s.l. : Kinetics and Catalysis, 2010, Vols. (51) 728-734.

176. *Deactivation of hydroprocessing catalysts.* **E. Furimsky, F.E. Massoth.** s.l. : Catalysis Today, 1999, Vols. (52) 381-495.

177. *Assignment of an average chemical structure to catalyst carbon deposits on the basis of quantitative 13C n.m.r. spectra.* **A. Fonseca, P. Zeuthen, J. Nagy.** s.l. : Fuel, 1996, Vols. (75) 1413-1423.

Capítulo 2

Objetivos

Capítulo 2

Objetivos

La investigación desarrollada en el curso de la Tesis Doctoral, y recopilada en esta memoria, comprende el trabajo realizado a lo largo de los últimos años en el Departamento de Estructura y Reactividad del Instituto de Catálisis y Petroleoquímica del Consejo Superior de Investigaciones Científicas dentro de un programa de trabajo relacionado con la fabricación de combustibles limpios y focalizado en la eliminación de oxigeno de compuestos oxigenados presentes en fracciones de biomasa mediante reacciones de hidrotratamiento en presencia de catalizadores heterogéneos. Este trabajo se enmarca dentro del proyecto "Hidrógeno: Producción y Usos Sostenibles" (HIREUS ENE2007-67533-C02-01) financiado por el Ministerio de Ciencia e Innovación.

Debido a la importancia creciente de los procesos de obtención de hidrocarburos limpios (sin heteroátomos y sin estructuras aromáticas) a partir de la biomasa, el objetivo principal que se ha perseguido durante el curso de la Tesis fue el diseño de nuevos catalizadores eficientes para eliminación de oxigeno de las fracciones líquidas derivadas de la pirolisis de biomasa, incidiendo tanto en las propiedades de los soportes como en la naturaleza de las fases activas en cada una

de las reacciones seleccionadas. Dado que el objetivo principal perseguido en esta Memoria fue la comparación de la actividad de los distintos sistemas catalíticos no se realizó ningún estudio cinético de las reacciones de desoxigenación estudiadas.

El programa de investigación planteado comprendió el estudio de los distintos catalizadores conforme a los puntos que se detallan a continuación:

- Preparación de una nueva generación de catalizadores de hidrotratamiento, variando sistemáticamente tanto el tipo de soporte como la naturaleza de las fases activas.

- Caracterización físico-química de los catalizadores frescos y usados en cada una de las reacciones seleccionadas, así como de sus precursores en forma de óxido utilizando técnicas convencionales y avanzadas, que permitan definir factores tan importantes como el grado de dispersión y estado químico de los componentes y evaluar cómo éstas varían en el curso de las diferentes etapas que comprenden la génesis y vida de los catalizadores.

- Estudio de la reactividad de los catalizadores en reacciones de hidrodesoxigenación (HDO) de una alimentación real que consiste en una mezcla de componentes presentes en la fracción desechable de producción de aceite de oliva, así como de alimentaciones de moléculas modelo (fenol y anisol).

- Establecimiento de las correlaciones entre la actividad de los catalizadores en la reacción de HDO y el tipo de especies activas en reacción.

- Aportación del conocimiento detallado de estos sistemas catalíticos que permita fijar los desarrollos de esta línea de investigación sobre los catalizadores de HDO e identificar algún sistema catalítico prometedor que sirva de guía para futuros desarrollos.

- Análisis detallado de la bibliografía relacionada con la temática de trabajo de forma que ayudase a elaborar un cuerpo de trabajo novedoso y a plantear estrategias de avance viables y precisas.

Para una mejor exposición y comprensión durante la lectura, la presente Memoria se ha estructurado en 9 capítulos. En el primer capítulo de INTRODUCCIÓN se revisa el estado de arte de los procesos de eliminación de oxigeno de fracciones líquidas resultantes de la transformación de la biomasa y los catalizadores utilizados hasta la fecha. El segundo capítulo describe los OBJETIVOS planteados en esta investigación. En el tercer capítulo dedicado a los MATERIALES Y MÉTODOS se describen las técnicas experimentales utilizadas así como la metodología general de preparación de los catalizadores. Los siguientes cuatro capítulos (del 4 al 8) contienen los RESULTADOS experimentales tanto de los estudios de caracterización como de las medidas de actividad de las diferentes series de los catalizadores preparados. Por último, en el capítulo 9 de las CONCLUSIONES, se presentan las conclusiones más relevantes que se han obtenido en el curso de la presente investigación. Con el fin de facilitar el acceso a la bibliografía, al final de cada capítulo se encuentran recogidas las referencias de los trabajos citados en cada uno de ellos.

Capítulo 3

Materiales y métodos

Capítulo 3

Materiales y Métodos

En este capítulo se describen los fundamentos y procedimientos experimentales de las técnicas de caracterización empleadas en la Tesis Doctoral. De igual modo, se detalla el equipo de reacción y la metodología utilizada para las medidas de actividad catalítica y el análisis de los productos de reacción de hidrodesoxigenación (HDO) de diferentes moléculas modelo. La descripción de la preparación de los diferentes catalizadores se realizará dentro de cada uno de los capítulos de resultados y discusión.

3.1. Materiales utilizados

3.1.1. Gases

Los gases empleados tanto en los tratamientos de atmósfera controlada como en las medidas de actividad catalítica, fueron suministrados por Air Liquide España. Los tipos, características y usos de dichos gases se encuentran resumidos en la **Tabla 3.1**.

Tabla 3.1. Características de los gases utilizados.

Gas	Tipo (Pureza %)	Utilización
H_2	N-50 (99.995%)	Cromatografía, agente reductor, reactivo en medidas de actividad.
H_2/Ar	H_2: 10.03 ± 0.2% molar	TPR
Aire sintético	N-50 (99.999%)	Cromatografía
He	N-50 (99.999%)	Cromatografía, TPR, TPD-NH_3
N_2	UN-45 (99.999%)	Atmósferas inertes
H_2/H_2S	H_2S: 10.03 ± 0.2% molar	Agente sulfurante
CO	N-37 (99.97%)	Quimisorción (DRIFT)
NO	N-50 (99.99%)	Quimisorción (DRIFT)
NH_3/He	NH_3: 5%	TPD-NH_3

3.1.2. Líquidos y sólidos

En la preparación de catalizadores mediante impregnación de los soportes con sales solubles, se utilizó agua bidestilada mili-Q tipo II de la clasificación A.S.T.M.. Para las medidas de actividad HDO, los disolventes utilizados fueron hexadecano (Sigma Aldrich, 99%) y una mezcla de isómeros cis-trans de tetrahidronaftaleno (decalina) (Sigma Aldrich, 99%), usados sin posterior purificación. La calibración cromatográfica de los reactivos y productos de reacción de HDO se realizó con Anisol (99%, Sigma Aldrich) y Fenol (99%, Sigma Aldrich) como compuestos modelo oxigenados, Benceno (99.9%, Sigma Aldrich), Ciclohexanol (99%, Sigma Aldrich) Ciclohexano (99.7%, Sigma Aldrich), Ciclohexeno (99%, Sigma Aldrich), Tolueno (99.5%, Panreac), o-Xilenol (99 %,

Sigma Aldrich), Naftaleno (99%, Sigma Aldrich), Metilciclopentano (99.5%, Sigma Aldrich), o-Metilanisol (99%, Sigma Aldrich), o-Cresol (99%, Sigma Aldrich).

3.1.3. Soportes y fases precursoras

En la **Tabla 3.2** se recopilan los soportes utilizados en la preparación de los distintos catalizadores usados.

Tabla 3.2. Soportes utilizados en los diferentes capítulos de la Tesis.

Capítulo	Soporte
Capítulo 4	HMS
Capítulo 4	DMS-1
Capítulo 4, 5 y 6	SBA-15
Capítulo 4 y 5	SBA-16
Capítulo 6	$2TiO_2/SiO_2$
Capítulo 6	Ti-SBA-15
Capítulo 6	TiO_2
Capítulo 7 y 8	HY
Capítulo 7	ZSM-5
Capítulo 8	γ-Al_2O_3

Las sales usadas como precursoras de las fases activas de los catalizadores se recopilan en la **Tabla 3.3**.

Tabla 3.3. Sales usadas como precursoras de las fases activas de los diferentes catalizadores.

Capítulo	Metal	Sal
Capítulo 4 y 5	Co	$Co(NH_3)_2 \cdot 6\ H_2O$
Capítulo 4 y 5	Mo	$(NH_4)_6Mo_7O_{24} \cdot 4\ H_2O$
Capítulo 5	W	$(NH_4)_6H_2W_{12}O_{40} \cdot XH_2O$
Capítulo 6	Ni	$Ni(NO_3)_2 \cdot 6H_2O$
Capítulo 6	Zn	$Zn(NO_3)_2 \cdot 6H_2O$
Capítulo 7	Pt	$H_2PtCl_6 \cdot 6H_2O$
Capítulo 7	Ir	$IrCl_3 \cdot H_2O$
Capítulo 8	Pd	H_2PdCl_6

3.2. Preparación de catalizadores

Los parámetros de preparación, como: a) procedimiento de impregnación, b) contenido en metal, c) temperatura de calcinación, d) procedimiento de activación y e) la presencia de aditivos, influyen de forma significativa en la estructura, morfología y estado químico de las especies activas formadas en los catalizadores soportados de hidrotratamiento. El conocimiento detallado de los efectos que estos parámetros tienen sobre la estructura del catalizador, es importante para el establecimiento de las condiciones óptimas de preparación.

En la bibliografía hay revisiones en las que se describen con cierto detalle los métodos de preparación de los catalizadores de hidrotratamiento (1) (2) (3). Entre ellos, los métodos de impregnación e intercambio iónico para zeolitas (4) son

los más ampliamente utilizados en la preparación de los catalizadores de hidrotratamiento.

La impregnación consiste básicamente en poner en contacto el soporte y la solución que contiene los elementos que se quieren incorporar. El tamaño y la forma de las partículas del soporte proporcionan la conformación final del mismo. Normalmente, el soporte se introduce en la disolución de la sal del metal a incorporar que no reaccione con él, se llenan los poros con la disolución y el exceso del disolvente se retira por evaporación, depositando en la pared del soporte la sal del metal. Otra variante de este método es la denominada impregnación por humedad incipiente (5). Puesto que se suele conocer el volumen de poro del soporte, es posible añadir solución suficiente (ligeramente superior al volumen de poro, aproximadamente un 30%) para obtener el contenido seleccionado de metal, quedando el sólido como una pasta. Debido a la escasa interacción, no se realiza ningún lavado después de la impregnación, ya que podría eliminar fácilmente la fase del precursor. Las principales variables que afectan al proceso de impregnación son: (i) concentración del soluto, (ii) el pH de la solución impregnante y (iii) la temperatura a la que se realiza la impregnación, que afecta a la solubilidad del precursor y la viscosidad de la solución impregnante. Un control apropiado de las condiciones de operación durante la impregnación y secado determina el perfil de composición en el catalizador final (6).

3.2.1. Catalizadores

En esta Tesis se planteó el diseño de nuevos catalizadores de hidrotratamiento incidiendo en las funcionalidades de: (i) soporte y (ii) naturaleza de las fases activas. La preparación de los mismos se encuentra detallada en cada

uno de los capítulos de resultados y discusión. Para ello se prepararon cuatro series de catalizadores:

(1) Catalizadores bimetálicos de CoMo soportados sobre materiales mesoporosos DMS-1, HMS, SBA-15, SBA-16.

(2) Catalizadores trimetálicos de CoMoW soportados sobre materiales mesoporosos SBA-15 y SBA-16 modificados con P.

(3) Catalizadores bimetálicos de Ni y Zn soportados sobre material mesoporoso SBA-15, modificado con titanio Ti-SBA-15, TiO_2 comercial y una mezcla física de titania- sílica 2Ti-Si.

(4) Catalizadores mono y bimetálicos de Pt e Ir soportados sobre zeolita ZSM-5 y zeolita ultraestable (HY).

(5) Catalizadores monometálicos de Pd soportados sobre zeolita ultraestrable (HY), γ-Al_2O_3 y mezcla de ambos soportes.

3.3. Caracterización físico-química de los catalizadores

La catálisis es un fenómeno confinado a la superficie de los catalizadores a una escala esencialmente atómica, por lo tanto la identificación de las estructuras responsables de aquella se hace imprescindible. En el Departamento de Estructura y Reactividad del Instituto de Catálisis y Petroleoquímica del C.S.I.C. se ha venido desarrollando una labor investigadora sobre las características de superficie de óxidos y sulfuros metálicos así como de los metales reducidos soportados, para

establecer vínculos entre las propiedades estructurales de los catalizadores y las diferencias que presentan en su comportamiento catalítico.

Sobre los catalizadores preparados, tanto en estado oxidado como reducido o sulfurado, se aplicarán diversas técnicas físico- químicas que permitan definir las características de la estructura másica y superficial del catalizador. Las propiedades físicas y químicas de la superficie y el tipo y estructura de la fase activa, determinarán la actividad y selectividad de los catalizadores en estas reacciones. Los resultados del análisis fisicoquímico proporcionarán una idea precisa de la naturaleza y abundancia de las fases activas y de cómo éstas varían en el curso de las diferentes etapas de vida de un catalizador, así como su comportamiento químico en el contexto de la reactividad en la reacción estudiada. A tal efecto, se aplicaron las siguientes técnicas de análisis: determinación de las superficies específicas, quimisorción selectiva de moléculas sonda y análisis por espectroscopia infrarroja, reducciones térmicas programadas, difracción de rayos X y espectroscopia fotoelectrónica de rayos X. Con ayuda de estas técnicas se ha intentado establecer alguna correlación entre la actividad y selectividad catalítica y las propiedades fisicoquímicas de las superficies. A continuación se detallan los procedimientos experimentales seguidos en la aplicación de todas estas técnicas.

3.3.1. Análisis elemental por espectrometría de emisión atómica con plasma acoplado (*Inductively Coupled Plasma-Atomic Emission Spectroscopy*, ICP-AES)

La Espectroscopia de Emisión Atómica es una técnica de análisis multielemental capaz de determinar y cuantificar la mayor parte de los elementos de la Tabla Periódica.

El fundamento teórico de la técnica se basa en el análisis del espectro de emisión atómica. Un átomo en su estado fundamental (M_0) se irradia con una onda electromagnética, absorbe energía y pasa a un estado excitado (M*). Cuando el átomo regresa de forma espontánea al nivel fundamental emite una radiación con una energía característica ($E = h\nu$), que es la diferencia entre la energía del estado excitado y la energía del estado fundamental. Puesto que cada elemento posee una configuración electrónica distinta y específica, la radiación absorbida por un átomo necesaria para alcanzar el estado excitado y la radiación emitida cuando regresa al estado fundamental son propias de ese elemento, por lo que pueden ser empleadas para caracterizarlo de forma unívoca.

El aporte energético para la excitación atómica en este tipo de análisis se consigue mediante la formación de un plasma, que consiste en un gas parcialmente ionizado, microscópicamente neutro y que emite radiación. La principal ventaja del uso de un plasma de acoplamiento inductivo como fuente de ionización frente a la llama o cámara de grafito es la elevada temperatura que alcanza (727 °C) (7). Esto, además de mejorar la eficiencia en la excitación e ionización, reduce o elimina muchas de las interferencias químicas encontradas en llamas y hornos. El argón es el gas que se emplea para formar el plasma, ya que por ser un gas monoatómico su espectro de emisión es muy simple. Además, al ser un gas noble, no forma compuestos con otros elementos y posee un potencial de ionización lo suficientemente elevado (15.76 eV) como para impedir su ionización en condiciones normales de trabajo.

El sistema de análisis químico por ICP-AES consiste en (8): Un sistema de aporte físico de muestra (constituido por una bomba peristáltica, un nebulizador y una cámara de nebulización), un sistema generador de plasma (constituido por la

antorcha, generador de radiofrecuencias y plasma plasmógeno), un sistema óptico de separación de longitudes de onda de la emisión policromática (monocromador) y un detector de estado sólido.

El análisis de las muestras por ICP-AES requiere que éstas se encuentren en forma de disolución líquida. Para ello se toma una pequeña cantidad (< 0.5 mg) de base seca de la muestra y se disgrega habitualmente con ácidos (en el caso de metales y/o sales metálicas) en un horno microondas (MLS 1200 MEGA de Millestone, 750 W de potencia máxima). Una vez disgregada la muestra, se procede a su análisis en un equipo Perkin-Elmer Optima 3300 DV. El equipo dispone de un nebulizador neumático de flujo cruzado (Babington), un monocromador de red plana con dispersión cruzada y dos detectores de estado sólido, un detector UV con intervalos entre 165-400 nm. El gas plasmógeno empleado fue el argón con un caudal total de 12 L/min.

3.3.2. Fluorescencia de rayos X por reflexión total (*Total Reflection X-ray Fluorescence*, TXRF)

La fluorescencia de rayos X por reflexión total (TXRF) es una técnica microanalítica que permite analizar cualitativa- y cuantitativamente los elementos comprendidos entre Si (Z = 14) y U (Z = 92) en materiales como aleaciones, catalizadores o cerámicas, tanto a niveles mayoritarios (porcentaje en peso) como elementos traza (ppb) (9). La técnica se basa en el estudio de las emisiones de fluorescencia de los rayos X generados por la excitación de los electrones con un número cuántico principal n = 1 capa K, n = 2 capa L, n = 3 capa M, debido a la irradiación de la muestra a medir, en estado sólido o líquido, por medio de un haz procedente de una fuente de rayos X. Los electrones de las capas internas se

arrancan o se promocionan a niveles de energía superiores. Como resultado, los electrones de otras capas minimizan su energía, ocupando los huecos electrónicos que quedan libres, de modo que la energía asociada a dichas transiciones se reemite en forma de fotones en cualquier dirección del espacio. Estas emisiones son conocidas como emisiones de fluorescencia o radiación secundaria y, presentan unas energías características del átomo que las genera, así como una intensidad que depende directamente de la concentración de dicho átomo en la muestra. Los tiempos de desexcitación de los electrones previamente excitados son muy cortos, del orden de 10^{-8} -10^{-9} s, siendo un método analítico extraordinariamente rápido. El resultado de la excitación-desexcitación es un espectro de dispersión de energías, donde aparecen todas las líneas asociadas a los elementos químicos presentes. Caracterizando estas emisiones de fluorescencia de rayos X es posible determinar los átomos que la generan y averiguar la composición de la materia presente en el medio.

Los análisis se llevaron a cabo en el Servicio Interdepartamental de Investigación de la Universidad Autónoma de Madrid (SIdI UAM) siguiendo el protocolo desarrollado por Fernández- Ruíz y col. (10).

3.3.3. Adsorción- desorción de N_2

El área superficial y la distribución de tamaño de poros de las muestras se determinan por medio de la técnica de adsorción de nitrógeno. Este estudio se ha realizado en las muestras preparadas después de calcinar, con el fin de estudiar la variación de la textura con los tratamientos térmicos. La textura está definida por diferentes variables entre las que se destacan (11): (i) área superficial, que consiste en la superficie por unidad de masa del sólido; (ii) el volumen específico de poro,

que es el volumen de la totalidad de poros por unidad de masa del sólido y (iii) el radio de la sección transversal de cada poro o cavidad. En general la forma de los poros en un catalizador no es geométricamente perfecta, por lo que esta magnitud se considera como el valor que tendría el radio de la sección transversal de un poro cilíndrico que, a efectos catalíticos, se comportase igual que el poro real.

La descripción de la estructura porosa del catalizador se obtiene mediante la "distribución de tamaños de poro", que indica el volumen de poro correspondiente a cada valor de radio considerado. La IUPAC (12) hace las siguientes distinciones de acuerdo al tamaño de poro: (i) microporos, tamaño inferior a 2 nm; (ii) mesoporos, tamaño comprendido entre 2 y 50 nm, y (iii) macroporos, cuyo tamaño es superior a 50 nm.

El procedimiento más extendido para analizar la estructura porosa se basa en la determinación de la isoterma de adsorción-desorción de nitrógeno a su temperatura de ebullición (-196 °C). Consiste en una representación del volumen de nitrógeno adsorbido por gramo de sólido frente a la presión de nitrógeno en equilibrio, normalmente expresada como presión relativa (P/P_0), donde P_0 es la presión de saturación del N_2 a -196 °C. La cantidad de gas adsorbido a la presión de equilibrio viene dado por la diferencia entre la cantidad de gas introducida y la requerida para llenar el espacio alrededor del adsorbente, es decir, el volumen muerto, a la presión de equilibrio. La isoterma de adsorción se construye punto a punto mediante introducción de cargas sucesivas de gas sobre el adsorbente, con la ayuda de una técnica volumétrica de dosificación y la aplicación de las leyes de los gases ideales. El volumen muerto se conoce con precisión, por admisión de un gas cuya adsorción sea despreciable, como es el caso del helio. Antes de la

determinación de una isoterma de adsorción, la muestra debe desgasificarse, eliminando todas las especies fisisorbidas de la superficie de la misma.

El análisis de la morfología de la isoterma (ramas de adsorción- desorción) da información acerca de la textura porosa, mientras que la superficie específica se determina por el método conocido como BET (Brunauer, Emmett y Teller) (13). Este método consiste en calcular el volumen de la monocapa (V_m) del adsorbato. A partir de este valor, la superficie específica BET (S_{BET}) se puede deducir según la ecuación 3.1.:

$$S_{BET} = \left(\frac{V_m}{M \cdot g} \right) \cdot N_A \cdot \sigma \qquad \textbf{Ecuación 3.1}$$

donde V_m, es el volumen de monocapa; M es el volumen molar; g es el peso de la muestra de adsorbente empleado; N_A es el número de Avogadro (6.023×10^{23} moléculas/mol) y σ es el área ocupada por una molécula de adsorbato en la monocapa. Para el caso de N_2 líquido, el valor de σ es de 0.162 nm^2 según la IUPAC (14). El valor de V_m se obtiene del ajuste de los datos experimentales de adsorción a la isoterma B.E.T.:

$$\frac{P}{V_{ads}(P_0 - P)} = \frac{1}{V_m C} + \frac{C-1}{V_m C}\frac{P}{P_0} \qquad \textbf{Ecuación 3.2}$$

donde P es la presión parcial del gas que se adsorbe; P_0 es la presión de vapor del gas a la temperatura a la que se realiza la adsorción; V_m es el volumen de gas adsorbido cuando se ha formado una monocapa; C es una constante que depende del calor de condensación y adsorción del adsorbato (cuanto más elevado sea su

valor, mayor es la interacción adsorbente-adsorbato), y V_{ads} es el volumen de gas adsorbido a la presión P.

Si se tiene en cuenta sólo la zona en que se está formando la monocapa inicial, la representación de los datos experimentales de P/V_{ads} (P_0-P) frente a P/P_0 será una línea recta según la **Ecuación 3.2.** A partir de la pendiente y de la ordenada en el origen de dicha recta se pueden calcular C y V_m, respectivamente.

El modelo B.E.T. es una ampliación de la teoría de Langmuir que contempla la adsorción en multicapas. La aplicación de este método está limitada a un rango de presiones reducidas donde la ecuación se ajusta bien a los datos experimentales y, por tanto, suministra información útil. En la práctica la linealidad se mantiene entre $0.05 < P/P_0 < 0.30$ aproximadamente, que es donde el modelo B.E.T. tiene validez. Por debajo de esta región de presiones relativas tiene lugar el llenado de microporos y además se favorece la adsorción de los centros más reactivos, mientras que por encima se da la condensación capilar. En ambos casos el modelo deja de ser válido.

Los datos experimentales de volumen adsorbido frente a la presión relativa permiten determinar la distribución de tamaño de poros del adsorbente. El método se basa en el hecho de que los vapores condensan en los espacios reducidos por un efecto capilar siguiendo la ecuación de Kelvin:

$$\log\frac{P}{P_0} = -\frac{2\gamma V}{rRT}\cos\theta \qquad \textbf{Ecuación 3.3}$$

siendo P la presión de vapor en el equilibrio de un líquido contenido en un poro de radio r y P_0 la presión de equilibrio del mismo líquido, pero dispuesto en una superficie plana. Los términos γ y V corresponden a la tensión superficial y el

volumen molar, respectivamente, y θ es el ángulo de contacto entre el líquido y las paredes del poro.

Para el caso del nitrógeno, la ecuación de Kelvin se transforma en:

$$r_k = \frac{-4.14}{\log(P/P_0)}$$ **Ecuación 3.4**

El radio real del poro r, está relacionado con el radio de Kelvin r_k, por la relación:

$$r = r_k + t$$ **Ecuación 3.5**

siendo t el espesor de la capa adsorbida previamente al momento en que se produce la condensación.

A partir del conjunto de datos experimentales [V_{ads}= f(P/P_0)] se puede determinar el volumen desorbido o adsorbido, para cada intervalo de P/P_0, y a partir de ahí, y por aplicación de la ecuación de Kelvin, los radios de poro r_k correspondientes. Si a ese volumen se le suma posteriormente el volumen de la fracción ya adsorbida se obtendrá el volumen total de poros con radio r.

Para la determinación de las isotermas de N_2 se utilizó un equipo Micromeritics ASAP- 2000 conectado a un ordenador que controla, almacena y procesa los datos. Las muestras entre 0.7 y 1 g se desgasificaron previamente a 250 °C (350 °C para los catalizadores de base zeolítica) a $5 \cdot 10^{-3}$ mbar de presión hasta eliminación de la mayor parte de los contaminantes gaseosos y/o líquidos retenidos en los poros y la superficie externa (aproximadamente 12-14 h).

3.3.4. Difracción de rayos X (*X-ray Diffraction*, XRD)

La difracción de rayos X es una técnica muy útil en el área de catálisis, puesto que nos permite la identificación de estructuras cristalinas presentes y la medida del tamaño de cristal de las fases soportadas.

La identificación de las fases cristalinas presentes se llevó a cabo por comparación de los patrones de difracción obtenidos con las bases de datos de intensidad y posición de los picos de difracción de las fichas de A.S.T.M. del *Joint Committee on Power Diffraction Spectroscopy* (J.C.P.D.S.). El tamaño de partícula de las fases cristalinas presentes en los catalizadores se calculó mediante la ecuación de Debye- Scherrer (15) . La fórmula de Sherrer es, sin lugar a duda, el método más común en la literatura catalítica ya que permite extraer información sobre el tamaño de partícula a partir de los datos de difracción. Este método se basa en el hecho de que el ensanchamiento de una línea de difracción a media altura $\beta_{1/2}$, se relaciona con el tamaño efectivo del cristal (t) por la relación:

$$\beta_{1/2} = \frac{K\lambda}{t\cos\theta} \qquad \textbf{Ecuación 3.6}$$

donde $\beta_{1/2}$ es la anchura de pico a media altura (radianes); K es una constante que depende de las condiciones experimentales (0.89-1.39); λ es la longitud de onda de la radiación empleada; t es la dimensión media del cristal normal a los planos de reflexión y θ es la posición angular del máximo del pico de difracción.

Según la **Ecuación 3.6**, el valor de $\beta_{1/2}$ es inversamente proporcional al tamaño del cristal que difracta. En la aplicación de este método se supone que el único factor que influye en el ensanchamiento de una línea de difracción es la variación del tamaño de partícula. Sin embargo, existen otros factores tales como la

presencia de microtensiones y faltas de apilamiento que contribuyen al aumento de la anchura del pico de difracción. No hay ningún método para separar el ensanchamiento producido por el tamaño de cristal, de aquel proveniente de microtensiones y defectos de apilamiento. También contribuyen al ensanchamiento factores instrumentales, como falta de alineación del difractómetro, estructura espectral de la radiación X utilizada ($K_{\alpha 1}/K_{\alpha 2}$), etc. (16). Se pueden realizar correcciones que compensen el ensanchamiento instrumental mediante la obtención de un difractograma de una muestra del mismo material del que se va a realizar el estudio del tamaño de partícula, pero de un tamaño de partícula grande. De esta forma, se establece un perfil de referencia. Si los picos de la muestra y la de referencia son gaussianos, entonces la anchura de pico corregida (B_G) se puede deducir de las anchuras observadas (B_o) y de referencia (B_r) de la forma:

$$B_G^2 = B_o^2 - B_r^2 \qquad \textbf{Ecuación 3.7}$$

mientras que si los picos presentan formas de Cauchy, entonces:

$$B_G = B_o - B_r \qquad \textbf{Ecuación 3.8}$$

En las medidas realizadas, la anchura intrínseca debida a los factores instrumentales es de 0.09^o evaluada tomando como patrón interno silicio de alta pureza analítica. Por último indicar que las dificultades experimentales para medir el tamaño de partícula a partir de la anchura de pico de difracción, aumentan con el tamaño de partícula medido, siendo el límite superior de tamaño para la aplicación de la técnica de unos 200 nm.

Los catalizadores se caracterizaron por esta técnica mediante un difractómetro Seifert 3000P que utiliza la radiación $CuK_{\alpha=1/2}$ (λ = 0.15406 nm) con un filtro de níquel. Las condiciones de trabajo fueron 40 kV, 25 mA y una

velocidad de barrido de 0.02 grados cada 0.5 s en un intervalo de ángulos de Bragg (2θ) entre 5° y 75°. El equipo tiene acoplado un sistema informático de tratamiento de difractogramas y un registro gráfico. El método escogido es el diagrama de polvo cristalino, para ello las muestras se molieron y depositaron sobre una placa de vidrio amorfo que no da interferencias en la línea base.

3.3.5. Difracción de Rayos X *in-situ* de alta resolución (Sincrotrón ALBA de Barcelona) *(In situ high resolution X-ray Difraction)*

Una fuente de luz sincrotrón es extremadamente brillante y modulable en el rango energético de los RX, lo que supone una gran mejora con respecto a las fuentes de RX en laboratorio. Para experimentos de difracción el alto brillo de la luz sincrotrón permite disminuir significativamente los tiempos de adquisición (de varias horas a minutos) y, combinado con el empleo de un detector de alta resolución, permite además distinguir pequeñas modificaciones en la simetría de la muestra.

Para los estudios de la reducción *in-situ* de las muestras, se utilizó la técnica de difracción de rayos X con alta resolución en la línea de luz BL04-MSPD (λ = 0.4246 Å) del Sincrotrón ALBA de Barcelona (**Figura 3.1**) con la colaboración de su plantilla (17). Los patrones de difracción de rayos X lineales se recogieron por escaneo contínuo en un detector MAD26 (Multicrystal Analyser Detectors) compuesto de 13 cristales de analizadores de silicio (reflexión Si 111) acoplados a detectores basados en tubos fotomultiplicadores de centelleo separados. Cada uno de los 13 canales tiene una separación angular de 1.5° (18). Se recogió la señal de cada muestra en un rango de 2θ entre 8 a 14°, con un tiempo de adquisición de 6

minutos por difractograma. La muestra (5-10 mg) se cargó en una célula capilar de cuarzo de 1 mm de diámetro, que se acopló a un sistema de flujo. Como fuente de calor se utilizó una pequeña resistencia enrollada debajo del capilar. La temperatura se controló con un termopar de cromo-aluminio de 1.0 mm colocado dentro del capilar cerca de la muestra. La reducción *in situ* a 500 ºC se llevó a cabo con un flujo de 10 mL/min con una mezcla al 5% de H_2 en He y una rampa de temperatura de 5 °C/min.

Además de la simplicidad de la preparación de las muestras, las principales ventajas en comparación con los rayos X producidos en el laboratorio son:

- El mayor poder de penetración de la radiación en la materia a causa de su menor longitud de onda, lo que permite introducir mayor cantidad de muestra en capilares siendo los correspondientes análisis tanto estructurales como cuantitativos más fiables.

- La menor anchura de la función instrumental como consecuencia de la pequeña divergencia vertical del haz emitido (por debajo del mrad) y la posibilidad de usar analizadores de Ge (o Si). Con ello se reduce el solapamiento de los máximos de difracción en los diagramas de polvo.

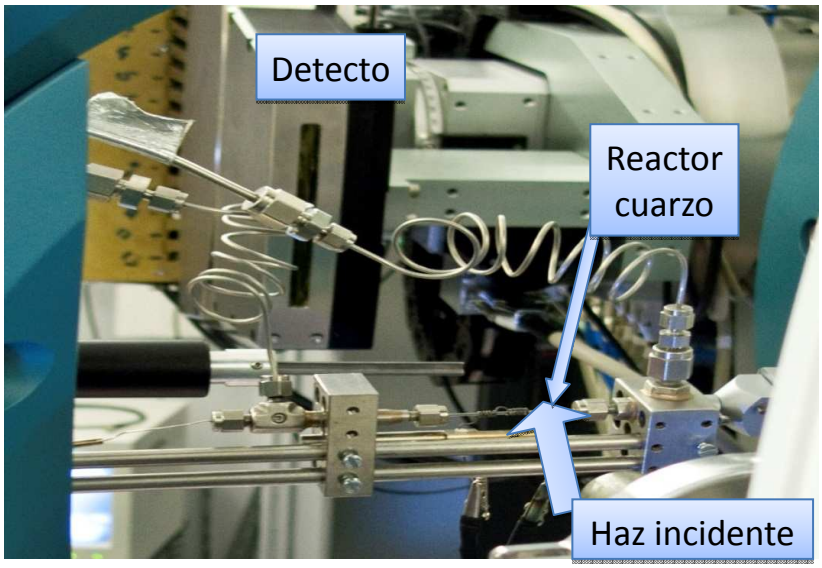

Figura 3.1. Estudio *in situ* de la reducción de las muestras mediante Difracción de Rayos X de alta resolución.

- El elevado flujo y el factor de polarización constante (para goniómetros verticales) reduce considerablemente el tiempo de análisis y mejora la relación señal/ruido, lo cual es especialmente importante en el estudio de los catalizadores y en la reducción de los límites de detección en análisis cualitativos y cuantitativos.

3.3.6. Reducción a temperatura programada (*Temperature-Programmed Reduction* TPR)

Los estudios de reducción a temperatura programada permiten seguir de forma continua las reacciones consecutivas de reducción de especies con el incremento de temperatura. Esta técnica permite, por tanto, obtener información

sobre la dispersión de las especies activas, así como de las interacciones metal-metal y metal-soporte (19), ya que todos estos efectos influyen en la reducibilidad de las especies. Adicionalmente, la técnica permite explorar la correlación existente entre la reducibilidad del precursor oxídico y la actividad de los catalizadores en estado sulfurado (20) (21).

Para el estudio de reducción a temperatura programada se utilizó un equipo Micromeritics TPR/TPD 2900 con un detector de conductividad térmica (TCD). Se usó una mezcla reductora al 10% en volumen de hidrógeno en helio con un caudal total de 50 mL/min. La corriente de gas se divide en dos, de igual caudal, que al entrar al equipo se dirigen al detector (referencia) y la muestra. La muestra se coloca en un reactor tubular de cuarzo en forma de U en el interior del horno. La temperatura se controló con un programador lineal que recoge la señal de dos termopares tipo K situados en la pared del horno y en el interior del reactor, en contacto íntimo con la muestra. La corriente de salida se pasa por una trampa fría, refrigerada con 2-propanol fundente, que mantiene una temperatura de -88 °C durante todo el experimento a fin de condensar el agua procedente de la reducción. De allí pasa al detector (TCD), que trabaja con una corriente de 50 mA. La adquisición de datos se realizó con un ordenador acoplado al equipo que permite la adquisición de datos en contínuo y su posterior procesado. Las medidas se realizaron con 30 mg de catalizador situados en el reactor sobre un tapón de lana de cuarzo. La velocidad de calentamiento para todos los casos fue de 10 °C/min hasta alcanzar los 1050 °C, temperatura en la que se daba por finalizado el ensayo.

3.3.7. Desorción de NH_3 a temperatura programada (*T*emperature-*P*rogrammed *D*esorption of ammonia, **TPD-NH_3)**

Los estudios de acidez de los precursores calcinados y de los catalizadores frescos sulfurados se llevaron a cabo mediante deserción de NH_3 a temperatura programada. Se eligió el NH_3 porque hay estudios (21) (22) que confirman que esta molécula puede estabilizarse en sitios ácidos y penetrar en poros estrechos, debido a su fuerte basicidad y pequeño tamaño.

Las medidas se llevaron a cabo en el equipo descrito para TPR. En una primera etapa, se llevó a cabo un pretratamiento para limpiar la superficie de la muestra (50 mg) bajo un flujo de He a 250 °C durante 1 h. Después se enfrió a 100 °C y se saturó con un flujo de una mezcla al 5% en volumen de NH_3 en helio, con un caudal total de 50 mL/min. Después se pasó un flujo de helio a 100 °C durante 15 min, y finalmente se estudió la desorción del amoníaco calentando en helio hasta 700 °C, usando una rampa de 15 °C/min. Para determinar la acidez total de los catalizadores se integró el área bajo la curva. La distribución de centros ácidos se obtuvo por una deconvolución de los picos, asignando aquellos centros de acidez débil, media y fuerte a las componentes a temperatura baja, media y alta, respectivamente.

3.3.8. Microscopía Electrónica de Transmisión (*T*ransmission *E*lectron *M*icroscopy**, TEM)**

La microscopía electrónica de transmisión (TEM) es una técnica muy útil para la investigación de la topografía de superficies, determinación directa de formas, distribución de tamaños y localización de componentes específicos, como es el caso de

las partículas metálicas de catalizadores soportados. La técnica permite realizar dicha caracterización a una escala nanométrica superior al umbral inferior de utilización de difracción de rayos X (> 5 nm).

La técnica de microscopía electrónica de transmisión permite analizar la forma y tamaño de las fases activas de los sistemas catalíticos en la escala nanométrica. Esta técnica se fundamenta en la interacción con la materia de un haz monocinético de electrones (200-400 kV), acelerado bajo una diferencia de potencial de varios cientos de kilovoltios, que es colimado, enfocado y orientado por distintas lentes electromagnéticas. Estos electrones se producen por un filamento de W o LaB_6, y son acelerados al pasar a través de una gran diferencia de potencial (23). En un microscopio electrónico de transmisión, la muestra se ilumina con un haz de electrones producidos por el cañón situado en la parte superior del microscopio. Este cañón puede ser termoiónico o de emisión de campo.

El haz de electrones lleva asociada una longitud de onda del orden de décimas de A, que depende del voltaje de aceleración y que finalmente determinará la resolución espacial alcanzable en las imágenes. Antes de alcanzar la muestra, el haz de electrones se modifica por las lentes condensadoras para mejorar su coherencia. Cuando este haz interacciona con una muestra de bajo espesor (0.1-0.5 μm), da lugar a haces difractados transmitidos y dispersados. El enfoque de los haces difractados por la lente objetivo en el plano focal trasero origina un diagrama de difracción de electrones, mientras que su enfoque en el plano imagen permite obtener una proyección bidimensional del material observado. La primera imagen intermedia se aumenta a continuación por una serie de lentes proyectoras para llegar a hacerse visible en una pantalla fluorescente, que puede elevarse para permitir que los

electrones sean recogidos sobre una película fotográfica o a través de una cámara digital.

Para las medidas de TEM se utilizó un microscopio JEM 2100F que alcanza un potencial de aceleración de 200 kV. Los catalizadores sulfurados, reducidos y/o usados en reacción se pulverizaron en un mortero de ágata y se suspendieron en isooctano. Se dispersaron en un baño de ultrasonidos durante 15 minutos. Una gota de la suspensión así obtenida se depositó sobre la rejilla de cobre que tiene depositada en su superficie una capa de carbón como soporte eléctricamente conductor. Las muestras se dejaron secar al aire. Las rejillas así preparadas se colocaron en el portamuestras del microscopio y se sometieron al tratamiento de vacío preciso para operar el equipo ($3 \cdot 10^{-5}$ Pa). Se tomaron al menos 10 imágenes representativas de cada catalizador.

Los tamaños medios de partícula (d) se calcularon como el valor medio de los tamaños de partícula de, al menos, 250 partículas y utilizando la aproximación de Borodziński *et al.* (24) para un grupo de partículas de semejante forma pero distinto tamaño:

$$d = \frac{\sum_i n_i d_i^3}{\sum_i n_i d_i^2} \qquad \textbf{Ecuación 3.9}$$

donde n_i es el número de partículas de diámetro d_i.

La desviación estándar acompaña a cada valor de tamaño medio de partícula, ya que es una medida del grado de dispersión de los tamaños de partícula con respecto al valor medio. Las distribuciones de tamaño de partícula representan la frecuencia en porcentaje con el que un determinado rango de tamaños se repite.

3.3.9. Microscopía electrónica de barrido (*Scanning Electron Microscope*, SEM)

La microscopía electrónica de barrido (SEM) utiliza electrones para producir imágenes de mucha más alta resolución que la microscopia óptica. Esta técnica se utilizó para estudiar la morfología de los cristales obtenidos.

Las señales utilizadas comúnmente para la imagen de SEM son las de electrones secundarios y retrodispersados, que ofrecen el contraste topográfico y el contraste debido al número atómico (Z). El microscopio SEM posee un objetivo en la parte superior de la muestra y en él pueden encontrarse varios tipos de detectores (secundarios, retrodispersados, etc.). Tiene dos bobinas deflectoras del haz electrónico en las direcciones x e y, que determinan el barrido del área seleccionada por la muestra. El haz de electrones pasa a través de las lentes condensadoras y de objetivo, y es barrido a lo largo de la muestra por las bobinas de barrido mientras un detector cuenta el número de electrones secundarios de baja energía emitidos por cada punto de la superficie. La potencia empleada varía entre 1 y 40 kV (25).

Las lentes se usan para ampliar y enfocar el haz de electrones sobre la superficie de la muestra. Las grandes ventajas de este tipo de microscopio son el rango de ampliación y la profundidad del campo de la imagen. Dentro de los fenómenos que tienen lugar en la muestra bajo el impacto de electrones, el más importante es la emisión de electrones secundarios con energías de unas cuantas decenas de eV, seguido de la emisión de electrones retrodispersados con energías más elevadas. Hay detectores adecuados que discriminan los electrones en función de su energía, permitiendo por tanto formar imágenes tanto con electrones secundarios como retrodispersados. Los electrones secundarios se emiten por la

muestra en procesos inelásticos de ionización debido a la colisión del haz incidente, altamente energético. Estos electrones al ser de baja energía vuelven a ser absorbidos por átomos adyacentes pudiendo escapar de la muestra tan solo los electrones secundarios generados cerca de la superficie.

La preparación de la muestra es sencilla. La mayoría de los microscopios electrónicos de barrido sólo requieren que éstas sean conductoras y algunos ni siquiera lo necesitan. Además de las imágenes obtenidas, también se puede realizar un análisis de composición química de la muestra mediante energía dispersiva de rayos X (EDX). Esta técnica consiste en la excitación de la muestra con rayos X monocromáticos y la detección de los rayos X emitidos por ésta. En esta tesis se empleó un microscopio Hitachi TM-1000.

3.3.10. Espectroscopia Fotoelectrónica de Rayos X (*X-Ray Photoelectron Spectroscopy*, XPS)

La espectroscopia fotoelectrónica de rayos X es una técnica de análisis químico que se emplea para determinar la composición superficial de la muestra, el estado de oxidación de los átomos y su entorno químico en la muestra. Esta técnica está basada en el efecto fotoeléctrico, que consiste en la emisión de los electrones de los niveles internos de los átomos de la muestra cuando se irradia con fotones de rayos X. Un detector hemiesférico detecta los electrones emitidos y registra su energía para obtener el espectro de emisión fotoelectrónica. La energía cinética de los electrones emitidos está relacionada con su energía de ligadura (*binding energy,* BE), que es característica de los elementos presentes en la muestra y de las interacciones electrónicas que existen entre ellos (26) .

La radiación excitante puede penetrar en la materia de 1 a 10 μm, pero los electrones arrancados a esa profundidad disipan su energía mediante colisiones inelásticas. Solamente los electrones que poseen recorridos libres entre 0.5 y 4 nm llegan al detector, por lo que la espectroscopia fotoelectrónica tiene un carácter eminentemente superficial, proporcionando información química de solo iunas pocas capas atómicas próximas a la superficie de la muestra.

Como consecuencia de la emisión de fotoelectrones, la muestra se va cargando positivamente durante la medida. En muestras conductoras el efecto se minimiza a través de la conexión a tierra del portamuestras, pero en muestras aislantes el efecto se maximiza, al no poder recuperar la neutralidad a través de la conexión a tierra. El resultado es que los electrones se ven atraídos por el potencial positivo de la muestra, los picos del espectro se desplazan hacia una energía de enlace mayor y su energía cinética se reduce en un valor C denominado efecto de carga. Usualmente para subsanar este problema, se requiere la utilización del algún patrón interno para calibrar la energía de ligadura, en nuestro caso se utilizaron los picos correspondientes al Si 2p (Binding Energy, BE = 103.4 eV) o el C1s (BE = 284.8 eV).

La energía cinética que poseen estos electrones, se relaciona con la energía de enlace del electrón de ese átomo en ese nivel según la ecuación que rige el efecto fotoeléctrico:

$$E_c = h\nu - BE - \phi_s \qquad \textbf{Ecuación 3.10}$$

donde: hν es la energía del fotón incidente (Mg Kα= 1253.6 eV) y BE es la energía de enlace del electrón. La ecuación clásica del efecto fotoeléctrico se corrige con ϕ_s, función de trabajo del espectrómetro.

La energía de ligadura del electrón emitido de un orbital concreto depende principalmente del número atómico y del estado de oxidación y del entorno químico del elemento, es decir, de un modo general, depende de la densidad electrónica del elemento en un compuesto determinado.

El equipo que se ha empleado es un espectrómetro VG Escalab 200R provisto de un analizador de electrones semiesférico, con cinco detectores tipo *channeltron* y una fuente de emisión de rayos X de doble ánodo Mg (K_α = 1253.6 eV) / Al (K_α = 1486.6 eV), que opera a 12 kV y 10 mA. La presión de trabajo en la cámara de análisis es inferior a 1.07×10^{-8} mbar. Los catalizadores, en forma de polvo, se colocaron en un portamuestras de acero inoxidable con un hueco con forma de cilindro (8 mm de diámetro y 1 mm de altura), y son compactadas con un disco de teflón o polietileno. Previo al análisis se llevó a cabo una etapa de desgasificación a 130 ˚C durante 1 h y posteriormente se realizaron análisis de la muestra sin tratar y tras un tratamiento térmico en hidrógeno (en los distintos capítulos se especifican las condiciones de tratamiento). El registro de espectros fue realizado con una energía de paso de 50 eV, acumulando espectros hasta conseguir una buena relación señal/ruido. La precisión de las líneas espectrales es de ± 0.2 eV.

Los picos observados en los espectros se deconvolucionaron en varias componentes, en función de las distintas contribuciones observadas, con una combinación lineal de curvas *lorentzianas* y *gaussianas* en proporción 90G/10L mediante el programa informático de tratamiento de espectros *XPS Peak* 4.0, escogiendo el mejor ajuste por minimización de residuos χ^2. La determinación cuantitativa de la composición atómica superficial se obtuvo mediante la aplicación de los factores de sensibilidad atómica (27).

3.3.11. Análisis Termogravimétrico (*Thermo Gravimetric Analysis-Differential Thermal Analysis*, TGA-DTA)

Esta técnica determina los cambios de peso de las muestras, usualmente en forma porcentual, en función de la temperatura (28) (29). Esta medida es de gran utilidad para determinar la estabilidad térmica de los materiales empleados. Para ello se coloca la muestra en una microbalanza donde el platillo con la muestra está introducido en un horno de alta precisión, y en una atmósfera dinámica o estática de un gas determinado. El aumento o disminución del peso se registra en función de la temperatura o del tiempo teniendo en cuenta la velocidad de calentamiento del horno.

La cantidad de coque depositado de los catalizadores usados en reacción se determinó con un equipo termogravimétrico TGA/ SDTA 851 (Mettler Toledo), midiendo los cambios de peso que sufren las muestras durante la oxidación a temperatura programada (TPO). Cada muestra se calentó para homogeneizar el coque y eliminar los compuestos volátiles hasta 500 °C durante 1h en N_2 (10 °C/min; 200 mL/min). Después de enfriar a temperatura ambiente con una velocidad de 5 °C/min, la muestra se calentó hasta una temperatura final de 900 °C (10 °C/min con un flujo de 50 mL/min de una mezcla 20% O_2/N_2). La cantidad de coque presente en el catalizador usado en reacción se calculó por diferencia entre el peso inicial y final, siendo el peso inicial tomado después del pretratamiento a 500 °C durante 1h en N_2.

3.3.12. Espectroscopia infrarroja (*Infrared spectroscopy,* IR)

La espectroscopia infrarroja (IR) estudia la interacción de la materia con la región del espectro electromagnético que incluye radiación de longitudes de onda comprendidas entre 2.5 y 25 μm o, en número de ondas, entre 4000 y 400 cm^{-1}. En esta región del espectro se producen las transiciones energéticas debidas a las vibraciones de los enlaces que constituyen una molécula. La representación de la intensidad de la radiación IR en función del número de ondas se denomina espectro IR y permite la identificación de grupos funcionales mediante la comparación de dicho espectro con los existentes en la bibliografía científica.

La modalidad de *reflectancia difusa* (***D**iffuse Reflectance Infrared Fourier Transform*, DRIFT) se emplea en materiales de difícil compactación y/o materiales opacos que no permiten el paso directo de la radiación. La muestra se coloca en un receptáculo dentro de un dispositivo o celda que permite la dosificación y circulación de gases a través de la muestra. Dispone de un sistema de cierre hermético (duomo) con dos ventanas por donde entra y sale la radiación IR. La radiación incidente alcanza la muestra, donde se absorbe, se refracta y se refleja. La *radiación difusa reflejada* se dirige al detector del espectrómetro mediante un sistema complejo de espejos. Otra ventaja de esta disposición es que permite realizar estudios *in situ* mientras circula a través de la muestra una corriente gaseosa de interés catalítico. Por tanto, es una herramienta potente para estudiar intermedios de reacción y especies activas.

De forma general, un espectrómetro IR consta de una fuente de radiación IR, con un sistema de selección de longitudes de onda y un detector. Inicialmente se empleaban monocromadores como elementos dispersivos, pero hoy en día los equipos comerciales hacen uso del fenómeno de la interferencia. Se habla de

espectrómetros por transformada de Fourier (***F**ourier **t**ransform **i**nfra**r**ed spectroscopy*, FTIR).

La modalidad DRIFT para estudiar los modos de adsorción de NO en los catalizadores de CoMoW que se detallan en el Capítulo 5 se realizó con un espectrómetro Jasco FTIR-6300A provisto de un detector MCT. Para estudiar los modos de adsorción del CO sobre la superficie de los catalizadores prereducido de Pd que se detallan en el Capítulo 8 se utilizó un un Nicolet 5ZDX Fourier Transform con una resolución de 4 cm^{-1} en todo el rango espectral y un promedio de más de 100 exploraciones para ambos equipos. Los catalizadores (espesor aproximadamente de 10 mg/cm^{-2}) se redujeron en un flujo de hidrógeno a 300 ° C durante 1 h y luego se desgasificaron a vacío a 450 °C durante 1 h antes de la exposición a 30 mbar de CO.

3.4. Medidas de actividad catalítica

3.4.1. Instalación experimental

Los catalizadores se ensayaron en una instalación experimental de flujo contínuo a escala de laboratorio, que permite trabajar a presiones de 5º bar (en la **Figura 3.1** se muestra un esquema de esta instalación) que para su descripción se ha dividido en dos partes: (i) sistema de alimentación y (ii) sistema de reacción.

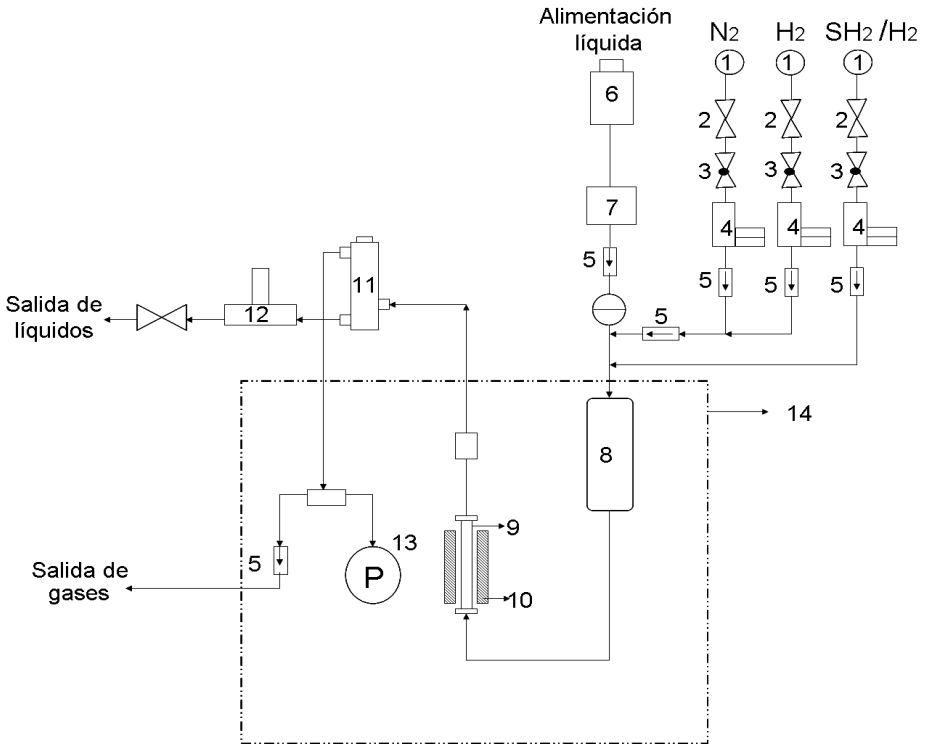

Figura 3.2. Esquema de la instalación experimental usada en las medidas de actividad catalítica: 1 – botellas de gases; 2 – manorreductores; 3- válvulas todo o nada; 4 – controladores de flujo másico (gases); 5- válvula antirretorno; 6- depósito de alimentación; 7- bomba de flujo másico (líquido); 8- precalentador-mezclador de líq-gas; 9- reactor; 10- horno; 11- condensador peltier; 12- descargador de líquidos; 13- medidor de presión; 14- caja caliente.

(i) Sistema de alimentación

En la instalación experimental, los reactivos se alimentan en dos fases distintas: por una parte el compuesto tipo a ensayar se alimenta en fase líquida, y por otra el hidrógeno, el sulfuro de hidrógeno (como agente activante del catalizador) y el nitrógeno (como inerte) se alimentan en estado gaseoso.

(1) Líquidos. El líquido a alimentar al sistema se almacena en un depósito de 500 mL de capacidad. El caudal de alimentación líquida introducido al sistema se controla con una bomba reguladora de flujo másico para líquidos HPLC K-120 Knauer de 10 mL. La conducción de salida del regulador de flujo másico se conecta con el mezclador de líquido-gas.

(2) Gases. Como ya se ha señalado se utilizan tres gases, dos reactivos (hidrógeno y sulfuro de hidrógeno) y nitrógeno como generador de atmósferas inertes. Cada gas se introduce en una línea independiente (dos de alta presión para hidrógeno y nitrógeno y una de presión atmosférica para el sulfuro de hidrógeno). Cada uno de los gases se almacenó en botellas de alta presión con sus correspondientes manorreductores para fijar la presión de salida. El caudal gaseoso de cada uno de ellos se regula por medio de controladores de flujo másico Bronkhorst High-Tech (rango 0-100 mL/min), conectados a la unidad de control ICP FC31, que permite el ajuste de puntos de consigna y visualización de caudales de proceso. Las conducciones de salida de los respectivos reguladores, que poseen válvulas antirretorno HOKE 4F, se encuentran conectadas al mezclador líquido-gas.

(ii) Sistema de reacción

Todos los elementos que componen el sistema de reacción se encuentran localizados en una caja caliente construida en acero inoxidable 316 (temperatura máxima 200 °C). La existencia de una temperatura de 120 °C, lograda por circulación forzada de aire, en todo el trazado, evita la posible condensación de productos en el recorrido del proceso al tiempo que precalienta eficazmente los reactivos. El sistema de reacción está constituido por un reactor tubular de lecho

fijo y flujo descendente construido en acero inoxidable 316 de y 180 mm de longitud. Con una placa porosa situada a 100 mm de la parte superior del reactor, con 9.5 mm de diámetro exterior y 2.5 m de espesor. El esquema simplificado se muestra en la **Figura 3.3**.

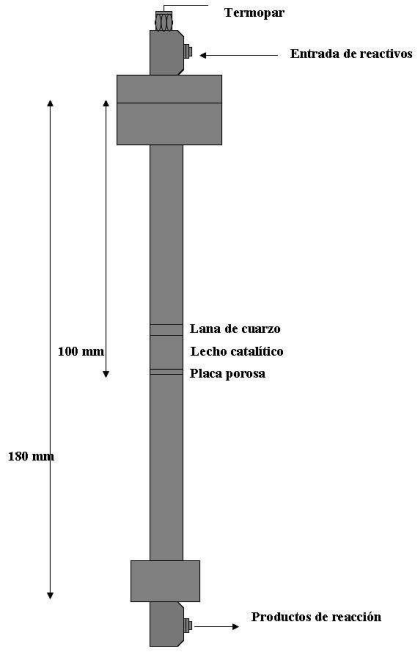

Figura 3.3. Esquema del reactor utilizado en las medidas de actividad catalítica.

El reactor posee una placa porosa que sirve de soporte del catalizador. El termopar de tipo K, de 1.5 mm de diámetro, se encuentra situado coaxialmente al reactor y localizado 10 mm por encima de la placa porosa en contacto directo con el lecho catalítico. La calefacción del reactor se realiza con un horno de 550 W (temperatura máxima 600 °C), de baja inercia térmica que permite introducir puntos de consigna y visualizar la temperatura del reactor.

3.4.2. Operación

En esta sección se explica la metodología general seguida en los diferentes capítulos de resultados, sin detallar los caudales, composiciones de alimentación, presiones, ni temperaturas de operación, ya que todos estos datos se indicarán en cada capítulo de resultados.

3.4.2.1. Preparación de la mezcla de reacción

Tabla 3.4. Mezcla de reacción para los diferentes capítulos de la Tesis.

Capítulo	Molécula modelo/ disolvente	Composición (% en peso)
Capítulo 4	Subproducto del aceite de oliva	Detallada en el capítulo 4
Capítulo 5	Anisol	20%
Capítulo 5	Hexadecano	80%
Capítulo 6, 7 y 8	Fenol	2%
Capítulo 6, 7 y 8	Decalina (cis + trans)	98%

En el caso del hidrotratamiento de los compuestos modelos, la dosificación de la mezcla se realiza pesando la cantidad necesario del compuesto tipo para obtener el porcentaje seleccionado para el ensayo y completándose con el disolvente orgánico correspondiente al peso total de alimentación a preparar.

3.4.2.2. Preparación del lecho catalítico

Para la preparación del lecho catalítico se añadió el catalizador diluido con carburo de silicio, con la intención de aumentar la eficacia en el precalentamiento

de la mezcla reaccionante y minimizar los efectos de cola a la salida del reactor. La granulometría utilizada, tanto en el carburo de silicio como en las partículas de catalizador, fue de 0.25-0.30 mm. Se cubre la parte superior del lecho con lana de vidrio a fin de evitar el arrastre de partículas de catalizador. Finalmente se monta el reactor en la instalación y se comprueba que no existen fugas a la máxima presión de trabajo, utilizando gas inerte (N_2) en la presurización.

3.4.2.3. Activación del catalizador

La activación es generalmente el paso final de conversión del precursor del catalizador (óxidos de los metales introducidos depositados sobre los diferentes soportes) a su forma activa de trabajo ya sean sulfuros o metales reducidos en el caso de la hidrodesoxigenación (HDO). El método de activación aplicado al catalizador influirá en el comportamiento catalítico del mismo, ya que determinará la naturaleza y abundancia de las especies formadas (30) (31).

En este trabajo para la reacción de hidrodesoxigenación los procedimientos de activación fueron diferentes de acuerdo a la naturaleza de las fases activas de los catalizadores: sulfuros en el caso de los metales Mo y W, por tanto su método de activación es la sulfuración y metales reducidos para el caso de los metales nobles Pt e Ir con lo que será la reducción su procedimiento de activación.

- **Sulfuración** (catalizadores CoMo y CoMoW)

El procedimiento de activación más ampliamente utilizado en la bibliografía es la sulfuración directa del precursor calcinado en una corriente de H_2 conteniendo H_2S (2-10 % volumen) a una temperatura próxima a 400-450 °C. La temperatura de activación y la composición de la mezcla de sulfuración son los

factores que con mayor peso específico influyen en el estado final del catalizador activado. Massoth (20) encontró que, para una temperatura y tiempo de sulfuración dados, un incremento en la concentración del H_2S en la corriendo de sulfuración se traduce en un incremento en el contenido de azufre del catalizador, alcanzando un valor constante por encima del 4% de H_2S en H_2. El efecto de la temperatura de sulfuración también se ha estudiado por numerosos autores (30) (32) (33). Se ha encontrado que temperaturas de sulfuración muy altas provocan pérdida de dispersión de las fases activas así como la segregación de fases.

Teniendo en cuenta los estudios anteriores, la activación de los catalizadores se realizará por sulfuración directa a presión atmosférica utilizando una corriente de sulfuración de H_2/H_2S (90: 10 en volumen) a una temperatura de 400- 450 °C. El procedimiento de activación comienza con el secado previo del catalizador bajo corriente de N_2 (100 mL/min) a 150 °C durante 1 h. Una vez secó y enfriado a temperatura ambiente, se procede a la sulfuración "*in situ*". El reactor se calienta a una velocidad de 10 °C/min hasta 400-450 °C bajo corriente de N_2 (100 mL/min). Una vez alcanzada la temperatura de activación, se introduce la mezcla de hidrógeno y sulfuro de hidrógeno (100 mL/min) y se activa a esa temperatura durante 4 h. Transcurrido ese tiempo se vuelve a pasar nitrógeno con el fin de desorber el sulfuro de hidrógeno que haya podido quedar retenido en el lecho, se enfría a temperatura ambiente y se almacena durante la noche en atmósfera inerte bajo un flujo de N_2 de 5 mL/min.

- **Reducción** (Catalizadores de NiZn y PtIr)

Tras un proceso de secado análogo al descrito en el apartado anterior, se procede a la reducción "*in situ*" del catalizador. La reducción se realiza utilizando una mezcla H_2/N_2 (10:1 en volumen) bajo un caudal constante de 55 mL/min. Bajo

dicho caudal se calienta el catalizador situado en el interior del reactor hasta 300-350°C. A esta temperatura permanece durante 2- 3 h. Transcurrido este tiempo, se enfría bajo la corriente reductora hasta la temperatura de reacción almacenándose durante la noche bajo atmósfera inerte (N_2, 5 mL/min).

3.4.2.4. Reacción en el reactor de lecho fijo (flujo de pistón)

El proceso se inicia presurizando el equipo con N_2 hasta el valor de 30 bar. A continuación se calienta a razón de 10 °C/min hasta 310 °C (temperatura a la que los catalizadores resultaron más activos en un ensayo previo) bajo flujo del mismo gas. Cuando se alcanza la temperatura y las condiciones de reacción son estables, se corta la entrada de inerte y se da comienzo a la alimentación del líquido a hidrotratar e hidrógeno. El reactivo líquido se arrastra por el gas portador hacia el reactor, pasa a través del lecho catalítico y se condensa en el refrigerante a la salida del reactor. El período de tiempo necesario para la estabilización de las condiciones fluido-dinámicas en el reactor es de 60 min, comprobándose que transcurrido dicho período de tiempo, los caudales y la composición de los gases y líquidos efluentes se mantienen prácticamente constantes. Se inicia entonces el período de reacción propiamente dicho. La actividad catalítica se determina sobre los catalizadores activados a 310 °C. Se toma muestra cada hora durante 4 h, acumulando muestra durante 15 min, tomando la precaución de vaciar el depósito para evitar mezclas de productos de distintas temperaturas. Dichas muestras se analizan por cromatografía de gases, técnica que permite el seguimiento y cuantificación detallada de las variaciones de composición de las muestras.

3.4.2.5. Reacción en el reactor tipo "batch"

Durante mi estancia en Lyon evalué la actividad catalítica de los catalizadores de la serie de los catalizadores PtIr del que se incluye en el Capítulo 7. Los catalizadores se evaluaron en la reacción de hidrodesoxigenación de fenol en un reactor tipo *batch* con un volumen de 300 mL. Una reacción en discontinuo sirve para observar los intermedios de reacción y así determinar el camino de reacción. El autoclave está equipado con un agitador para máxima dispersión del gas en la fase líquida (900 rpm). Las muestras se recogen mediante un tubo de diámetro 1/8. El hidrógeno se introdujo en el reactor a través de un regulador de presión que mantiene una presión constante durante todo el experimento. El reactivo (10.6 mmol fenol) se disolvió en tetralina (80 mL) usando hexadecano como patrón estándar interno. Se usaron 100 mg de catalizador previamente reducido (350 °C, 3 h). El sistema se calentó bajo flujo de N_2 el sistema hasta la temperatura de reacción (200 °C). Después el N_2 se reemplaza por H_2 y se presuriza hasta 30 bar.

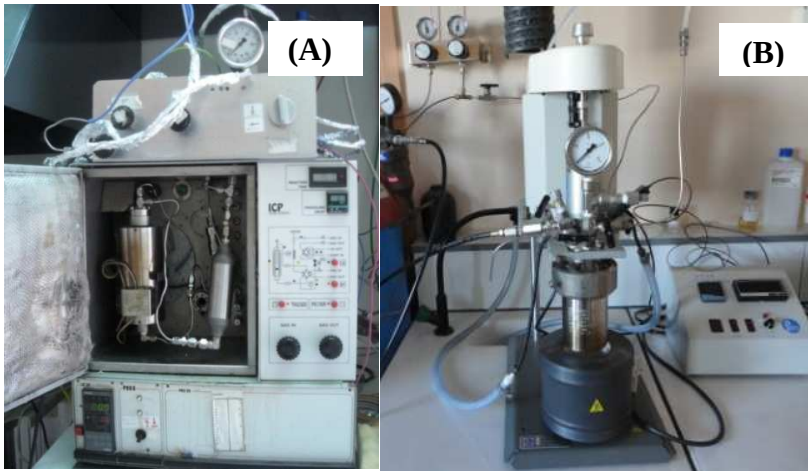

Figura 3.4. (A) Equipo de flujo de lecho fijo (reacción en continuo)(ICP-CSIC, Madrid. (B) Autoclave (reacción en discontinuo) (CNRS- Lyon).

3.4.2.6. Análisis de productos

Los productos de reacción se analizaron por cromatografía gaseosa usando un cromatógrafo Agilent 6890A (**Figura 3.5**) conectado a un detector de ionización de llama (FID) para el análisis de hidrocarburos y diferentes compuestos oxigenados de la reacción de hidrodesoxigenación de anisol. Para la separación cromatográfica, se utilizó una columna ATTM-1HT de 30 m de longitud y 0.25 mm de diámetro interno, con espesor de 0.1 micras, con una relación de split 300:1 y una columna HP-Innowax (Crosslinked Polyethylene Glycol) de 30 m de longitud y 0.25 mm de diámetro interno, con espesor de 0.25 mm, con una relación de split 300:1. Para buena separación de los productos de interés, es necesario realizar análisis termoprogramado. El programa comienza con una temperatura inicial de 35 °C durante 2.5 min, seguido de un calentamiento (velocidad de calentamiento 10 °C/min) hasta la temperatura final de 160 °C, manteniéndose en esa temperatura 15 min. De esta forma se logra una perfecta separación de los productos de interés.

Figura 3.5. Cromatógrafo Agilent 6890A (ICP-CSIC, Madrid)

Durante la estancia en Lyon (**Figura 3.6**) el cromatógrafo usado fue un Hewlett-Packard 5890A. Equipado con un detector FID y con una columna capilar DB-1 de 30 m de longitud y 0.45 mm de diámetro interno; con espesor de 2.55 μm. Los productos se separaron a una temperatura de 250 °C. Los factores de respuesta y reactivos y productos fueron tomados de disoluciones de concentraciones conocidas.

Figura 3.6. Cromatágrafo Hewlett-Packard 5890A (Lyon, Francia)

3.4.2.7. Tratamiento de datos

Una vez identificado cada pico con el sistema de análisis, se elabora un patrón con los tiempos de retención de cada compuesto (**Tabla 3.5**), dichos tiempos son función del método cromatográfico utilizado. A partir de los datos de las áreas de los picos cromatográficos, del peso de muestra líquida y del flujo de gases de salida, se calculó el número de moles de cada uno de los productos obtenidos y a partir de ellos se calcularon los correspondientes balances de materia (**Ecuación 3.11**). Los factores de respuesta para los productos de la reacción de hidrodeoxigenación del anisol se recopilan en la **Tabla 3.5.** Los resultados obtenidos a partir de la integración de las áreas de los picos registrados en el cromatograma se introdujeron en una hoja Excel que se diseñó con el objetivo de obtener la conversión y selectividad de los productos de una forma rápida y sencilla.

$$\%peso_a = \frac{area_a \cdot factor_a}{\Sigma areas \cdot factores}$$ **Ecuación 3.11**

Tabla 3.5. Tiempos de retención y factores de respuesta correspondientes a la reacción de HDO del anisol

Compuesto	**Tiempo de retención (min)**	**Factor de respuesta (área·mmol^{-1})**
Metilciclopentano	1.380	423.7
Benceno	1.446	211.7
Ciclohexano	1.470	197.2
Ciclohexeno	1.524	202.4
Tolueno	1.965	238.8
Anisol	3.851	221.0
Fenol	5.215	199.6
Orto-metilanisol	5.509	249.3
Orto-cresol	6.358	1012
2,6-Xilenol	6.993	1529

.

Para la reacción HDO del anisol (o fenol), los valores de los parámetros estudiados se calcularon suponiendo el esquema de reacción presentado en la **Figura 3.7.** En esta figura se presenta un esquema de la reacción HDO de fenol:

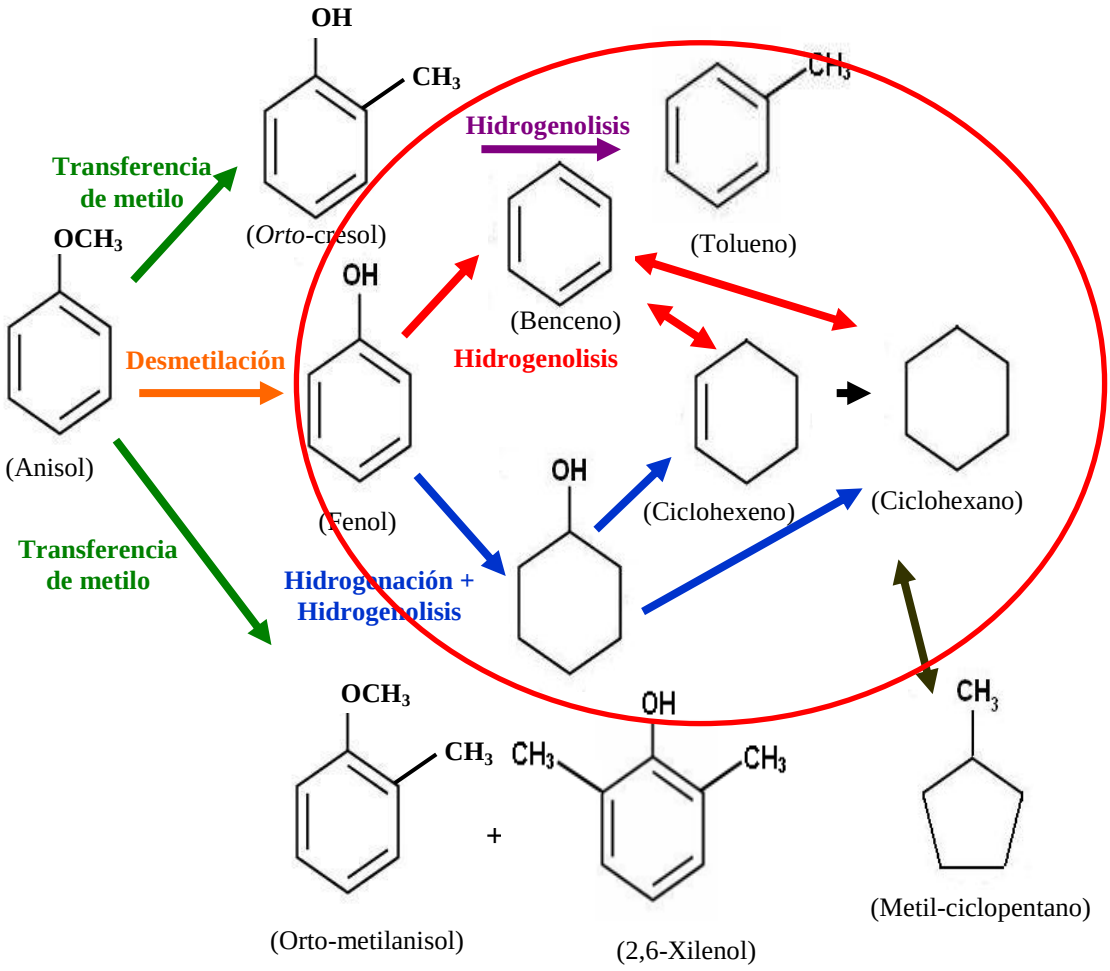

Figura 3.7. Esquema de la reacción de hidrodesoxigenación de anisol y de fenol.

Las conversiones y selectividad a los productos se calculan de acuerdo a las expresiones:

- Conversión de anisol (fenol)

$$X = \frac{\text{moles de anisol (fenol) reaccionados}}{\text{moles de anisol (fenol) alimentados}} x100$$

- Selectividad hacia los distintos productos (S_{prod})

$$S_{prod} = \frac{\text{moles de producto formado}}{\text{moles de anisol (fenol) reaccionados}} x100$$

-Velocidad espacial

$$\frac{F}{W} = \frac{\text{moles de reactante alimentado h}^{-1}}{\text{gramos de catalizador}}$$

-Rendimiento a producto *i* (R_i)

$$R_i = \frac{\text{moles de producto i formados}}{\text{moles de anisol (fenol) alimentados}} x100$$

3.5. Bibliografía

1. *Proceedings 4th International Congress On the Chemistry and Uses of Molybdenum.* **Hall, W.K.** s.l. : H.T. Barry, P.C.H. Mitchell. Climax Molybdenum Company Ltd., 1982. 224.

2. *Proceedings 9th International Congress on Catalysis.* **Knözinger, H.** s.l. : M.J. Philips, M. Ternan., 1988. 20-53.

3. *Recent advances in catalysis over sulphides.* **Zdrazil, M.** s.l. : Catalysis Today, 1988, Vols. 3 (4) 269-365.

4. *Catalyst preparation methods.* **C. Perego, P. Villa.** s.l. : Catalyisis Today, 1997, Vols. (34) 281-305.

5. **Bond, G.C.** *Heterogeneous Catalysis, Principles and Applications.* s.l. : 2º Ed. Oxford Science Publications, 1987.

6. *Design and Preparation of Impregnated Catalysts.* **Komiyama, M.** s.l. : Catalysis Reviews, 1985, Vols. (27) 341- 372.

7. **A. Montaser, D.W. Golightly.** *Inductively coupled plasmas in analytical atomic spectrometry.* s.l. : VCH Publisehrs inc, New York, 1987.

8. **C.E. Boss, J. Freeden.** *Concepts, Instrumentation and Techniques in inductively coupled plasma atomic emission spectrometry .* s.l. : The Perkin Elmer Corporation, Norwalk (CT), 1990.

9. *Total reflection X-ray spectrometry: method and applications.* **Prange, A.** s.l. : Spectrochimica Acta Part B: Atomic Spectroscopy, 1989, Vols. (44) 437- 452. .

10. *First approximation to the analysis of Ru and Se in carbon nanoparticles as a new voltaic pile system by TXRF.* **R. Fernández- Ruíz, P. Ocón, M. Montiel.** s.l. : Journal of Analytical Atomic Spectrometry, 2009, Vols. (24) 785-791.

11. **E. Hermana Tezanos, F. Calvo Mondelo.** s.l. : Química e Industria, 1992, Vol. (18) 5.

12. *Manual on catalyst characterization.* **Haber, J.** s.l. : Pure and Applied Chemistry, 1991, Vols. (63) 1227-1246.

13. *Adsorption of Gases in Multimolecular Layers.* **S. Brunauer, H. Emmett, E. Teller.** s.l. : Journal of the American Chemical Society, 1938, Vols. (60) 309-319.

14. *Reporting physisorption for gas/ solid systems.* **K.S.W. Sing, D.H. Everett, R.A.W. Haul, L. Moscou, R.A. Pierotti, J. Rouquerol, T. Siemieniewska.** s.l. : Pure and Applied Chemistry, 1985, Vols. (57) 603-619.

15. **Cullity, B.T.** *Elements of X-Ray Diffraction.* s.l. : Addison- Wesley, 1978.

16. **Wagner, C.N.J.** *Local Atomic Arregements Studied by X-Ray Diffraction .* s.l. : J.B. Cohen, J.F. Hilliard. Gordon and Breach, New York, 1996.

17. *The new Material Science Powder Diffraction beamline at ALBA Synchrotron.* **F. Fauth, I. Peral, C. Popescu, M. Knapp.** s.l. : Powder Diffraction, 2013, Vols. (28) 360-370.

18. *Design and construction of multicrystal analyser detectors using Rowland circles: Application to MAD26 at ALBA.* **I. Peral, J. McKinlay, M. Knapp, S. Ferrer.** s.l. : Journal of Synchrotron Radiation, 2011, Vols. (18) 842-850.

19. *Temperature programmed analysis and its applications in catalytic systems.* **S. Bhatia, J. Beltramini, D.D. Do.** s.l. : Catalysis Today , 1990, Vols. 7 (3) 309- 438.

20. *Studies of molybdena-alumina catalysts: IV. Rates and stoichiometry of sulfidation.* **Massoth, F.E.** s.l. : Journal of Catalysis, 1975, Vols. (36) 164- 184.

21. *The CoO single bond MoO3 single bondγ-Al2O3 catalyst: VI. Sulfur content analysis and hydrodesulfurization activities.* **V.H.J. de Beer, C. Bevelander, T.H.M. van Sint Fiet, P.G.A.J. Werter, C.H. Amberg.** , s.l. : Journal of Catalysis, 1976, Vols. 43 (1-3) 68-77.

22. *Infrared, microcalorimetric, and electron spin resonance investigations of the acidic properties of the H-ZSM-5 zeolite.* **J.C. Védrine, A. Auroux, V. Bolis, P. Dejaifve, C. Naccache, P. Wierzchowski, E.G. Derouane, J.B. Nagy, J.P. Gilson, J.H.C. van**

Hooff, J.P. van den Berg, J. Wolthuizen. s.l. : Journal of Catalysis , Vols. (59) 248-262.

23. **D.B. Williams, C.B. Carter.** *Transmission electron microscopy vol.1: Basics.* s.l. : Plenum, cop. New York and London, 1996.

24. *Relation between crystallite size and dispersion on supported metal catalysts.* **A. Borodziriski, M. Bonarowska.** s.l. : Langmuir, 1997, Vols. (13) 5613-5620.

25. **al., M.T. Postek et.** *Scanning electron microscopy: a student's handbook.* s.l. : Ladd Research Institute Inc., 1980.

26. *Empirical atomic sensitivity factors for quantitative analysis by electron spectroscopy for chemical analysis.* **C.D. Wagner, L.E. Davis, M.V. Zeller, J.A. Taylor, R.H. Raymond, L.H. Gale.** s.l. : Surface and Interface Analysis, 1981, Vols. (3) 211-225.

27. **C.D. Wagner, W.M. Riggs, L.E. Davis, J.F. Moulder.** *Handbook of X-ray photoelectron spectroscopy.* s.l. : Perkim Elmer Corp, Minesota, 1978.

28. **Wendlant, W.** *Thermal Analysis .* s.l. : New York, 1984.

29. **G.C. Keatch, D. Dollimore.** *An introduction to Thermogravimetry .* s.l. : 2nd Ed., Heyden and Son Ltd, London , 1995.

30. *FTIR Studies of Mo/Al2O3-Based Catalysts: I. Morphology and Structure of Calcined and Sulfided Catalysts .* **N.Y. Topsoe, H. Topsoe.** s.l. : Journal of Catalysis, 1993, Vols. (139) 631-640.

31. *Activation of Cobalt-Molybdenum Hydrodesulfurization Catalysts : Influence of the Sulfidation Procedure on the Physico-Chemical Properties and Catalytic Activity .* **R. Prada Silvy, P. Grange, B. Delmon.** s.l. : Studies in Surface Science and Catalysis, 1990, Vols. (53) 233-260.

32. *Roman spectroscopic study of Co-Moγ-Al2O3 catalysts .* **J. Medema, C. van Stam, V.H.J. de Beer, A.J.A. Konings, D.C. Koningsberger.** s.l. : Journal of Catalysis, 1978, Vols. (53) 386-400.

33. *Hydrodesulfurization and hydrogenation properties of promoted MoS2 and WS2 catalysts under medium pressure conditions.* **V.H.J. de Beer, J.G.J. Dahlmans, J.G.M. Smeets.** s.l. : Journal of Catalysis, 1976, Vols. (42) 467-470.

Chapter 4

Upgrading of bio-liquids on different mesoporous silica-supported CoMo sulfide catalysts

Chapter 4

Upgrading of bio-liquids on different mesoporous silica-supported CoMo sulfide catalysts

In this chapter, the upgrading of an olive oil production-derived by-product has been conducted in a down-flow fixed-bed reactor at 280 °C, 3 MPa and WHSV= 46.4 h^{-1} with sulfided CoMo catalysts. The catalysts were prepared by successive impregnation (with Mo being introduced first) and supported on different mesoporous silicates (DMS-1, SBA-15, SBA-16, HMA) with the aim to study the effect of support morphology on the catalytic response of sulfided CoMo catalysts. The supports and/or calcined catalysts were characterized by N_2 adsorption-desorption isotherms, XRD, TPR and TPD-NH_3 techniques. In addition, spent catalysts were studied by XPS, HRTEM and TPO/TG techniques. All sulfide CoMo catalysts were stable for 5 h of time-on-stream (*TOS*) reaction and recorded higher activity than a commercial sulfide NiMo/Al_2O_3 catalyst. The catalysts supported on the SBA-15, SBA-16 and DMS-1 materials were much more effective for oxygen removal than the HMS-supported one. The enhancement of activity was explained in terms of the higher active phase exposure and increased acidity. It was found that support morphology affected the distribution of useful products. Considering

the balance of desirable and undesirable products, the CoMo/SBA-16 catalyst had an optimal performance.

4.1. Introduction

Transportation fuels derived from renewable sources are potentially good alternatives for conventional fossil-derived fuels. This is because the availability of biomass-derived products in countries with no fossil fuels and the low sulfur and metal content of vegetable oils contribute to the neutrality of produced CO_2 (1). Accordingly, the by-products from olive oil production in Spain have a range of potential applications. In contrast to petroleum-derived feedstocks, bio-liquids contain large amounts of O-containing compounds, i.e. carboxylic acids, esters, aliphatic and aromatic alcohols, ethers, ketones, and aldehydes. As a consequence of such composition, the biomass possesses high viscosity, non-volatility, poor heating value, corrosiveness, immiscibility with fossil fuels, thermal instability, and a tendency to polymerize during storage and transportation (2) (3). Moreover, there is an undesirable formation of carbon deposits in parts of automotive engines upon combustion (especially, in compression–ignition engines, i.e. diesel engines). Bio-liquids therefore need to be upgraded by reducing their oxygen content. This means that oxygen should be removed from bio-liquids via hydrotreatment in a petroleum refinery infrastructure. The catalysts commonly used for hydrotreatment are sulfide CoMo/ Al_2O_3 and NiMo/Al_2O_3 systems (4). In literature, liquid fuel production by low-severity hydrotreating of biocrude over NiMo/alumina (Haldor Tøpsøe TK-751) and CoMo/spinel catalysts was reported by Elliott and Neuenschwander (5). In contrast to the former, the test with the latter showed a dramatic effect of lower catalyst activity. This is because without a

strong hydrotreating catalyst effect in the reactor, exothermic pyrolysis condensation reactions cause major temperature excursions and lead to coke buildup on the catalyst surface (5).

Considering the key role of the support morphology, mesoporous silicate materials with ordering pore structure have recently been intensively studied. In particular, mesoporous structures of the MCM-41 family with hexagonal ordering of the pores have attracted widespread attention as new potential materials for the preparation of novel supported hydrotreating catalysts (6) (7) (8) (9) (10) (11). For example, the mesoporous aluminosilicates Al-MCM-41 were found to be very active in the catalytic cracking of palm oil toward the production of gasoline (12) (13) (14) and for the pyrolysis of biomass (15) (16). MCM-41 possesses very interesting textural properties (high specific surface area in the 600–1000 m^2/g range and homogeneous pore diameters from 1.5 to 10 nm) (17), which are required when bulkier molecules need to be processed. Furthermore, their high surface area favors active phase dispersion, and a lower strength of acidic OH groups than those in zeolites leads to lower coke formation. Subsequent to MCM-41, the synthesis of another hexagonal mesoporous sieve such as HMS was reported (18) (19). However, the more remarkable advance in the synthesis of mesoporous materials was the preparation of SBA-15, with enhanced thermal and hydrothermal stability with respect to MCM-41 due to the formation of thicker walls (typically between 3 and 9 nm) (20). SBA-15 material, which has hexagonal pores in a 2D array with long 1D channels (*P6mm* plane group) (21), proved to be effective for supporting CoMo hydrotreating catalysts (6) (7). Another material employed in this chapter as support was SBA-16. This material was initially synthesized by Zhao et al. (20) in the presence of triblock copolymer Pluronic F127.

Contrary to SBA-15, a cubic (*Im3m*) cage-structured mesoporous silica material (SBA-16) is scarcely used as support for hydrotreating catalysts (22) (23) although both SBA-15 and SBA-16 materials were stable in boiling water for 48 h (24). In the SBA-16 material, each mesopore in its body-centred structure is connected to its eight nearest neighbors (25). This allows easier diffusion of large molecules into pores (22). Finally, disordered mesoporous silica (DMS-1) was selected in order to compare its morphology with that of materials with hexagonal and cubic mesoporous silica structures (HMS, SBA-15 or SBA-16). DMS-1 has the disordered arrangement of its micropores with high surface area (in the 600–1000 m^2/g range) while the atomic arrangement is disordered in a similar manner to the mesoporous silica (26). However, to date, the application of the DMS-1 material as support for the CoMo hydrotreating catalyst for the HDO of bio-liquids has not been reported.

In this chapter, we compare for the first time the catalytic behavior of the sulfided CoMo catalysts supported on DMS-1, SBA-15, SBA-16 and HMS materials in bio-liquids upgrading by hydrotreating. The principal objective was to study the effect of support morphology on catalytic activity and active phase dispersion.

4.2. Experimental

4.2.1. Support preparation

The siliceous mesoporous SBA-15, SBA-16 and DMS-1 materials were synthesized according to the procedure described by Flodström and Alfredsson (27). SBA-15 was prepared by using Pluronic triblock copolymer (BASF, EO_{20}-PO_{70}-EO_{20}, P123) as the structure-directing agent, whereas the preparation of SBA-16 and DMS-1 involved different concentrations of Pluronic F127 (2.5 and 4% wt,

respectively). In all cases, tetraethyl orthosilicate (TEOS, purity 98%, Aldrich) was used as a silica source. In a typical synthesis, the triblock copolymer was dissolved in a solution of water and HCl under stirring, and then the required amount of TEOS was added to the above solution at 35 °C and kept under stirring for 24 h. The mixture was then transferred into polypropylene bottles and heated at 85 °C for 24 h in static conditions. After synthesis, the solid obtained was filtered, thoroughly washed with distilled water, dried at 100 °C and finally calcined at 500 °C for 6 h to remove the organic template.

The HMS molecular sieve was prepared at room temperature by the procedure suggested by Zhang et al. (28) using TEOS (purity 98%, Aldrich) as the neutral silica precursor and dodecylamine (DDA, purity 98%, Aldrich) as the neutral structure director. Mesitylene (MES, purity 97%, Aldrich) was used as a swelling agent. Briefly, the surfactant (DDA) and the corresponding amount of water were mixed under vigorous stirring to obtain a homogeneous solution. MES was added to the surfactant solution and stirred for 15 min. TEOS was then added to the surfactant-auxiliary solution and the mixture was allowed to react under stirring at room temperature for about 20 h. As the pH increases during the synthesis, the pH of the gel was adjusted several times using acids in order to obtain hydrothermally stable mesoporous silica materials (29). After synthesis, the solid residue obtained was filtered, thoroughly washed with distilled water and dried in air. Consequently, the sample was dried at 100 °C in air for 24 h and finally calcined at 540 °C in air for 6 h.

4.2.2. Catalyst preparation

The respective support was loaded with molybdenum (10 wt%) and cobalt (3 wt%) by incipient wetness successive impregnation that is a commonly used technique for the synthesis of heterogeneous catalysts. Typically, the active metal precursor is dissolved in an aqueous solution. Then the metal-containing solution is added to a catalyst support containing the same pore volume as the volume of the solution that was added. Capillary action draws the solution into the pores. Solution added in excess of the support pore volume causes the solution transport to change from a capillary action process to a diffusion process, which is much slower. The catalyst can then be dried and calcined to drive off the volatile components within the solution, depositing the metal on the catalyst surface. The maximum loading is limited by the solubility of the precursor in the solution. Mo was introduced first from solutions of ammonium heptamolybdate tetrahydrate (Aldrich, A.C.S. reagent) and after cobalt (II) nitrate hexahydrate (purity 98%, Aldrich) was added to achieve a Co: Mo molar ratio of 1:3. After impregnation, the samples were dried overnight at 110 °C in air and then calcined for 3 h at 500 °C in air. The catalysts are coded as CoMo/SBA-15; CoMo/SBA-16, CoMo/HMS and CoMo/DMS-1.

4.2.3. Feedstock

The feedstock used for catalyst activity evaluation was a byproduct from olive oil production in Spain. Its elemental composition is the following: C: 75.9%; H: 11.8%; O: 12% (the latter was calculated by difference); N: < 0.1%, S: < 0.1% and

traces of Cl. The C, H and N contents were determined by CHN-600 (LECO), whereas the S content was determined by SC132 (LECO) apparatus.

Table 4.1. Chemical composition of the feedstock[a].

Compound	Formula	(wt %)
2-Phenylhydrazinecarboxamide	$C_7H_9N_3O$	61.66
9-Hexadecanoic acid	$C_{16}H_{30}O_2$	18.83
Octadecanoic acid	$C_{18}H_{36}O_2$	7.85
Undecane	$C_{11}H_{24}$	2.47
Palmitic acid	$C_{16}H_{32}O_2$	2.24
Nonane	C_9H_{20}	1.35
Oxacyclotetradecan-2-one	$C_{13}H_{24}O_2$	1.12
Oleic acid, 3-hydroxypropyl ester	$C_{21}H_{40}O_3$	0.67
Octadecanoic acid, 2-hydroxy-1,3- propanediyl ester	$C_{39}H_{76}O_5$	0.45
Benzene, 1,2,3(4)-trimethyl-	C_9H_{12}	0.45
Naphthalene, decahydro-, trans/cis	$C_{10}H_{18}$	0.22
Spiro[4,5]decane	$C_{10}H_{18}$	0.22
Nonane, 2-methyl-	$C_{10}H_{22}$	0.22
Silane, trimethyl[5-methyl-2- (1-methylethyl)phenoxy]-	$C_{13}H_{22}OSi$	0.22
(6Z,9Z)-6,9-Pentadecadien-1-ol	$C_{15}H_{28}O$	0.22
Hexadecane	$C_{16}H_{34}$	0.22
Palmitic acid, tetradecyl ester	$C_{30}H_{60}O_2$	0.22
Stearic acid hydrazine	$C_{18}H_{38}N_2O$	0.22
Linolin, 2-mono-	$C_{21}H_{38}O_4$	0.22
Stearic anhydride	$C_{36}H_{70}O_3$	0.22
1-Heptatriacotanol	$C_{37}H_{76}O$	0.22
[(1,4-Diethyloctyl)oxy](trimethyl)silane	$C_{15}H_{34}OSi$	0.22
2-Amino-4,4,6,6-tetramethyl-4,6-dihydrothieno[2,3-c]furan-3-carbonitrile	$C_{11}H_{14}N_2OS$	0.22
Mass balance		98.4

[a] By-product from olive oil production in Spain.

The heating value of bio-liquid was 9287 cal/g, as determined by AC300 (LECO) calorimetric pump. In order to decrease feedstock density (0.901 g/mL at 30 °C), the bio-liquid was diluted in n– decane to obtain a 5 vol% solution (density

of 0.772 g/mL). Weight content of solvent in the mixture (bio-liquid + solvent) was of 55.5 wt%. This value was selected in order to minimize the concentration gradients over the catalytic bed, thus decreasing the impact of mass and heat transfer limitations. As expected, the composition of feedstock was complex (**Table 4.1**).

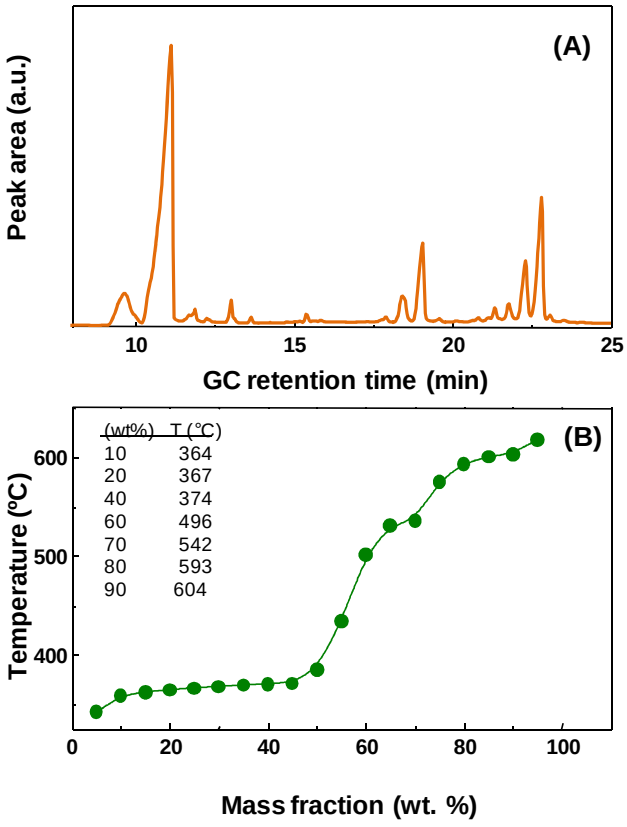

Figure 4.1. Simulated distillation chromatogram of the feedstock **(a)** and the boiling points distribution **(b)**, as obtained from the bio-liquid simulated distillation.

Bio-liquid (as received) simulated distillation was performed with a Varian CP 3800 GC device using Simulated Distillation Software (STAR SIMDIST) and a capillary column with a length of 10 m and a diameter of 0.53 mm. This analysis method gives the amounts of product in terms of lumps of boiling ranges.

Figure 4.1 (a) and **(b)** shows the typical chromatogram and boiling-point distribution, respectively. As seen in **Figure 4.1 (b)**, as received bioliquid did not have compounds in the gasoline range (C5: T < 215 °C) and possesses mainly compounds in the range of light cycle oil (LCO: T = 215–325 °C) and heavy cycle oil (HCO: T > 325 °C). The latter has been divided up further into four fractions: light heavy cycle oil (10% LHCO: 325–360 °C), fatty acids (35% FA: 360–400 °C), intermediates (13% INT. 400–520 °C), and triglycerides (36% TGL: T > 520 °C) (30).

4.2.4. Catalytic activity measurements

The hydroconversion of the bio-liquid was performed in a high pressure laboratory-scale set-up equipped with a down-flow fixed-bed catalytic reactor. The feedstock mixture (bio-liquid + solvent) was injected (0.25 mL/min) by a high-pressure pump (HPLC Knauer) into a hydrogen stream (60 mL/min). The reaction was carried out at 250 °C, 3 MPa of total pressure, H_2 flow rate = 7 L (STP) h^{-1}, WHSV bio-liquid = 2.7 h^{-1} and employing 0.25 g of the catalyst diluted with 5 g of SiC. Before catalyst activation, the catalyst was dried under a N_2 flow of 100 mL/min at 150 °C for 0.5 h. The catalyst was then sulfided in situ at 400 °C and atmospheric pressure by a mixture of 10 vol% of a H_2S:H_2 at a rate of 60 mL/min for 4 h (isothermal). After sulfidation, the catalyst was purged under a N_2 flow of

100 mL/min at 400 °C for 0.5 h and then stored overnight under a N_2 flow of 3 mL/min.

Before the experimental runs, the N_2 pressure was increased to the desired value, and the catalytic bed was heated to the reaction temperature. GC–MS (Shimadzu GCMS-QP2010) equipped with a Tracer TRB1-MS capillary column (30 m and i.d. 0.32 mm; a 0.10- mm thick methylsilicone layer; material: fused-silica) was used to identify the components of the reaction mixture. For the calculation of product distribution, it was assumed that the percentage of peak area of the GC–MS chromatogram is linear with compound concentration. Indeed, there are literature reports in which an estimation of organic composition of bio-liquids was based on the peak areas of GC/MS chromatograms (the percentage area of the GC–MS chromatogram was considered linear with the compound concentration) (15) (31). A commercial $NiMo/Al_2O_3$ catalyst (HR-348 from Procatalyse; S_{BET} = 164 m^2/g; and Mo, Ni, and P loading of 10.7, 2.5, and 2.64 wt%, respectively) was used as a reference.

4.3. Results and discussion

4.3.1. Characterization of the oxide precursors

4.3.1.1. Chemical analysis

All catalysts were prepared by the incipient wetness impregnation (pore-filling method), with molybdenum being introduced first (successive impregnation method). According to this method, the deposition of metal precursors takes place

mainly in the drying step via precipitation in the bulk solution (bulk precipitation) leading to a relatively low dispersion of the supported phases after catalyst calcination (32). The final metal oxide loading of the catalysts compiled in **Table 4.2** differs from the nominal one probably because the complex mechanism of incipient wetness impregnation when supports with different morphology are employed. Chemical analysis of the calcined catalysts indicates that CoMo/SBA-15 and CoMo/DMS-1 catalysts record the lowest and highest metal oxide loading, respectively. For all catalysts, cobalt oxide loading varies within 2.2–4.7 wt% range, whereas for molybdenum oxide it ranges from 6.4 to 10.1 wt%.

Table 4.2. Chemical analysis from TXRF measurements of the calcined CoMo catalysts supported on SBA-15, SBA-16, HMS and DMS-1 materials.

Catalyst	Co (wt%)	Mo (wt%)
CoMo/HMS	4.65	6.94
CoMo/SBA-15	2.21	6.37
CoMo/SBA-16	2.81	7.17
CoMo/DMS-1	4.30	10.12

4.3.1.2. Nitrogen adsorption- desorption isotherms

Since the goal of this research was to determine the effect of support in bio-liquid upgrading over supported CoMo catalysts, a detailed characterization of the calcined catalysts was conducted by means of nitrogen adsorption–desorption isotherms, with the aim being to visualize the differences in the support morphologies (**Figure 4.3**). According to IUPAC classification, the N_2 adsorption–desorption isotherm of all the oxide precursors are of type IV (33). The shape of

this isotherm is characteristic of mesoporous materials with a narrow pore size distribution. The isotherm shows a small desorption step at ca. P/P0 = 0.4 originating from inkbottle- type pores. The nitrogen isotherm of the CoMo/SBA-15 reveals a hysteresis loop of type H1, which is typical for SBA-15 substrate (21). Its characteristic two-step desorption branch is due to the silica pores plugging (21). In contrast with CoMo/SBA-15, both N_2 adsorption–desorption isotherms of CoMo/SBA-16 catalyst are very flat. The H1-type hysteresis loop, which starts at a relative pressure of ca. 0.4, is characteristic of the cage-like structure of the SBA-16 material. The isotherm of this catalyst is similar to that reported in literature for SBA-16 mesoporous material (23). Finally, both CoMo/DMS-1 and CoMo/HMS catalysts record isotherms extended over a large range of relative pressures, indicating the presence of both mesoporosity and macroporosity.

Table 4.3. Textural properties of the calcined CoMo catalysts supported on SBA-15, SBA-16, HMS and DMS-1 materials.

Catalyst	S_{BET}	NS_{BET}	V_{total}	d (nm)
CoMo/HMS	428 (951)	0.48	0.80 (1.30)	6.6 (5.6)
CoMo/SBA-15	377 (933)	0.43	0.50 (1.10)	5.9 (4.7)
CoMo/SBA-16	407 (830)	0.52	0.30 (0.50)	3.0 (2.6)
CoMo/DMS-1	320 (730)	0.47	0.55 (0.90)	10.3 (2.4)

Data of the pure supports are given in parenthesis. S_{BET}: BET surface area ($m^2/g_{support}$); NS_{BET}: normalized S_{BET}; V_{total}: adsorption total pore volume (m^3/g); d: average pore diameter (nm) calculated from the adsorption branch of N_2 isotherm.

The first hysteresis, which starts at a relative pressure of ca. 0.4, indicates the presence of framework mesoporosity, whereas the second hysteresis loop,

which starts at a relative pressure of ca. 0.8, is due to textural interparticle mesoporosity or macroporosity. Thus, in addition to framework-confined porosity, the HMS- and DMS-1-supported catalysts have a complementary porosity (textural porosity). For the DMS-1-supported catalyst, the H1- type hysteresis loop is characteristic of a cage-like structure and/or a percolation effect caused by small particles of the metal oxides located within mesopores forming ink-bottle-type pores (34) (35).

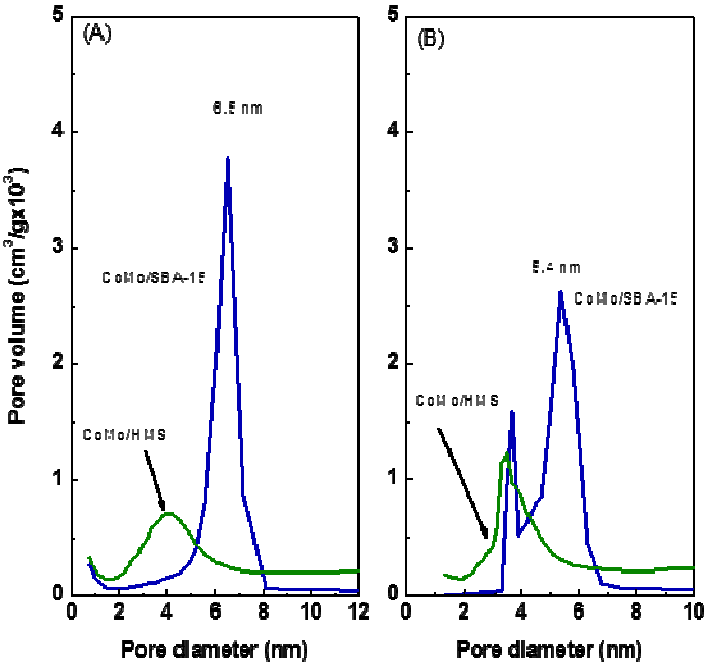

Figure 4.2. Pore size distribution of the calcined CoMo catalysts supported on SBA-15, SBA-16, HMS and DMS-1 materials.

The pore size distributions of the oxide catalysts are shown in the insets in **Figure 4.2**. The pore size distribution of CoMo/HMS catalyst reveals one narrow

peak centred at 3.5 nm (structural mesoporous) and another broad peak centred at 27 nm (textural mesoporous). For the CoMo/SBA-15 sample, the pore size distribution shows two distinct peaks: one located in the pore width range < 4 nm, indicating the presence of small complementary pores (mainly micropores), and a second one of 5.5 nm representing the ordered mesopores (36). Similarly, the pore size distribution of CoMo/DMS-1 shows the expected bimodal pore system presenting one peak centred at 3.4 nm (structural mesopores) and another peak with a maximum at 17.1 nm (textural mesopores). The CoMo/SBA-16 sample is unique among the catalysts studied, showing a narrow BJH pore size distribution n centred at 3.3 nm; its narrow and uniform pore size distribution suggests that the supported species are uniformly distributed.

The desorption branch of N_2 isotherms are shown in the insets in **Figure 4.3.** A clearer view of the occurrence of pore blocking can be obtained by calculating the BET specific areas of oxide CoMo catalysts referred to unit mass of support. The respective values collected in **Table 4.2** show S_{BET} specific areas in the range of 320 m^2/g (CoMo/DMS-1) to 428 m^2/g (CoMo/HMS), which follows the same trend as total pore volume. By comparing the total and micropore volume of the catalysts and supports (**Table 4.2**), it can be inferred that Co and Mo oxides block the substrate pores, mainly the micropores. This is probably the reason for the increase in the average pore diameter after impregnation with CoMo (the microporosity is lost). The normalized specific areas for all catalysts fall in the 0.43–0.52 range, indicating that Mo and Co oxide species are located mainly in the internal pore network of the mesoporous systems.

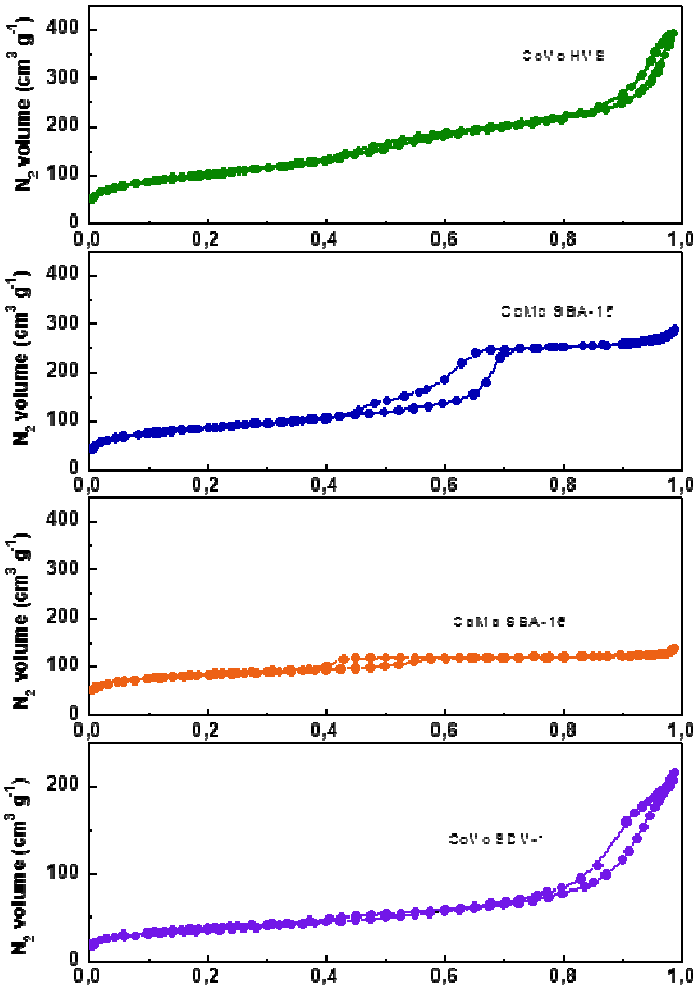

Figure 4.3. N_2 adsorption desorption isotherms at -196°C of the calcined CoMo catalysts supported on SBA-15, SBA-16, HMS and DMS-1 materials.

4.3.1.3. X-Ray Diffraction (XRD)

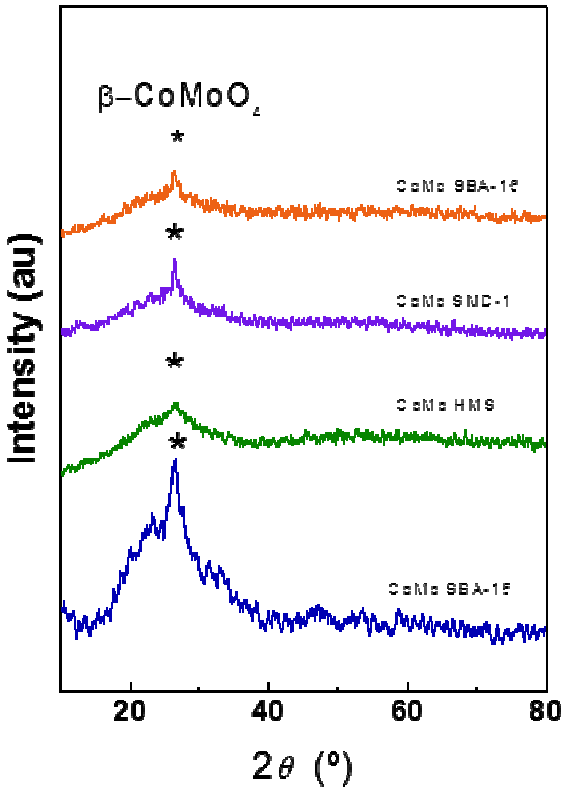

Figure 4.4. X-ray diffraction patterns of the calcined CoMo catalysts supported on HMS, SBA-15, SBA-16 and DMS-1 materials.

The wide-angle X-ray diffraction patterns of the calcined catalysts are presented in **Figure 4.4**. The CoMo/HMS sample does not display any diffraction lines due to Co and/or Mo oxide phases. This might indicate that the oxide phases incorporated are either amorphous (or not fully crystalline) or their crystal size is

less than 4 nm, so they do not diffract. On the other hand, the XRD patterns of the CoMo/SBA-15 catalyst record a small peak at ca. 23.48 2θ and another narrow and intense one at 26.68 2θ; both assigned to β-$CoMoO_4$ crystalline phase (JCPDS card 21-868). Using this peak, the crystal size of the β-$CoMoO_4$ phase, calculated according to Scherrer's equation, is ca. 6.8 nm (**Table 4.2**). The same phase was detected when using SBA-16- and DMS-1-substrates. For these systems, only a much less intense peak at 26.38 2θ is observed, whereas the peak at 23.48 2θ is not detected. Similar calculations for these CoMo/SBA-16 and CoMo/DMS-1 systems gave crystallite size values of 30.3 and 24.8 nm, respectively, for the β-$CoMoO_4$ phase (**Table 4.2**).

Table 4.4. XRD data of the oxide precursors and pure supports. The crystal size of β-$CoMoO_4$ phase as calculated by Scherrer equation from line at 2θ = 26.38.

Catalyst	β-$CoMoO_4$ size (nm)
CoMo/HMS	n.d.
CoMo/SBA-15	6.8
CoMo/SBA-16	30.3
CoMo/DMS-1	24.8

4.3.1.4. Temperature Programmed Reduction (TPR- H_2)

Temperature programmed reduction (TPR) experiments provide information about the dispersion states of the metal oxides as well as some insights on the metal-support (or Co–Mo) interactions. **Figure 4.5** displays the TPR profiles of the CoMo phases deposited on HMS, SBA-15, SBA-16 and DMS-1 substrates.

The observed hydrogen consumption is related to the reduction of oxide phases according to the following stoichiometry:

$$M^{x+} + H_2 \text{--- >} M^{o} + (x/2)\ H_2O$$

where M is either Co or Mo and x is the oxidation state. For all catalysts, TPR profiles show a narrow peak with a maximum at temperatures in the 450–600 °C range and a broad shoulder extending in the 605–847 °C temperature range. In line with the XRD profiles (vide supra) and previous literature reports (37) (38), this sharp TPR peak can reasonably be ascribed to a reduction in the $CoMoO_4$ phase. Since cobalt oxide is reduced more easily than MoO_3, it is likely that free cobalt oxide species also contribute to some extent to that H_2-consumption peak. For the monometallic Co/SiO_2 catalyst, it was shown that the reduction of Co oxide occurs at 360 and 445 °C (39). However, the somewhat higher reduction temperature observed here is a consequence of the polarization of the Co–O bond by the Mo^{6+} ions, which makes it more ionic and consequently more difficult to reduce (39).

Table 4.5. H_2 uptake (±10%) for calcined CoMo catalysts as obtained by Gaussian deconvolution of the TPR patterns.

H_2 uptake ($\mu mol/g_{cat}$)	**I peak**	**II peak**	**Total**
CoMo/HMS	95.8	112.0	207.8
CoMo/SBA-15	161.0	66.1	227.1
CoMo/SBA-16	710	190.0	261.0
CoMo/DMS-1	134.0	178.0	312.0

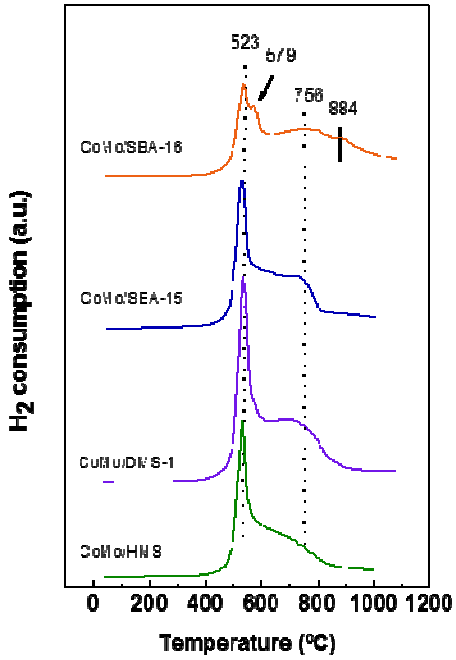

Figure 4.5. TPR profiles of the calcined CoMo catalysts supported on different mesoporous silicas.

Owing to the similarity of the isoelectric points of silica and MoO_3, one may assume that molybdenum forms polymolybdate structures on the silica surface at any loading. Laine et al. (40) assigned the H_2-consumption peak at 756 °C to dispersed polymolybdates linked to the silica surface, while the one located at the highest temperature (884 °C) is most likely due to poorly crystalline MoO_2 generated from the reduction of the MoO_3 phases.

After Gaussian deconvolution of the TPR profiles (not shown here), H_2 consumption amounts were calculated by considering the area of the peaks (**Table 4.5**). The amounts of H_2 consumed follow the order: CoMo/DMS-1 > CoMo/SBA-16 > CoMo/SBA-15 > CoMo/ HMS. It can thus be inferred that a larger quantity of $CoMoO_4$ phase is formed in the DMS-1 substrate.

4.3.1.5. Temperature Programmed Desorption of ammonia (TPD-NH_3)

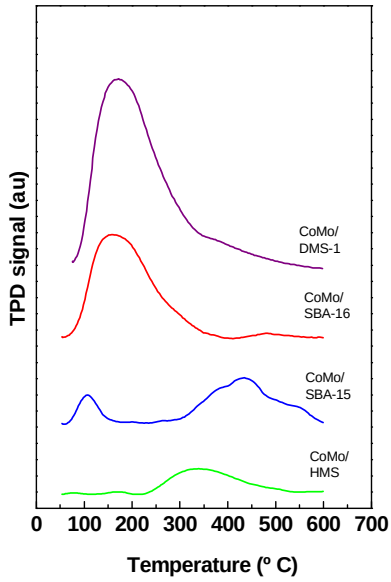

Figure 4.6. TPD profiles of NH_3 adsorbed on the calcined CoMo catalysts (normalized to BET surface area).

Experiments of temperature-programmed desorption of ammonia (TPD-NH_3) were conducted to compare the acidity of these mesoporous silica-supported

CoMo catalysts. The TPD-NH_3 profiles of the catalysts normalized to BET surface area (from **Table 4.2**) are displayed in **Figure 4.6**. Acidity distribution was derived from experimental TPD curves by fitting to Gaussian lines (not shown here), in which two peaks were used to represent medium (T < 300 °C) and strong (300 °C < T < 600 °C) acid sites, respectively (41). As seen in this figure, all catalysts show clear differences in the quantity of medium strength acid sites (CoMo/DMS-1 > CoMo/SBA-16 >> CoMo/SBA-15 ≈ CoMo/HMS (none)). The total acidity and acid distribution of the samples are listed in **Table 4.6**, according to NH_3-TPD profiles. CoMo/SBA-15 catalyst shows the largest amount of strong acid sites, whereas CoMo/SBA-16 and CoMo/DMS-1 exhibit the largest amount of medium strength acid sites.

Table 4.6. Acid sites distribution[a] and H_2 uptake[b] (±10%) for calcined CoMo catalysts[a]

	Acid sites concentration (μmol NH_3 g_{cat}^{-1})		
	Medium <300°C	**Strong 300-600 °C**	**Total**
CoMo/HMS	0.00	0.030	0.025
CoMo/SBA-15	0.03	0.054	0.057
CoMo/SBA-16	0.047	0.031	0.077
CoMo/DMS-1	0.081	0.025	0.107

[a] Amount of desorbed ammonia normalized to BET surface area (from **Table 4.2**) as determined by TPD of NH_3.

4.3.2. Oxygen removal from bio-liquid

The general aim of this study is to produce O-free bio-liquid with high content of desirable products such as paraffins, olefins, alcohols, ketones and naphthenes. Elemental analysis indicated that total oxygen content in the as-received bio-liquid is ca. 12% (4.56%, as determined by stoichiometric calculation). The bioliquid upgrading via catalytic hydrotreating over sulfided CoMo catalysts was performed in a down-flow reactor at 250 °C, 3 MPa of total hydrogen pressure and WHSV $_{\text{bio-liquid}}$ = 2.7 h^{-1}. The effect of support morphology on catalytic response of sulfided CoMo catalysts supported on HMS, SBA-15, SBA-16 and DMS-1 substrates has been evaluated. A commercial NiMo/Al_2O_3 catalyst was used as reference because it is known that Ni has a higher HYD activity than Co.

The main compounds present in the bio-liquid, as determined by the GC/MS technique, are listed in **Table 4.1**. As seen in this table, the feedstock contains mainly 2-phenylhydrazinecarboxamide (61.7 wt%), carboxylic acids (28.8 wt%), a relatively small amount of paraffins (4.3 wt%) and other compounds such as alcohols, ketones, esters, naphthenes, etc. (ca. 5.0 wt%). The carboxylic acids present in the bio-liquid were mainly 9-hexadecanoic acid ($C_{16}H_{30}O_2$; 18.8 wt%), octadecanoic acid ($C_{18}H_{36}O_2$; 7.9 wt%) and palmitic acid ($C_{16}H_{32}O_2$; 2.2 wt%). Phenylhydrazinecarboxamide and carboxylic acids have to be removed from biomass because low pH values mean that they have a corrosive effect on engine parts.

The total oxygen percentage before and after HDO of bio-liquid are shown in **Table 4.7**. As seen in this table, the catalysts supported on SBA-15, SBA-16 and DMS-1 substrates were the most effective toward oxygen removal followed by

CoMo/HMS. However, 9-hexadecanoic acid still remained after the HDO reaction over three former catalysts, whereas the partial oxygen elimination from octadecanoic acid octyl ester and oleic acid occurs on the latter. In addition, it is emphasised that the commercial $NiMo/Al_2O_3$ catalyst is not effective for oxygen removal from the octadecanoic acid octyl ester. In general, all supported CoMo catalysts proved to be more active than this reference.

Table 4.7. Oxygen percentages[a] corresponding to different O-containing products before and after bio-liquid HDO (T = 250 °C, P = 3 MPa, TOS = 5 h) over supported CoMo catalysts and reference sample[b].

Compounds		Feed	CoMo /HMS	CoMo /SBA-15	CoMo /SBA-16	CoMo /DMS-1	[b]NiMo/ Al_2O_3
Total Oxygen (%)		4.561	0.485	0.127	0.132	0.123	0.540
Hydrozainecarboxamine, N-phenyl-	$C_7H_9N_30$	2.9	-	-	-	-	-
n-Hexadecanoic acid	$C_{16}H_{32}O_2$	0.1	-	-	-	-	-
9-Hexadecanoic acid	$C_{16}H_{32}O_2$	1.1	-	0.1	0.1	0.1	-
Octadecanoic acid, octyl ester	$C_{26}H_{52}O_2$	0.4	0.2	-	-	-	0.4
Oxacyclotetradecan-2-one	$C_{13}H_{24}O_2$	0.1	-	-	-	-	-
Oleic acid	$C_{18}H_{34}O_2$	-	0.2	-	-	-	0.1

[a]From stoichiometric analysis.
[b]A commercial $NiMo/Al_2O_3$ (HR-348).

A comparison of catalyst performance and TPD-NH_3 results (**Table 4.6**) reveals that lower oxygen content is achieved upon bioliquid HDO on sulfide CoMo catalysts with a larger amount of acid sites per unit area (CoMo/SBA-15, CoMo/SBA-16, CoMo/DMS-1). The lowest activity for O-removal of CoMo/HMS catalyst could be linked to its lower amount of acid sites. Other factors, which

could to influence on the catalytic response, are the specific surface area and metal loadings of the catalysts (**Table 4.2 and 4.3**). In order to clarify this point, the oxygen content after 5 h on-stream was normalized to S_{BET} as well as to metal loadings (**Figure 4.7 (A)** and **(B)**, respectively). In both cases, it was found that catalyst activity follows the order: CoMo/DMS-1 ≈ CoMo/SBA-15 ≈ CoMo/SBA-16 >> CoMo/HMS > reference catalyst. This might indicate the larger extent of O-removal over the three former catalysts is linked with the active phase dispersion rather than with specific surface area of the catalysts.

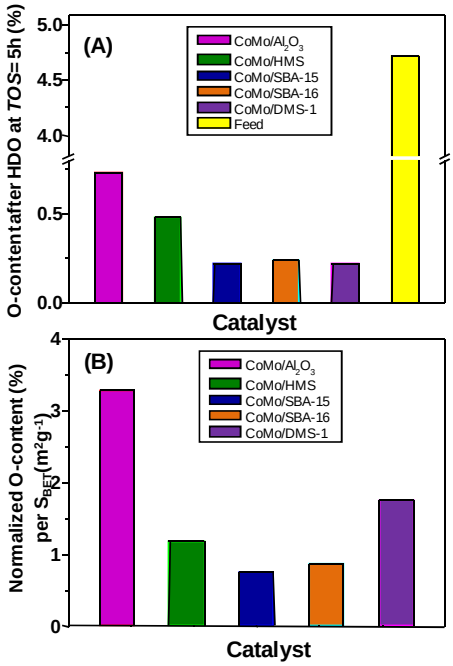

Figure 4.7. Influence of support on the total oxygen content after HDO of bio-liquid over sulfided CoMo catalysts (T = 250 °C, P = 3 MPa, WHSV = 2.7 h^{-1}, TOS = 5 h) normalized to S_{BET} **(A)** and mmol of Co and Mo **(B)**.

4.3.3. Effect of support morphology on the product distribution

Table 4.8. Product distribution after feedstock's hydrotreatment[a] over sulfided catalysts.

Compounds (wt%)	CoMo/HMS	CoMo/SBA-15	CoMo/SBA-16	CoMo/DMS-1	Ref.[b]
Nonane (C_9H_{20})	2.47	1.79	1.79	1.60	3.36
Nonane,2-methyl- ($C_{10}H_{22}$)	0.22	0.22	0.22	0.22	0.22
n-Decane formed ($C_{10}H_{22}$)	80.27	89.24	62.11	14.57	69.96
Undecane ($C_{11}H_{24}$)	2.69	2.9	2.91	2.91	0.90
Undecane, 2,5-dimethyl- ($C_{13}H_{28}$)	-	-	-	41.26	-
n-Tridecane ($C_{13}H_{28}$)	-	-	-	-	0.22
Pentadecane ($C_{15}H_{32}$)	0.45	-	-	-	1.57
Hexadecane ($C_{16}H_{34}$)	–	0.22	0.22	0.22	1.35
Spiro[4,5]decane ($C_{10}H_{18}$)	-	-	0.22	-	-
1-Hepten-5-yne, 2-methyl-3-methylene- (C_9H_{12})	-	-	0.22	-	-
1-Hexene, 3,4-dimethyl- (C_8H_{16})	-	-	-	24.44	-
(2Z)-2-Benzyl-3-phenyl-2-propenal ($C_{15}H_{12}O$)	0.22	-	-	-	-
9-Octadecanal ($C_{18}H_{34}O$)	-	-	-	-	0.22
Stearaldehyde ($C_{18}H_{36}O$)	-	-	-	-	0.22
Methanol (CH_4O)			27.13	9.87	
1-Eicosanol ($C_{20}H_{42}O$)			0.22		
1-Pentadecanol ($C_{15}H_{32}O$)					0.22
1-Octadecanol ($C_{18}H_{38}O$)					1.57
9-Hexadecanoic acid ($C_{16}H_{30}O_2$)	-	2.24	2.46	2.24	-
Palmitic acid ($C_{16}H_{32}O_2$)	0.45	0.45	0.45	0.45	0.67
Octadecanoic acid ($C_{18}H_{36}O_2$)	0.90	0.45	0.45	0.45	2.47
Palmitic acid, tetradecyl ester ($C_{30}H_{60}O_2$)	-	-	-	-	0.90
Oleic acid, 3-hydroxypropyl ester ($C_{21}H_{40}O_3$)	0.22	-	-	-	-
Benzene, 1,2,3(4)-trimethyl- (C_9H_{12})	0.22	0.45	0.22	0.45	-
Naphthalene, decahydro-, trans and/or cis ($C_{10}H_{18}$)	1.79	1.12	0.45	0.45	3.14
Mass balance	98.87	99.55	99.77	99.78	98.20

[a] Reaction conditions were: T = 250 °C; P = 3 MPa and TOS = 5 h.

[b] A commercial $NiMo/Al_2O_3$ (HR-348).

Table 4.8 compiles the product distribution achieved over all catalysts after 5 h of on-stream reaction. For all catalysts, the 2- phenyl hydrazinecarboxamide (main compound of bio-liquid) disappeared completely and a drastic decrease in carboxylic acids occurs being CoMo/SBA-15 and CoMo/DMS-1 catalysts the most effective for their elimination. 9-hexadecanoic acid remained only after the HDO reaction over SBA-15-, SBA-16 and DMS-1-supported catalysts. The octadecanoic acid octyl ester and oleic acid still remained after 5 h of on-stream reaction over CoMo/HMS and reference sample.

Analyzing the products distribution recompiled in **Table 4.8**, it is clear that the reactions occurring during bio-liquid hydroprocessing are elimination of nitrogen as ammonia from 2-phenylhydrazinecarboxamide, elimination of oxygen as water, and hydrogenation–hydrocracking of large molecules. According to literature (42), ammonia is a strong inhibitor of all hydrotreating reactions over CoMo and NiMo catalysts but does not affect the hydrogenation of the ketonic groups. On the contrary to ammonia, water has no influence (or very little inhibiting effect) for all reactions except for the promotion of hydrolysis of carboxylic esters. However, one might expect that the use of down-flow reactor could minimize the effect of ammonia.

In order to facilitate understanding of the selectivity trends, the products were grouped in compound families (**Table 4.9**). The identified liquid products, grouped into desirable and undesirable groups, are compared in **Figure 4.8**. The group of desirable products contains paraffins, olefins, alcohols and naphthenes, whereas the group of undesirable products includes aromatics, acids and esters, the latter due to their high O-content. **Figure 4.9** compares the GC–MS signal for all catalysts corresponding to retention time in the range 10–12 min. For comparison,

the MS–GC chromatogram of the feedstock (5% of biomass in n-decane) is included. As seen in **Figure 4.9**, the $C_{10}H_{18}$ (naphthalene, decahydro-, trans/cis; spiro [4,5] decane) is mainly formed over a commercial $NiMo/Al_2O_3$ followed by CoMo/HMS and CoMo/SBA-15 catalysts.

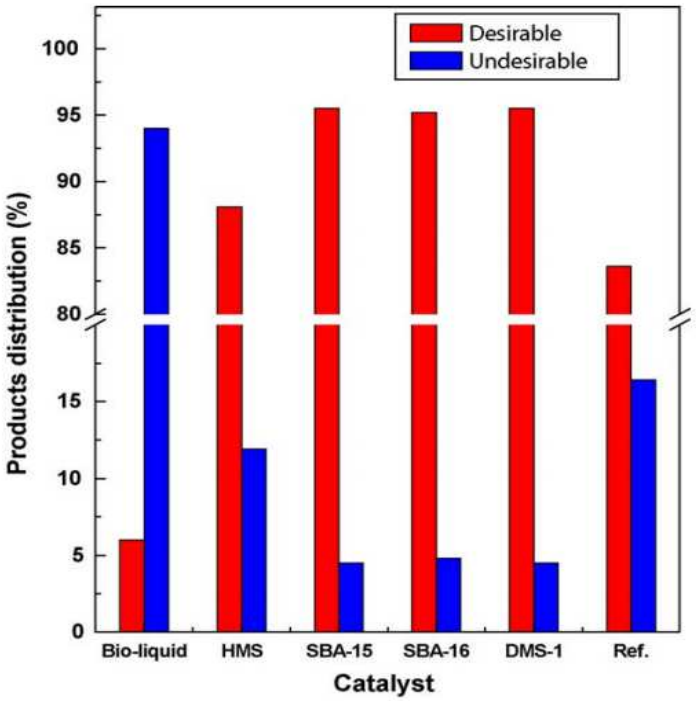

Figure 4.8. Distribution of desirable and undesirable products after bio-liquid hydrotreatment at T = 250 °C, P = 3 MPa, TOS = 5 h.

Irrespective of the support morphology, the SBA-15-, SBA-16-, DMS-1-supported CoMo catalysts show similar total yields of desirable products, indicating that more complex factors than support morphology affect product distribution on those catalysts. While paraffins are mainly formed on all catalysts, large amounts of olefins and alcohols are formed on the CoMo/DMS-1 and

CoMo/SBA-16 catalyst, respectively. The paraffins formation follows the trend: CoMo/SBA-15 > CoMo/HMS > a commercial catalyst > CoMo/SBA-16 ≈ CoMo/DMS-1 (**Table 4.9**). The high olefin content (1-hexene, 3,4-dimethyl-; C_8H_{16}) of the CoMo/DMS-1 is in line with the lowest paraffins formation on this catalyst (**Table 4.9**). The high formation of 3,4- dimethyl-1-hexene on the CoMo/DMS-1 sample is surprised with a hydrogenation process. Further study is needed in order to explain this phenomenon. On the contrary, high methanol formation in the bio-liquid upgrading over CoMo/SBA-16 sample is not surprising since the direct production of alcohols via acid hydrogenation is well-known over heterogeneous catalysts (43). Moreover, an analysis of product distribution in **Table 4.8** reveals that CoMo/SBA- 16 and the commercial catalyst are the only ones that effectively reduce the polyaromatics (PAH), which must be eliminated from bio-liquid because they are considered as hazardous for the environment (44).

Table 4.9. Product distribution after bio-liquid hydrotreatment at TOS = 5 h over sulfided CoMo catalysts and reference sample

	Feedstock	**CoMo/ HMS**	**CoMo/S BA-15**	**CoMo/S BA-16**	**CoMo/D MS-1**	**Reference sample[b]**
Desirable (%)						
Paraffins	4.3	86.3	94.4	67.2	60.8	78.5
Olefins	-	-	-	0.2	24.4	
Alcohols	0.4	-	-	27.4	9.9	1.8
Ketones	1.1	-	-	-	-	-
Naphthenes	0.2	1.8	1.1	0.4	0.4	3.4
Undesirable (%)						
Amines	61.7	-	-	-	-	-
Esters	1.6	5.4	0.4	0.7	0.7	9.2
Aromatics	0.4	1.1	0.4	0.2	0.4	0.2
Acids	28.8	5.2	3.1	3.7	3.1	5.8
Others	1.5	0.2	0.6	0.2	0.3	1.2

[a] Hydrozainecarboxamine, N-phenyl- ($C_7H_9N_3O$).

[b] A commercial $NiMo/Al_2O_3$ (HR-348).

PAHs are formed on CoMo/HMS catalyst, whereas the two SBA-15- and DMS-1 counterparts are not at all effective for their reduction.

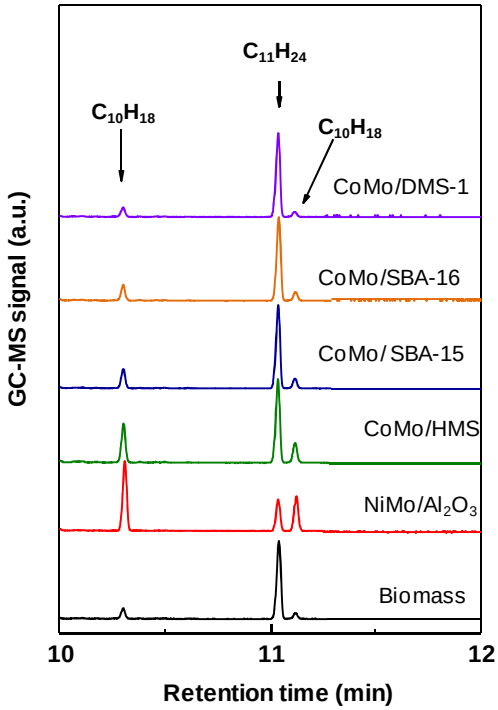

Figure 4.9. MS–GC chromatographs corresponding to retention time in range 10–12 min. For comparison, the MS–GC chromatograph of the feedstock is included

Finally, one might expect that the course of hydrogenation reaction could be substantially influenced by the type of solvent used (polar or nonpolar) (45). For the activity test, the bio-liquid was diluted with n-decane (5 vol%). Considering the study by Bejblová et al. (45), it is expected that the use of n-decane as solvent led to fast consecutive hydrogenation of aromatic rings of polycyclic aromatic

hydrocarbons (PAH), which are present in the feedstock. Moreover, although an inert solvent does not participate in the reaction process, it is expected that it may compete with the reactants for the adsorption on active sites on the catalyst surface (46). However, in our study no parallel reactions of n-decane (hydroisomerization/ hydrocracking) were observed. Thus, one might deduce that under reaction condition employed, the completive adsorption of n-decane and bio-liquid's compounds on the active sites did not occur. On the contrary, the n-decane was additionally formed due to cracking of the large compounds present in the feedstock (**Table 4.8**).

4.3.4. Characterization of the spent catalysts

4.3.4.1. X-Ray Diffraction (XRD)

To exclude the deterioration of the porous structure of the catalysts by the water product arising from the HDO reaction, low angle X-ray diffraction profiles of the spent CoMo/SBA-15 and CoMo/SBA-16 catalysts were recorded (**Figure 4.10**).

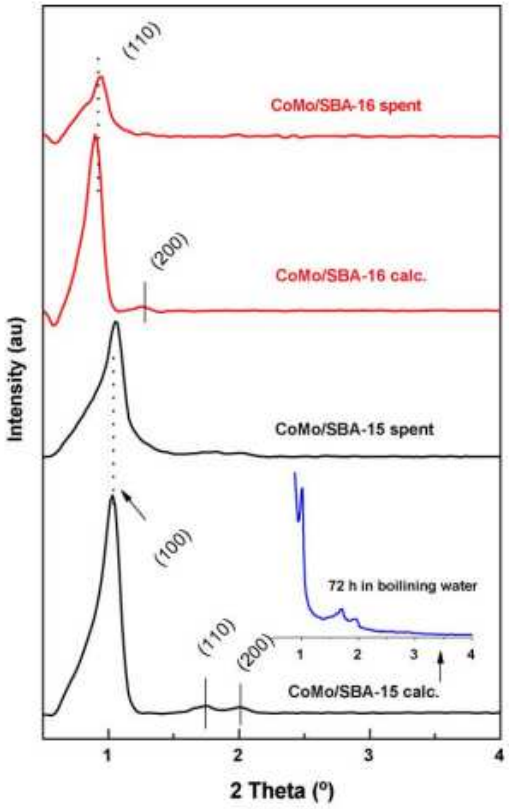

Figure 4.10. Low-angle XRD measurements of the calcined and spent CoMo/SBA-15 and CoMo//SBA-16 catalysts. XRD diffractogram of the calcined CoMo/SBA-15 created with boiling water for 72 h is shown in inlet of this figure.

The most intense XRD lines of spent CoMo/SBA-15 catalyst belong to the hexagonal arrangement of the support pore structure, whereas that of the CoMo/SBA-16 catalyst corresponds to the cubic arrangement of its pores. For the spent CoMo/SBA-15, the half-width of the diffraction peak associated to the (1 0 0) plane of the *P6mm* structure (at 2u = 1.0) is wider than the corresponding signal of its calcined precursor. The smaller signals observed in the enlargement of the diffraction profile indicate the presence of some hexagonal order in agreement

with the TEM pictures (**Figure 4.11**). As compared with the respective calcined catalysts, the intensity of the XRD peak after on-stream reaction decreases, with this decrease being larger for SBA-16 than for SBA-15-supported catalyst. Thus, from these diffraction profiles it can be concluded that both CoMo/SBA-16 and CoMo/SBA-15 catalysts remain stable under the reaction conditions applied. In order to verify the stability of CoMo catalysts supported on mesoporous silica during long time exposure to H_2O, additional experiment was performed in which CoMo/SBA-15 catalyst was exposed to boiled H_2O for 72 h. After this, the catalyst was dried at room temperature for 18 h and then dried at 110 °C for 18 h. A low-angle XRD of this sample (inlet of **Figure 4.10**) confirmed that structure of SBA-15 material was preserved after this long treatment. Similarly, the hydrophobicity of the pure-silica MCM-41 was confirmed by water adsorption experiments by Chen et al. (47); with temperatures as high as 850 °C in air with 8 mbar water vapour before structure collapse begins.

4.3.4.2. Transmission Electron Microscopy (TEM)

The stability of the pore structure during on-stream reaction was confirmed also by transmission electron microscopy (TEM). **Figure 4.11** displays TEM images, viewed at different sample orientations, for spent CoMo/SBA-15 and CoMo/SBA-16 catalysts. The TEM images belonging to CoMo/SBA-15 clearly reveal a 2Dhexagonal pore arrangement and long-range mesoporous-ordering, which is characteristic of the good-quality SBA-15 material.

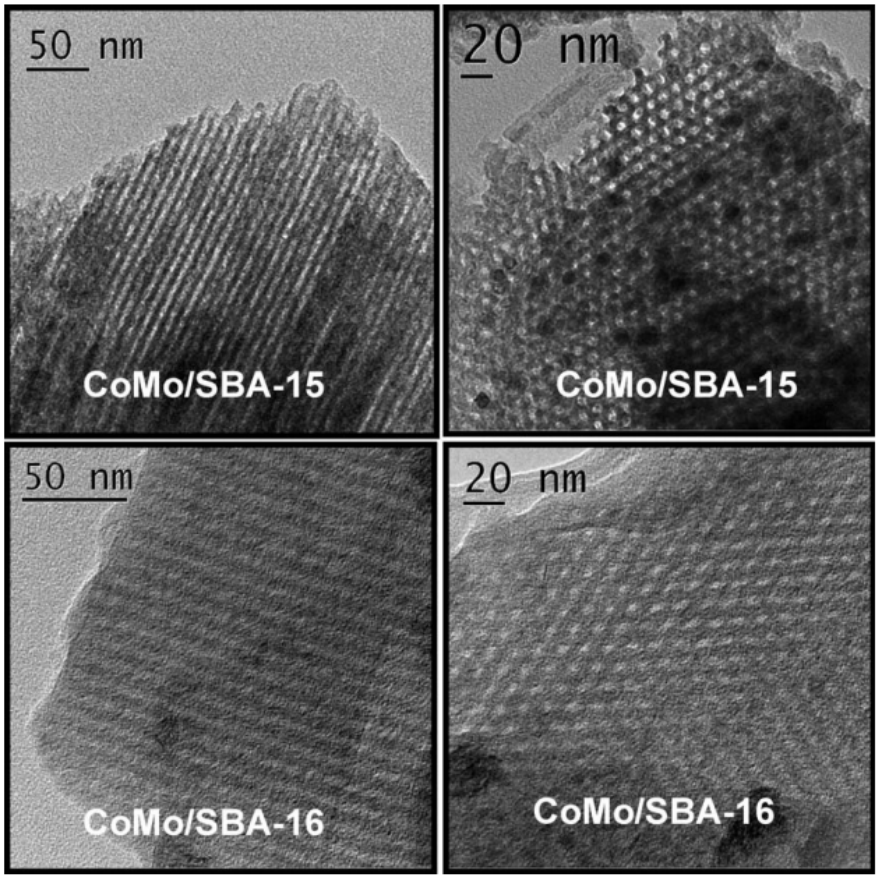

Figure 4.11. TEM images of the spent CoMo/SBA-15 and CoMo/SBA-16 catalysts viewed through different orientations

Similarly, the 3D cubic pore arrangement could be inferred for the spent CoMo/SBA-16. Thus, formation of water during on-stream reaction does not alter the regular ordered array of mesopores of both catalysts in agreement with the low-angle XRD data (**Figure 4.10**). Since the water produced in the HDO reaction may affect the stability the sulfided catalysts by hydrolyzing the sulfide phases

(48), the morphology of the spent CoMo/SBA-15 and CoMo/SBA-16 catalysts was studied by means of transmission electron microscopy (**Figure 4.12**).

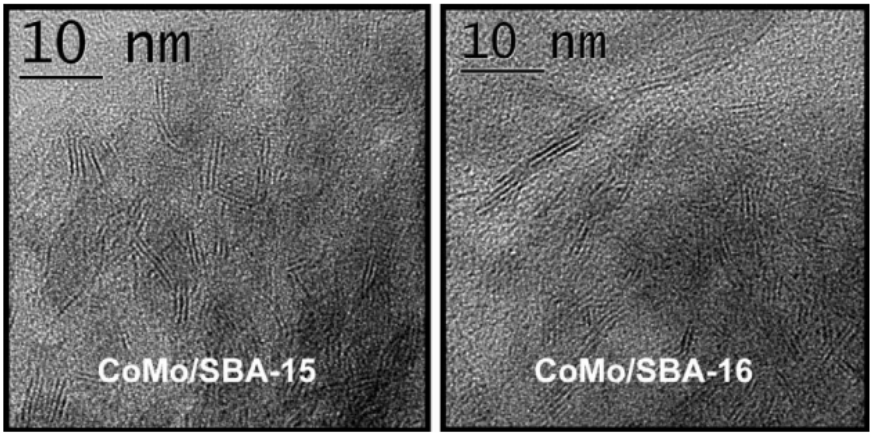

Figure 4.12. High magnification of MoS_2 sheets observed with spent CoMo/SBA-15 and CoMo/SBA-16 catalysts.

TEM micrographs of both samples show MoS_2 particles with a very irregular shape. However, the MoS_2 particles appear to be more homogeneously dispersed in the SBA-15 than in the SBA-16-based catalyst. The number of stacking layers for the spent CoMo/SBA-15 is between 3 and 4, with an average of 2.3 layers. The average slab length is calculated to be 5 nm. On the other hand, the slabs for the spent CoMo/SBA-16 appear heterogeneously distributed. Some nest-like stacks, in which several slabs are cross-linked, were observed in some of the micrographs. The stacks are higher than those in the case of SBA- 15-based catalyst and consist of up to 5 layers. The average number of stacking layers is 2.8 and the average slab length is the same as for CoMo/SBA-15. From the distribution of MoS2 stacking (**Figure 4.13**), higher stacking is observed for the SBA-16-supported catalyst than

for its SBA-15-supported counterpart. This indicates a weaker interaction between the SBA-16 support and supported MoS_2 species. **Figure 14(a)**

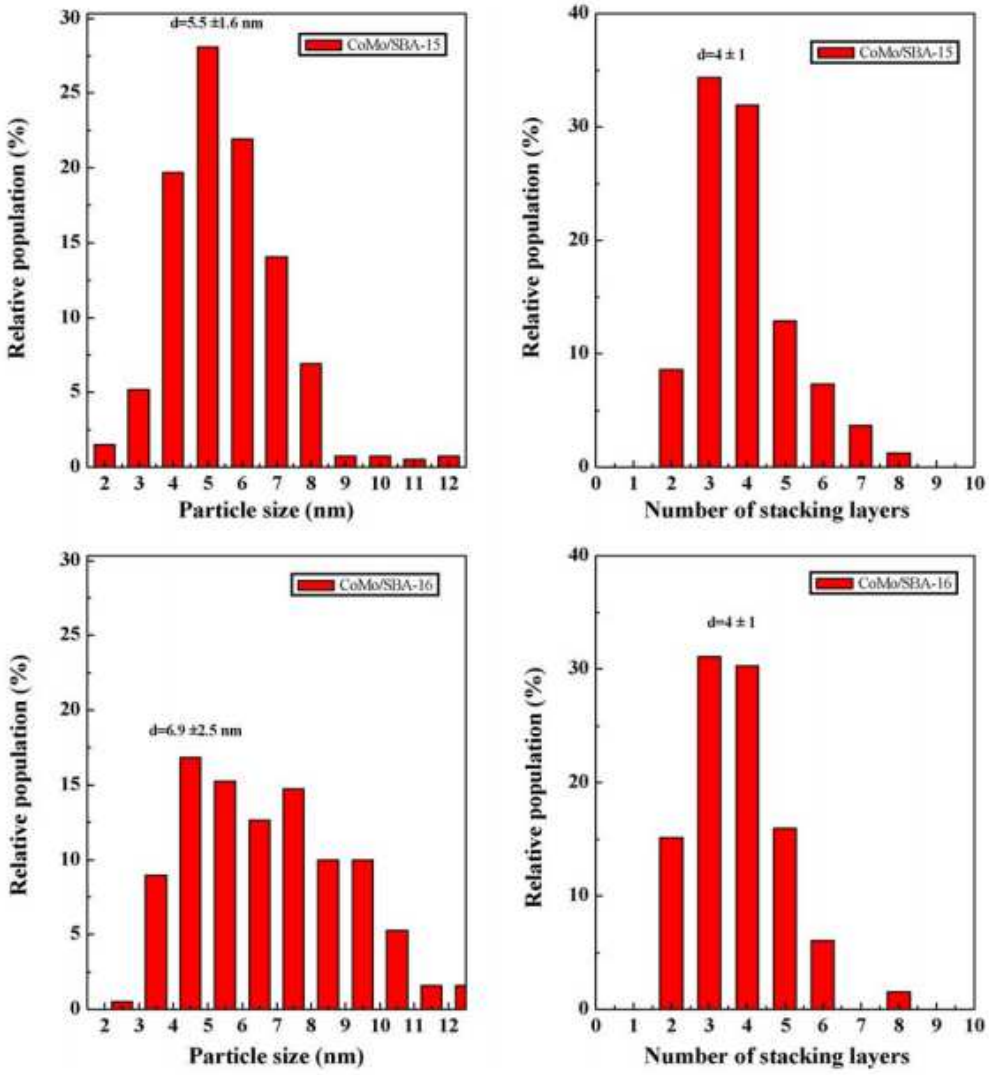

Figure 4.13. Histograms of the metal sulfide particle size distribution (left) and stacking layers (right) of the spent CoMo/SBA-15 (top) and CoMo/SBA-16 (bottom) catalysts.

4.3.4.3. X- Ray Photoelectron Spectroscopy (XPS)

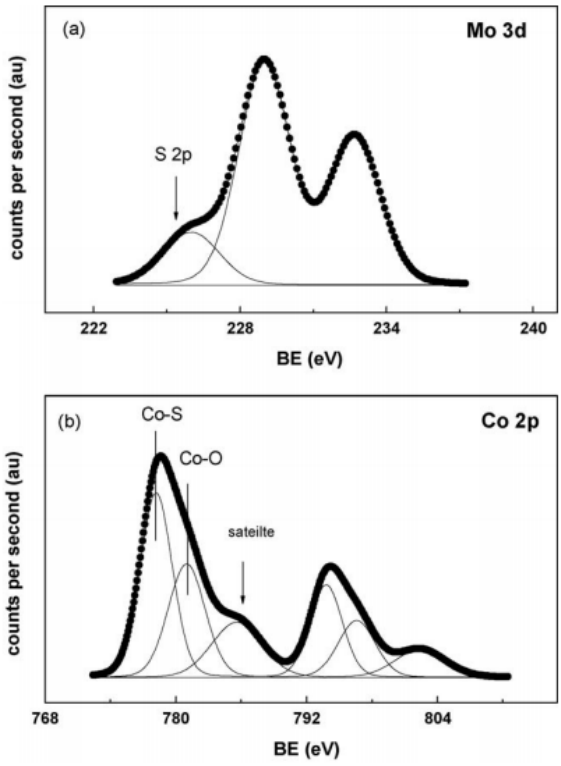

Figure 4.14. Mo 3d **(a)** and Co 2p **(b)** and core levels XPS spectra of the spent CoMo/DMS- 1 catalyst.

The surface composition and chemical state of the components in spent catalysts were investigated by XPS technique. The BE values of the Si 2p, Mo $3d_{5/2}$, Co 2p and S 2p core levels are compiled in **Table 4.10**. As an example, the Mo 3d and Co 2p core-level spectra of the spent CoMo/DMS-1 catalyst are shown in **Figure 14(a)** and **(b)**, respectively. After on-stream conditions, all the catalysts record Mo $3d_{5/2}$ binding energies of 229.0 ± 0.1 eV, which are typical of Mo^{4+} in

MoS_2 phase (49). The S $2p_{3/2}$ binding energy of 162.0 ± 0.1 eV is characteristic of the S^{2-} type ligands present in this phase. Irrespectively of the support employed, Mo species are completely sulfided for all catalysts. On the other hand, the Co $2p_{3/2}$ core-level spectra make two contributions: a minor one at 778.0– 778.2 eV characteristic of Co-sulfide species (50), and another at 781.1–781.6 eV belonging to non-sulfided Co species.

Table 4.10. Binding energies (eV) and surface atomic ratios of the spent CoMo catalysts tested in the bio-liquid hydrotreating[a].

	CoMo/HMS	**CoMo/SBA-15**	**CoMo/SBA-16**	**CoMo/DMS-1**
Si 2p	103.3	103.4	103.4	103.4
Mo $3d_{5/2}$	229.0	228.9	229.0	229.1
Co $2p_{3/2}$	778.1 (53) 781.1 (47)	778.4 (49) 781.6 (51)	778.5 (44) 781.5 (56)	778.2 (47) 781.2 (53)
S 2p	162.1	161.9	162.0	162.0
Mo/Si	0.042	0.052	0.092	0.069
Co total/Si	0.022	0.032	0.057	0.044
Co-S/Si	0.012	0.016	0.025	0.021
S/(Mo + Co)	1.54	1.03	1.11	1.38
S/ Si	0.097	0.093	0.182	0.157

[a] Reaction conditions were: T = 250 °C; P = 3 MPa; $WHSV_{bio\text{-}liquid}$ = 2.7 h^{-1} and TOS = 5 h.

Considering the sulfidation degree, the S/(Mo + Co) atomic ratios of the catalysts follow the trend (**Table 4.10**): CoMo/ HMS > CoMo/DMS-1 > CoMo/SBA-16 > CoMo/SBA-15. Thus, the sulfidation of the CoMo/SBA-15 catalyst is considerably retarded as compared with the other catalysts, in good agreement with XRD data indicating the formation of large-size β-$CoMoO_4$ crystallites (cf. **Figure. 4.3**). Considering the absence of correlation between the sulfidation degree of Co species and catalytic activity, the incomplete sulfidation of the Co species does not appear to be a serious drawback for catalytic activity, which is in good

agreement with observations by Venezia et al. (51). As the binding energies of Co 2p peaks are very high and characteristic of ionic Co^{2+} species interacting with the silicate surface, it is inferred that the fraction of non-sulfided cobalt does not interact with molybdenum and may therefore be responsible for Si–O–Co linkages rather than for the $CoMoO_4$ phase.

The XPS information on the active phase surface exposure is in line with that derived from the N_2 adsorption–desorption isotherms of the calcined precursors (vide supra). A plot of surface Mo/Si atomic ratio (from XPS) versus bulk Mo/Si atomic ratio (from chemical analysis) clearly indicates that HMS and DMS-1- supported catalysts possess their molybdenum species mainly located within the inner porous structure (**Figure 4.15**). This is in good agreement with their N_2 isotherms of the calcined precursors (**Figure 4.2**) whose hysteresis loops indicate the presence of large mesopores formed by nanosize particles (52). In comparison with the CoMo/HMS and CoMo/DMS-1, the CoMo/SBA-15 catalyst possesses a larger amount of molybdenum species located on the external support surface. Indeed, the type H1 hysteresis loop of its N_2 isotherm is characteristic of the mesoporous materials with metal-free 1-D cylindrical channels (**Figure 4.2**). Finally, the N_2 isotherm of the calcined CoMo/SBA-16 showed a triangular H2-type adsorption–desorption hysteresis loop characteristic of mesoporous materials with cage-like pores (**Figure 4.2**) indicating that its porous structure is metal-free (53). In line with this, the XPS data indicate that molybdenum species are located on the external support surface of the CoMo/SBA-16 sample.

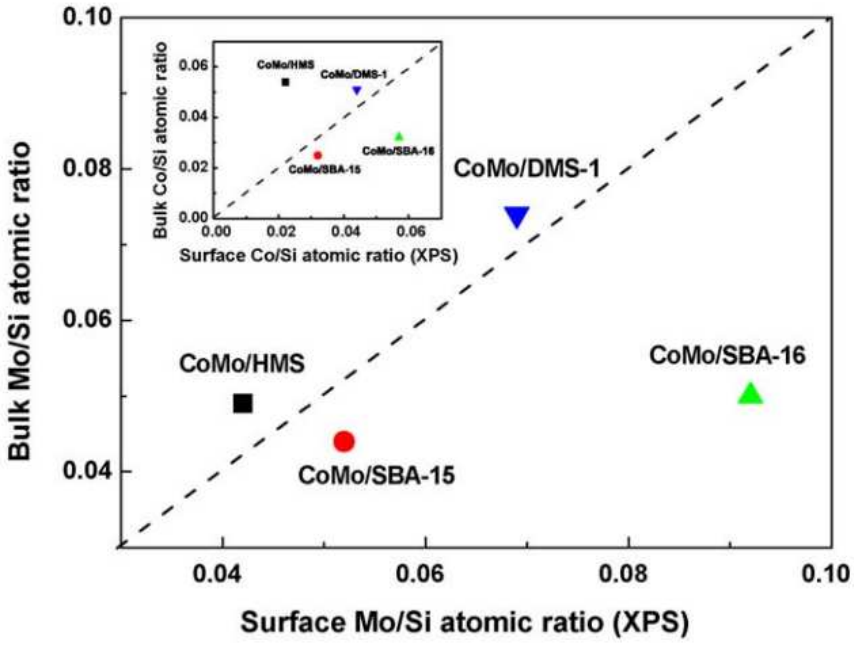

Figure 4.15. Bulk Mo/Si atomic ratio of the calcined catalysts (from chemical analysis) versus surface Mo/Si atomic ratio of the sulfided catalysts (from XPS). Data corresponding to cobalt species are shown in inlet of this figure.

4.3.4.5. Thermogravimetric analysis (TG/DTG)

In this study, the nature and extent of coke formation on spent catalysts were studied by means of TG/DTG technique, measuring the weight losses of the coked catalysts upon oxidation in 20% O_2/N_2 mixture. The TG and DTG profiles of the spent catalysts are displayed in **Figure 4.16**. TPO results pointed out that carbon deposits strongly depend on the type of support. For all catalysts, the low temperature peak (ca. 375 °C) in TPO/DTG profiles lies within the region where metal sulfide phases are oxidized into the respective oxides. The weight loss

corresponding to SO_2 evolution follows the trend: CoMo/DMS-1 (9.2%) > CoMo/HMS (6.3%) ≈ CoMo/SBA-16 (6.1%) > CoMo/SBA-15 (3.9%) indicating the largest stability of the latter catalyst.

For all catalysts, the DTG peaks at temperature > 500 °C are ascribed to the combustion of coke, being more graphitic as temperature increases. Considering the amount of coke formed during 5 h of on-stream operation, the observed trend is: CoMo/ HMS (2.4%) > CoMo/SBA-15 ≈ CoMo/SBA-16 ≈ CoMo/DMS-1 (1.5–1.7%). Coke formation follows the same trend as total oxygen content after TOS = 5 h. This might indicate that the lowest activity of the HMS-supported catalyst is linked with the largest deactivation of its active sites by coke. No correlation is found between catalyst acidity and the extent of coke formation, indicating that coke reactivity depends basically on the catalyst structure, which is closely related to the morphology of the catalyst (54). The genesis of coke in biomass upgrading by hydrotreating over the catalysts studied cannot be elucidated from these results. Further work is in progress in order to unravel the mechanism of coke formation on these catalysts.

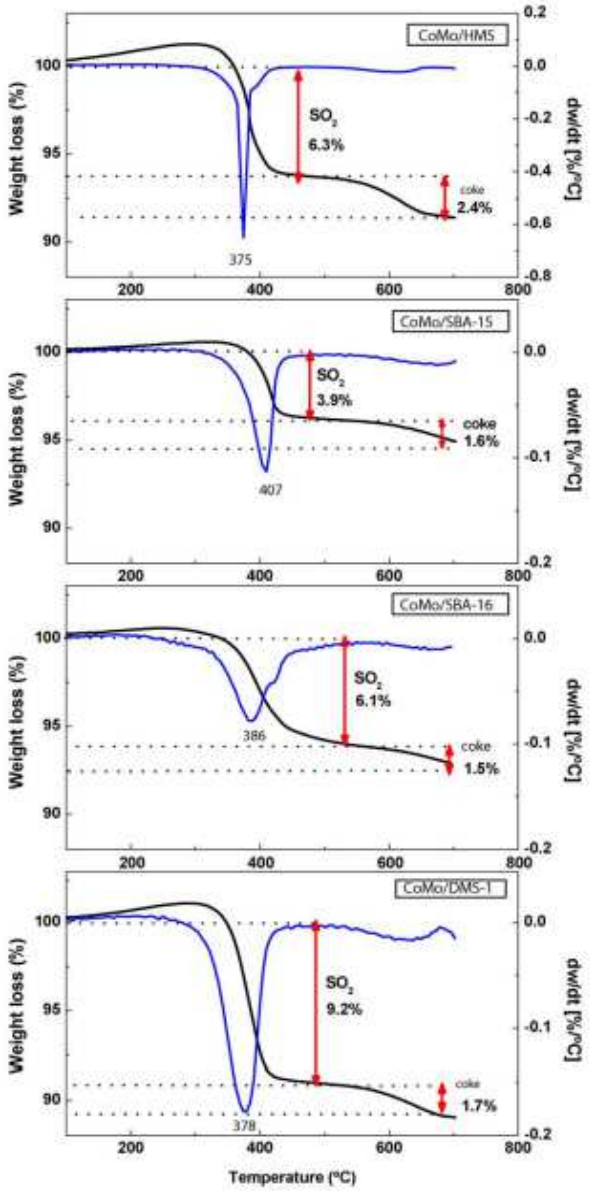

Figure 4.16. TPO/TG profiles of the spent CoMo catalysts supported on mesoporous silica

In short, the HDO activity of the catalysts studied is strongly influenced by the support acidity and much less so by the sulfidation degree of exposed cobalt species. During 5 h of on-stream reaction, the catalysts preserved their morphology, as was confirmed by low-angle XRD. For all catalysts, deactivation by coke was relatively low (1.5–2.4%). In general, the specific surface area of catalysts does not influence the HDO reaction in the biomass upgrading over CoMo catalysts. However, considering the yields of desired products (paraffin, alcohols or olefins), the cubic cage structured SBA-16 is the most optimized material followed by SBA-15 (hexagonal pores and 1D channels) and DMS-1 (disordered arrangement of pores). In this sense, the CoMo/SBA-16 catalyst is the most effective for alcohol production and the elimination of polyaromatics. The higher surface concentrations of Co and Mo species, as well as the easier sulfidation of Co species, contributed to the enhancement of the HDO reaction over the SBA-15, SBA-16 and DMS-1-supported catalysts with respect to the CoMo/HMS sample. TPR techniques confirmed the enhancement of metal oxide species reduction on the SBA-15, SBA-16 and DMS-1- supported catalysts with respect to the HMS-supported counterpart, suggesting a lower metal-support interaction on the three former catalysts.

4.4. Conclusions

Upgrading olive oil production by-products via hydrotreating was performed on sulfided CoMo catalysts supported on different mesoporous silicates (SBA-15, SBA-16, DMS-1, and HMS). The main conclusions derived from this work are the following:

(i) All CoMo catalysts supported on mesoporous silicates are muchmore active than a commercial NiMo/Al_2O_3 catalyst.

(ii) The CoMo/SBA-16, CoMo/SBA-15 and CoMo/DMS-1 catalysts are more effective for oxygen removal and more selective toward desirable products than their CoMo/HMS counterpart.

(iii) The HDO activity of the catalysts studied is strongly influenced by the support acidity and much less so by the sulfidation degree of surface cobalt species. All catalysts were stable during on-stream reaction, and deactivation by coke was relatively low (1.5–2.4%).

(iv) The selectivity toward desired products is influenced by support morphology. The CoMo/SBA-16 catalyst is the most appropriate considering the formation of desirable products (paraffins and alcohols) and the removal of oxygen-containing products and polyaromatics (PAH). This sample is a good candidate for the first of a two-stage process to produce hydrocarbon fuels from biomass.

4.5. References

1. *From biomass to fuels: Hydrotreating of oxygenated compounds.* I. Gandarias, V.L. Barrio, J. Requies, P.L. Arias, J.F. Cambra, M.B. Güemez. **s.l. : International Journal of Hydrogen Energy, 2008, Vols. (33) 3485-3488.**

2. *Catalytic hydrodeoxygenation.* **Furimsky, E.** s.l. : Applied Catalysis A: General , 2000, Vols. (199) 147-190.

3. *Catalytic conversion of biomass pyrolysis products by mesoporous materials: Effect of steam stability and acidity of Al-MCM-41 catalysts.* **E.F. Iliopouloua, E.V. Antonakoub, S.A. Karakoulia, I.A. Vasalos, A.A. Lappas, K.S. Triantafyllidis.** s.l. : Chemical Engineering Journal, 2007, Vols. (134) 51-57.

4. **H. Topsoe, B.S. Clausen, F.E. Massoth.** *Hydrotreating Catalysts: Science and Technology.* Germany : Springer, 1996. p.22.

5. **D.C. Elliott, G.G. Neuenschwander, in: A.V. Bridgwater, D.G.B. Boocock (Eds.).** *Developments in Thermochemical Biomass Conversion, Vol. 1.* London : Blackie Academic & Professional, 1996. pp.611-621.

6. *CoMo/Ti-SBA-15 catalysts for dibenzothiophene desulfurization.* **R. Nava, R.A. Ortega, G. Alonso, C. Ornelas, B. Pawelec, J.L.G. Fierro.** s.l. : Catalysis Today, 2007, Vols. (127) 70-84.

7. *Comparison of the morphology and reactivity in HDS of CoMo/HMS, CoMo/P/HMS and CoMo/SBA-15 catalysts .* **R. Nava, B. Pawelec, J. Morales, R.A. Ortega, J.L.G. Fierro.** s.l. : Microporous Mesoporous Materials , 2009, Vols. (118) 189-201.

8. *Removal of refractory S-containing compounds from liquid fuels on novel bifunctional CoMo/HMS catalysts modified with Ti .* **T.A. Zepeda, B. Pawelec, J.L.G. Fierro, T. Halachev.** s.l. : Applied Catalysis B: Environmental, 2007, Vols. (71) 223-236.

9. *Synthesis and Characterization of Ti-HMS and CoMo/Ti-HMS Oxide Materials with Varying Ti Content.* **T.A. Zepeda, J.L.G. Fierro, B. Pawelec, R. Nava, T. Klimova, G.A. Fuentes, T. Halachev.** s.l. : Chemistry of Materials, 2005, Vols. (17) 4062-4073.

10. *Hydrodesulfurization of dibenzothiophene over CoMo/HMS and CoMo/Ti-HMS catalysts.* **T.A. Zepeda, T. Halachev, B. Pawelec, R. Nava, T. Klimova, G.A. Fuentes, J.L.G. Fierro.** s.l. : Catalysis Communications, 2006, Vols. (7) 33-41.

11. *HDS of dibenzothiophene over polyphosphates supported on mesoporous silica.* **B. Pawelec, S. Damyanova, R. Mariscal, J.L.G. Fierro, I. Sobrados, J. Sanz, L. Petrov.** s.l. : Journal of Catalysis, 2004, Vols. (223) 86-97.

12. *Liquid hydrocarbon fuels from palm oil by catalytic cracking over aluminosilicate mesoporous catalysts with various Si/Al ratios, .* **F.A. Twaiq, R.A. Mohamed, S. Bhatia.** s.l. : Microporous Mesoporous Mater, 2003, Vols. (64) 95-107.

13. *Liquid hydrocarbon fuels from palm oil by catalytic cracking over aluminosilicate mesoporous catalysts with various Si/Al ratios.* **F.A. Twaiq, R.A. Mohamed, S. Bhatia.** s.l. : Microporous Mesoporous Materials, 2003, Vols. (64) 95–107.

14. *Performance of composite catalysts in pulm oil cracking for the production of liquid fuels and chemicals.* **F.A.A. Twaiq, A.R. Mohamad, S. Bhatia.** s.l. : Fuel Processing Technology , 2004, Vols. (85) 1283–1300.

15. *In situ catalytic upgrading of biomass derived fast pyrolysis vapours in a fixed bed reactor using mesoporous materials .* **J. Adam, E. Antonakou, A. Lappas, M. Stöcker, M.H. Nilsen, A. Bouzga, J.E. Hustad, G. Øye.** s.l. : Microporous and Mesoporous Materials, 2006, Vols. (96) 93-101.

16. *Pyrolysis of biomass in the presence of Al-MCM-41 type catalysts.* **J. Adam, M. Blazsó, E. Mészáros, M. Stöcker, M.H. Nilsen, A. Bouzga, J.E. Hustad, M. Grønli, G. Øye.** s.l. : Fuel, 2005, Vols. (84) 1494-1502.

17. *Ordered mesoporous molecular sieves synthesized by a liquid-crystal template mechanism.* **C.T. Kresge, M.E. Leonowicz, W.J. Roth, J.C. Vartuli, J.S. Beck.** s.l. : Nature , 1992, Vols. (359) 710-712.

18. *Titanium-containing mesoporous molecular sieves for catalytic oxidation of aromatic compounds.* **P.T. Tanev, M. Chibwe, T.J. Pinnavaia.** s.l. : Nature, 1994, Vols. (368) 321-323.

19. *A Neutral Templating Route to Mesoporous Molecular Sieves.* **P.T. Tanev, T.J. Pinnavaia.** s.l. : Science , 1995, Vols. (267) 865-867.

20. *Triblock Copolymer Syntheses of Mesoporous Silica with Periodic 50 to 300 Angstrom Pores.* **D. Zhao, J. Feng, Q. Huo, N. Melosh, G.H. Fredrickson, B.F. Chmelka, G.D. Stucky.** s.l. : Science, 1998, Vols. (279) 548-552 .

21. *Investigation of the Morphology of the Mesoporous SBA-16 and SBA-15 Materials.* **W.J.J. Stevens, K. Lebeau, M. Mertens, G. Van Tendeloo, P. Cool, E.F. Vansant.** s.l. : The Journal of Physical Chemistry B, 2006, Vols. (110) 9183-9187.

22. *Comparison of the morphology and HDS activity of ternary Co-Mo-W catalysts supported on P-modified SBA-15 and SBA-16 substrates.* **R. Huirache-Acuña, B. Pawelec, E. Rivera-Muñoz, R. Nava, J. Espino, J.L.G. Fierro.** s.l. : Applied Catalysis B: Environmental, 2009, Vols. (92) 168-184.

23. *NiMo catalysts supported on titania-modified SBA-16 for 4,6-dimethyldibenzothiophene hydrodesulfurization.* **J.C. Amezcua, L. Lizama, C. Salcedo, I. Puente, J.M. Domínguez, T. Klimova.** s.l. : Catalysis Today, 2005, Vols. (107-108) 578-588.

24. *Nonionic Triblock and Star Diblock Copolymer and Oligomeric Surfactant Syntheses of Highly Ordered, Hydrothermally Stable, Mesoporous Silica Structures.* **D. Zhao, Q. Huo, J. Feng, B.F. Chmelka, G.D. Stucky.** s.l. : Journal American Chemical Society , 1998, Vols. (120) 6024-6036.

25. *Direct imaging of the pores and cages of three-dimensional mesoporous.* **Y. Sakamoto, M. Kaneda, O. Teresaki, D. Zhao, J.M. Kim, G.D. Stucky, H.J. Shin, R. Ryoo.** s.l. : Nature , 2000, Vols. (408) 449-453.

26. *Highly active disordered extra large pore titanium silicate .* **A. Bhaumik, S. Samanta, N.K. Mal.** s.l. : Microporous and Mesoporous Materials, 2004, Vols. (68) 29-35.

27. *Influence of the block length of triblock copolymers on the formation of mesoporous silica.* **K. Flodström, V. Alfredsson.** s.l. : Microporous and Mesoporous Materials, 2003, Vols. (59) 167–176.

28. *Mesoporous Titanosilicate Molecular Sieves Prepared at Ambient Temperature by Electrostatic (S+I-, S+X-I+) and Neutral (S°I°) Assembly Pathways: A Comparison of Physical Properties and Catalytic Activity for Peroxide Oxidations.* **W. Zhang, M. Fröba, J. Wang, P.T. Tanev,J. Wong, T.J. Pinnavaia.** s.l. : Journal of the American Chemical Society, 1996, Vols. (118) 9164-9171.

29. *Postsynthesis Hydrothermal Restructuring of M41S Mesoporous Molecular Sieves in Water.* **L. Chen, T. Horiuchi, T. Mori, K. Maeda.** s.l. : Journal of Physical Chemistry B, 1999, Vols. (103) 1216-1222.

30. **C.D. Wagner, W.M. Riggs, L.E. Davis, J.F. Moulder, in: G.E. Muilenberg.** *Handbook of X-ray Photoelectron Spectroscopy.* USA : Perkin Elmer Corporation; Eden Prairie, 1979.

31. *Catalyst evaluation for catalytic biomass pyrolysis.* **M.C. Samolada, A. Papafotica, I.A. Vasalos.** s.l. : Energy Fuels, 2000, Vols. (14) 1161-1167.

32. *The Role of the Liquid-Solid Interface in the Preparation of Supported Catalysts.* **K. Bourikas, C. Kordulis and A. Lycourghiotis.** s.l. : Catalysis Reviews-science and Engineering, 2006, Vols. (48) 363-444.

33. **S.J. Gregg, K.S.W. Sing.** *dsorption, Surface Area and Porosity.* London : Academic Press, 1982.

34. *Oxide loaded ordered mesoporous oxides for catalytic applications.* **F. Schüth, A. Wingen, J. Sauer.** s.l. : Microporous Mesoporous Materials, 2001, Vols. (44-45) 465-476.

35. *Nanometric monodispersed titanium oxide particles on mesoporous silica: synthesis, characterization, and catalytic activity in oxidation reactions in the liquid phase.* **A. Tuel, L.G. Hubert-Pfalzgraf.** s.l. : Journal of Catalysis, 2003, Vols. (217) 343-353.

36. *Characterization of the Porous Structure of SBA-15.* **M. Kruk, M. Jaroniec, C. Hyun Ko, R. Ryoo,.** s.l. : Chemistry of Materials, 2000, Vols. (12) 1961-1968.

37. *Development of new catalysts for deep hydrodesulfurization of gas oil.* **K. Segawa, K. Takahashi, S. Satoh.** s.l. : Catalysis Today, 2000, Vols. (63) 123-131.

38. *Synthesis of mesoporous zeolites and their application for catalytic conversion of polycyclic aromatic hydrocarbons .* **K.M. Reddy, C. Song.** s.l. : Catalysis Today, 1996, Vols. (31) 137-144.

39. *Loss of single-walled carbon nanotubes selectivity by disruption of the Co–Mo interaction in the catalyst.* **J.E. Herrera, D.E. Resasco.** s.l. : Journal of Catalysis, 2004, Vols. (221) 354–364.

40. *Structure and activity of NiCo-Mo/SiO2 hydrodesulfurization catalysts.* **J. Laine, J.L. Brito, F. Severino.** s.l. : Journal of Catalysis, 1991, Vols. (131) 385-393.

41. *Influence of the preparation method on the activity of phosphate-containing CoMo/HMS catalysts in deep hydrodesulphurization.* **R. Nava, J. Morales, G. Alonso, C. Ornelas, B. Pawelec, J.l.G. Fierro,.** s.l. : Applied Catalysis A: General, 2007, Vols. (321) 58-70.

42. *A review of catalytic hydrotreating processes for the upgrading of liquids produced by flash pyrolysis .* **R. Maggi, B. Delmon.** s.l. : Studies in Surface Science and Catalysis, 1997, Vols. (106) 99-113.

43. **Augustine, R.L.** *Heterogeneous Catalysis for the Synthetic Chemist.* New York : Marcel Dekker, 1996. p.462.

44. *Removal of PAH Compounds from Liquid Fuels by Pd Catalysts.* **B. Pawelec, J.M. Campos-Martin, E. Cano-Serrano, R.M. Navarro, S. Thomas, J.L.G. Fierro.** s.l. : Environmental Science & Technology, 2005, Vols. (39) 3374-3381.

45. *Hydrodeoxygenation of benzophenone on Pd catalysts.* **Martina Bejblová, Petr Zámostný, Libor Červený, Jiří Čejka.** s.l. : Applied Catalysis A: General, 2005, Vols. (296) 169-175.

46. *Solvent effect in gas–liquid hydrotreatment reactions.* **A. Guevara, R. Bacaud, M. Vrinat,.** s.l. : Applied Catalysis A: General, 2003, Vols. (253) 515-526.

47. *Studies on mesoporous materials: I. Synthesis and characterization of MCM-41.* **C.H. Chen, H.X. Li, M.E. Davis.** s.l. : Microporous Materials, 1993, Vols. (2) 17-26.

48. *Hydrodeoxygenation of aliphatic esters on sulphided NiMo/γ-Al2O3 and CoMo/γ-Al2O3 catalyst: The effect of water .* **O.İ. Şenol, T.R. Viljava, A.O.I. Krause.** s.l. : Catalysis Today, 2005, Vols. (106) 186-189.

49. *Formation of cobalt–molybdenum sulfides in hydrotreating catalysts: a surface science approach.* **A.F.H. Sanders, A.M. de Jong, V.H.J. de Beer, J.A.R. van Veen, J.W. Niemantsverdriet.** s.l. : Applied Surface Science, 1999, Vols. (144-145) 380-384.

50. **D. Briggs, M.P. Seah.** *Practical Surface Analysis, Auger and X-ray Photoelectron Spectroscopy, .* New York : Wiley/Salle and Sauerländer , 1990. p. 607..

51. *A.M. Venezia, R. Murania, G. Pantaleo, G. Deganello.* **effects, Nature of cobalt active species in hydrodesulfurization catalysts: Combined support and preparation method.** s.l. : Journal of Molecular Catalysis A: Chemical, 2007, Vols. (271) 238–245.

52. *Synthesis of Silica Nanoparticles Having a Well-Ordered Mesostructure Using a Double Surfactant System.* **K. Suzuki, K. Ikari, H. Imai.** s.l. : Journal of the American Chemical Society, 2004, Vols. (126) 462-463.

53. *Density Functional Theory of Adsorption in Spherical Cavities and Pore Size Characterization of Templated Nanoporous Silicas with Cubic and Three-Dimensional Hexagonal Structures.* **P.I. Ravikovitch, A.V. Neimark.** s.l. : Langmuir, 2002, Vols. (18) 1550-1560.

54. *Burning of coke on Pt Re/Al_2O_3 catalyst: Activation energy and oxygen reaction order.* **C.L. Pieck, R.J. Verderone, E.J. Jablonski, J.M. Parera.** s.l. : Applied Catalysis, 1989, Vols. (55) 1-10.

Chapter 5

Hydrogenolysis of anisole over mesoporous Co-Mo-W/SBA-15(16) sulfide catalysts

Chapter 5

Hydrogenolysis of anisole over mesoporous Co-Mo-W/SBA-15(16) sulfide catalysts

This chapter describes the effect of SBA-15(16) support modification with variable quantity of P_2O_5 (0.5 and 1.0 wt%) on the catalytic response of supported ternary CoMoW catalysts in the gas-phase hydrogenolysis of anisole, as a model compound for pyrolysis oil. The catalysts were characterized by a variety of techniques (N_2 adsorption-desorption isotherms, XRD, TPD-NH_3, XPS, UV-vis DRS, Raman, TPR, DRIFT of adsorbed NO, XPS, HRTEM and coke combustion followed by TG/DTG). Under steady-state conditions, the sulfided CoMoW/SBA-16 catalyst modified with a small amount of phosphate (0.5 wt.%) recorded the highest activity and stability in anisole transformation at 310 ºC and 3.0 MPa of hydrogen pressure. All catalysts exhibited similar selectivities at the same anisole conversion (38%), indicating that catalyst morphology did not influence catalytic behavior. Regardless of the carrier, deoxygenation was not significant, with demethylation (phenol) and isomerization (*o*-cresol, *o*-xylenol) being the main reaction routes. The highest activity recorded by the phosphate-containing CoMoW/SBA-16 catalyst is associated with its highest total acidity, the largest population of Mo(W)S_2 phases located mainly within the inner support porous

structure, the greatest sulfidation degree of W species and major stability during time-on-stream operation with respect to other catalysts.

5.1. Introduction

Nowadays, there is considerable interest in developing alternative materials for fuel production from bio-liquids (1) (2). Liquefied biomass can be used as a refinery feed, or it could be mixed with traditional feedstock after first removing of any oxygen-containing compounds. Removing oxygen from bio-liquids is an obligatory process because high oxygen content contributes to high viscosity, non volatility, poor heating value, corrosiveness, immiscibilitywith fossil fuels, thermal instability and a tendency to polymerization during storage and transportation (3). Thus, the total or partial removal of oxygenates from bio-liquids is required (4).

Accordingly, removing oxygen from bio-oils via hydrotreatment over conventional sulfide Co(Ni)Mo/Al_2O_3 catalysts allows using the existing petroleum refining infrastructure (2). However, such catalysts were found to quickly deactivate by coke deposition because of the acidity of the reactants (5). The challenge is therefore to design new bifunctional catalysts capable of maintaining stability during the on-stream conditions of bio-oil hydrotreatment.

Due to the highly complex composition of any bio-liquid (4) (6). it is common practice to test new catalytic systems in the HDO of model compounds (5) (7) (8) (9) (10) (11) (12) (13) (14) (15) . Among O-containing model compounds, anisole is the one less studied (11) (12) (13) (14) (15), even though its structure is similar to the main products of lignin depolymerisation during the fast pyrolysis of

wood. A very early study by Huuska (13) showed that bifunctional (acid and metal) catalysts are needed for the hydrogenolysis and hydrocracking of the carbon–oxygen bond of anisole, but also that catalyst acidity should be optimized because of the large decrease in anisole conversion due to coke formation on standard CoMo catalysts, in close agreement with our previous observations on hydrotreating catalysts (16). The selection of catalysts for the HDO of bio-liquids depends heavily on both feedstock and operating conditions, with sulfided $CoMo/Al_2O_3$ catalysts being the preferred option in a hydrotreating reaction at low hydrogen pressure and high space velocities (17).

A recent study has revealed that metallic-like so-called brim sites, not sulfur anion vacancies (CUS sites), are involved in the hydrogenation reactions on sulfided CoMo catalysts, with the support interactions being responsible for the change both in the tendency to form vacancies and in the properties of the brim sites (17) (18) (19). Indeed, it is well known that Type II MoS_2-based structures, with only weak interactions with the support, have a higher catalytic activity than Type I MoS_2-based structures, where Mo–O linkages to the alumina are present (18). Brønsted acid centers associated with Mo atoms together with the SH^- groups (involved in providing Brønsted acid sites and in the supply of hydrogen) were proposed as hydrogenolysis sites (20) (21). In order to substitute the standard alumina support, metal sulfides supported on neutral materials such as carbon, silica, alumina modified by K and mesoporous silicas for the HDO reaction have been studied (6) (7) (8) (9).

Compared with silica, the mesoporous silica SBA-15 and SBA-16 materials have the advantages of high surface-to-volume ratio, variable framework compositions and high thermal stability. Both materials possesses interesting

textural properties such as the large specific surface areas (above 1000 m^2 g^{-1}), uniform-sized pores (about 4 nm), thick framework walls, small crystallite size of primary particles and complementary textural porosity (22) (23). Thus, their wide pore openings are expected to minimize the mass transfer problems of bulky reactants and products, which may be encountered in other materials such as zeolites (23).

The morphology of the SBA-15 and SBA-16 materials is very different. On one hand, the SBA-15 possesses hexagonal pores in a 2D array with long 1D channels (*P6mm* plane group) (24). On the other hand, the SBA-16 has a 3D cubic arrangement of mesopores corresponding to *Im3m* space group symmetry (25). For this material, high-resolution electron microscopy demonstrated that each mesopore in the body-centered cubic array is connected with its eight neighbors (26). This provides more favorable mass transfer than in the unidirectional pore system of other hexagonal mesoporous materials such as SBA-15 (27). This prompts us to compare the effect of phosphate incorporation into both SBA-15 and SBA-16 materials. The catalyst surface grafting with H_3PO_4 is a common practice to enhance the acidity of the alumina-supported catalysts (28). However, as far as we know, the effect of phosphate incorporation onto these materials is not reported in literature. For the alumina-supported catalysts, the literature reports suggest that the phosphorous effect depends on its content, nature of phosphorous precursor, method of phosphorous introduction and pH of preparative solution (28). All those factors might affect the following aspects of the final catalyst: (i) its structural and textural properties (S_{BET}); (ii) its thermal stability, (iii) the distribution between the different Co and Mo structures in the oxide precursors and/or (iv) the morphology of MoS_2 and "Co-Mo-S" type structures formed after precursor sulfidation (28).

This study seeks to determine the factors influencing anisole transformation over sulfided Co–Mo–W catalysts supported on SBA-15 and SBA-16 materials. In particular, we are interested to see whether activity and selectivity are impacted by a decrease in support interaction by decorating the surface of SBA-15 and SBA- 16 materials with P_2O_5 clusters. Factors influencing on the catalyst deactivation have been discussed.

5.2. Experimental

5.2.1. Support preparation

The siliceous SBA-15 and SBA-16 mesoporous materials were synthesized according the procedure described by Flodström and Alfredsson (29). For the synthesis of SBA-15 material, Pluronic P123 ($EO_{20}PO_{70}EO_{20}$, BASF) was used as the structure directing agent. Typically, the Pluronic P123 was dissolved in a solution of water and HCl 4M under stirring. After this, the required amount of tetraethyl orthosilicate (TEOS, 98%, Aldrich) was added to the solution, which was stirred at 35 °C for 24 h. The mixture was subsequently transferred into polypropylene bottles and heated at 80 °C for 24 h. After this, the solid obtained was filtered, washed thoroughly with deionized water, dried first in air at room temperature and then to 110 °C for 18 h and calcined at 500 °C for 6 h in order to remove the organic template.

A very similar procedure was used to synthesize the SBA-16 support where Pluronic F127 ($EO_{106}PO_{70}EO_{106}$, BASF) triblock copolymer used as the structure directing and the corresponding amount of water and HCl 2M were mixed under stirring. After dissolution, TEOS was added and allowed to react at room temperature for about 24 h. Then, the mixture was transferred into

polypropylene bottles and heated at 80 °C for 48 h. The solid residue was filtered, washed and dried at room temperature and then at 110 °C for 24 h. Finally, the sample was calcined at 550 °C in air for 6 h.

The support modification with phosphate was performed employing the post-synthesis method (grafting). Typically, the SBA-15 or SBA-16 materials were impregnated with aqueous solutions of H_3PO_4 of appropriate concentrations to obtain substrates with P_2O_5 loadings of 0.5 and 1.0 wt%. After water evaporation at room temperature, the solid was dried at 110 °C for 4 h and then calcined at 500 °C for 4 h.

5.2.2. Catalyst preparation

Two series of CoMoW catalysts were prepared using the P-free and P-containing SBA-15 and SBA-16 substrates. Each support was loaded with fixed amounts of molybdenum (8.53 wt% as MoO_3), tungsten (13.75 wt% as WO_3) and cobalt (3.81 wt% as CoO), by simultaneous impregnation via incipient wetness method. For this, an aqueous solution containing ammonium heptamolybdate tetrahydrate ($(NH_4)_6Mo_7O_{24}.4H_2O$, Aldrich), ammonium metatungstate ($(NH_4)_6H_2W_{12}O_{40}.xH_2O$, Aldrich) and cobalt nitrate hexahydrate ($Co(NO_3)_2.6H_2O$, Aldrich, 98%) was prepared. The concentrations were calculated to achieve a Mo/W atomic ratio of 0.5 and a Co/Mo atomic ratio of 0.3. The impregnate were dried at 85 °C for 16 h and then calcined at 500 °C for 4 h.

5.2.3. Catalytic activity measurements

The hydroconversion of the anisole was performed in a high-pressure laboratory-scale set-up equipped with a down-flow fixed bed catalytic reactor. Each experiment used 0.1 g of catalyst (particle diameter: 0.25–0.30 mm) mixed with 0.30 g of SiC (diameter 0.5 mm). Before catalyst activation, the catalyst was dried under a N_2 flow of 100 mL min^{-1} at 150 °C for 0.5 h. The catalyst was then sulfided in situ at 400 °C for 4 h at atmospheric pressure by a mixture of 10 vol% of a H_2S:H_2. After sulfidation, the catalyst was purged under a N_2 flow of 100 mL min^{-1} at 400 °C for 0.5 h and then stored overnight under a N_2 flow. Before the experimental run, the N_2 pressure was increased to the desired value (3.0 MPa), and the catalytic bed was cooled down to the temperature of the HDO reaction (310 °C). After that, N_2 flow was shut down, the liquid feed (20 vol% of anisole dissolved in hexadecane) injected by a high-pressure HPLC Knauer pump (WHSV = 24.5 h^{-1}) into a hydrogen stream was fed to the preheated reactor. Owing to the high boiling point of the reactant and the solvent, on-line analysis of the reaction products was not convenient. Consequently, the reactor effluents were condensed, and liquid samples were analyzed by a GC Agilent 6890A with a FID detector.

Activity at steady-state conditions is described in terms of the specific reaction rate according to Eq: $r = X \cdot F/m$ where r is the specific rate ($mol_{anisole}\ g_{cat}^{-1}\ s^{-1}$), X is the conversion of anisole, F is the molar flow rate of this reactant (mol s^{-1}), and m refers to the catalyst weight (g).

5.3. Results and discussion

5.3.1. Characterization of support and calcined precursors

5.3.1.1. Textural properties

The textural properties of the catalysts were evaluated based on their adsorption-desorption isotherms of N_2 at -196 ° C recorded in the entire range of relative pressures. Physical adsorption onto porous solid is characterized by the observation of a phenomenon called hysteresis, which is that the adsorption isotherm does not match the desorption. In **Figures 5.1(A)** and **5.1(B)** are compared the N_2 adsorption/desorption isotherms of the calcined catalysts with their respective SBA-15- and SBA-16-based supports. For the SBA-15 series, the N_2 isotherms are of type IV and show a clear H_1 type hysteresis loops suggesting that those materials have very regular mesoporous channels (**Figure 5.1(A)**). The pure supports shows a one step desorption branch, with high porosity characteristics, indicating the existence of an open pore structure. On the contrary, the SBA-15-based catalysts show two-step desorption branch due to metal oxide plugs inside the pores. Comparison of the isotherms of supports and catalysts revealed considerable shift in the relative pressure indicating the formation of new mesopores after metal loading into supports. On the other hand, the isotherms of all SBA-16-based samples have the shape of a typical SBA-16 isotherm showing a steep desorption step at relative pressure of ca. 0.42 linked with the presence of inkbottle-type pores (30).

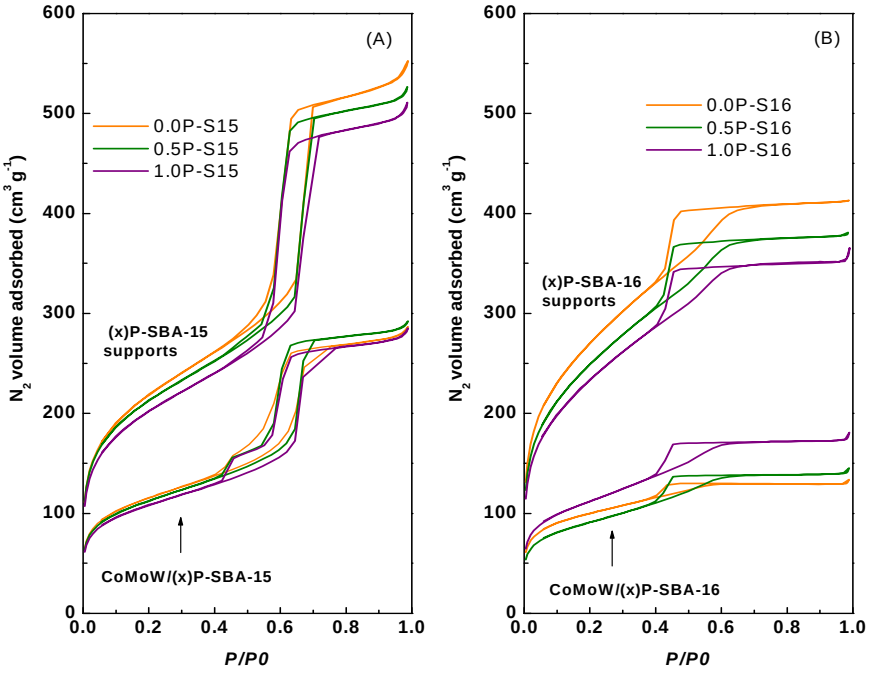

Figure 5.1. Comparison of the N_2 adsorption-desorption isotherms of pure supports and calcined catalysts.

Analyzing the effect of phosphate incorporation, the comparison of the isotherms of P-modified SBA-15 and SBA-16 supports revealed no considerable shift in the relative pressure (P/P^0), in which hysteresis was observed for P-free SBA-15 and SBA-16 samples. This indicates that the pore diameters of both materials did not change significantly after phosphorous loading. Indeed, for both SBA-15- and SBA-16-based series the volume of N_2 adsorbed-desorbed changes very little going from P-free to P-containing material with a largest P content indicating that the pores occlusion by P species did not occur (**Table 5.1**).

The main textural properties of the bare supports, calcined and sulfided SBA-15- and SBA-16-based catalysts are listed in Table 5.1. As seen in this table, irrespectively of the support (SBA-15 vs. SBA-16), the support modification with phosphorous led to decrease of both specific surface area (S_{BET}) and total pore volume (V_t). Irrespectively of the P-loading, all SBA-16-based materials show a larger specific surface area (755-942 m^2/g) with respect to their SBA-15-based counterparts (682-742 m^2/g). For the SBA-15- and SBA-16-based materials, the average pore diameters are ca. 4.5 nm and 2.5 nm, respectively.

Table 5.1. Textural properties of the calcined and fresh sulfided CoMoW/(x))P-SBA-15(SBA-16) catalysts and corresponding pure supports

Sample **x = wt% of P**		**S_{BET} (m^2 g^{-1})**		**Total pore volumen (cm^3 g^{-1})**		**Pore diameter (nm)**	
		SBA-15	SBA-16	SBA-15	SBA-16	SBA-15	SBA-16
x= 0.0	**support**	742	942	0.80	0.58	4.4	2.5
	calcined	388	374	0.41	0.18	4.6	2.7
	sulfided	223	208	0.28	0.14	5.1	2.6
x = 0.5	**support**	717	869	0.76	0.54	4.4	2.5
	calcined	380	366	0.42	0.21	4.5	2.7
	sulfided	229	187	0.30	0.15	5.2	3.3
x = 1.0	**support**	682	817	0.74	0.52	4.5	2.6
	calcined	364	382	0.41	0.23	4.6	2.9
	sulfided	208	296	0.29	0.22	5.5	2.9

The pore size distributions of the sulfided SBA-15- and SBA-16-based catalysts, calculated from the adsorption branch of N_2 isotherm, are shown in **Figure 5.2(A)** and **5.2(B)**, respectively. As seen in the **Figure 5.2(A)**, the sulfided CoMoW/(x)P-SBA-15 catalysts shows a very narrow pore size distribution centred at about 6.2 nm. On the contrary, their SBA-16-supported counterparts show bimodal pore size distribution centred at about 2.8 and 4.3 nm. In general, regardless of the support, the loss of surface area due to the addition of P was rather small whereas the deposition of the active phases results in a dramatic decrease of the surface area. This is expected considering much smaller maximum phosphorous content in comparison with total metals loadings (2 vs. 26.1 wt%). Taking also into account that the size of pore diameter does not change significantly, one might to conclude that the introduction of the active phases followed by calcination resulted in the blocking of pores of the substrates. Indeed, the resulting decrease in surface area is more pronounced in the case of SBA-16 which has more narrow pores, than in case of SBA-15-based catalysts. An increase of the pore diameter going from the support to the calcined catalysts could be explained considering that template were not completely removed during calcination of support whereas an increase of the pore diameter going from calcined to sulfided samples indicate that catalyst sulfidation led to segregation of metal oxide phases on the outer support surface. This explanation is consistent with the loss of specific surface area after sulfidation due to the blocking of pore's entrance by the clusters of metal oxides (**Table 5.1**).

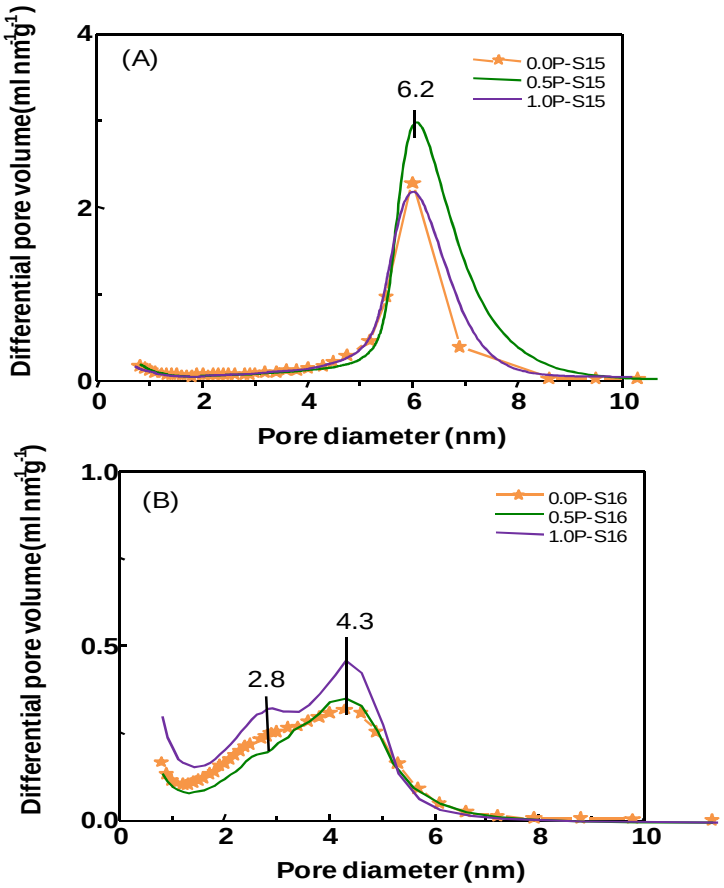

Figure 5.2. Pore size distribution of the fresh sulfided catalysts as determined from adsorption branch of the N_2 isotherm **(A)** CoMoW/(x)P-SBA-15 and **(B)** CoMoW/(x)P-SBA-16 (x = 0, 0.5 and 1.0% P).

In summary, results of nitrogen adsorption and pore size distribution analysis indicate that the presence of metal oxide clusters results in the blocking of pores of the substrates. The resulting decrease in surface area is more pronounced in the case of SBA-16 which has more narrow pores than SBA-15.

5.3.1.2. X-ray diffraction (XRD)

The low-angle X-ray diffractograms confirmed the mesoporous structure of the (x)P-SBA-15 and (x)P-SBA-16 oxide precursors **(Figures 5.3(A)** and **(B),** respectively). Thus, the SBA-15-based materials show three well-resolved typical diffraction peaks, which are associated with a bi-dimensional *p6mm* hexagonal symmetry of the pores of SBA-15 material: one high-intensity peak at about 2θ = 1.0° (100) and two low-intensities peaks at about 2θ = 1.7 and 2.0º corresponding to (110) and (200) reflections, respectively. The observed loss of peaks intensities could be due to decreasing contrast between walls and pores due to the filling of the pores, as described before (31).

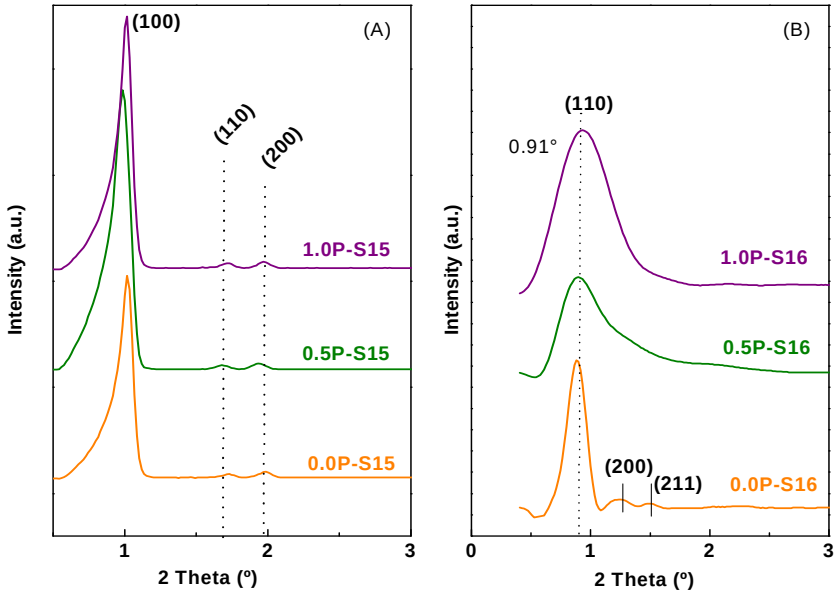

Figure 5.3. Low angle profiles of oxide precursors: **(A)** CoMoW/(x)P-SBA-15 and **(B)** CoMoW/(x)P-SBA-16 (x = 0, 0.5 and 1.0% P).

Similarly, the low-angle XRD patterns of the SBA-16-based materials (**Figure 5.3(B)**) show three peaks corresponding to reflections indexes as (110), (200) and (211) (30) indicating that pore structure was preserved after metal oxides incorporation into SBA-16 material. After P-loading, the first most intense peak at 2θ of 0.86° becomes much broader indicating that the best structural ordering was achieved for the P-free SBA-16 material.

Wide angle XRD profiles were recorded with the aim to investigate the presence of any crystallite species in the catalysts. **Figures 5.4(A)** and **5.4(B)** illustrates the diffraction profiles of the CoMoW/(x)P-SBA-15 and CoMoW/(x)P-SBA-16 oxide precursors, respectively.

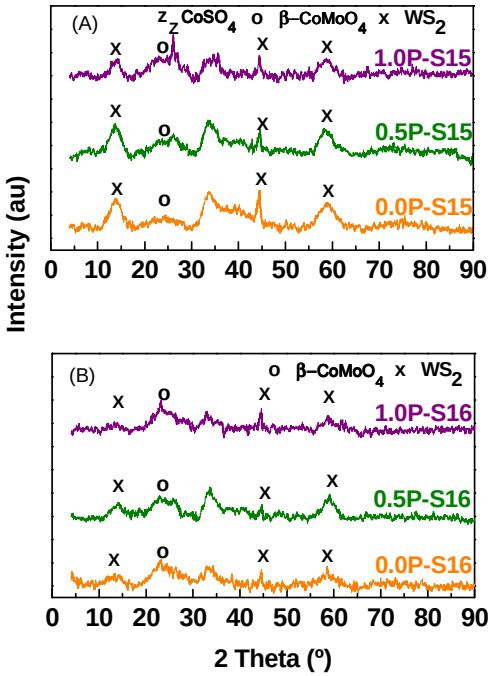

Figure 5.4. Wide-angle XRD patterns of the calcined **(A)** CoMoW/(x)P-SBA-15 and **(B)** CoMoW/(x)P-SBA-16 (x = 0, 0.5 and 1.0% P).

All oxide catalysts reveal typical diffraction patterns, with a very broad peak at around 2θ = 24°, typical of amorphous silica (32). Moreover, the XRD patterns of CoMoW/SBA-15, CoMoW/0.5P-SBA-15 and CoMoW/1P-SBA-15 catalysts, contain low peak intensities at 2θ = 25, 28, 32.5, 38, 43, 48, 57 y 59.5° corresponding to β-$CoMoO_4$ phase (JCPDS-card 00-021-868) at 2θ = 25, 28, 32.5, 38, 43, 48, 57 and 59.5° and $Mo_xW_{1-x}O_3$ (JCPDS-card 00-028-0668 x=0.2; JCPDS-card 00-076-1279 x=0.29; JCPDS-card 00-076-1280 x=0.6) at 2θ = 24, 26.5 and 61°. The low intensity of the peaks indicates that most of the supported species should be widely dispersed on the surfaces of all catalysts. The $CoMo(W)O_4$ species might exist on the surface of the CoMoW/SBA-16 catalyst but they are amorphous or their crystal size is below the detection limit of XRD technique (< 4 nm). In general, a better dispersion was observed for SBA-16-based catalysts.

5.3.1.3. UV-vis diffuse reflectance spectra (DRS)

The coordination environment of Co^{2+} and $Mo^{6+}(W^{6+})$ ions in the calcined catalysts was studied by UV-Vis diffuse reflectance spectroscopy. The DRS spectra of the calcined catalysts are plotted in **Figure 5.5** as a Kubelka-Munk-Schuster function. Regardless of the support and P-loading, all catalysts show two strong bands at about 210-270 nm and 320-350 nm. The first one imply the presence of a ligand-to-metal charge transfer involving isolated transition metal sites which is ascribed in literature to tungsten in tetrahedral coordination, like that in the WO_4^{2-} group (33), but differed form that in the WO_3 crystal (34). The second one is assigned in literature to O^{2-}-Mo^{6+} (W^{6+}) ligand-to-metal charge transfer transition (LMCT) of molybdenum and tungsten ions having octahedral coordination (35) (36).

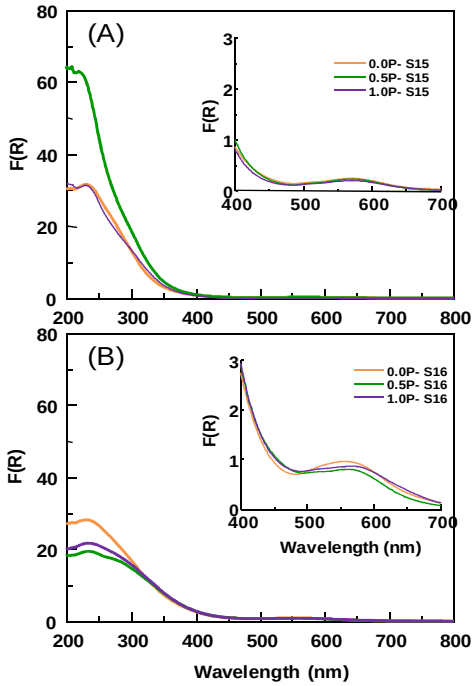

Figure 5.5. UV-visible spectra of the calcined (A) CoMoW/(x)P-SBA-15 and (B) CoMoW/(x)P-SBA-16 (x = 0, 0.5 and 1.0% P) catalysts in the ranges 200-450 nm and 450-700 nm (inlet of each figure).

A displacement observed for the mentioned bands could be attributed to the influence of tungsten on the electronic properties of this kind of catalysts. It is noteworthy that all SBA-15-supported catalysts showed similar amount of $Mo^{6+}(W^{6+})$ ions in octahedral coordination and a larger amount of those ions in tetrahedral coordination than their SBA-16-supported counterparts. Concerning the phosphorus effect, one might note that after P incorporation into the CoMoW/SBA-16, the amount of the $Mo^{6+}(W^{6+})$ ions in tetrahedral coordination

decreased suggesting the inhibition of the strong metal-support interaction by phosphorous species located on the support surface. Interestingly, for the SBA-15 supported catalysts, the phosphorus effect is opposite. Taking into account a larger pore diameter of the SBA-15 with respect to SBA-16 (4.6 vs. 2.7 nm) this is because the location of phosphorous species within the inner porous structure of the former catalysts which did not inhibited a strong metal-support interaction. As a consequence, for the SBA-15-supported catalyst the formation of the species having Mo^{6+}/W^{6+} ions in tetrahedral coordation is favored.

In contrast to the SBA-15-based catalysts, the visible spectra of the SBA-16-based catalysts exhibit bands in the 470-650 nm region (inlet in **Figure 5.5**), which are ascribed to *d–d* transitions ($^4T_{2g}$ to $^4A_{2g}$ and $^4T_{2g}$ to $^4T_{1g}$ (P)) of high spin octahedral Co complexes (37) (38). The bands are very similar to those ascribed to both α- and β-$CoMoO_4$ compounds, in which Co is in an octahedral environment (37). As shown in the inlet in **Figure 5.5**, the DRS spectra clearly indicate that incorporation of P species into SBA-16 carrier diminish the amount of the Co tetrahedral species. Additionally, the DR spectra provide strong evidence that well-dispersed octahedral cobalt species are present on the surface of (x)P-SBA-16 substrates (shoulder at 525 nm).

5.3.1.4. Micro-Raman

Considering that Raman spectroscopy is effective for detecting the presence of crystalline as well as amorphous oxides, the calcined catalysts were studied by this technique. The Raman spectra of the SBA-15- and SBA-16-supported catalysts are shown in **Figures 5.6(A)** and **5.6(B)**, respectively. For all

catalysts, the absence of the band at about 1040-1060 cm^{-1} confirm that nitrate ions were completely removed by calcination at 500 °C for 4 h.

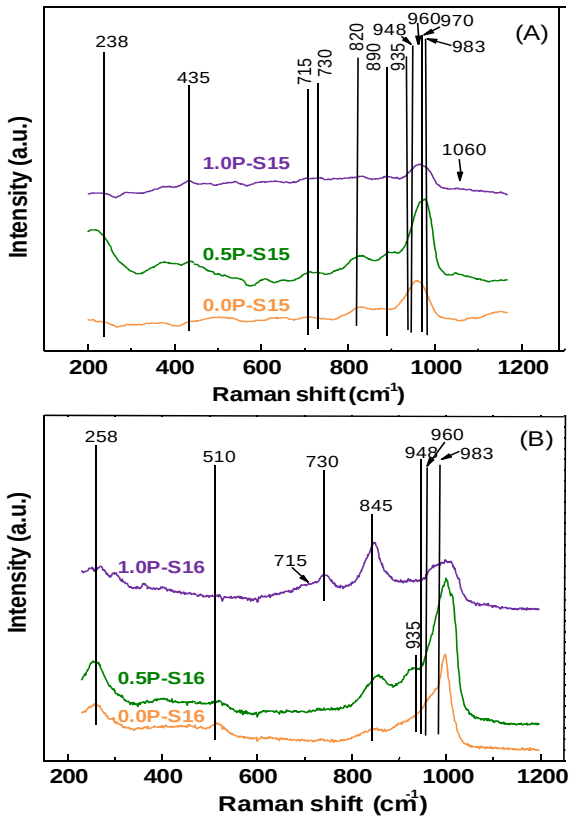

Figure 5.6. Raman spectra of the calcined **(A)** CoMoW/(x)P-SBA-15 and **(B)** CoMoW/(x)P-SBA-16 (x = 0, 0.5 and 1.0% P)

Regardless of the support and P-loading, Raman spectra of all catalysts show a major peak in the region between 900 and 1000 cm^{-1}. The broadness and position of this peak indicate the presence of several W and Mo species with

different symmetries. Considering nominal metal loading of the catalysts studied (WO_3 = 13.75 wt%; MoO_3 = 8.53 wt%; CoO = 3.81 wt%), one might to expect that the mayor contribution to the intensity of this peak might to came from the W species. Thus, the band at around 960 cm^{-1} may arise from the W=O symmetric stretching vibration mode of $W_7O_{24}^{6-}$ species having W in the octahedral coordination (39).

Contribution from surface dioxo species $Mo(=O)_2$ species (970-975 cm^{-1}) (32) and $Mo_7O_{24}^{6-}$ species (948 cm^{-1}) (40) are also possible considering the broadness of the main peak. For all catalysts, the band at about 935 cm^{-1} could be ascribed as due to symmetric stretching vibrations of the W=O bond of tetrahedrally coordinated tungsten oxide hydrated species (WO_4^{2-} ions) (41) (42). The formation of those species is confirmed also by the presence of peak at ~730-740 cm^{-1}, which is attributed to the asymmetric vibration of W^{6+}-O bonds (O-W-O stretching modes). Additionally, small features at 715 cm^{-1} and 435 cm^{-1} corresponding to WO_3 (43) (44) and the band at ~510 cm^{-1} assigned to W-O-W linkages found in solvated polytungstates clusters (42) could be observed. Finally, considering the intermediate frequencies region, the band in the 200-300 cm^{-1} range corresponds to W−O−W bending modes of the bridging oxygen (45).

Concerning the Mo species, both SBA-15 and SBA-16 series show the band at ca. 983 cm^{-1} which is in the Mo-O-Mo stretching region of various polymolybdates havening irregular form (bankrupt, with a higher number of edge atoms) (46). For the CoMoW/SBA-16 and CoMoW/0.5P-SBA-16 catalysts, the strong intensity of the band at 983 cm^{-1} indicates the presence of a large amount of polymerized Mo-oxide species. For SBA-16-based catalysts, the presence of the β-$CoMoO_4$ species is deduced from the band at 890 cm^{-1} (Mo-O-Co stretching vibrations) (40) (47). Moreover, the band at around 845 cm^{-1} can be associated with

the asymmetric stretching mode of the Mo-O-Mo bridge bond of the octahedral molybdate species [38]. Finally, the band at about 820-825 cm^{-1} is due to Mo-O-Mo linkage in the orthorhombic MoO_3 (47).

To conclude, the Raman spectra demonstrated that both the phosphorus incorporation and the morphology of SBA-16 material favor the polymerization degree of the W and Mo species. Regardless of the support, the addition of small amount of phosphorous (0.5 wt%) led to the enhancement of the formation of polymolybdates havening bankrupt forms with a higher number of edge atoms as well as to the larger formation of $W_7O_{24}^{6-}$ species having W in the octahedral coordination.

5.3.1.5. Temperature Programmed Reduction (TPR- H_2)

Reducibility of different oxides on the catalyst surface was evaluated by Temperature Programmed Reduction. **Figure 5.7** shows the TPR profiles of the calcined catalysts. The samples display quite similar TPR profiles although the tungsten incorporation modifies to some extent the reduction temperature of Mo oxide. However, these TPR profiles are different to the TPR profiles of the free tungsten catalysts, CoMo/SBA-15 and CoMo/SBA-16 (Chapter 4). Indeed, the tungsten presence in the catalysts provoke certain changes in the TPR profiles: (i) shifting of the two peaks reduction at higher temperatures, from 542 and 755°C (to the free W catalysts) to 550 and 800°C (to the catalysts containing W) and (ii) decreasing in intensity of the first peak reduction and increasing in intensity of the second peak reduction. It can be stated that the tungsten incorporated in CoMo catalysts affects the reduction behavior of the catalysts resulting in a higher reducibility species, like tungsten in octahedral coordination. Moreover, there is a

strong influence of P-loading on the reduction profiles. The P-free catalysts show the lowest reduction temperature among the catalysts studied. The TPR profiles display a well defined narrow peak at 500-550 °C and another broad one between 700-800 °C. The former is more intense and broad when P-loading increases. As cobalt species are reduced at lower temperatures than $Mo(W)O_3$, it is likely that free cobalt oxide species can contribute to the first H_2 consumption peak. The hydrogen consumption at ca. 550 °C was ascribed in literature for the reduction of very small Co particles strongly interacted with HMS (48). In addition, the TPR profiles show some shoulders between the temperature intervals of 550-700 °C, which have often been ascribed to the reduction of Mo and W species interacting with Co (32) (49) (50) (51). Therefore a strong Co-Mo-W interaction is expected to be developed in a common crystalline structure. Our TPR profiles are very similar to that reported by Herrera et al. (37) for $CoMo/SiO_2$. However, the presence of shoulders in the temperature interval of 550-700 °C could indicate the presence of a small amount of segregated WO_3 species which are generally reduced in this temperature range (49) (50) (51).

In order to get an idea of the degree of interaction of the supported phases with support, total H_2-consumption was determined (**Table 5.2**). As seen in this table, the CoMoW/SBA-15 shows larger H_2 consumption than the CoMoW/SBA-16. Regardless of the support used, P-loading induces an increase of H_2 consumption, in good agreement with literature (52). However, P-loading on the SBA-16 led to a larger increase in H_2 consumption than in case of SBA-15-supported catalysts indicating a larger enhancement of the metal oxides reduction after P-loading on the former material. A similar trend was observed for the sulfidation degree as determined by XPS analysis (*vide infra*).

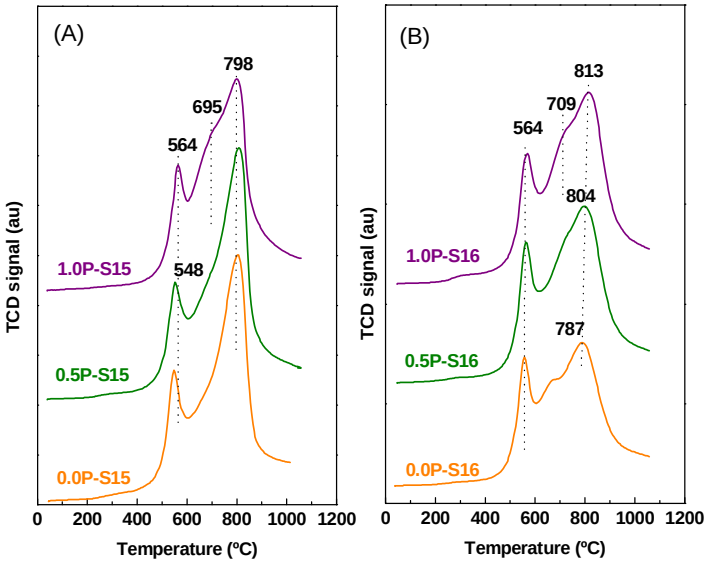

Figure 5.7. TPR profiles of the calcined **(A)** CoMoW/(x)P-SBA-15 and **(B)** CoMoW/(x)P-SBA-16 (x = 0, 0.5 and 1.0% P).

Table 5.2. H_2 uptake (±10%) from TPR[a]

Sample	H_2 uptake (mmol/g cat)			
	I peak	II peak	III peak	Total
0.0P-S15	0.8	3.2	1.7	5.7
0.5P-S15	0.8	3.9	1.3	6.0
1.0P-S15	0.9	1.4	3.4	5.7
0.0P-S16	1.0	0.8	2.8	4.6
0.5P-S16	1.1	0.9	4.0	6.0
1.0P-S16	1.2	1.2	3.9	6.3

[a] As obtained by Gaussian deconvolution of the TPR patterns.

5.3.1.6. Temperature Programmed Desorption of NH_3 (TPD-NH_3)

The acidity of the oxide precursors was assessed by TPD-NH_3 experiments (**Figure 5.8)**. The strength of the acid sites can be determined by the temperature at which the adsorbed NH_3 desorbs. Based on the desorption temperature, the acid sites were classified as weak (100-250 °C) and medium (250-400 °C) strength acid sites. The concentrations of weak and medium strength acid sites (expressed as μmol of desorbed NH_3 per g of catalyst) are listed in **Table 5.3**. For the P-containing catalysts, the presence of P-OH defect sites in the SBA-15 (SBA-16) matrix might contribute to an increase of the population of medium strength acid sites. For temperatures higher than 300 °C, ammonia desorption peaks probably corresponds to the structural acid sites (53) whereas the small peak observed at highest desorption temperature is probably due to the Lewis acid sites.

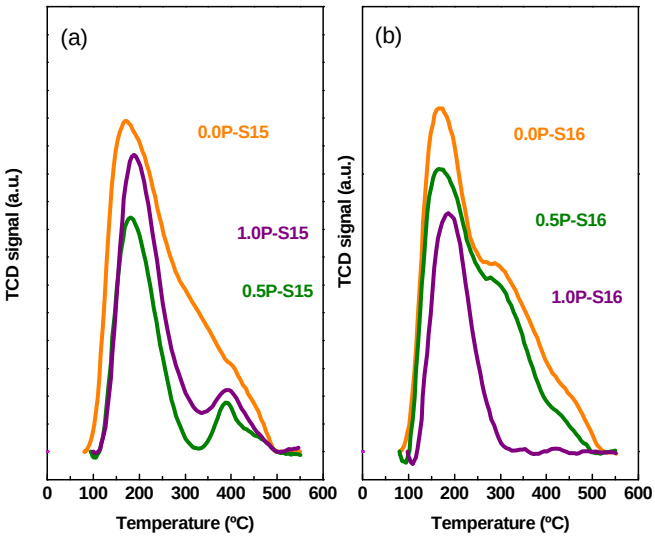

Figure 5.8. TPD-NH_3 patterns of the oxide precursors showing the influence of support (SBA-15 vs. SBA-16) and its modification with P on the catalyst acidity.

From **Table 5.3** we can see that the acidity trend is: 0.5P-S16 > 0.0P-S16 ≈ 1.0P-S16 ≈ 0.0P-S15 > 1.0P-S15 ≈ 0.05P-S15. Thus, one might conclude that the P-free CoMoW/SBA-16 catalyst possesses larger amount of acid sites than its CoMoW/SBA-15 counterpart. On the contrary to SBA-15, phosphate incorporation to SBA-16 substrate leads to an increase of the amount of medium strength acid sites. An increase in acidity after P-loading could be explained considering that the interaction of phosphoric acid at the SBA-16 surface occurs through formation of $P(OH)_2$-O-Si bonds or even free $OP(OH)_3$ entities interacting with the surface via H-bonding (54). For P/γ-alumina materials, it was found that the different alumina hydroxyls react with H_2PO_4 preferentially depending on their basicity up to critical concentration of ca. 1 x 10^{12} H_3PO_4 cm^{-2}. The authors proposed that above this concentration H_3PO_4 reacts not only with Al-OH groups but also with P-OH groups to form polyphosphate species (55).

Tabla 5.3. Acid sites distribution for oxide precursors as obtained by Gaussian deconvolution of the TPD-NH_3 patterns*.

Catalizador	Acid sites concentration (μmol NH_3 g_{cat}^{-1})		
	Weak <250 °C	**Medium 250-400 °C**	**Total**
0.0P-S15	9 (161 °C)	13 (229 °C)	22
0.5P-S15	5 (164 °C)	11 (213 °C)	16
1.0P-S15	7 (176 °C)	11 (222 °C)	18
0.0P-S16	13 (167 °C)	18 (262 °C)	31
0.5P-S16	13 (160 °C)	21 (250 °C)	34
1.0P-S16	10 (172 °C)	11 (230 °C)	21

*Maximun temperature is given in parenthesis

For the SBA-15-supported atalysts, the decrease in total acidity after P loading could be explained by considereing that during co-impregnation there is a higher preference of Mo (W) ions for P-OH groups than cobalt ones (56). Accordingly, the reaction of Mo(W) ions with phosphate anions led to the formation of phosphomolybdic (phosphotungstic) acid and/or phosphomolybdates (phosphotungstates), which are decomposed during calcination and form $Mo(W)O_3$ species adsorbed on basic sites, whereas the phosphate ions are adsorbed on more acidic sites (57).

5.3.2. Characterization of fresh sulfide catalysts

5.3.2.1. Adsorption-desorption isotherms of N_2

The textural properties of sulfided catalysts were evaluated by nitrogen adsorption–desorption isotherms at −196 °C. Their main textural properties are collected in **Table 5.1** *(vide supra).* For all catalysts, the specific surface area (S_{BET}) is in the 187–296 $m^2\ g^{-1}$ range. The 1.0P-S16 and 0.5P-S16 catalysts have the largest and lowest S_{BET}, respectively, among the catalysts studied.

The comparison of the N_2 adsorption-desorption isotherms of pure supports, calcined and fresh sulfided 0.0P-S15 and 0.0P-S16 catalysts are shown in the **Figure 5.9**. The N_2 adsorption–desorption isotherms of all sulfided catalysts are of Type IV, with the SBA-15 having a characteristically larger adsorption–desorption hysteresis loop. All isotherms have clear H1 type hysteresis loops, suggesting that those materials have a very regular mesoporous structure. It is noteworthy that mean pore diameter and pore volume for the SBA-16 are half those of the corresponding SBA-15 materials. As expected from low phosphate

content, the textural properties of the phosphate-containing sulfide catalysts are similar to those of their phosphate-free counterparts.

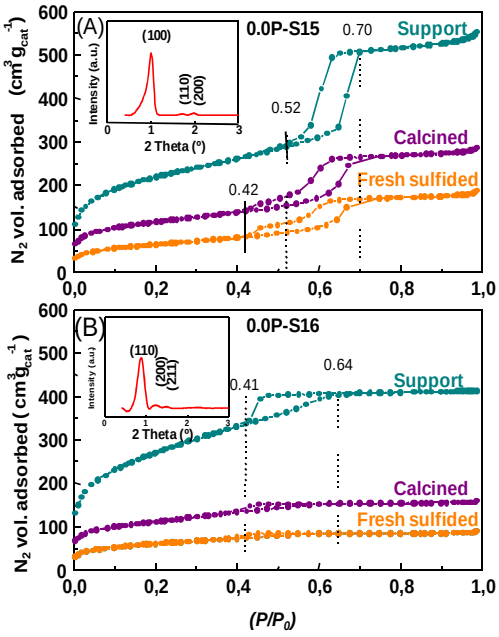

Figure 5.9. Comparison of the N_2 adsorption-desorption isotherms of pure supports, calcined and fresh sulfided 0.0P-S15 **(A)** and 0.0P-S16 **(B)** catalysts.

The values of surface area and pore size volume for these catalysts are reported in **Table 5.1**. In general, it is observed a decrease in the specific surface area and pore size probably due to pore blocking due to the presence of metal sulfide clusters (187-296 m^2 / g). This causes a decrease in surface area more pronounced on SBA-16 serie (2.6-3.3 nm) than SBA-15 serie (5.1-5.5 nm). Furthermore, there was a slight increase in the pore diameter at all catalysts.

The results show some changes in the surface properties of the catalysts, however the introduction of Co, Mo and W does not destroy the structure of the mesoporous supports as seen in the TEM images and X-ray analysis.

5.3.2.2. X-Ray Difraction (XRD)

The high-angle XRD technique was used to investigate the presence of any crystallite species in the sulfided catalysts. **Figure 5.10** shows the profiles of X-ray diffraction of the P-free sulfided catalysts.

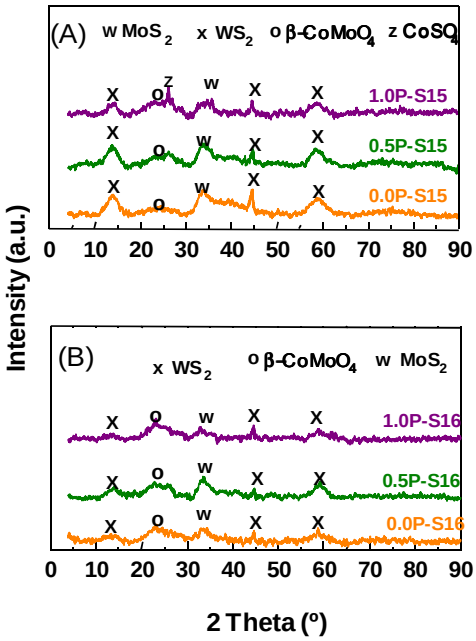

Figure 5.10. Wide-angle XRD patterns of the sulfided **(A)** CoMoW/(x)P-SBA-15 and **(B)** CoMoW/(x)P-SBA-16 (x = 0, 0.5 and 1.0% P)

The X-ray patterns of the catalysts show a broad line between 20° and 30°, which is attributed to the amorphous part of the substrates, and the peaks at 2θ (°) = 13.8, 23.3, 33.3, 44.4 and 58.6. Considering our previous study (58) (59) (31) the peak at 2θ of 23.3° is assigned to β-CoMoO4 crystallites (JCPDS card 21-868). Additionally, the 1.0P-S15 sample shows a peak at 2θ = 25.9° indicative of the formation of the $CoSO_4$ phase (JCPDS card 00-028-0386). The peak at 2θ (°) = 13.8, 44.4 and 58.6 could be assigned to WS_2 (JCPDS card 00-002-0237), whereas the peak at 2θ of 33.3° is probably due to the MoS_2 phase (JCPDS card 01-075-1539). The WS_2 crystal size calculated by the Debye–Scherrer equation for the XRD line at 44.4° follows the trend: 0.5P-S16 ≈ 0.0P-S15 (10.8 nm) < 0.5P-S15 (11.3 nm) < 1.0P-S16 (14.3 nm) < 0.0P-S16 (14.6 nm) < 1.0P-S15 (15.3 nm). Thus, with the exception of 0.5P-S16, the decrease in metal-support interaction due to the presence of phosphate species on the support surface led to the formation of large WS_2 particles. The formation of large metal sulfide species blocking the support pores was also inferred from the N_2 physisorption data (*vide supra*).

5.3.2.3. Diffuse Reflectance Infrared Fourier Transform of NO (DRIFT NO)

The adsorption of NO at room temperature coupled spectroscopy allowed us to evaluate the active centers of the catalysts sulfur. DRIFT spectra corresponding to the absorption of NO at room temperature in fresh sulfided catalysts supported on SBA-15 and SBA-16 are plotted in **Figures 5.11 (A)** and **5.11(B),** respectively.

In good agreement with our previous report (58), the SBA-15-based catalysts have bands around 1892, 1867, 1813 and 1708 cm-1, whereas the positions

of the bands for the SBA-16-based counterparts were: 1902, 1859, 1821 and 1713 cm-1. In our case, we obtain similar values.

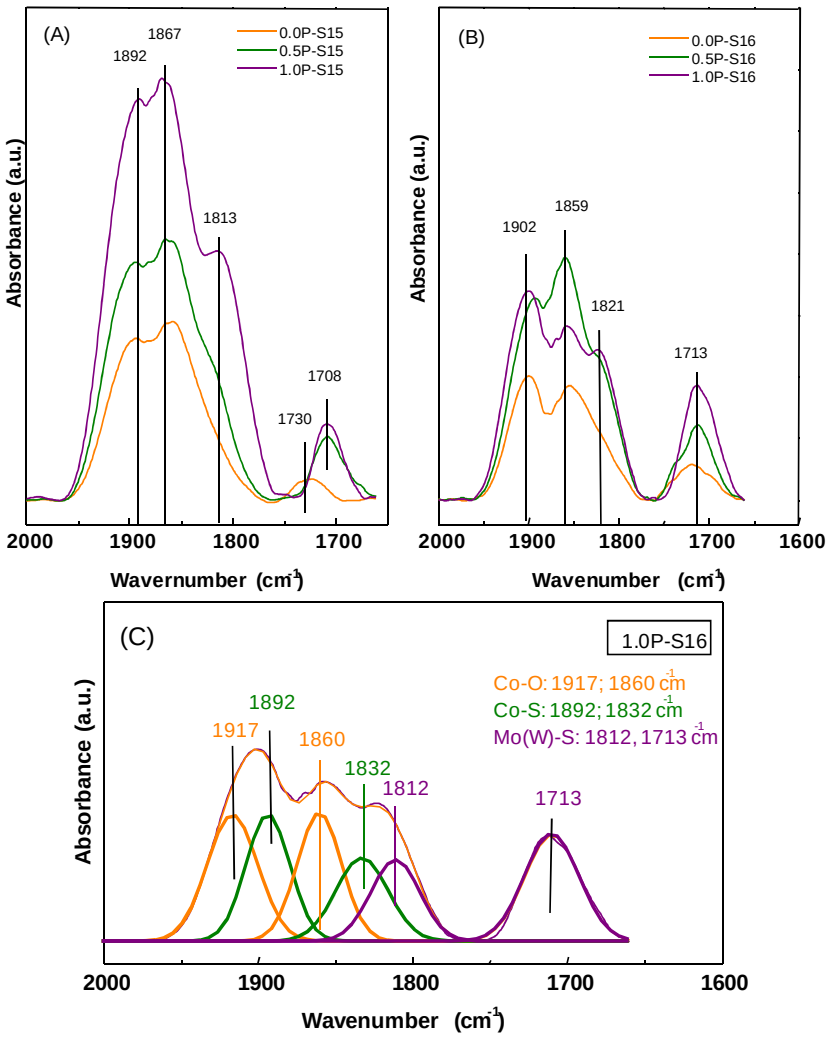

Figure 5.11. IR spectra of adsorbed NO at room temperature on sulfided P-free and P-containing CoMoW/SBA-15 **(A)** and CoMoW/SBA-16 **(B)** catalysts. As an example, shows the Gaussian deconvolution spectrum of the 1.0P-S16 catalyst **(C)**.

In general, as shown in **Figure 5.11**, the intensity of the bands increases with increasing phosphorus content. For catalysts based on SBA-15 (**Figure 5.11. (A)**), the bands are more intense than for their counterparts based on SBA-16 (**Figure 5.11. (B)**). It showed a more intense peak at 1859 cm^{-1} in the catalyst 0.5P-S16 in comparison to the other catalysts of the same series, the most intense peak (1867 cm^{-1}) also appears for all catalysts supported on SBA-15 corresponding to the absorption of NO in Co-O bonds. The bands at 1812 and 1713 cm^{-1} corresponding to the dimers of NO adsorbed phase $Mo(W)S_2$ increases with increasing the amount of phosphorus for the two series of catalysts generally being more intense for the series supported on SBA-16.

The breakdown of those broad bands into Gaussian peaks (**Figure 5.11(C)**) provides three sets of doublets due to the dinitrosyl species on Co^{2+}–O (1917 and 1860 cm^{-1}), Co–S (1892 and 1832 cm^{-1}) and Mo(W)–S (1812 and 1713 cm^{-1}). The bands at 1812 and 1713 cm^{-1} can be assigned to the symmetric and antisymmetric stretching vibrations of NO dimers adsorbed on $Mo(W)S_2$, whereas the doublet bands centered at 1892 and 1832 cm^{-1} can be ascribed to symmetric and antisymmetric stretching vibration modes of NO dimers adsorbed on Co sulfide species, respectively (60) (61) (62). Considering the IR study of NO adsorption on the oxidic form of $CoMo/Al_2O_3$ catalysts (63), the bands at 1917 and 1860 cm^{-1} have a common origin in the symmetric and antisymmetric stretching modes vibration, respectively, of the dinitrosyl species adsorbed on the Co^{2+} ions surrounded by oxide ions. Thus, all catalysts show two types of dinitrosyl species: one adsorbed on Co surrounded by O^{2-} ions and the other one adsorbed on Co^{2+} surrounded by S^{2-} ions. It is commonly accepted that when the "CoMo(W)S" phase is formed, the Co atoms are located at the edge sites of the $Mo(W)S_2$ phases (60) (61) (62).

Thus, for both P-free samples, the lowest intensity of their broad band at ca. 1710 cm-1 (1730 cm-1 for 0.0P-S15) strongly suggests that the edge sites of Mo(W)S2 particles are covered by Co ions constituting "CoMo(W)S" phases. Therefore, regardless of the type of support, both P-free samples have more Co ions constituting "CoMo(W)S" phases than their P-containing counterparts.

5.3.3. Catalytic activity in anisole hydrotreating

The time-on-stream behavior of SBA-15- and SBA-16-based catalysts in the anisole hydroconversion reaction is shown in **Figure 5.13 (A)** and **(B)**, respectively. As seen, all catalysts deactivate during the first 3 h of on-stream operation, with the 0.5P-S16 sample being the most stable among the catalysts studied. The steady-state conversion data are listed in **Table 5.5**. According to this table, the activity of the catalysts follows the trend: 0.5P-S16 > 0.0P-S15(16) ≈ 1.0P-S15 > 0.5P-S15 > 1.0P-S16. Thus, contrary to the SBA-15 substrate, the presence of a small amount of phosphate (0.5 wt%) on the surface of the SBA-16 substrate has a positive effect for the catalytic response of the 0.5P-S16 sample. Both P-free SBA-15(16)-based catalysts have similar activities, indicating that support morphology is not the principal factor influencing the catalytic behavior of those materials.

In a fixed bed high-pressure flow reactor and under operating conditions (T = 310 °C, P = 3 MPa, WHSV = 24.5 h^{-1}), the products identified by GC were phenol, o-cresol, methylanisole, o-xylenol and benzene. A study of the selectivity at an anisole conversion of 38% reveals almost the same selectivity for all catalysts studied (**Table 5.5**). An analysis of selectivity results suggests that two independent reaction paths are operative in anisole transformation over

CoMoW/SBA-15(16) catalysts: demethylation of anisole and methyl transfer to benzene ring. The scheme of reactions involved in the hydrodeoxygenation of anisole under our conditions (310 ° C, P = 3 MPa, t = 4 h, WHSV = 24.5h^{-1}) on the catalysts CoMoW / (x) P) / SBA-15 (16) is shown in **Figure 5.14**.

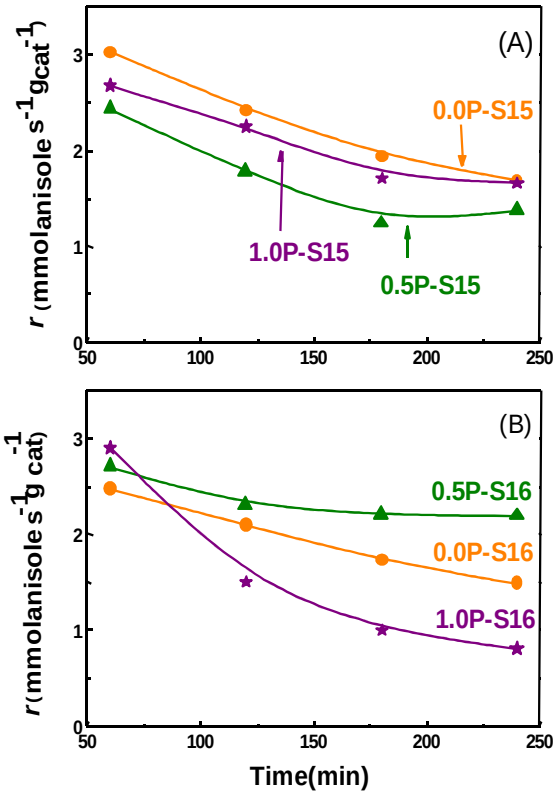

Figure 5.13. Time-on-stream behavior of sulfided **(A)** CoMoW/(x)P-SBA-15 and **(B)** CoMoW/(x)P-SBA-16 (x = 0, 0.5 and 1.0% P) in the hydroconversion of anisole at T = 310 °C, P = 3 MPa and WHSV = 24.5 h^{-1}.

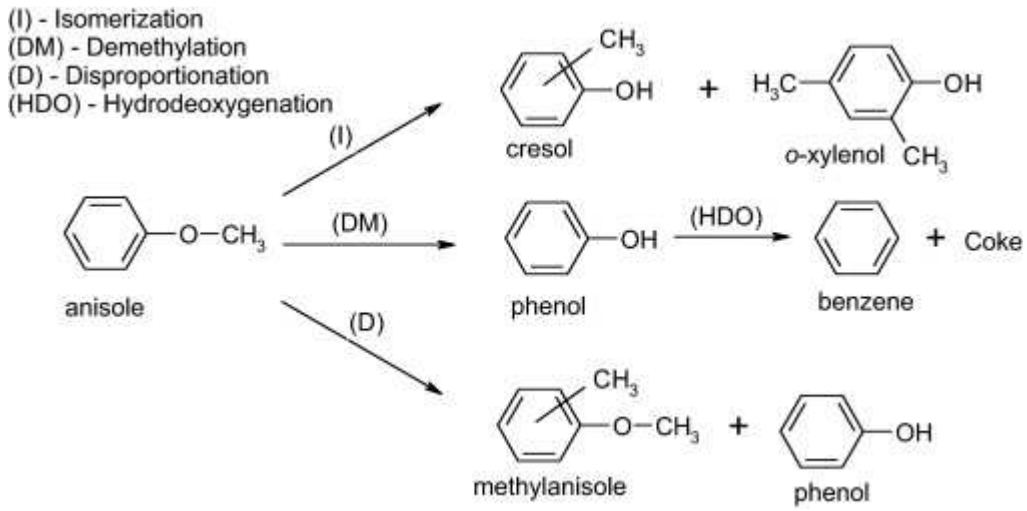

Figura 5.14. The reaction schemes involved in the HDO of anisole under the conditions used (T = 310 ° C, P = 3 MPa, t = 4 h, WHSV = 24.5h^{-1}) on the catalysts CoMoW/(x)P-SBA-15 and CoMoW/(x)P-SBA-16 (x = 0, 0.5 and 1.0% P).

The former reaction route led to the formation of phenol (selectivity in the 60.6–65.9% range), whereas the latter led to the formation of o-cresol and o-xylenol (selectivity in the 22.0–25.9% and 8.4–11.2% ranges, respectively). Thus, anisole transformation over sulfide CoMoW/SBA-15(16) catalysts occurs mainly via the cleavage of the alicyclic carbon and oxygen bond, with phenol being the main reaction product. The direct hydrogenolysis of phenol (HDO selectivity) led to the formation of benzene, although deoxygenation over all catalysts was not significant (selectivity ca. 2%). As expected, the direct splitting of the methoxy group of anisole did not occur because the bond between the alicyclic carbon and oxygen is weaker than the bond between the aromatic carbon and oxygen (15). This is consistent with the literature (15), even though the catalysts and/or reaction conditions were different. For example, the reported selectivity in the gas phase hydrodeoxygenation of anisole when the commercial sulfided Co–Mo catalysts

(Albemarle Co.) were used under mild conditions (T = 300 °C, P = 1.0 MPa) was: 41% phenol, ca. 30% methylphenols isomers, 23% benzene and 5% cyclohexane (15), and the results are fairly consistent with those in this study.

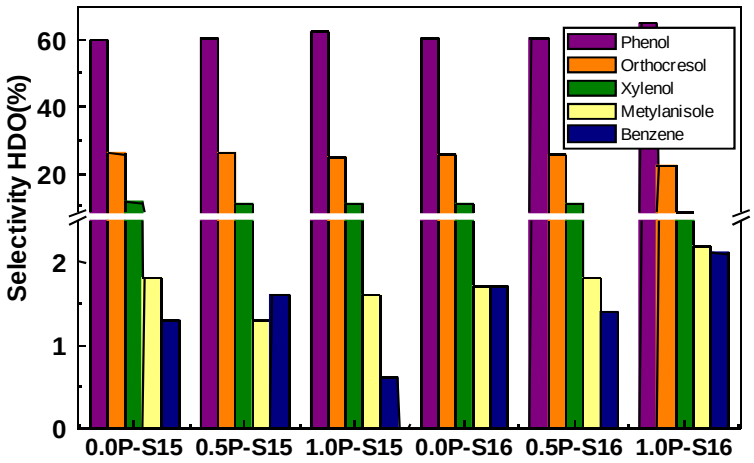

Figure 5.12. Selectivity toward reaction products of anisole HDO (T = 310 °C, P = 3MPa, t = 4 h, WHSV = 24.5h^{-1}) on the **(A)** CoMoW/(x)P-SBA-15 and **(B)** CoMoW/(x)P-SBA-16 (x = 0, 0.5 and 1.0% P) catalysts.

Figure 5.12 shows the reaction products selectivity for the CoMoW / (x)P / SBA-15 (16). The main reaction products were phenol, ortho-cresol and xylenol. Thus, regardless of the medium used and the phosphorus content present all catalysts showed higher selectivity to phenol (60-65%), ortho-cresol (22-26%) and xylenol (8-11%), the first one via demethylation and the other two via isomerization (**Figure 5.11**). The other minor products were methylanisole (1-2%) by disproportionation and benzene (1-2%) which resulted from phenol

hydrodeoxygenation (**Figure 5.11**). For all catalysts, the selectivities are similar and independent of the reaction time which indicates that both the morphology of the support and the presence of phosphate at the surface of the catalysts does not influence the selectivity. The catalysts supported on SBA-16 showed better performance (not significant) to benzene than their counterparts supported on SBA-15 (**Table 5.5** and **Figure 5.12**).

Table 5.5. Activity, selectivity in the hydrotreating of anisole (T = 310 ° C, P = 3 MPa, t = 4 h) over sulfided catalysts.

Catalyst	Conversion (%)	Yield (%)				
		Phenol	Orthocresol	Xylenol	Metylanisole	Benzene
0.0P-S15	36.4	21.81	9.40	4.08	0.67	0.47
0.5P-S15	25.3	15.25	6.56	2.76	0.34	0.39
1.0P-S15	33.2	20.68	8.24	3.55	0.53	0.20
0.0P-S16	31.2	18.81	7.94	3.37	0.51	0.53
0.5P-S16	37.8	22.96	9.57	4.08	0.66	0.52
1.0P-S16	24.3	15.74	5.41	2.05	0.54	0.51

Concerning catalyst stability during on-stream conditions, a common practice for maintaining the catalyst activity in HDO on sulfided catalysts involves the addition of a sulfiding agent (H_2S or CS_2). However, this practice does not avoid the deactivation of the sulfided Co–Mo/γ-Al_2O_3 catalysts (15) (64). In this study, the sulfiding agent was not added to the feed mixture because our objective was to study the effect of acidity on the catalyst performance, which could be masked by H_2S addition because–SH groups formed on the support surface could be involved in the HDO reaction (20). Moreover, the competitive adsorption of the S-containing compound and anisole on the same active sites (sulfur adsorbs on CUS sites and affects the reactions occurring on these sites) is expected to be

avoided without masking the catalyst sensitivity toward deactivation by water (H_2S might to compensate the inhibition by water produced during HDO reaction (65)).

The 0.5P-S16 catalyst was the most active of all the catalysts studied, showing an increasement in activity with respect to its phosphorus unmodified counterpart. This catalyst has the optimum amount of P on its surface (0.5 wt%) because increasing the amount of P added 0.5 to 1.0 wt% resulted in a sudden decrease in activity compared to the unmodified catalyst (**Table 5.5**). For all the catalysts supported on SBA-15 the addition of a small amount of phosphorus do not provide an improvement in the conversion of anisole or the products selectivity without oxygen.

Concerning the possible lost of active sites due to transformation of the metal sulfides into metals, the XPS measurements of the spent catalysts did not reveal formation of metal phases upon reaction conditions employed (*vide supra*).

5.3.4. Characterization of spent catalysts

5.3.4.1. High Resolution Transmission Electron Microscopy (HRTEM)

The aim of HRTEM measurements was also to compare the morphology of the sulfided phases on the SBA-15 and SBA-16-based spent catalysts. As expected, all spent catalysts present the typical fringes of $Mo(W)S_2$ crystallites. The arrangement of $Mo(W)S_2$ layers parallel to the substrate indicates the basal plane attachment. The fact that the particles consist of pure $Mo(W)S_2$ was confirmed by EDX and by considering the interlayer lattice distance. The slab length, stacking number of $Mo(W)S_2$ particles and their surface density are compiled in **Table 5.6**.

As seen in this table, all catalysts record a similar length of $Mo(W)S_2$ particles and the same number of their stacking layers (3 ± 1 layers). In general, the SBA-16-based systems have higher $W(Mo)S_2$ slab density than their SBA-15 counterparts, with the 0.5P-S16 sample having the largest population of $Mo(W)S_2$ crystallites among the catalysts studied. The destruction of the support morphology by produced water did not occur, as it was confirmed by HRTEM of spent catalysts (**Figure 5.13**).

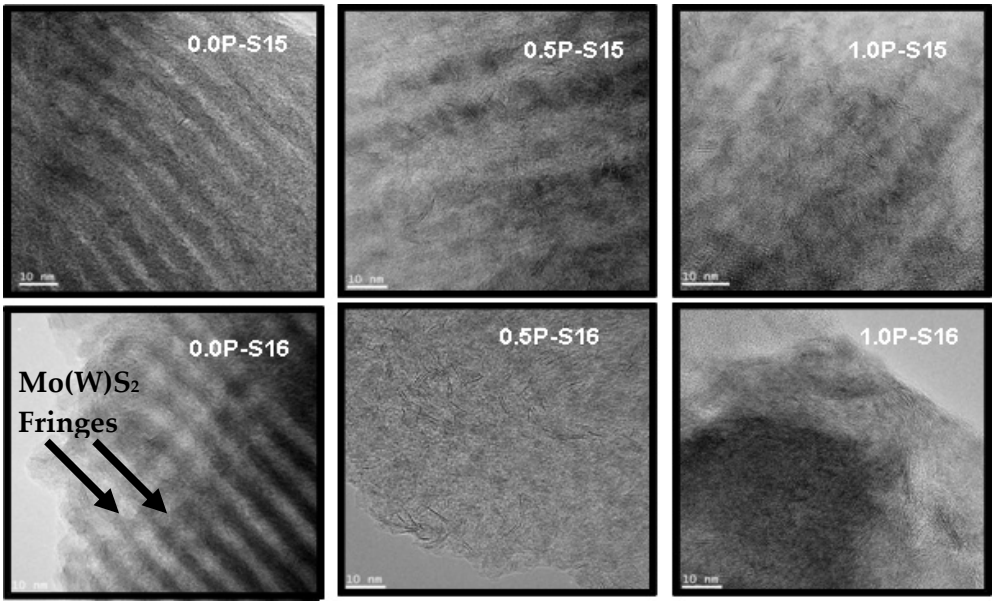

Figure 5.13. HRTEM images of spent CoMoW/(x)P-SBA-15 and CoMoW/(x)P-SBA-16 (x = 0, 0.5 and 1.0% P) catalysts.

Concerning the support morphology, HRTEM images confirmed the regular porous arrangement of the SBA-15- and SBA-16-supported catalysts (**Figure 5.13**). For all catalysts, EDX microanalysis performed over several areas on the HRTEM micrographs of the sulfided catalysts show a non-uniform distribution

of Co, Mo and W on the surface (**Table 5.6**). In general, P-containing catalysts showed larger W content than the respective P-free samples.

It is known that both MoS_2 and WS_2 phases adopt a layered structure with a Mo(W) atoms situated in trigonal prismatic coordination sphere. As expected, all catalysts display the typical fringes of MoS_2 (WS_2) crystallites. The location of MoS_2 (WS_2) fringes on the channel's walls of SBA-15 substrate is shown in **Figure 5.13**.

Table 5.6. Chemical composition and HRTEM parameters of the spent CoMoW/(x)P-SBA-15 and CoMoW/(x)P-SBA-16 (x = 0, 0.5 and 1.0% P) catalysts

Catalyst	Co (%wt)	Mo (%wt)	W (%wt)	P (%wt)	Average length (nm)	Stacking number	Surface density (Mo(W)S_2/ 100000 nm^2)
0.0P-S15	2.1	3.7	5.2	0.0	5.1 ± 1.0	3±1	111 ± 23
0.5P-S15	1.4	5.4	8.4	0.8	4.9 ± 0.9	3±1	97 ± 18
1.0P-S15	2.6	6.1	11.2	1.3	4.6 ± 1.0	3±1	97 ± 11
0.0P-S16	2.4	2.5	4.2	0.0	4.7 ± 1.1	3±1	91 ± 27
0.5P- S16	2.4	4.0	4.5	0.7	5.2 ± 1.0	3±1	185 ± 87
1.0P-S16	2.2	5.7	9.1	0.9	5.5 ± 1.6	3±1	111 ± 57

In **Figure 5.13** are compared high magnification Mo(W)S_2 sheets observed on catalysts. For all catalysts, the arrangement of W(Mo)S_2 layers parallel to the substrate indicates the basal plane attachment. No edge-plane attachment was observed because such species easily escape detection. In general, the SBA-16-based systems show higher W(Mo)S_2 slabs density than on their SBA-15 counterparts (**Table 5.6**). It is noteworthy that the SBA-15-based catalysts show the W(Mo)S_2 layers parallel to the surface and attached to the walls of channels

whereas their SBA-16-based counterparts show disordered curved fringes of the W(Mo)S_2.

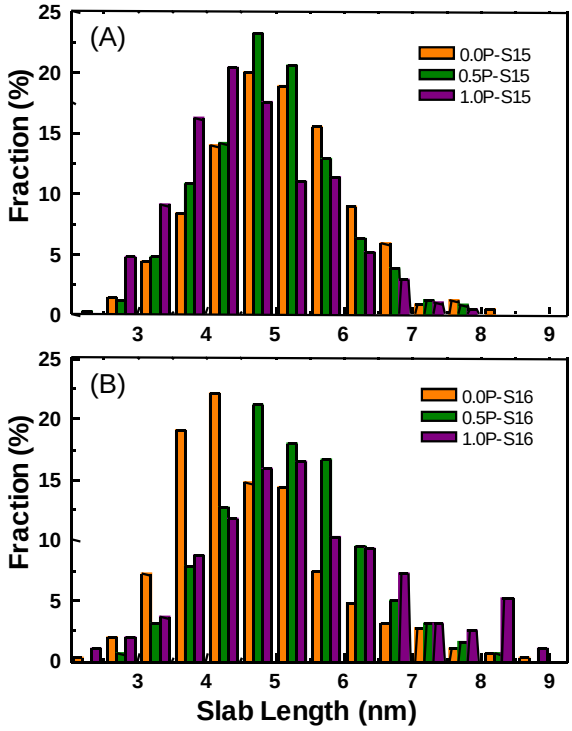

Figure 5.14. Influence of support and its modification with phosphate on the distribution of slab length of Mo(W)S_2 particles as observed by HRTEM in **(A)** CoMoW/(x)P-SBA-15 and **(B)** CoMoW/(x)P-SBA-16 (x = 0, 0.5 and 1.0% P) catalysts.

More information on the morphology of phases formed can be revealed by statistical evaluation of about 250 particles from 12 HR-TEM images. The distribution of slab length and stacking number of Mo(W)S_2 particles are shown in **Figure 14(A)** and **(B)**, respectively, whereas **Table 5.6** summarizes the average

length and stacking number of the $Mo(W)S_2$ particles. TEM data are evaluated as follows: (i), a little larger $Mo(W)S_2$ particles are formed on 0.0P-S16 than on 0.0P-S15 (5.1 vs. 4.7 nm); (ii) 0.5P-S16 spent catalyst showed a density of active centers doubly than other catalysts; (iii), the morphology of support and their modification with P did not influence on the number of stacking layers showing all catalysts a highly stacked layers of $Mo(W)S_2$ particles (4 ± 1 layers). Finally, for both P-free samples, the inter-layer spacing was similar and a little larger than those of the pure $Mo(W)S_2$ phase (0.65 vs. 0.62 nm).

5.3.4.2. X- Ray Photoelectron Spectroscopy (XPS)

In order to investigate the nature of the surface species of Co, Mo and W and the sulphidation degree on sulfided catalysts at 450 °C, were recorded photoelectron spectra (XPS) core level of Si 2p, W 4f, Mo 3d, Co 2p, S 2p and P 2p of the catalysts used in reaction. **Table 5.7** compiles the binding energy (BE) values corresponding to the W $4f_{7/2}$, Mo $3d_{5/2}$ and Co $2p_{3/2}$ core-levels. As seen in this table, all catalysts record similar BE values, suggesting that the coordination environment for the active sites is similar.

Spent catalysts were also studied by X-ray photoelectron spectroscopy. The Si 2p core level peak was close to 103.3 eV for all catalysts, which is characteristic of SiO_2 (66). The chemical environment of silicon ions was not affected by the presence of other components. As expected, all samples recorded a binding energy of 162.0 eV, which is characteristic of S^{2-} species (54). The binding energy of the P 2p core-level of the P-containing samples ca. 134.0 eV is indicative of phosphate species (67). This BE value is much lower than that corresponding to P_2O_5 (135.2 eV), indicating that the phosphorus species remain highly dispersed on the support surface.

Table 5.7. Binding energies (eV) of the spent catalysts (XPS) tested in the hydroconversion of anisole. C 1s peak at a BE of 284.8 eV was taken as internal reference.

Catalyst	Co $2p_{3/2}$	Mo $3d_{5/2}$	W $4f_{7/2}$	S 2p	P 2p	$\frac{W\ S(32eV)}{W\ O(33.7eV)}$ ratio
0.0P-S15	778.3	229.0	32.1 (68) 33.6 (32)	162.0	-	2.1
0.5P-S15	778.3	229.0	32.1 (74) 33.6 (26)	161.9	134.1	2.8
1.0P-S15	778.3	229.0	32.1 (71) 33.6 (29)	162.0	134.2	2.4
0.0P-S16	778.3	229.0	32.1 (75) 33.6 (25)	162.9	-	3.0
0.5P-S16	778.2	229.0	32.2 (85) 33.8 (15)	161.8	134.0	5.7
1.0P-S16	778.2	229.0	32.2 (80) 33.8 (20)	161.9	134.0	4.0

The Co $2p_{3/2}$ peak at a binding energy ca. 778.3 eV indicates the formation of a segregated Co_9S_8 phase (BE at 778.4 eV) (68). Indeed, the difference in binding energies between the Co $2p_{3/2}$ peak and the S 2p peak is 616.4 eV, which is close to the range of 615.7–616.2 eV reported by Alstrup et al. (68) for the Co_9S_8 phase. On the other hand, the Mo $3d_{5/2}$ binding energy at 229.0 eV is characteristic of Mo^{4+} ions in MoS_2 and an S $2p_{3/2}$ binding energy of 161.9 eV is consistent with the S^{2-} type ligands present in this phase (69). Contrary to the molybdenum species, the W 4f core level spectra of all spent catalysts has two doublets, each one with the $4f_{7/2}$ and $4f_{5/2}$ components from the spin-orbit splittin. The presence of two doublets indicates there are two different W-species. Thus, the W $4f_{7/2}$ core level spectra shows peaks associated with sulfided tungsten species (BE at 32.2 ± 0.1 eV) and oxysulfide W species (BE at 33.7 ± 0.1 eV), which both have a terminal oxygen and a terminal sulfur (70). It is noteworthy that, in the absence of sulfiding agent in the feed, the partial

reduction of metal sulfides upon high hydrogen pressure did not occur. The XPS technique could not detect the W^{3+} species because the W^{3+} ions did not produce a signal that could overcome the more intense WS_2 signal (71). Considering the percentage of sulfided W species (given in parentheses in **Table 5.8**), it appears that the sulfidation degree of the W species in all catalysts was relatively high (68–85%). In addition to the more difficult sulfidation of the W oxide species compared to the Mo oxide, due to differences in the polarization of the metal–oxygen bond (72), the percentage of W sulfide species in the 0.5P-S16 sample was significantly larger than that found for the other catalysts.

The distribution of supported Co, Mo and W species was estimated by comparing Co/Si, W/Si and Mo/Si atomic intensity ratios (**Table 5.8**). In general, it was found that the SBA-16-based catalysts showed larger Co, Mo and W surface exposure than their SBA-15-based counterparts. In particular, one might to note that the SBA-16-supported catalysts show two-times larger cobalt species surface exposure than the SBA-15-supported ones. Since all catalysts were prepared by the same method and employing similar conditions, one might to suppose that the lower cobalt species surface exposure could be due to their main location within inner porous structure of SBA-15. In order to confirm this, the bulk atomic ratios were calculated considering EDX data of chemical analysis (**Table 5.8**). The comparison of bulk and surface atomic ratios strongly suggested that: (i) Regardless of support morphology, the cobalt sulfide species are mainly located on the external catalyst surface, (ii) Contrary to the Co species, the Mo and W species are mainly located within the inner support structure; (iii) The P incorporation onto both SBA-15 and SBA-16 materials did not have a clear effect on the surface exposure of metal sulfide species.

Table 5.8. XPS data of the spent catalysts tested in the hydroconversion of anisole. C 1s peak at a BE of 284.8 eV was taken as internal reference.

Catalyst	Co/Si at	Mo/Si at	W/Si at	S/(Co+Mo+W) at	P/Si at
0.0P-S15	0.052 (0.018)[a]	0.013 (0.052)[a]	0.010 (0.141)[a]	1.66	-
0.5P-S15	0.042 (0.013)[a]	0.014 (0.081)[a]	0.008 (0.241)[a]	1.79	0.004 (0.004)[a]
1.0P-S15	0.049 (0.026)[a]	0.009 (0.098)[a]	0.007 (0.343)[a]	1.70	0.013 (0.007)[a]
0.0P-S16	0.101 (0.020)[a]	0.034 (0.035)[a]	0.015 (0.112)[a]	1.73	-
0.5P-S16	0.093 (0.021)[a]	0.033 (0.057)[a]	0.021 (0.123)[a]	1.79	0.004 (0.003)[a]
1.0P-S16	0.110 (0.021)[a]	0.047 (0.088)[a]	0.033 (0.267)[a]	1.75	0.009 (0.005)[a]

[a] The atomic ratios nominal by EDX .

5.3.4.3. Coke quantification (TPO/TGA-DTG)

The influence of the support morphology (SBA-15 vs. SBA-16) as well as the effect of support modification by phosphate on the coking behavior of sulfided CoMoW catalysts in HDO reaction was evaluated from the weight change of the coked catalysts during temperature-programmed oxidation by means of TG-DTG technique. **Figure 5.15** presents the TPO/TG-DTG plots of the spent SBA-15- and SBA-16-based catalysts, respectively, after 4 h of reaction time.

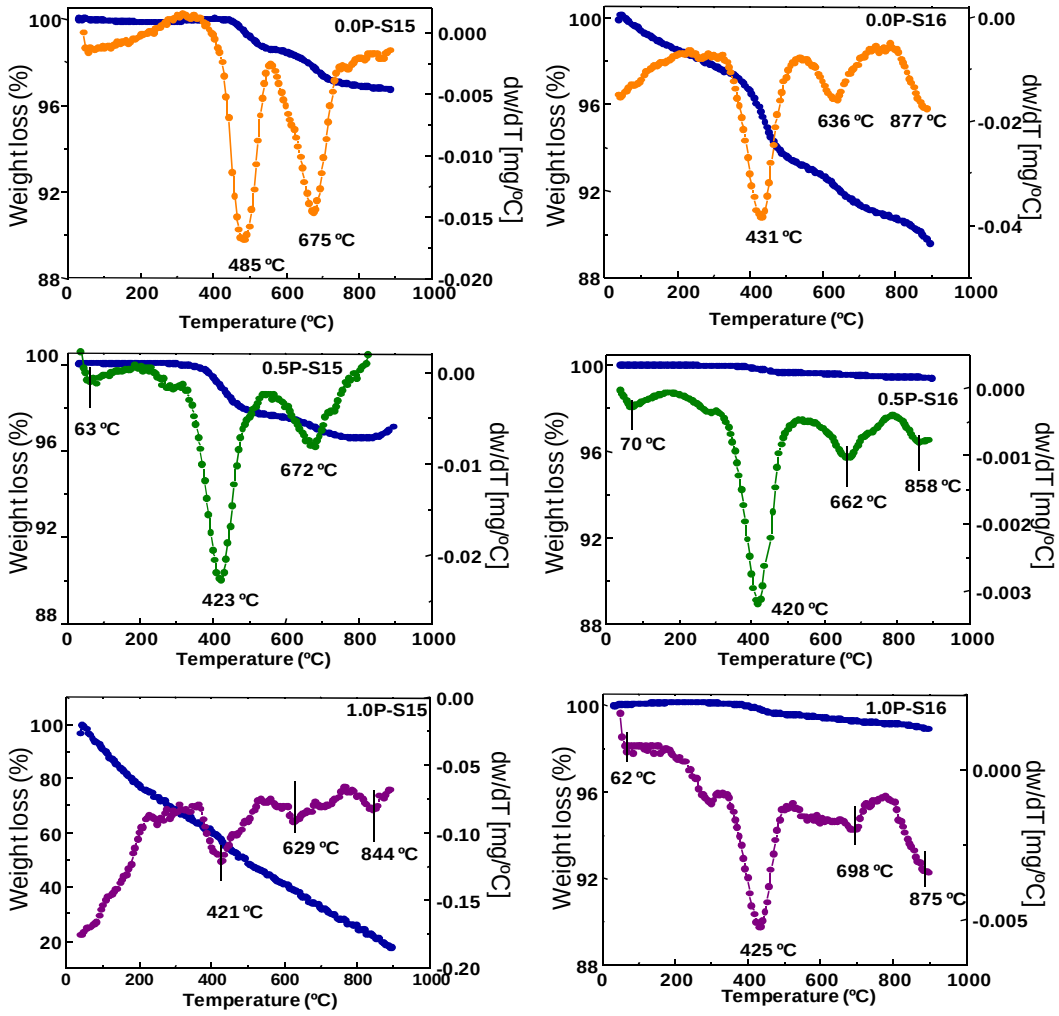

Figure 5.15. TPO/TG profiles of the spent CoMoW/(x)P-SBA-15 and CoMoW/(x)P-SBA-16 (x = 0, 0.5 and 1.0% P) catalysts.

Before the TPO analysis, the spent catalysts were pretreated at 500 °C for 1 h under flowing nitrogen to remove adsorbed reaction-mixture components. However, a period of 1 h was not enough taking into account the small weight loss in

temperature range 30–300 °C attributed to desorption of reactant/products adsorbed in the catalyst pores (73). As expected, all catalysts recorded a weight loss at ca. 400 °C ascribed to the loss of sulfur atoms from the oxysulfide species and a second weight loss corresponding to the DTG peak centered at ca. 600 °C, which was due to coke oxidation (74). The amounts of coke, SO_2 formed (as determined by catalyst weight loss at about 400 and 600 °C, respectively) and the percentage of catalyst deactivation calculated from **Equation 5.2** is listed in **Table 5.9**.

$$\frac{(X_{1h}-X_{4h})\times 100\%}{X_{1h}} \qquad \textbf{(Equation 5.1)}$$

As seen in this table, the most active 0.5P-S16 catalyst recorded the lowest deactivation among the catalysts studied. Since the HDO reaction paths depend heavily on the state of the catalyst surface during on-stream reaction (75), the catalyst's coking behavior was evaluated from the weight change of the coked catalysts during temperature-programmed oxidation (TPO), followed by the TG-DTG technique (**Figure 5.15**).

As seen in this table, the most active 0.5P-S16 shows the lowest deactivation during on-stream reaction (18.9%) linked with absence of coke formation (0.2%) and the largest stability of metal sulfide phases. On the contrary, the 1.0P-S15 sample showed the lowest stability of their metal sulfide phases and the largest deactivation due to coke formation (**Table 5.9**). With exception of this sample, coke reactions in all catalysts were negligible (0.2–1.9%), suggesting that neither the catalyst morphology nor the presence of a small amount of phosphate on the support surface influenced coke formation. This might explain the similar selectivities recorded in the HDO of anisole over all catalysts.

Table 5.9. Desactivación de los catalizadores CoMoW/(x)P-SBA-15(16) usados en el hidrotratamiento de anisol (T=310 °C, P= 3.0 MPa, WHSV= 24.5 h^{-1})

Catalyst	Deactivacion (%)[a]	Coke (%)[b]	SO_2 (%)[b]
0.0P-S15	44.4	1.9	1.3
0.5P-S15	43.2	1.2	2.2
1.0P-S15	38.2	28.0	17.1
0.0P-S16	39.7	2.2	4.4
0.5P-S16	18.9	0.2	0.3
1.0P-S16	72.4	0.7	0.4

5.3.5. Catalyst activity-structure correlation

Considering the similar or even larger average length of Mo(W)S_2 phase (from HRTEM) with respect to catalyst pore diameter (**Table 5.1**), it is clear that active phases in all catalysts studied are located on the support surface. Such location is even more evident in the case of SBA-16-based catalysts. The results demonstrate the catalytic activity of the support SBA-15 is less effective than the SBA-16. This can be explained taking into account the specific morphology of each. In general, the systems supported on SBA-16 showed a higher density of active phases than their counterparts supported on SBA-15.

From the catalyst activity–structure correlation, the best catalytic response of the sulfided 0.5P-S16 sample in the hydroconversion of anisole could be explained by considering a combination of various effects. The first is the largest surface exposure of the active phases, as determined by HRTEM, presenting active phases homogeneously dispersed on both internal and external catalyst surfaces.

Moreover, the 0.5-PS16 catalyst records the largest total acidity among the catalysts studied (**Table 5.4**). Thus, the major activity of this sample could be explained by considering that the cleavage of the methyl carbon–oxygen bond might take place on both metal sulfides and on acidic sites of the support, as proposed by Huuska et al. (12) (13). In such a case, one might assume that a homolytic splitting of the methyl carbon–oxygen bond might occur on the metal sulfides followed by a rapid hydrogenation of the radicals formed, whereas a dominating reaction of heterolytic scission might occur on the acidic sites of the support. If so, the methyl carbonium ion formed would attack the aromatic ring. Since those ions possess a non-planar adsorption state, the attack occurs preferentially in the ortho position (12). This mechanism would justify the best catalytic behavior of the 0.5P-S16 sample in the target reaction.

The factor which could contribute to catalyst deactivation is the partial reduction of metal sulfides under high hydrogen pressure. However, the XPS measurements of spent catalysts preclude this possibility. Since water is always present in the reactor during HDO reaction, it is more likely that adsorption of H_2O molecules on the active sites contributes to catalyst deactivation (65). The largest stability of the 0.5P-S16 sample during on-stream reaction indicated that modification of SBA-16 material with small amount of phosphate (0.5 wt%) prevent catalyst deactivation by water and coke, the latter confirmed by TPO-TGA measurement. Thus, in the worst scenario of absence of sulfiding agent, the most active 0.5P-S16 catalyst showed a good stability during on-stream HDO reaction indicating that the catalyst deactivation (**Figure 5.16 (A)**) by coke and water can be diminished by appropriate modification of the surface chemistry of the SBA-16 support with optimized amount of phosphate. Our previous study described in **Chapter 4** on the upgrading of olive oil production-derived by-products via

hydrotreating on sulfided CoMo/SBA-15(16) mesoporous silica demonstrated that those catalysts were more active than a commercial $NiMo/Al_2O_3$ catalyst. Interestingly, considering the formation of desirable products (paraffins and alcohols) and the removal of oxygen-containing products and polyaromatics, the SBA-16-based catalyst was found to be more appropriate for upgrading of bio-liquid than its SBA-15 counterpart. Contrary to the binary CoMo/SBA-15(16) systems studied previously (**Chapter 4**), the ternary CoMoW/SBA-15(16) catalysts tested in the HDO of model feed exhibited a low selectivity toward O-free products indicating that their hydrogenolysis capability needs to be improved for the HDO of pyrolysis oils.

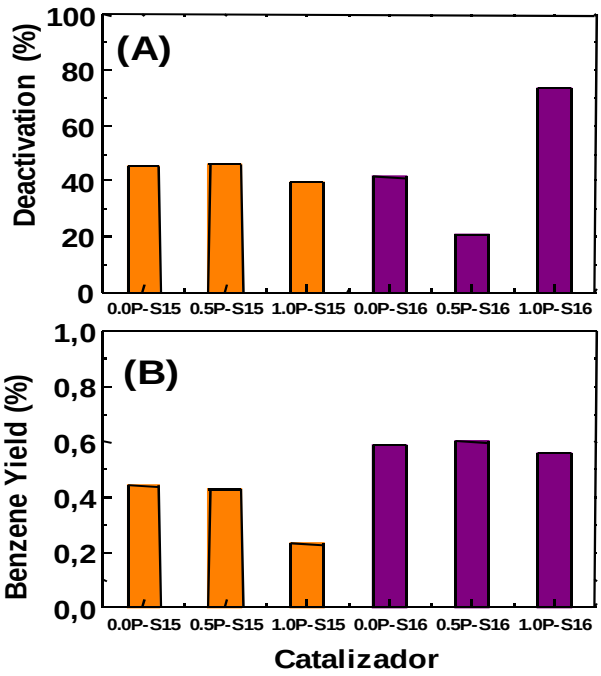

Figure 5.16. Catalysts deactivation after time on stream 4h **(A)** and benzene yield **(B)** (T=310 °C, P=3 MPa, t=4 h, *WHSV*=24.5h^{-1})

Finally, it was found that all catalysts exhibited a low selectivity toward benzene formation (**Figure 5.16(B)**) suggesting the absence of the metallic-like so-called brim sites, which were recently shown to be involved in hydrogenation reactions (17) (18) (76). On the other hand, a large selectivity toward isomerization products confirms the hypothesis that the HDO reaction requires two types of active sites: one for the activation of dihydrogen, with the other being a metal oxide with a variable oxidation state (support) for the activation of oxy-groups (18).

5.4. Conclusions

The main conclusions of this chapter are:

(i) In contrast to the catalyst 0.0P-S15, the steady-state activity of the catalyst supported on SBA-16 increased by 47% after modification with the optimized amount of phosphorus (0.5 wt%), indicating the effect of the incorporation of phosphorus depends on the morphology of the support.

(ii) Supported catalysts SBA -16 show a higher benzene yield and greater dispersion of the phases of their counterparts metal sulfide supported on SBA- 15. However, the product yield was too low to be considered for possible use in removing oxygen from biomass.

(iii) The improvement of the catalyst activity 0.5P-S16 in the reaction is related to the surface enrichment of the active phase, the higher total acidity and higher stability during the reaction time.

(iv) The activity of the catalysts is strongly influenced by the acidity of the support and to a lesser extent by the degree of sulfidation of cobalt species on the surface. We found a correlation between the number of strong acid sites and the catalytic activity, which points to the involvement of these centers in the reaction mechanism.

(v) The reaction mechanism for the transformation of anisole CoMoW sulphide catalysts supported on SBA -15 (16) is bifunctional, being greater involvement of acidic centers metal centers, as deduced from the participation and isomerization no hydrogenation of the aromatic ring.

5.5. References

1. *An overview of fast pyrolysis of biomass.* **A.V. Bridgwater, D. Meier, D. Radlein.** s.l. : Organic Geochemistry, 1999, Vols. (30) 1479-1493.

2. *Historical developments in hydroprocessing bio-oils .* **Elliott, D.C.** s.l. : Energy Fuels, 2007, Vols. (12) 1792-1815.

3. *Catalytic hydrodeoxygenation.* **Furimsky, E.** s.l. : Applied Catalysis A: General, 2000, Vols. (199) 147-190.

4. **E.G. Baker, D.C. Elliott.** *Method of upgrading oils containing hydroxyaromatic hydrocarbon compounds to highly aromatic gasoline. 5180868* U.S., 19 January 1993.

5. **E. Laurent, A. Centeno, B. Delmon.** Coke formation during the hydrotreating of biomass pyrolysis oils: Influence of guaiacol type compounds. [aut. libro] G.F. Froment B. Delmon. *Studies in Surface Science and Catalysis.* s.l. : Elsevier (88) 573-657, 1994.

6. *Upgrading of bio-liquids on different mesoporous silica-supported CoMo catalysts.* **R. Nava, B. Pawelec, P. Castaño, M.C. Alvarez-Galvan, C.V. Loricera, J.L.G. Fierro.** s.l. : Applied Catalysis B: Environmental, 2009, Vols. (92) 154-167.

7. *Influence of the support of CoMo sulfide catalysts and of the addition of potassium and platinum on the catalytic performances for the hydrodeoxygenation of carbonyl, carboxyl, and guaiacol-type molecules.* **A. Centeno, E. Laurent, B. Delmon.** s.l.: Journal of Catalysis, 1995, Vols. (154) 288-298.

8. *CoMo/carbon hydrodeoxygenation catalysts: influence of the hydrogen sulfide partial pressure and of the sulfidation temperature.* **M. Ferrari, S. Bosmans, R. Maggi, B. Delmon, P. Grange.** s.l. : Catalysis Today, 2001, Vols. (65) 257-264.

9. *Influence of the impregnation order of molybdenum and cobalt in carbon-supported catalysts for hydrodeoxygenation reactions.* **M. Ferrari, B. Delmon, P. Grange.** s.l. : Carbon, 2002, Vols. (40) 497-511.

10. *Synergy effect in the HDO of phenol over Ni–W catalysts supported on active carbon: Effect of tungsten precursors.* **S. Echeandia, P.L. Arias, V.L. Barrio, B. Pawelec, J.L.G. Fierro.** s.l. : Applied Catalysis B: Environmental, 2010, Vols. (101) 1-12.

11. *Hydrogenolysis and hydrocracking of the carbon-oxygen bond: I. Hydrocracking of some simple aromatic O-compounds.* **J. B-son Bredenberg, M. Huuska, J. Raty, M. Korpio.** s.l. : Journal of Catalysis, 1982, Vols. (77) 242-247.

12. *Effect of catalyst acidity on the hydrogenolysis of anisole .* **M. Huuska, J. RIntala.** s.l. : Journal of Catalysis, 1985, Vols. (94) 230-238.

13. *Effect of catalyst composition on the hydrogenolysis of anisole .* **Huuska, M.K.** s.l. : Polyhedron, 1986, Vols. (5) 233-236.

14. *Simultaneous hydrodesulfurization and hydrodeoxygenation: interactions between mercapto and methoxy groups present in the same or in separate molecules.* **T.-R. Viljava, E.R.M. Saari, A.O.I. Krause.** s.l. : Applied Catalysis A: General, 2001, Vols. (209) 33-43.

15. *Development of new catalytic systems for upgraded bio-fuels production from bio-crude-oil and biodiesel.* **V.A. Yakovlev, S.A. Khromova, O.V. Sherstyuk, V.O. Dundich, D.Yu. Ermakov, V.M. Novopashina, M.Yu. Lebedev, O. Bulavchenko, V.N. Parmon.** s.l. : Catalysis Today, 2009, Vols. (144) 362-366.

16. *Removal of PAH compounds from liquid fuels by Pd catalysts .* **B. Pawelec, J.M. Campos-Martin, E. Cano-Serrano, R.M. Navarro, S. Thomas, J.L.G. Fierro.** s.l. : Environmental Science & Technology, 2005, Vols. (39) 3374-3381.

17. *The role of reaction pathways and support interactions in the development of high activity hydrotreating catalysts .* **H. Topsøe, B. Hinnemann, J.K. Nørskov, J.V. Lauritsen, F. Besenbacher, P.L. Hansen, G. Hytoft, R.G. Egeberg, K.G. Knudsen.** s.l. : Catalysis Today, 2005, Vols. (107-108) 12-22.

18. *A Density Functional Study of the Chemical Differences between Type I and Type II MoS2-Based Structures in Hydrotreating Catalysts.* **B. Hinnemann, J.K. Nørskov, H. Topsøe.** s.l. : The Journal of Physical Chemistry B, 2005, Vols. (109) 2245-2253.

19. *A density functional study of inhibition of the HDS hydrogenation pathway by pyridine, benzene, and H2S on MoS2-based catalysts.* **A. Logadottir, P.G. Moses, B. Hinnemann, N.-Y. Topsøe, K.G. Knudsen, H. Topsøe, J.K. Nørskov.** s.l. : Catalysis Today, 2006, Vols. (11) 44-51.

20. *Hydrodeoxygenation of benzofuran over sulfided and reduced Ni–Mo/γ-Al2O3 catalysts: Effect of H2S.* **A.Y. Bunch, X. Wang, U.S. Ozkan.** s.l. : Journal of Molecular Catalysis, 2007, Vols. (270) 264-272.

21. *Investigation of the reaction network of benzofuran hydrodeoxygenation over sulfided and reduced Ni–Mo/Al2O3 catalysts .* **A.Y. Bunch, X. Wang, U.S. Ozkan.** s.l. : Journal of Catalysis, 2002, Vols. (206) 177-187.

22. *Perspectives in catalytic applications of mesostructured materials.* **D. Trong On, D. Desplantier-Giscard, C. Danumah, S. Kaliaguine.** s.l. : Applied Catalysis A: General, 2003, Vols. (253) 545–602.

23. *Ordered mesoporous materials in catalysis.* **A. Taguchi, F. Schüth.** s.l. : Microporous and Mesoporous Materials, 2005, Vols. (77) 1-45.

24. *Investigation of the Morphology of the Mesoporous SBA-16 and SBA-15 Materials.* **W.J.J. Stevens, K. Lebeau, M. Mertens, G. Van Tendeloo, P. Cool, E.F. Cansant.** s.l. : The Journal of Physical Chemistry: B, 2006, Vols. (110) 9183-9187.

25. *Triblock Copolymer Syntheses of Mesoporous Silica with Periodic 50 to 300 Angstrom Pores.* **D. Zhao, J. Feng, Q. Huo, N. Melosh, G.H. Fredrickson, B.F. Chmelka, G.D. Stucky.** s.l. : Science, 1998, Vols. (279) 548-552.

26. *Direct imaging of the pores and cages of three-dimensional mesoporous materials.* **Y. Sakamoto, M. Kaneda, O. Teresaki, D. Zhao, J.M. Kim, G.D Stucky, H.J. Shin, R. Ryoo.** s.l. : Nature, 2000, Vols. (408) 449-453.

27. *The effect and model of silica concentrations on physical properties and particle sizes of three-dimensional SBA-16 nanoporous materials.* **C.F. Cheng, Y.C. Lin, H.H. Cheng, Y.C. Chen.** s.l. : Chemical Physics Letters, 2003, Vols. (382) 496-501.

28. *Influence of Phosphorus on the Properties of Alumina-Based Hydrotreating Catalysts.* **R. Iwamoto, J. Grimblot.** s.l. : Advances in Catalysis, 1999, Vols. (44) 417-503.

29. *Influence of the block length of triblock copolymers on the formation of mesoporous silica.* **K. Flodström, V. Alfredsson.** s.l. : Microporous and Mesoporous Materials, 2003, Vols. (59) 167-176.

30. *Nonionic Triblock and Star Diblock Copolymer and Oligomeric Surfactant Syntheses of Highly Ordered, Hydrothermally Stable, Mesoporous Silica Structures.* **D.Y. Zhao, Q.S. Huo, J.L. Feng, B.F. Chmelka, G.D. Stucky.** s.l. : The Journal of the American Chemical Society, 1998, Vols. (120) 6024-6036.

31. *CoMo/Ti-SBA-15 catalysts for dibenzothiophene desulfurization .* **R. Nava, R.A. Ortega, G. Alonso, C. Ornelas, B. Pawelec, J.L.G. Fierro.** s.l. : Catalysis Today, 2007, Vols. (127) 70-84.

32. *Molecular Design and In Situ Spectroscopic Investigation of Multilayered Supported M1Ox/M2Ox/SiO2 Catalysts.* **E.L. Lee, I.E. Wachs.** s.l. : Journal of Physical Chemistry: C, 2008, Vols. (112) 20418- 20428.

33. **J.G. Graselli, B.J. Bulkin.** *Analytical Raman Spectroscopy.* New Cork : Wiley, 352, 1991.

34. *Synthesis, characterization, and catalytic testing of W-MCM-41 mesoporous molecular sieves.* **Z. Zhang, J. Suo, X. Shang, S. Li.** s.l. : Applied Catalysis A: General, 1999, Vols. (179) 11-19.

35. **Schoonheydt., R.A. in F. Delannay.** *Characterization of Heterogeneous Catalysts.* New York : Marcel Dekker, 125, 1984.

36. *W-Incorporated CoMo/γ-Al2O3Hydrodesulfurization Catalyst: II. Characterization.* **D.K. Lee, H.T. Lee, I.Ch. Lee, S.K. Park, S.Y. Bae, Ch.H. Kim, S.I. Woo.** s.l. : Journal of Catalysis, 1996, Vols. (159) 219-229.

37. *Loss of single-walled carbon nanotubes selectivity by disruption of the Co–Mo interaction in the catalyst.* **J.E. Herrera, D.E. Resasco.** s.l. : Journal of Catalysis, 2004, Vols. (221) 354-364.

38. *Fluorinated hydrotreatment catalysts effect of the deposition order of F− ions on F-CoMo/γ-AL2O3 catalysts.* **H.K. Matralis, Ch. Papadopoulou, A. Lycourghiotis.** s.l. : Applied Catalysis A: General , 1994, Vols. (116) 221-236.

39. *Nanostructured tungsten oxide with controlled properties: Synthesis and Raman characterization .* **A. Baserga, V. Russo, F. Di Fonzo, A. Bailini, D. Cattaneo, C.S. Casari, A. Li Bassi, C.E. Bottani.** s.l. : Thin Solid Films, 2007, Vols. (515) 6465-6469.

40. *Structural characterisation of silica supported CoMo catalysts by UV Raman spectroscopy, XPS and X-ray diffraction techniques.* **V. La Parola, G. Deganello, C.R. Tewell, A.M. Venezia.** s.l. : Applied Catalysis A: General, 2002, Vols. (235) 171-180.

41. *Structure of surface tungsten oxide species in the tungsten trioxide/alumina supported oxide system from x-ray absorption near-edge spectroscopy and Raman spectroscopy.* **J.A. Horsley, I.E. Wachs, J.M. Brown, G.H. Via, F.D. Hardcastle.** s.l. : The Journal of Physical Chemistry, 1987, Vols. (91) 4014-4020.

42. *Structural determination of supported vanadium pentoxide-tungsten trioxide-titania catalysts by in situ Raman spectroscopy and x-ray photoelectron spectroscopy.* **M.A. Vuurman, I.E. Wachs, A.M. Hirt.** s.l. : The Journal of Physical Chemistry, 1991, Vols. (95) 9928- 9937.

43. *Synthesis and characterization of WO3 nanostructures prepared by an aged-hydrothermal method.* **R. Huirache-Acuña, F. Paraguay-Delgado, M.A. Albiter, J. Lara-Romero, R. Martínez-Sánchez.** s.l. : Materials Characterization, 2009, Vols. (60) 932-937.

44. *Infrared and Raman study of WO3 tungsten trioxides and WO3, xH2O tungsten trioxide tydrates .* **M.F. Daniel, B. Desbat, J.C. Lassegues, B. Gerand, M. Figlarz.** s.l. : Journal of Solid State Chemistry, 1987, Vols. (67) 235- 247.

45. *Stability and Controlled Composition of Hexagonal WO3.* **I.M. Szilágyi, J. Madarász, G. Pokol, P. Király, G. Tárkányi, S. Saukko, J. Mizsei, A.L. Tóth, A. Szabó, K. Varga-Josepovits.** s.l. : Chemistry of Materials, 2008, Vols. (20) 4116-4125.

46. *Oxygen chemisorption and laser Raman spectroscopy of unsupported and silica-supported molybdenum oxide.* **A.N. Desikan, L. Huang, S.T. Oyama.** s.l. : The Journal of Physical Chemistry, 1991, Vols. (95) 10050-10056.

47. *Physicochemical characterization of the interaction between cobalt molybdenum oxide and silicon dioxide. 1. Influence of the cobalt-molybdenum ratio.* **P. Gajardo, P. Grange, B. Delmon.** s.l. : The Journal of Physical Chemistry, 1979, Vols. (83) 1771-1779.

48. *HMS mesoporous silica as cobalt support for the Fischer–Tropsch Synthesis: Pretreatment, cobalt loading and particle size effects.* **E. Lira, C.M. López, F. Oropeza, M. Bartolini, J. Alvarez, M. Goldwasser, F. López Linares, J.F. Lamonier, M.J. Pérez Zurita.** s.l. : Journal of Molecular Catalysis A: Chemical, 2008, Vols. (281) 146-153.

49. *Characterization of Silica-Supported Molybdenum and Tungsten Phosphide Hydroprocessing Catalysts by 31P Nuclear Magnetic Resonance Spectroscopy .* **P.A. Clark, X. Wang, S.T. Oyama.** s.l. : Journal of Catalysis, 2002, Vols. (207) 256-265.

50. *Alumina-supported molybdenum phosphide hydroprocessing catalysts.* **P.A. Clark, S.T. Oyama.** s.l. : Journal of Catalysis, 2003, Vols. (218) 78-87.

51. *Synthesis, characterization, and hydrotreating activity of carbon-supported transition metal phosphides.* **Y. Shu, S.T. Oyama.** s.l. : Carbon, 2005, Vols. (43) 1517-1532.

52. *Overview of support effects in hydrotreating catalysts.* **M. Breysse, P. Afanasiev, C. Geantet, M. Vrinat.** s.l. : Catalysis Today, 2003, Vols. (86) 5-16.

53. *Synthesis, characterization and catalytic properties of mesoporous TiHMA molecular sieves: selective oxidation of cycloalkanes.* **P. Selvam, S.K. Mohapatra.** s.l. : Microporous and Mesoporous Materials, 2004, Vols. (73) 137-149.

54. *Effect of phosphorus on the acidity of γ-alumina and on the thermal stability of γ-alumina supported nickel—molybdenum hydrotreating catalysts.* **A. Stanislaus, M. Absi-Halabi, K.Al. Dolama.** s.l. : Applied Catalysis, 1988, Vols. (39) 239-253.

55. *Adsorption mechanism of phosphoric acid on γ-alumina .* **J.M. Lewis, R.A. Kydd.** s.l. : Journal of Catalysis, 1991, Vols. (132) 465-471.

56. *Codeposition of Mo(VI) Species and Ni2+ Ions on the γ-Alumina Surface: Mechanistic Model.* **N. Spanos, A. Lycourghiotis.** s.l. : Journal of Colloid and Interface Science, Vols. (171) 306-318.

57. *NMR study of the adsorption of phosphomolybdates on alumina.* **W.C. Cheng, N.P. Luthra.** s.l. : Journal of Catalysis, 1988, Vols. (109) 163-169.

58. *Comparison of the morphology and reactivity in HDS of CoMo/HMS, CoMo/P/HMS and CoMo/SBA-15 catalysts .* **R. Nava, B. Pawelec, J. Morales, R.A. Ortega, J.L.G. Fierro.** s.l. : Microporous and Mesoporous Materials, 2009, Vols. (118) 189-201.

59. *Influence of the preparation method on the activity of phosphate-containing CoMo/HMS catalysts in deep hydrodesulphurization .* **R. Nava, J. Morales, G. Alonso, C. Ornelas, B. Pawelec, J.L.G. Fierro.** s.l. : Applied Catalysis A: General, 2007, Vols. (321) 58-70.

60. *NO chemisorption as a probe of the active precursors in Co-MoAl2O3 catalysts.* **N.Y. Topsøe, H. Topsøe.** s.l. : Journal of Catalysis, 1982, Vols. (77) 293-296.

61. *Characterization of the structures and active sites in sulfided Co-MoAl2O3 and Ni-MoAl2O3 catalysts by NO chemisorption.* **N.Y. Topsøe, H. Topsøe.** s.l. : Journal of Catalysis, 1983, Vols. (84) 386-401.

62. *Spectroscopoic Characterization of Heterogeneous Catalysts, Part B.* **Fierro, J.L.G.** Amsterdam : Elsevier Science Publishers, 1990, Vol. B67.

63. *Influence of the preparation conditions on the surface properties of HDS catalysts.* **C.V. Caceres, J.L.G. Fierro, M.N. Blanco, H.J. Thomas.** s.l. : Applied Catalysis, 1984, Vols. (10) 333-346.

64. *Effect of sulphiding agents on the hydrodeoxygenation of aliphatic esters on sulphided catalysts.* **O.İ. Şenol, T.R. Viljava, A.O.I. Krause.** s.l. : Applied Catalysis A: General, 2007, Vols. (326) 236-244.

65. *Hydrodeoxygenation of aliphatic esters on sulphided NiMo/γ-Al2O3 and CoMo/γ-Al2O3 catalyst: The effect of water.* **O.İ. Şenol, T.-R. Viljava, A.O.I. Krause.** s.l. : Catalysis Today, 2005, Vols. (106) 186-189.

66. *Practical Surface Analysis. Auger and X-Ray Photoelectron Spectroscopy.* **D. Briggs, M.P. Seah.** New York, Salle and Sauerländer : Wiley, 1990.

67. *HDS of dibenzothiophene over polyphosphates supported on mesoporous silica.* **B. Pawelec, S. Damyanova, R. Mariscal, J.L.G. Fierro, I. Sobrados, J. Sanz, L. Petrov.** s.l. : Journal of Catalysis, 2004, Vols. (223) 86-97.

68. *A combined X-Ray photoelectron and Mössbauer emission spectroscopy study of the state of cobalt in sulfided, supported, and unsupported Co-Mo catalysts.* **I. Alstrup, I. Chorkendorff, R. Candia, B.S. Clausen, H. Topsøe.** s.l. : Journal of Catalysis, 1982, Vols. (77) 397-409.

69. *Effects of Support Surface Chemistry in Hydrodeoxygenation Reactions over CoMo/Activated Carbon Sulfided Catalysts.* **G. de la Puente, A. Gil, J.J. Pis, P. Grange.** s.l. : Langmuir, 1999, Vols. (15) 5800-5806.

70. *XPS studies of the surface of nanocrystalline tungsten disulfide.* **A.P. Shpak, A.M. Korduban, L.M. Kulikov, T.V. Kryshchuk, N.B. Konig, V.O. Kandyba.** s.l. : Journal of Electron Spectroscopy and Related Phenomena , 2010, Vols. (181) 234-238.

71. *Studies of Nickel-Tungsten-Alumina Catalysts by X-Ray Photoelectron Spectroscopy.* **K.T. Nag, D.M. Hercules.** s.l. : The Journal of Physical Chemistry, 1976, Vols. (80) 2094-2102.

72. **J.P. Mangnus, B. Scheffer, J.A. Moulijn.** s.l. : Am. Chem. Soc. Petrol. Div. Prepar., 1987, Vol. (32) 329.

73. *Simultaneous Determination of Oil and Coke Contents in Spent Hydroprocessing Catalyst by Thermogravimetry.* **B.N. Barman, L. Skarlos, D.J. Kushner.** s.l. : Energy & Fuels, 1997, Vols. (11) 593-595.

74. *Characterization of carbonaceous products by TG and DTA.* **R.W. Soares, V.J. Menezes, M.V.A. Fonseca, J. Dwerck.** s.l. : Journal of Thermal Analysis, 1997, Vols. (49) 657-661.

75. *Catalytic hydrodeoxygenation: I. Conversions of o-, p-, and m-cresols .* **E.O. Odebunmi, D.F. Ollis.** s.l. : Journal of Catalysis, 1983, Vols. (80) 56-64.

76. *A density functional study of inhibition of the HDS hydrogenation pathway by pyridine, benzene, and H2S on MoS2-based catalysts .* **Á. Logadóttir, P.G. Moses, B. Hinnemann, N.Y. Topsøe, K.G. Knudsen, H. Topsøe, J.K. Nørskov.** s.l. : Catalysis Today, 2006, Vols. (111) 44-51.

Chapter 6

Designing multifunctional hydroprocessing catalysts based on Zn-Ni/SBA-15 for the removal of aromatics and oxygen

Chapter 6

Designing multifunctional hydroprocessing catalysts based on Zn-Ni/SBA-15 for the removal of aromatics and oxygen

This chapter describes the effect of the support (TiO_2, hybrid $2TiO_2$-SiO_2, SBA-15 and SBA-15 decorated with TiO_2 particles) on the catalytic activity of ZnNi catalysts in the gas-phase hydrodeoxygenation (HDO) of phenol. This reaction is representative of the one major challenges of the hydrotreating unit embedded in a sustainable refinery, decreasing oxygen content of bio-oils (produced in the pyrolysis of lignocellulosic biomass). The fresh and deactivated catalysts were characterized by XRD, N_2 adsorption-desorption, TPR, MS/TPD-NH_3, XPS, SEM, HRTEM and coke combustion. Under steady-state conditions, the ZnNi catalyst supported on SBA-15 decorated with TiO_2 particles displayed the highest activity in the hydrodeoxygenation of phenol (selectivity toward deoxygenated products > 95 %). It has been shown that dispersion of the active ingredient is favoured on the SBA-15 substrate.

6.1. Introduction

The more stringent environmental requirements related with the composition of fuels have attracted increasing attention to multifunctional catalysts for the elimination of aromatics, sulphur, nitrogen and oxygen from fossil and renewable oils. In diesel (fossil fuel), the removal of aromatics and sulfur is desired for increasing the ignition quality in terms of cetane number and for cutting the environmental impact (1) (2). In bio-liquids having a large amounts of O-containing compounds, the removal of oxygen is a challenge for meeting the specification of fuels in terms of viscosity, volatility, corrosiveness, miscibility and stability (3) (4).

In the existing petroleum refining infrastructure, traditional hydrotreatment process can be employed for upgrading both aromatics and oxygenates. The conventional hydrotreating catalysts are based on sulfides of Mo or W supported on γ-Al2O3 and promoted by Ni or Co (5). However, as these sulfides suffer deactivation by the water product originated during the HDO reaction, some kind of organosulfur compound must be added to the feed stream (6). Thus, the challenge is to design new multifunctional catalysts capable of maintaining stability during hydrotreatment of bio-liquids. In the case of fossil fuels, the noble metal-based catalysts employed in catalytic hydrogenation are not only expensive but also display low sulfur tolerance (2). Thus, the challenge is to design S-resistant and low-cost metal catalysts.

It is well established that the catalyst support plays a key role in all hydroconversion reactions. This is because the hydroconversion of aromatics and/or O-containing compounds over bifunctional catalysts involves (de)hydrogenation on metallic centres, and isomerisation/cracking on acid centres.

Unfortunately, when using alumina-supported catalysts, the presence of weak Lewis-type acidic sites on the support surface leads to accumulation of undesirable coke deposites (7) (8). In order to substitute the standard Al_2O_3 support, the use of less acidic or neutral supports such as silica, K-modified alumina, mesoporous silicas (MS) or activated carbon for the HDO (9) (10) (11) (12) reaction have been studied. In particular, the SBA-15 material having hexagonal pores in a 2D array with long 1D channels (*P6mm* plane group) proved a high specific surface and high thermal stability. Furthermore, the modification of mesoporous silicas with Ti ions enhances the active phase dispersion (13), and the catalytic performance (14). However, in the same conditions Ti nanoparticles tend to sintering, blocking the availability of reagents to the active metals (15). Considering the metallic function, nickel-based catalysts demonstrated to be an interesting alternative to noble metals ones in hydrogenation reactions (16), and both nickel and zinc have been proved to be effective and low-cost systems for the hydrogen transfer reductions of many functional groups (17). Moreover, it was found that the addition of Zn to Ni-based catalysts has a positive effect on the Ni dispersion (18) (19), the perfomance catalytic (19) (20) (21) as well as some electronic and geometric effects might occurs (22) (23).

Because Zn^{2+} ions have a more pronounced tendency toward tetrahedral coordination with oxygen ions at the support interface than Ni^{2+} ions (22), one might to expect that the incorporation of Zn into silica-supported nickel catalysts might to prevent the formation of undesired spinel $NiSiO_4$ phases, which are inactive in hydrotreating reactions. Thus, considering the high hydrogenation of ability of nickel and unique ability of zinc to stabilize hydrogenation intermediates, the Zn addition to metallic Ni catalysts seems to be promising for catalyzing hydrotreating reactions with a lower investment and operating cost.

With this premises, in this chapter we compare the catalytic behaviour of the Zn-Ni supported on TiO_2, $2TiO_2$-SiO_2, SBA-15 and SBA-15 decorated with TiO_2 and to determine effect of support in hydrodeoxygenation of phenol produced in the pyrolysis of lignocellulosic biomass.

6.2. Experimental

6.2.1. Support preparation

Four supports were employed to deposit ZnNi phases: (i) the siliceous SBA-15 mesoporous system (named hereafter as S15), which was synthesized according to the procedure described by Flodström and Alfredsson (24), using triblock copolymers Pluronic P123 ($EO_{20}PO_{70}EO_{20}$, BASF) as surfactant; (ii) the TiO_2/SBA-15 substrate, which was synthesized using the same procedure as for the SBA-15 system, except for dissolving the appropriate amounts of titanium(IV) butoxide (97%, Aldrich) in TEOS in order to obtain a support with Si/Ti molar ratio of 20; (iii) the $2TiO_2$-SiO_2 substrate (named hereafter as 2Ti-Si), which was prepared by physical mixture under stirring at room temperature of two moles of TiO_2 per mol SiO_2 in excess of distilled water; and (iv) the commercial TiO_2 (P25, Degussa, 80% anatase) support (named here after as Ti).

6.2.2. Catalysts preparation

Four ZnNi catalysts supported on the TiO_2 (Ti), $2TiO_2$-SiO_2 (2Ti-Si), SBA-15 (S15) and TiO_2/SBA-15 (Ti-S15) substrates were prepared by simultaneous impregnation following the incipient wetness method and using an aqueous solution containing zinc and nickel nitrates hexahydrate [$Zn(NO_3)_2 \cdot 6H_2O$ and

$Ni(NO_3)_2 \cdot 6H_2O$, Aldrich, 98%] to achieve a Ni:Zn molar ratio of 3:1 (Ni 29 wt.% and Zn = 11 wt.%). After impregnation, the samples were dried overnight in air at 110 °C and then calcined at 400 °C for 3 h.

6.2.3. Catalytic activity measurements

The hydroconversion of the phenol was performed in a high-pressure laboratory-scale set-up equipped with a down-flow fixed bed catalytic reactor. Each experiment used 0.15 g of catalyst (particle diameter: 0.25–0.30 mm) mixed with 0.30 g of SiC (diameter 0.5 mm). Before catalyst activation, the catalyst was dried under a N_2 flow of 100 mL min^{-1} at 150 °C for 0.5 h. The catalyst was then reduced in situ at 450 °C for 2 h at atmospheric pressure by a mixture flow of 55 mL of 10:1 of H_2:N_2. After reduction, the catalyst was purged under a N_2 flow of 100 mL min^{-1} at 400 °C for 0.5 h and then stored overnight under a N_2 flow. Before the experimental run, the N_2 pressure was increased to the desired value (3.0 MPa), and the catalytic bed was cooled down to the temperature of the HDO reaction (310 °C). After that, N_2 flow was shut down, the liquid feed (2 vol% of phenol dissolved in decaline) injected by a high-pressure HPLC Knauer pump (WHSV = 2.57 h^{-1}) into a hydrogen stream was fed to the preheated reactor. Owing to the high boiling point of the reactant and the solvent, on-line analysis of the reaction products was not convenient. Consequently, the reactor effluents were condensed, and liquid samples were analyzed by a GC Agilent 6890A with a FID detector.

6.3. Results and discussion

6.3.1. Characterization of the oxide precursors

6.3.1.1. Nitrogen adsorption- desorption isotherms

The textural characterization of the catalysts was studied by means of N_2 adsorption–desorption isotherms at − 196 °C (**Figure 6.1**). According to IUPAC classification, the N_2 adsorption–desorption isotherms of both SBA-15-based catalysts are of type IV (25). The shape of their isotherms is characteristic of mesoporous systems with a narrow pore size distribution. The isotherm shows a smaller desorption step at P/P0 = 0.4 which is characteristic of ink-bottle pores [30 Tuel]. The nitrogen isotherm and Zn-Ni/Ti-S15 reveals Zn-Ni/S15 hysteresis loop type H1, which is typical of SBA-15 system (26), it could be caused by small metal oxides particles being located within the mesopores as well as on the support surface. Thus, the information from adsorption-desorption isotherms was not conclusive for the location of metal oxides particles. In contrast with the ZnNi/S15 and ZnNi/Ti-S15 samples, the N_2 adsorption–desorption isotherms of ZnNi/Ti and ZnNi/2Ti-Si samples extend over a large range of relative pressures, indicating the presence of mesoporosity and/or macroporosity. The hysteresis loop, which starts at a relative pressure of ca. 0.8, is due to textural interparticle mesoporosity or macroporosity. Thus, in addition to framework-confined porosity, the TiO_2 and $2TiO_2$-SiO_2 supported catalysts have a complementary porosity (textural porosity). The specific BET area (S_{BET}) of all catalysts was in the range of 35-365 m^2/g and follows the order: Zn-Ni/S15 ≈ Zn-Ni/Ti-S15 >> Zn-Ni/2Ti-Si > Zn-Ni/Ti (**Table 6.1**).

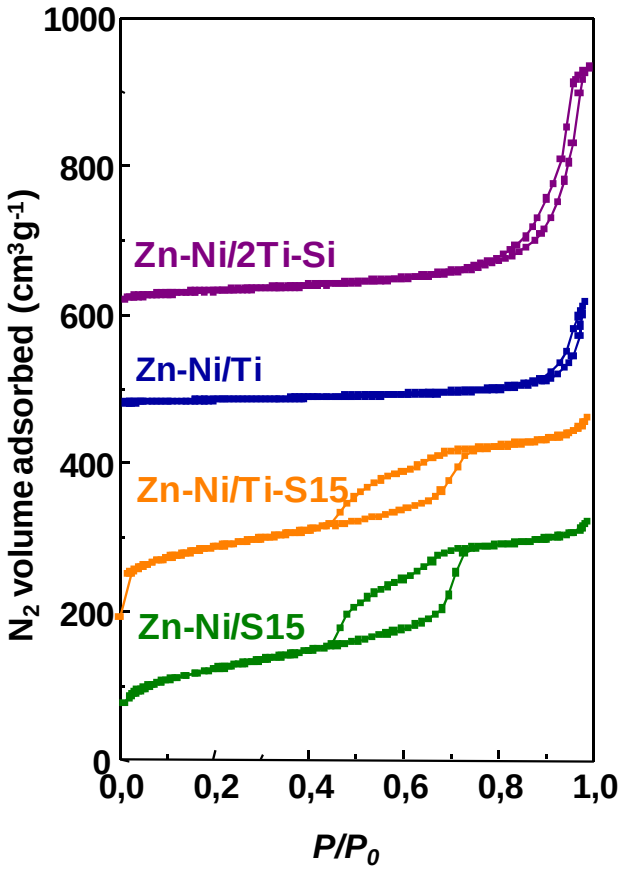

Figure 6.1. N_2 adsorption–desorption isotherms at – 196 °C of Zn-Ni calcined samples.

The main textural properties of the catalysts are reported in **Table 6.1**.

Tabla 6.1. Textural properties of the catalysts calcined Zn-Ni determined by adsorption-desorption isotherms of N_2 at -196 ° C.

Catalyst	Nomenclature	S_{BET} (m^2/g)	d (nm)	V_{total} (cm^3/g)
Zn-Ni/TiO_2	Zn-Ni/Ti	35	20.7	0.21
Zn-Ni/2TiO_2-SiO_2	Zn-Ni/2Ti-Si	91	19.2	0.49
Zn-Ni/Ti-SBA-15	Zn-Ni/TiS15	356	3.8	0.43
Zn-Ni/SBA-15	Zn-Ni/S15	365	4.0	0.47

The pore size distributions of calcined samples, as derived from the desorption branch of N_2 isotherms, are shown in **Figure 6.2**. The pore distribution of Zn-Ni/Ti catalyst reveals a narrow peak centred at 3.6 nm (structural porosity) and another broad peak centred at 42.0 nm (textural porosity). The Zn-Ni/2Ti-Si sample shows two broad peaks centred at 18 and 32.4 nm (textural porosity). For the Zn-Ni/S15 and Zn-Ni/Ti-S15 samples, the pore size distribution shows two distinct peaks: the main one located in the pore width range < 4 nm, representing the ordered mesopores (27); and a second and much less intense one at a pore width of 6.0 nm indicating the presence of complementary pores possibly due to deposition of Zn-Ni metal mixed oxides, which have their own specific surface area as previously observed for other phases (28).

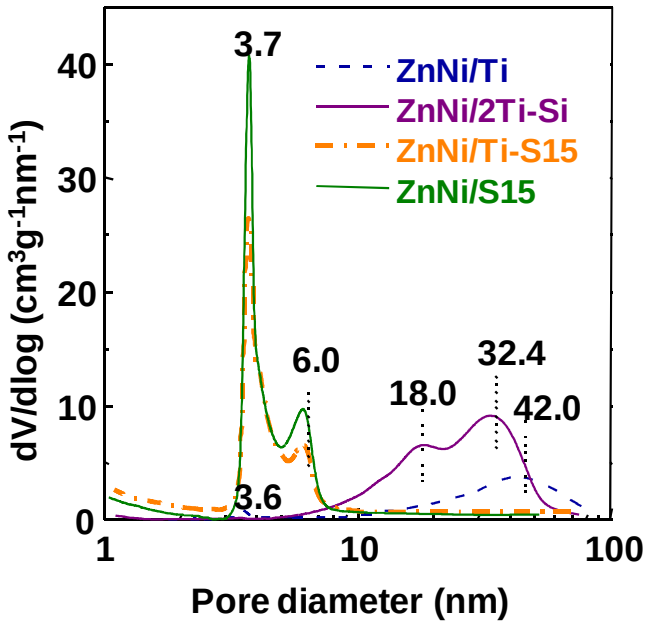

Figure 6.2. Pore size distributions of supported calcined ZnNi catalysts as determined by N_2 adsorption–desorption isotherms at −196 °C.

6.3.1.2. Inductively Coupled Plasma- Atomic Emission Spectrometry (ICP-AES)

The main chemical properties of the calcined catalysts, as determined by ICP-AES is compiled in **Table 6.2**. For all catalysts, the chemical analysis reveals that the metal loading is similar to the nominal one; no metal loss occurs during the preparation and calcination steps.

Table 6.2. Chemical properties of the calcined catalysts ZnNi.

Catalyst	Nominal (%wt)		ICP-AES (%wt)	
	Ni	Zn	Ni	Zn
Zn-Ni/Ti	29.2	10.8	25.4	9.9
Zn-Ni/2Ti-Si			24.4	9.5
Zn-Ni/TiS15			26.7	10.2
Zn-Ni/S15			25.2	10.1

6.3.1.3. X- Ray Difraction (XRD)

The small-angle XRD patterns of Zn-Ni/S15 and Zn-Ni/Ti-S15 catalysts (**Figure 6.3**) show three well-resolved typical diffraction peaks associated with the bi-dimensional *p6mm* hexagonal symmetry: one high-intensity peak at about 2θ = 0.9° (100) and two low-intensity peaks at about 2θ = 1.5 and 1.8° corresponding to indicate that their mesoporous structure was maintained after the support impregnation with metal precursors and calcination.

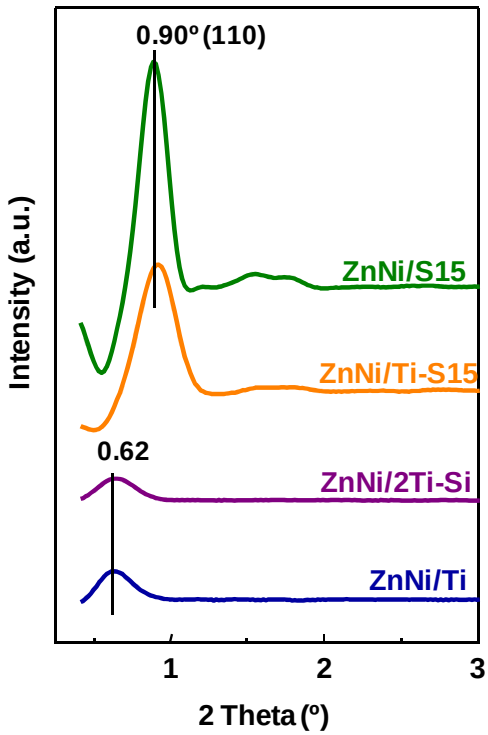

Figure 6.3. Low angle profiles of the catalysts calcined XRD of Zn-Ni.

The wide-angle XRD technique was used to study the formation of crystallite species in the calcined catalysts (**Figure 6.4**). The X-ray patterns of both SBA-15-based catalysts show the peaks at 2θ (°) = 37.2, 43.3, 62.8, 75.4 and 79.4 due to the formation of NiO crystallites (JCPDS card 01-044-1159). On the contrary, both Zn-Ni/Ti and Zn-Ni/2Ti-Si catalysts show peaks at 2θ (°) = 37.0, 43.0, 62.5, 74.9 and 78.8 due to the formation of $Ni_{0.8}Zn_{0.2}O$ alloy phase (JCPDS card 01-075-0271). Additionally, the Zn-Ni/Ti catalyst shows peaks at 2θ (°) = 31.7, 34.4, 36.2 and 62.8 indicating the presence of ZnO phase (JCPDS card 01-076-0704) together with the peaks at 2θ (°) = 27.5, 36.2 and 56.6 corresponding to titania (rutile) (JCPDS card 01-

078-1510), and the peaks at 2θ (°) = 25.3, 37.8, 48.1, 54.2, 55.0, 69.1, 70.3 and 83.0 corresponding to titania (anatase) (JCPDS card 01-084-1285). The absence of diffraction lines of the ZnO phase in the Zn-Ni/S15, Zn-Ni/Ti-S15 and Zn-Ni/2Ti-Si samples cannot discard its formation; it could be in the form of small particles being under the XRD detection limit.

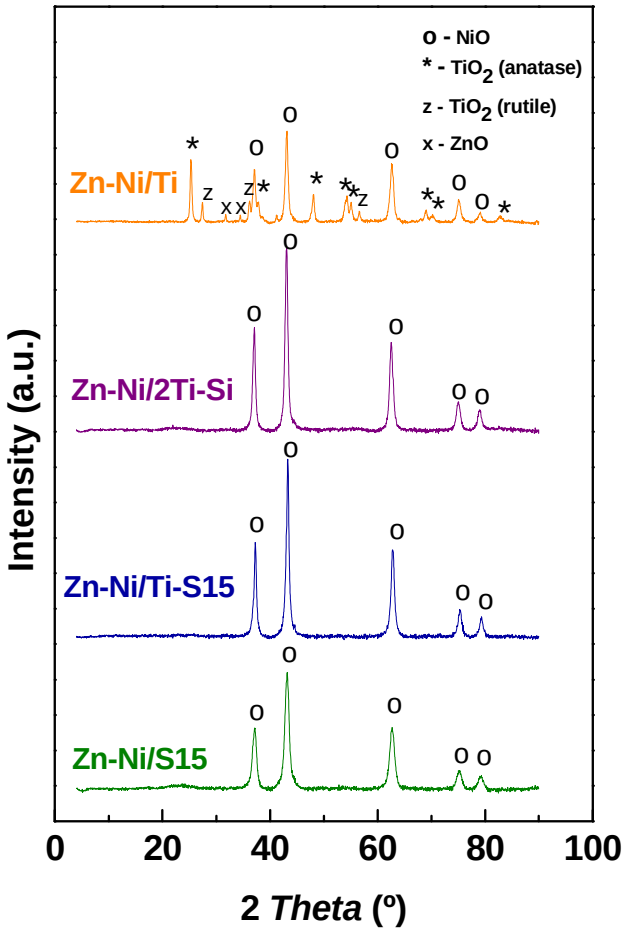

Figure 6.4. Wide- angle XRD patterns of calcined Zn-Ni catalysts.

Considering the NiO phase diffraction line, these are more intense for catalysts supported on mesoporous materials aimed at the formation of crystalline phase of NiO. By applying Scherrer's equation to the main diffraction signal at 2θ (°) = 43.3, calculated the particle size of NiO. The smaller size of the crystallites is observed in the catalyst Zn-Ni/S15 and the largest on the catalyst Zn-Ni/Ti-S15. The trend is: Zn-Ni/Ti-S15 (17.3 nm) ≈ Zn-Ni/Ti (17.2 nm)> Zn-Ni/2Ti-Si (16.1 nm)> Zn-Ni/S15 (10.8 nm).

6.4.1.4. Temperature Programmed Reduction (TPR-H_2)

It is known that the interaction between nickel oxide and the support can affect the reduction temperature. In case of weak interaction, the nickel species can be reduced at lower temperature than in case of a strong interaction. In this chapter, the reducibility of the supported oxide compounds was studied by temperature-programmed reduction with hydrogen.

The H_2-TPR patterns are shown in **Figure 6.5**. For all catalysts, the maximum of reduction was found to be located at 478-605 °C. Taking into account that the reduction of NiO supported on mesoporous material, prepared from nitrate type precursor, occurs at much lower temperature 300-400 °C (29), the observed blue shift of reduction temperature strongly suggest that the presence of Zn induces the formation of smaller particles interacting strongly with the material support.

In order to make the discussion easier, the TPR were decomposed and the hydrogen consumption quantified. As an example, **Figure 6.5(B)** shows the decomposition of the TPR profile of the Zn-Ni/Ti sample. As seen in this figure, the

TPR profile of this sample present four reduction peaks belonging to the reduction of ZnO and Ni^{2+} ions placed in different environments.

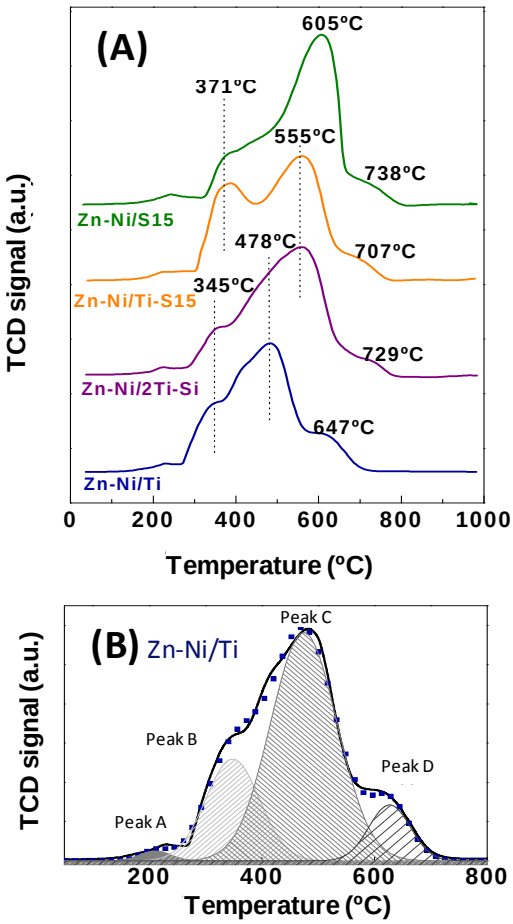

Figure 6.5. H_2 –TPR profiles of the calcined catalysts (A), and an example of Gaussian deconvolution of peaks (B) for the Zn-Ni/Ti.

The small low temperature reduction peak (A) at ~200 °C is assigned in the literature to the reduction of trace amounts of Ni^{3+} (30). The amount of hydrogen

consumed in this reduction step is hardly the same in all cases. The second reduction peak (B in **Figure 6.5(B)**) is placed is close to that corresponding to the reduction of bulk NiO (340 °C) (31), indicating the presence of a variable fraction of large NiO particles, depending on the support employed. The NiO particles are larger than these associated with the reduction bands appearing at higher temperatures. For both Zn-Ni/Ti and Zn-Ni/2Ti-Si catalysts, this peak appears at 345 °C, while the catalysts supported on SBA-15 (Zn-Ni/S15 and Zn-Ni/Ti-S15) present this peak at higher temperatures, 371 °C, usually assigned to the reduction of "free" NiO clusters interacting weakly with the support (32). The intensity of this peak is much more important for Zn-Ni/Ti-S15 catalysts pointing to the presence of larger NiO cluster, in agreement with XRD patterns. The amount of hydrogen consumed on peak B follows the order: Zn-Ni/Ti-S15 >> Zn-Ni/Ti > Zn-Ni/S15 ≈ ZnNi/2Ti-Si.

Thus, in good agreement with XRD data (**Table 6.3**), the former sample show a larger amount of "free" NiO clusters among the catalysts studied. The third reduction peak (C in **Figure 6.5(B)**) is ascribed to the reduction of highly dispersed nickel oxide particles. For the Zn-Ni/Ti catalyst, the second reduction peak is at 478 °C and close to the value reported for the reduction of highly dispersed nickel oxide on titania surface (33). For Zn-Ni/2Ti-Si this peak shifts to higher temperature, whose maximum is located at 555 °C but presenting a shoulder at 478 °C. It should be considered that this support is a physical mixture of TiO_2 and SiO_2 and therefore the peak at 555 °C could be ascribed to the reduction of NiO interacting with SiO_2 while the shoulder at 478 °C should come from the reduction of NiO interacting with TiO_2 and indicating a higher interaction of these small NiO particles with SiO_2 than with TiO_2. The same conclusion can be extracted from the

catalysts supported on mesoporous materials. Thus, the reduction temperature increases in absence of titanium Zn-Ni/S15 (605 °C) > Zn-Ni/Ti-S15 (555 °C).

Table 6.3. H_2 uptake (± 10%) and metallic properties of fresh reduced[b-d] and spent[e] ZnNi catalysts.

Catalizador	H_2 uptake[a] ($mmol/g_{cat}$)	S_{met}[b] ($m^2\ g_{cat}^{-1}$)	S_{met}[c] ($m^2\ g_{cat}^{-1}$)	d[d] (nm) XRD[d]	d[e] (nm) TEM
Zn-Ni/Ti	8.2	10.3	1.40	11.3	12.2 ± 2.0
Zn-Ni/2Ti-Si	9.1	13.3	2.32	11.5	10.6 ± 1.7
Zn-Ni/Ti-S15	9.4	15.8	3.52	12.9	13.0 ± 4.9
Zn-Ni/S15	9.8	16.7	3.36	9.2	7.8 ± 1.6

[a] Gaussian deconvolution of TPR peak profiles.

This specific behaviour confirms the existence of Ni(II) species strongly interacting with the support, whose interaction increases on mesoporous materials and in absence of TiO_2. These particles are also more difficult to reduce, avoiding the sintering of the metal particles during the reduction process. The hydrogen consumption in this reduction process follows the order: ZnNi/S15 >> ZnNi/2Ti-Si > ZnNi/Ti-S15 > ZnNi/Ti. From these data it can be concluded that the presence of titanium reduces the amount of highly dispersed NiO particles.

Finally, the peak observed at temperatures higher than 550 °C is assigned to the reduction of nickel species interacting strongly with the support. For the Zn-Ni/Ti catalyst, the band at 647 °C should be due to $NiTiO_3$ compound (34). For the silica-containing catalysts, the reduction of nickel silicates occurs at higher temperatures than those of the $NiTiO_3$ phase, as deduced from the shift of centre of this peak from 647 to 738 °C. Interestingly, the Zn-Ni/Ti sample consumed more hydrogen for reduction of its $NiTiO_3$ species than its silica-containing counterparts for reduction of nickel silicates.

6.3.2. Characterization of fresh reduced catalysts

6.3.2.1. H_2 Chemisorption

H_2 chemisorption measurements at 35 °C were carried out in order to know the accessible metallic area of the reduced catalysts. The corresponding values are compiled in **Table 6.4**. The metallic area is doubled for the Zn-Ni/S15 and Zn-Ni/Ti-S15 catalysts with respect to the Zn-Ni/Ti catalyst, due to the fact that SBA-15 support enhances the dispersion of the metal. Additionally, the presence of Ti increases the metallic surface.

Table 6.4. H_2 upgrading(± 10%) and metalic properties of fresh reduced [b-d] and used[e] Zn-Ni catalyst.

Catalizador	H_2 upgrading [a] ($mmol/g_{cat}$)	S_{MET}[b] ($m^2\ g_{cat}^{-1}$)	S_{MET}[c] ($m^2\ g_{cat}^{-1}$)	d^d(nm) DRX[d]	d^e(nm) TEM
Zn-Ni/Ti	8.2	10.3	1.40	11.3	12.2 ± 2.0
Zn-Ni/2Ti-Si	9.1	13.3	2.32	11.5	10.6 ± 1.7
Zn-Ni/TiS15	9.4	15.8	3.52	12.9	13.0 ± 4.9
Zn-Ni/S15	9.8	16.7	3.36	9.2	7.8 ± 1.6

[a]Obtained by Gaussian deconvolution of TPR profiles.
[b]Metallic surface from volume of chemisorbed and physisorbed H_2 at 35 °C.
[c]Metallic surface from volume of chemisorbed H_2 at 35 °C.
[d]Crystal size estimated by Sherrer ecuation of profiles of XRD.
[e]Average particle size of the catalysts used in phenol HDO.

6.3.2.2. X-Ray Difraction (XRD)

Figure 6.6 shows XRD patterns of fresh reduced catalysts. As seen in this figure, all catalysts exhibit characteristic peaks of metallic Ni at 2θ (°) = 44.5 and

51.9 (JCPDS-00-001-1260) whose intensity depends on the support employed. Both ZnNi/Ti and ZnNi/2Ti-Si catalysts shows more defined both peaks suggesting a better reducibility of their nickel oxide phase.

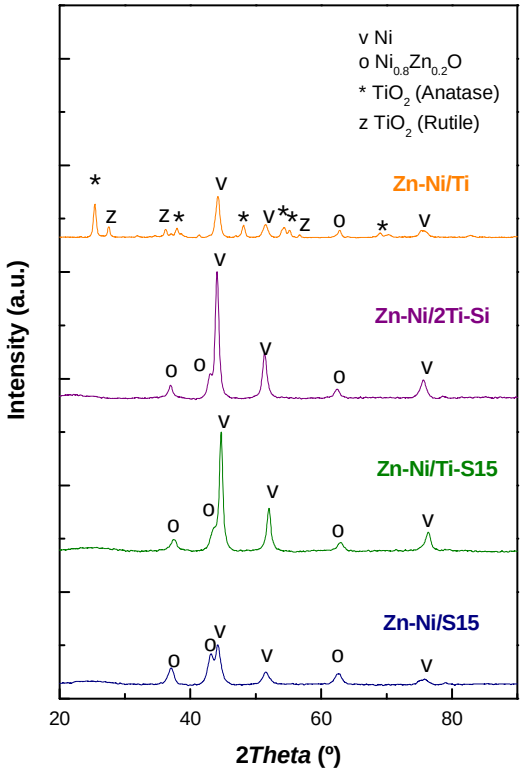

Figure 6.6. Wide- angle XRD patterns of reduced Zn-Ni catalysts.

The crystal size, as calculated by the Debye-Scherrer equation from XRD line broadening of the diffraction peak at 2θ (°) = 51.9, were rather large and follows tend: Zn-Ni/Ti-S15 (12.9 nm) > Zn-Ni/2Ti-Si (11.5 nm) ≈ Zn-Ni/Ti (11.3 nm) > Zn-Ni/S15 (9.2 nm). Additionally, all XRD patterns of reduced samples show

diffraction peaks arising from non-reduced NiO indicating that a total reduction of nickel species has not been achieved under the reduction conditions employed.

6.3.2.3. Temperature Programmed Desorption of NH_3 (TPD-NH_3)

Temperature-programmed desorption of ammonia (TPD-NH_3) followed by mass spectrometry was carried out in order to compare the acidity of the reduced catalysts (**Figure 6.7**). The amount of NH_3 adsorbed, total acidity of the catalyst, has been calculated by difference between the total amount of adsorbed NH_3 at 150 °C and the amount of physisorbed NH_3 species.

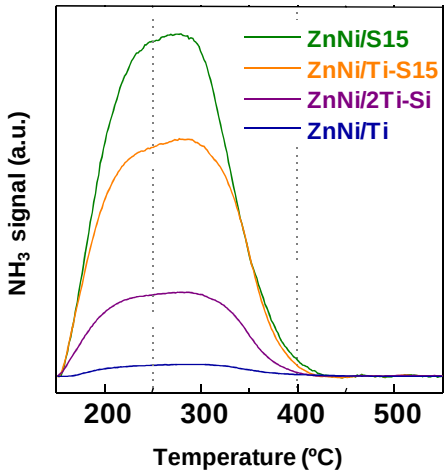

Figure 6.7. NH_3-TPD profiles of reduced catalysts. The desorbed species were monitored by mass spectroscopy.

Figure 6.7 shows the TPD-NH_3 profiles of the catalysts in the range 150-550 °C. We have used the MS signal of NH_3 instead of any other detection

procedure (gravimetric or TCD) since other thermal events may occur to the catalyst, including oxidation of Ni or desorption of some contaminants from the support.

Figure 6.7 shows that there are two types of acid sites on the catalyst, with maximums at 220 and 300 °C. The temperature of desorption of these sites indicates that the strength of the sites is very low, because the strongest acid sites are covered by the metallic function of the catalyst (Ni or Zn). Table 3 summarizes the acid site concentration of the catalysts displayed in Figure 6.5. As it happens, the trend of acidity is Zn-Ni/S15 > Zn-Ni/Ti-S15 >> Zn-Ni/2Ti-Si > Zn-Ni/Ti which is the same trend than that observed in the dispersion and S_{MET} (**Table 6.5**). The coordinately unsaturated Ni cations could serve as a kind of Lewis acid centres, which compensate the original acid sites being covered by the metals.

Table 6.5. Acid properties of the reduced catalysts as determined by TPD-NH_3 monitored by mass spectrometry.

Catalyst	Total acidity ($\mu mol_{NH3}\ g_{cat}^{-1}$)	Weak acidity ($\mu mol\ g_{cat}^{-1}$)[a]	Medium acidity ($\mu mol\ g_{cat}^{-1}$)[b]	Strong acidity ($\mu mol\ g_{cat}^{-1}$)[c]
Zn-Ni/Ti	15	4	9	2
Zn-Ni/2Ti-Si	99	38	60	1
Zn-Ni/TiS15	291	104	175	12
Zn-Ni/S15	389	139	227	23

[a] As obtained by the amount of NH_3 desorbed between 150-240 °C. [b] As obtained by the amount of NH_3 desorbed between 240-400 °C. [c] As obtained by the amount of NH_3 desorbed between 400-450 °C.

The degree of reducibility could not explain the increase in total acidity. In this regard, since the profiles of TPR-H_2 can be seen that trend continues reducibility following Zn-Ni/Ti > Zn-Ni/Ti-Si > Zn-Ni/Ti-S15 > Zn-Ni/S15. Thus for no mesoporous catalysts (Zn-Ni/Ti> Zn-Ni/Ti-Si) the ammonia desorption peak is less intense, while for catalysts supported on mesoporous materials, the profiles become more intense with decreasing reducibility and increased metal dispersion, as previously observed for the Ni-Ru catalyst (35).

6.3.2.4. X-Ray Photoelectron Spectroscopy (XPS)

To get an idea of the nature of surface species and degree of Ni reduction catalysts reduced at 350 °C, were recorded photoelectron spectra (XPS) the Ni 2p core level, Zn 2p, Si 2s, Ti 2p and O 1s the reduced catalysts. **Table 6.6** summarizes the binding energies of the main components.

The XPS technique has been used to determine the chemical state of elements and their surface proportions in the catalysts tested in HDO of phenol. The values of the binding energy of the most intense peaks of nickel (Ni $2p_{3/2}$), zinc (Zn $2p_{3/2}$), silica (Si 2p) and oxygen (O 1s) are listed in **Table 6.6**. For all Ti-containing catalysts, the BE of Ti $2p_{3/2}$ core level at 458.6-458.9 eV is indicative of Ti ions being in an octahedral (Ti-O-Ti) coordination (36). For the Zn-Ni/Ti-S15 sample, the absence of the second component of Ti $2p_{3/2}$ at BE about 460 eV exclude the presence of the Ti^{4+} ions in a tetrahedral arrangement (Si-O-Ti) of SBA-15 substrate (37). All Si-containing catalysts show Si 2p peak at BE of 103.4 eV characteristic of SiO_2 (38) and O 1s peak at a BE of 532.7 eV originated from Si-O-Si linkages whereas the Zn-Ni/Ti sample show a BE at 530.0 eV due o Ti-O-Ti bonds (39).

Table 6.6. Binding energies (eV) of core levels of fresh reducid Zn-Ni catalysts.

Catalyst	Ni $2p_{3/2}$	Zn $2p_{3/2}$	Si 2p	Ti $2p_{3/2}$	O 1s
Zn-Ni/Ti	852.1 (84) 854.6 (16)	1021.3	-	458.6	530.0
Zn-Ni/2Ti-Si	852.1 (82) 854.6 (18)	1021.4	103.4	458.9	-
Zn-Ni/TiS15	852.1 (91) 854.6 (9)	1021.4	103.4	458.8	532.7
Zn-Ni/S15	852.1 (93) 854.6 (7)	1021.4	103.4	-	532.7

A high-resolution XPS curve in the region of 1020-1025 eV was recorded, which shows an intense peak at 1021.4 eV which is characteristic of the Zn^{2+} (38). The Ni $2p_{3/2}$ core level spectra of all catalysts are displayed in **Figure 6.8**. Deconvolution of the Ni $2p_{3/2}$ core level in **Figure 6.8** shows two peak's maxima with binding energies around 852.1 and 854.6 eV indicating that metallic Ni and some of unreduced Ni^{2+} ions are both present in all catalysts. It can be noted that this binding energies are remarkably constant in all systems and independent of the support composition. The former peak at 852.1 eV can be assigned to Ni $2p_{3/2}$ peak of metallic nickel, since the same BEs was observed for reduced Ni/SiO_2 (40). The second component of the Ni $2p_{3/2}$ peak at 854.6 eV is related to the NiO species (41). For all catalysts, the presence of unreduced nickel species is confirmed by shake-up satellite line which is the fingerprint of Ni^{2+} ions in an environment of oxide anions.

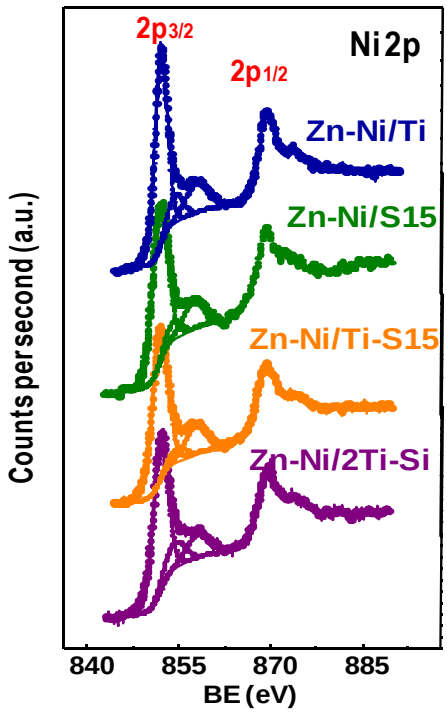

Figure 6.8. Ni 2p XPS spectra of H_2-reduced Zn-Ni catalysts.

The percentages of reduced and unreduced (Ni^{2+}) species, derived from XPS data, are summarized in **Table 6.6** (they are given in parenthesis in first column). These values indicate that the proportion of reduced and unreduced species depends on the support composition being nickel a little more reduced on both SBA-15-based catalysts. Quantitative XPS analysis of the catalysts are shown in Table 5. The total surface exposure of metallic nickel species follows the trend: Zn-Ni/Ti-S15 >> Zn-Ni/Ti > Zn-Ni/2Ti-Si >> Zn-Ti/S15. On the other hand, the surface exposure of zinc species, as determined by the Zn/Si(Ti) atomic ratio, follows different trend (Zn-Ni/Ti >> Zn-Ni/2Ti-Si ≈ Zn-Ti/S15 > Zn-Ni/S15). The

low surface concentration of nickel and zinc species in sample Zn-Ni/S15 is indicative of a poor dispersion of metals dispersion of these species. As XPS is very sensitive surface technique, the comparison of bulk (calculated from chemical analysis data) and surface Ni/Si(Ti) and Zn/Si(Ti) atomic ratios can give an idea on the location of Ni and Zn species along the catalyst's structure (**Table 6.7**). Thus, for the Zn-Ni/Ti, the much larger surface than bulk Ni(Zn)/Si(Ti) atomic ratios suggest the main location of nickel species on the TiO_2 support surface. On the contrary, the much larger bulk than XPS Ni(Zn)/Si(Ti) atomic ratios of both Zn-Ni/2Ti-Si and Zn-Ni/S15 catalysts suggest that nickel and zinc species are mainly located within the inner catalyst's porous structure. Noticeably, the Zn-Ni/Ti-S15 sample is unique among the catalysts studied which show homogenous distribution of nickel and zinc species.

Table 6.7. Surface atomic ratios of H_2-reduced Zn-Ni catalyst.

Catalyst	Ni^0/Si(Ti) at	Ni_{total}/Si(Ti) at		Zn/Si(Ti) at		Ti/Si at
		XPS	Bulk	XPS	Bulk	
Zn-Ni/Ti	1.184	1.410	0.533	0.808	0.255	-
Zn-Ni/2Ti-Si	0.166	0.203	0.915	0.120	0.436	0.015
Zn-Ni/TiS15	0.252	0.277	0.291	0.112	0.137	0.012
Zn-Ni/S15	0.090	0.097	0.399	0.068	0.143	-

6.3.3. Catalytic results

The catalysts were studied in the HDO of phenol carried out in a flow reactor at T = 310 °C, 3 MPa of total hydrogen pressure and WHSV = 2.57 h^{-1}. The values of steady-state conversions, yields of products and selectivity toward

deoxygenated compounds are listed in **Table 6.8**. As seen, the conversion of phenol follows the trend: ZnNi/Ti-S15 > ZnNi/S15 > ZnNi/2TiSi > ZnNi/Ti.

Table 6.8. Conversion, yield and selectivity of deoxygenated compounds (S_{doxy}) in the HDO of phenol on supported Zn-Ni catalysts (*T* = 310 °C, *P* = 3 MPa, *TOS* = 4 h, *WHSV* = 2.57 h^{-1}).

Catalyst	X $_{fenol}$ (%)	CH	CHE	B	CHO	S_{doxy}
Zn-Ni/Ti	10.3	5.6	3.1	0.9	0.7	93.2
Zn-Ni/2Ti-Si	21.0	18.4	0.4	2.1	0.1	99.5
Zn-Ni/TiS15	41.7	28.2	3.8	7.6	2.1	94.7
Zn-Ni/S15	35.4	34.3	0.2	0.9	0	100

[a] CH=Cyclohexane; CHE= Cyclohexene; B= Benzene; CHO= Cyclohexanol, S_{doxy}= selectivity of deoxygenation.

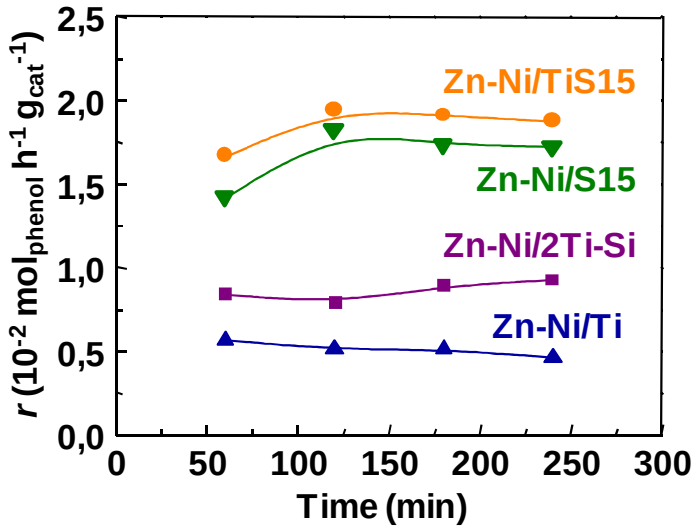

Figure 6.9. Evolution of reaction rates of phenol HDO with the TOS for the Zn-Ni catalysts: T= 310 °C, *P* = 3MPa and W*HSV* = 2.57 h^{-1}.

Figure 6.9 shows the evolution of the reaction rate with the time on-stream (TOS) for the studied Zn-Ni catalysts. As seen in this figure, all the catalysts were stable after 240 min. Both SBA-15-based catalysts (Zn-Ni/S15 and Zn-Ni/Ti-S15) suffer initial activation (0-120 min) followed by deactivation (120-240 min). The initial activation indicates the formation of new active phases upon high hydrogen pressure, probably Ni^0.

Under reaction conditions employed, the products identified by GC were: cyclohexane (CH), cyclohexene (CHE), cychohexanol (CHO) and benzene (B). As seen, three types of main reactions take place, i.e. hydrogenation, hydrogenolysis and isomerisation (Scheme 1). The most desired products are cyclohexane and methylcyclohexane, since their lack of oxygen and their higher octane number. All catalysts show a selectivity higher than 90% (**Table 6.8**) of the desired CH and a low selectivity of B.

At steady state conditions, the rate of reaction of phenol is described according to E**quation 6.1** where r is the rate of phenol HDO (molphenol g_{cat}^{-1} s^{-1}), X is the conversion of phenol, F is the molar flow rate of the reactant (mol s^{-1}), and Wc refers to the weight catalyst (g).

$$r = [X\ F] / W_c \qquad \textbf{Equation 6.1}$$

Considering the two main pathways of phenol HDO of Scheme 1: (i) an initial metal-catalyzed hydrogenation of the aromatic ring to form cyclohexanol/cyclohexenol followed by acid-catalyzed dehydration of cyclohexanol leading to the formation of cylohexane, cyclohexene; and (i) a direct cleavage of the C-O σ bond leading to benzene formation. The higher yield of B respect to CHO suggests that the main pathway of reaction occurs via (ii) pathway. Total elimination of the O-containing compounds was achieved over Zn-Ni

catalyst supported on SBA-15. Modification of this substrate with Ti leads to a large increase of the catalyst activity but poorer selectivity of O-free products. That is, Zn-Ni/Ti-S15 catalyzes effectively the cleavage of C-O bonds, whereas Zn-Ni/S15 is more effective for aromatic hydrogenation.

6.3.4. Characterization of the spent catalysts

6.3.4.1. High resolution transmission electron spectroscopy (HRTEM)

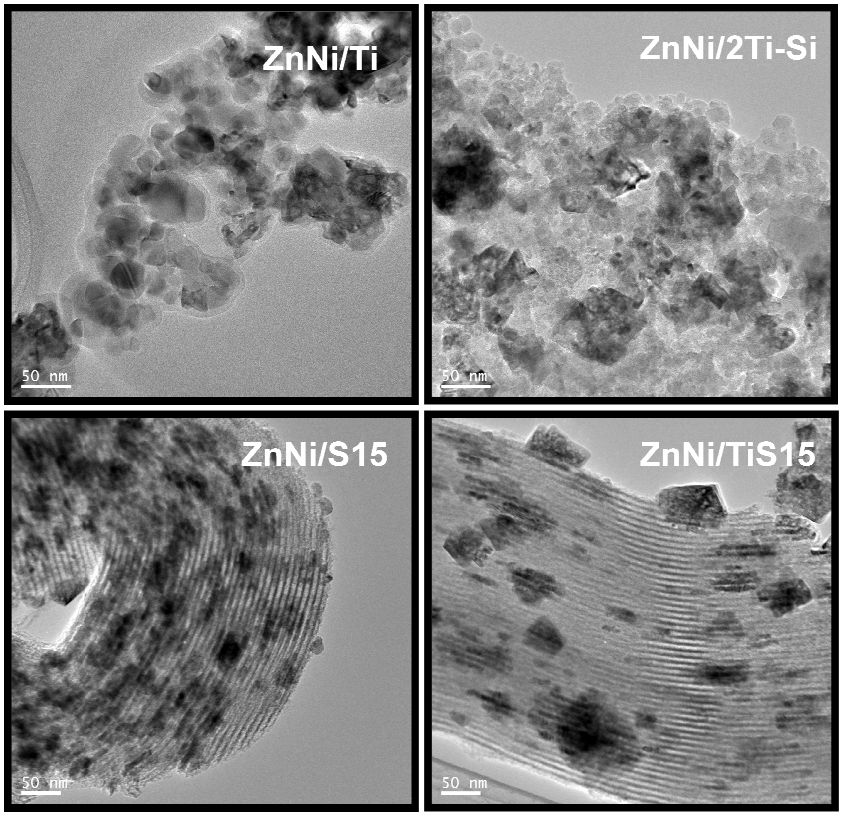

Figure 6.10. TEM micrographs of the Zn-Ni catalysts tested in HDO of phenol (T = 310 °C, P = 3MPa, $WHSV$ = 2.57 h^{-1}).

To determine the size and distribution of the metallic phases in the catalysts used in reacting phenol HDO, we studied the morphology of catalysts by High Resolution Transmission Electron Microscopy (HRTEM). Regarding the morphology of the catalysts, the TEM images (**Figure 6.10**) show a heterogeneous distribution of the metallic phase for all the catalysts. Catalysts based on SBA-15 showed a hexagonal conformation of its channels. As seen, spherical and rather non-homogeneously dispersed Zn-Ni clusters without aggregation were obtained on all the catalysts.

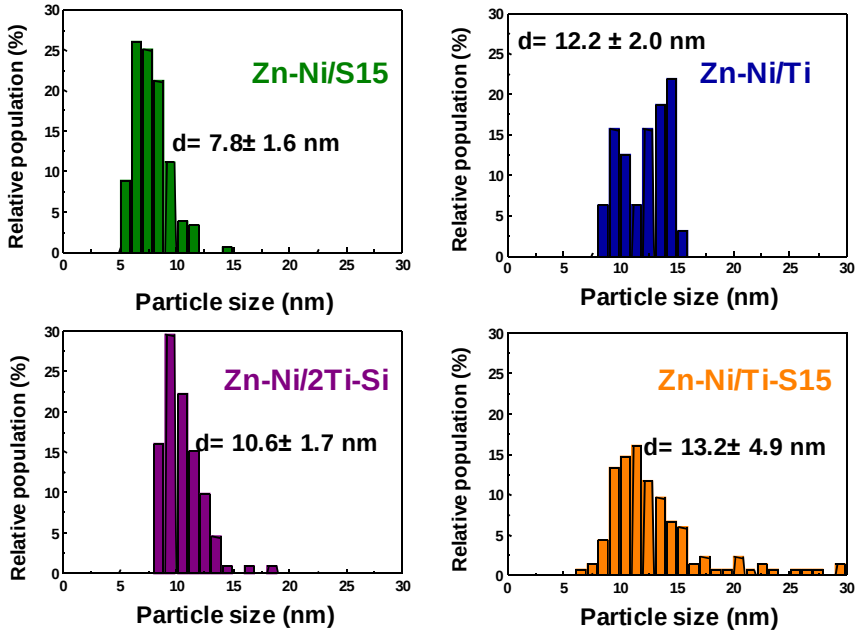

Figure 6.11. Histograms on particle size distribution of the Zn-Ni catalysts tested in HDO of phenol (T = 310 °C, P = 3MPa, $WHSV$ = 2.57 h^{-1}).

Statistical analysis was performed about 250 particles to calculate the average size of the metal particles of the catalysts. The results of this analysis are shown in the histograms in **Figure 6.11**. The size of the metallic particles follows the trend Zn-Ni/Ti-S15 (13.2 ± 4.9 nm) > Zn-Ni/Ti (12.2 ± 2.0 nm) > Zn-Ni/2Ti-Si (10.6 ± 1.7 nm) > Zn-Ni/S15 (7.8 ± 1.6 nm). As can be seen in **Figure 6.11**, the distribution of particle size of the catalyst Zn-Ni / Ti-S15 is relatively large with respect to other catalysts. For all catalysts, EDX and lattice parameter measurements on crystalline domains corroborate the formation of Zn^0 and Ni^0 phases, in good agreement with wide-angle XRD patterns.

6.3.4.2. Coke quantification (TPO/TGA-DTG)

After 240 min of reaction, the carbonaceous matter (coke) deposited on the spent catalysts tested in the HDO of phenol were analyzed by TG-TPO. The amount of coke follows the trend: Zn-Ni/S15 (2.4%) ~ Zn-Ni/Ti-S15 (2.2%) ~ Zn-Ni/2Ti-S15 (1.9%) > Zn-Ni/Ti (1.0%). This trend clearly indicates that the ZnNi/Ti catalyst show the lowest deposition of coke among the catalysts studied. Considering the experimental error of TG-TPO measurements, the other samples show similar deactivation, but it could be intuited that the incorporation of TiO_2 on SBA-15 material decreased the catalyst deactivation by coke deposition.

6.3.4.3. Scanning Electron Microscopy (SEM)

SEM techniques were employed to examine the surface morphology of spent catalysts tested in HDO reaction (**Figure 6.12**). For the Zn-Ni/Ti sample the grain size was appreciably larger when compared with other catalysts. In good agreement with its pore size distribution (**Figure 6.2**), this sample shows much

larger pores than both SBA-15-based catalysts. For the Zn-Ni/2Ti-Si sample, the metal particles did not show preference to any component of the $2TiO_2$-SiO_2 support and are randomly distributed in the entire volume of the catalyst. On the other hand, the silica particles in the SEM images of both SBA-15-based catalysts exhibit hexagonal cylinder-like morphologies which are parallel to the c direction. Moreover, in good agreement with the acidity data (**Table 6.5**), the surface of both Zn-Ni/S15 and Zn-Ni/Ti-S15 samples possesses defects and microholes which Lewis acidity contributed to the large acidity of this sample. Thus, the surface defects of the SBA-15 carrier might to behave as active sites for adsorption of aromatics.

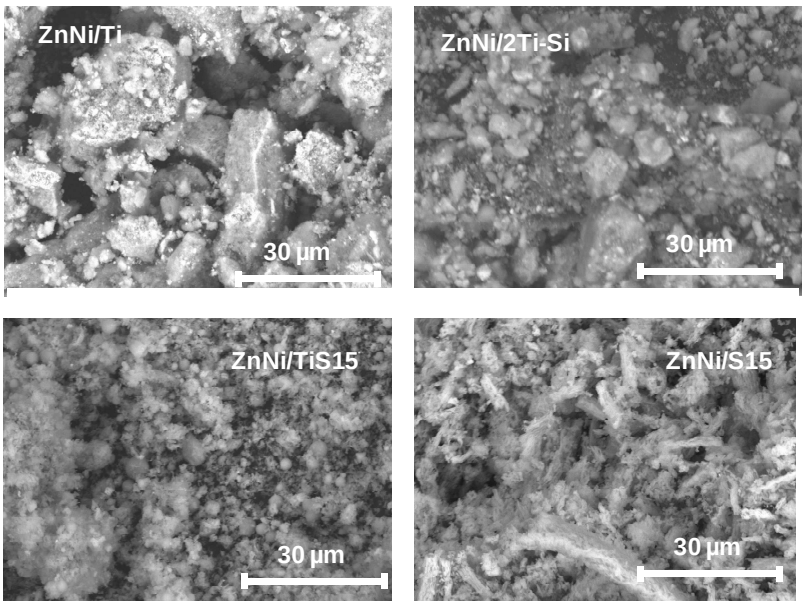

Figure 6.12. SEM micrographs of the Zn-Ni catalysts tested in HDO of phenol (T = 310 °C, P = 3MPa, $WHSV$ = 2.57 h^{-1}).

6.3.5. Correlation structure- activity

For structure-activity correlation of the catalyst, a number of factors govern the catalytic response Zn-Ni catalyst supported on HDO reaction. First, the presence of Zn and use of mesoporous solids favor the formation of Ni particles that interact strongly with the support.

The results of both XRD and TPR Zn-Ni/Ti-S15 suggest that the catalyst has the largest number of groups "free" NiO that appear to be precursors of the active phase formed after activation of the catalyst by reduction. Moreover, this catalyst also has a large proportion of highly dispersed NiO particles strongly interacting with the support (Peak C in TPR profiles). Both effects appear to determine the bifunctional character a hydrotreating catalyst should present. Activating the oxygen molecules is likely to take place through an electron receptor, typically associated with a transition metal oxide or Lewis acid site of the support. The hydrogen donor is the reduced form of the transition metals due to their ability to activate hydrogen (42) (43) but this activation could also occur at the interface of the metal support (44). There is a correlation between the acidity of the catalyst metal surface area and activity of HDO. Zn-Ni/S15 The catalyst is the most active catalyst in the hydrogenation of aromatic rings (benzene to phenol HDO). Interestingly, in order to activate the CO bond hydrogenolysis, Ti has a positive effect due to the fact that Ti stabilizes NiO clusters on the catalyst surface (larger amount of NiO in the catalyst Zn-Ni/Ti-S15). The balance between both types of sites appears to determine the catalytic activity of these catalysts.

This study provides experimental evidence that bimetallic ZnNi catalysts supported on the SBA-15 are the most active in the HDO of phenol than their TiO_2- and $2TiO_2$-SiO_2-supported counterparts suggesting that the SBA-15 substrate

should be promising carrier for tailoring novel hydrotreating catalysts. From the catalyst activity-structure correlation, the larger activities of the SBA-15-based catalysts with respect to TiO_2- and $2TiO_2$-SiO_2-supported counterparts could be linked with their larger amount of metal sites, as confirmed by H_2 chemisorption (**Table 6.4**) and a larger acidity (**Table 6.5**) confirming that bifunctional catalysts are needed for HDO reaction.

Deactivation of Zn-Ni catalysts is due to carbon deposition (6). There is a direct relationship between the HDO deactivation by coke and catalyst acidity (45) as both Lewis and the Brønsted acids are responsible for the formation of coke. While the Lewis acid sites species bind to the catalyst surface, the Brønsted acid sites act as proton donors forming carbocations that are responsible for the coking and cracking. Interestingly, regardless of the support acidity, all catalysts proved to be highly stable, with a coke formation lower than 2 wt.% for HDO. This result is related with the low to medium acid sites strength observed from NH_3-TPD experiments which are not strong enough to favour coke formation (45). Deactivation by sintering of the active phases can be ruled out because reaction temperature is too low as to sinter Ni particles in the course of both catalytic tests.

Interestingly, the Zn-Ni/Ti-S15 sample was found to be the most promising catalyst for O-removal from bio-liquids. To explain the origin of this unique behaviour of reduced ZnNi/Ti-S15 in the HDO of phenol, one might to have in mind that support surface of this catalyst is decorated with metallic particles (Ni, Zn) and TiOx moieties (**Figure 6.13(A)**) whereas the surface of Zn-Ni/S15 sample is decorated with small Ni and Zn particles only (**Figure 6.13(B)**). In such case, the partially reduced TiOx particles located at the metal interface region sample could contribute to the largest HDO activity of Zn-Ni/Ti-S15 sample, as it is visualized in **Figure 6.13(A)**. The same migration model was proposed previously for Ir/TiO_2

(46). On the other hand, the comparison of the Ni/Si and Zn/Si atomic ratio of both reduced Zn-Ni/Ti-S15 and Zn-Ni/S15 catalysts suggest that the former sample posses a larger amount of surface metallic Ni and Zn species than the latter, which are known to be necessary for activation of hydrogen. Thus, the Zn-Ni/Ti-S15 catalyst possesses a larger amount of anionic vacancies (coordinatively unsaturated sites: CUS) than Zn-Ni/S15 counterpart that can catalyze hydrogenolysis and hydrogenation reactions (47).

The low activities of both Zn-Ni/Ti and Zn-Ni/2Ti-Si in hydrotreating reactions can be explained taking into account their low amount of metal sites deduced from H_2 chemisorption data (**Table 6.4**) suggesting the encapsulation of the Ni with Zn overlayer (**Figure 6.13(C)**). Similarly, the loss of H_2 chemisorption reported previously for Zn-Ni/Al_2O_3 catalyst was explained as due to encapsulation of the Ni with Zn overlayer (48). Indeed, the close contact between Zn and Ni could be also deduced from XRD pattern of the calcined Zn-Ni/Ti and Zn-Ni/2Ti-Si catalysts showing the formation of $Ni_{0.8}Zn_{0.2}O$ phase. Additionally, for both catalysts, the decoration of metallic particles by the partially reduced TiOx moieties might to contribute to the suppression of H_2 chemisorption, as it was explained in terms of the migration model developed for Ir/TiO_2 catalyst (46).

Summarizing, a correlation exists between amount of metal and acid sites, and the catalyst activity of HDO. The Zn-Ni/Ti-S15 was found to be more active in the hydrodeoxygenation of phenol. The balance between metal and acid sites seems to determine the catalytic activity of supported Zn-Ni systems.

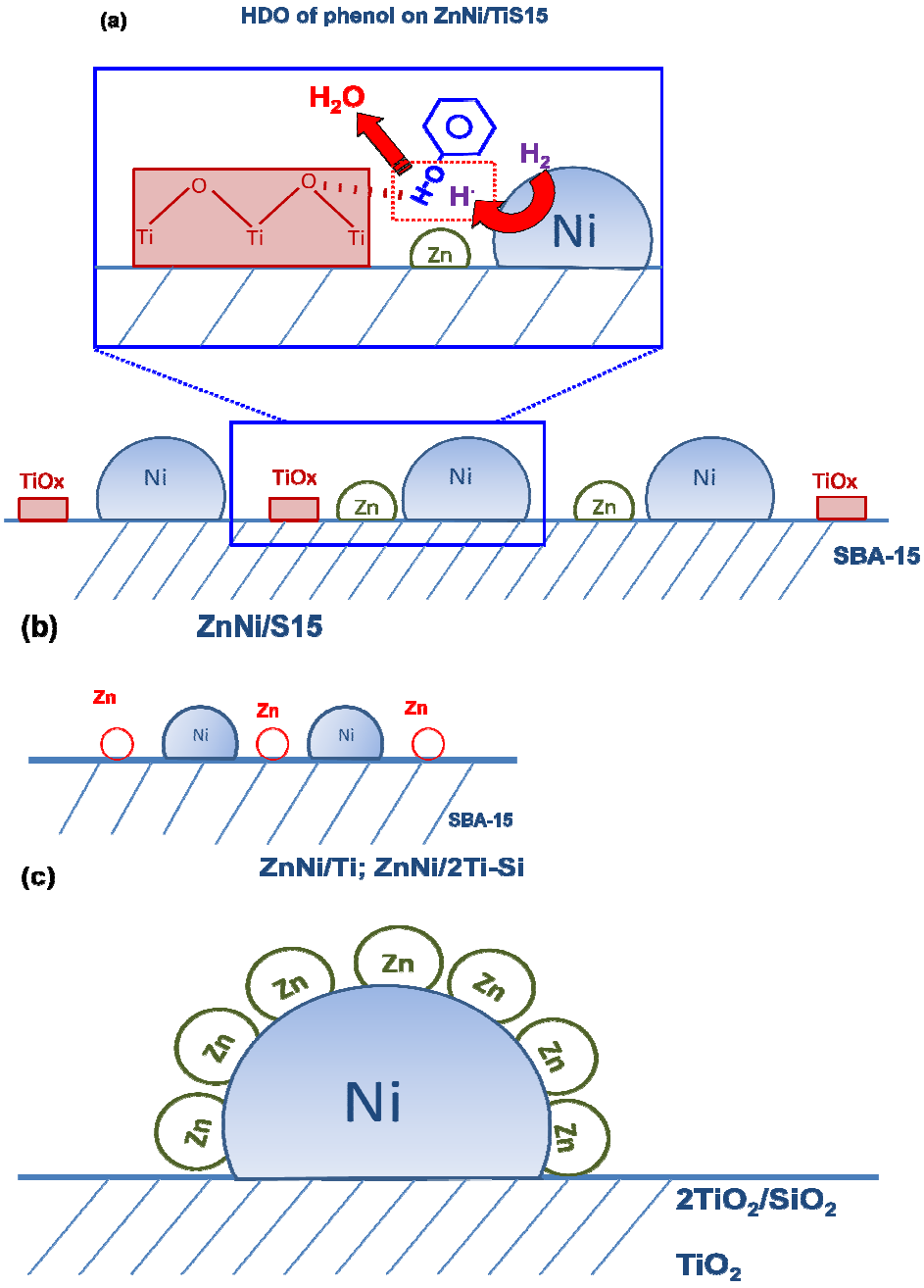

Figure 6.13. Mechanism of structure-activity for ZnNi catalyst serie supported over (A) Ti- SBA-15, (B) SBA-15 and (C) TiO_2 or $2TiO_2/SiO_2$.

6.4. Conclusions

The main conclusions of this chapter were:

(i) The bifunctional Zn-Ni catalyst supported on SBA-15 mesoporous silica material decorated with TiO_2 particles was found to be the most promising catalyst for O-removal from bio-liquids whereas the Zn-Ni catalyst supported on SBA-15 was found to be the most promising for hydrodearomatization of synthetic diesel.

(ii) Both SBA-15 and Ti-SBA-15 substrates were much effective as supports than TiO_2 and $2TiO_2$-SiO_2 counterparts due to their much larger BET specific surface area and acidities.

(iii) The catalyst activity, selectivity and stability were closely linked with the amount of accessible Ni, NiO and acid sites of the catalyst. A balance of these trees is required to design a multifunctional catalyst able to treat fossil and renewable fuels at once.

6.5. References

1. *Preferential formation of benzo[a]pyrene adducts at lung cancer mutational hotspots in P53.* **M.F. Denissenko, A. Pao, M. Tang, G.P. Pfeifer.** s.l. : Science, 1996, Vols. (274) 430-432.

2. *Hydrogenation of aromatics on sulfur-resistant PtPd Bimetallic catalysts.* **R.M. Navarro, B. Pawelec, J.M. Trejo, R. Mariscal, J.L.G. Fierro.** s.l. : Journal of Catalysis, 2000, Vols. (189) 184-194.

3. *Catalytic hydrodeoxygenation.* **Furimsky, E.** s.l. : Applied Catalysis A: General, 2000, Vols. (199) 147-190.

4. **E.G. Baker, D.C. Elliott.** *Method of upgrading oils containing hydroxyaromatic hydrocarbon compounds to highly aromatic gasoline. Patent Number 5180868* U.S., 19 de January de 1993.

5. *Historical developments in hydroprocessing bio-oils.* **Elliott, D.C.** s.l. : Energy & Fuels , 2007, Vols. (21) 1792-1815.

6. *A review of catalytic upgrading of bio-oil to engine fuels .* **P.M. Mortensen, J.D. Grunwaldt, P.A. Jensen, K.G. Knudsen, A.D. Jensen.** s.l. : Applied Catalysis A: General, 2011, Vols. (407) 1-19.

7. *Effects of Support Surface Chemistry in Hydrodeoxygenation Reactions over CoMo/Activated Carbon Sulfided Catalyst.* **G. de la Puente, A. Gil, J.J. Pis, P. Grange.** s.l. : Langmuir, 1999, Vols. (15) 5800-5806.

8. *Coke formation in catalytic cracking.* **W.G. Appleby, G.M. Good, J.W. Gibson.** s.l. : Industrial and engineering chemical process design and development, 1962, Vols. 1 (2) 102-110.

9. *Influence of the Support of CoMo Sulfide Catalysts and of the Addition of Potassium and Platinum on the Catalytic Performances for the Hydrodeoxygenation of Carbonyl,*

Carboxyl, and Guaiacol-Type Molecules. **A. Centeno, E. Laurent, B. Delmon.** s.l. : Journal of Catalysis, 1995, Vols. (154) 288-298.

10. *CoMo/carbon hydrodeoxygenation catalysts: influence of the hydrogen sulfide partial pressure and of the sulfidation temperature .* **M. Ferrari, S. Bosmans, R. Maggi, B. Delmon, P. Grange.** s.l. : Catalysis Today, 2001, Vols. (65) 257-264.

11. *Influence of the impregnation order of molybdenum and cobalt in carbon-supported catalysts for hydrodeoxygenation reactions .* **M. Ferrari, B. Delmon, P. Grange.** s.l. : Carbon, 2002, Vols. (40) 497-511.

12. *Synergy effect in the HDO of phenol over Ni–W catalysts supported on active carbon: Effect of tungsten precursors .* **S. Echeandia, P.L. Arias, V.L. Barrio, B. Pawelec, J.L.G. Fierro.** s.l. : Applied Catalysis B: Environmental, 2010, Vols. (101) 1-12.

13. *Impact of Al and Ti ions on the dispersion and performance of supported NiMo(W)/SBA-15 catalysts in the HDS and HYD reactions.* **A. Olivas, T.A. Zepeda.** s.l. : Catalysis Today, 2009, Vols. (143) 120-125.

14. *CoMo/Ti-SBA-15 catalysts for dibenzothiophene desulfurization.* **R. Nava, R.A. Ortega, G. Alonso, C. Ornelas, B. Pawelec, J.L.G. Fierro.** s.l. : Catalysis Today, 2007, Vols. (127) 70-84.

15. *Enhancement of biphenyl hydrogenation over gold catalysts supported on Fe-, Ce- and Ti-modified mesoporous silica (HMS).* **P. Castano, T.A. Zepeda, B. Pawelec, M. Makkee, J.L.G. Fierro.** s.l. : Journal of Catalysis, 2009, Vols. (267) 30-39.

16. *Enhancement of pyrolysis gasoline hydrogenation over Pd-promoted Ni/SiO2–Al2O3 catalysts.* **P. Castaño, B. Pawelec, J.L.G. Fierro, J.M. Arandes, J. Bilbao.** s.l. : Fuel, 2007, Vols. (86) 2262-2274.

17. *Heterogeneous catalytic transfer hydrogenation and its relation to other methods for reduction of organic compounds.* **R.A.W. Johnstone, A.H. Wilby, I.D. Entwistle.** s.l. : Chemical Reviews, 1985, Vols. (85) 129-170.

18. *Reductive Deposition of Ni-Zn Nanoparticles Selectively on TiO2 Fine Particles in the Liquid Phase.* **H. Takahashi, Y. Sunagawa, S. Myagmarjav, K. Yamamoto, N. Sato, A. Muramatsu.** s.l. : Materials Transactions, 2003, Vols. (44) 2414-2416.

19. *Enhancement of pyrolysis gasoline hydrogenation over Zn- and Mo-promoted Ni/γ-Al2O3 catalysts.* **Y. Qian, S. Liang, T. Wang, Z. Wang, W. Xie, X. Xu.** s.l. : Catalysis Communications, 2011, Vols. (12) 851-853.

20. *Study on Cu-Ni-Zn Catalyst for Catalytic Amination of Fatty Alcohol .* **Q. Li, G. Zhang, S. Peng.** s.l. : Chinese Journal of Catalysis, 2001, Vols. (22) 7-10.

21. *Study of the Individual Reactions of Hydrodesulphurization of Dibenzothiophene and Hydrogenation of 2-Methylnaphthalene on ZnNiMo/γ-Alumina Catalysts.* **C.F. Linares, M. Fernández.** s.l. : Catalysis Letters, 2008, Vols. (126) 341-345.

22. **J.L.G. Fierro, A. López-Agudo, P. Grange, B. Delmon.** Proc. 8th Intern. Congress on Catalysis. Berlín : s.n., 1984. Vols. vol 2. 363-373.

23. *Study of the Individual Reactions of Hydrodesulphurization of Dibenzothiophene and Hydrogenation of 2-Methylnaphthalene on ZnNiMo/γ-Alumina Catalysts.* **C.F. Linares, M. Fernández.** s.l. : Catalysis Letters, 2008, Vols. (126) 341-345.

24. *Influence of the block length of triblock copolymers on the formation of mesoporous silica.* **K. Flodström, V. Alfredsson.** s.l. : Microporous and Mesoporous Materials, 2003, Vols. (59) 167-176.

25. **S.J. Gregg, K.S.W. Sing.** Adsorption, Surface Area and Porosity. London : Academic Press, 1982.

26. *Investigation of the Morphology of the Mesoporous SBA-16 and SBA-15 Materials.* **W.J.J. Stevens, K. Lebeau, M. Mertens, G. Van Tendeloo, P. Cool, E.F. Vansant,.** s.l. : The Journal of Physical Chemistry B, 2006, Vols. (110) 9183-9187.

27. *Characterization of the Porous Structure of SBA-15.* **M. Kruk, M. Jaroniec, C. Hyun Ko, R. Ryoo.** s.l. : Chemistry of Materials, 2000, Vols. (12) 1961-1968.

28. *Effect of molybdenum and tungsten on Co/MSU as hydrogenation catalysts.* **A. Infantes-Molina, J. Mérida-Robles, E. Rodríguez-Castellón, J.L.G. Fierro, A. Jiménez-López.** s.l. : Journal of Catalysis, 2006, Vols. (240) 258-267.

29. *Hydrogenation and Ring-Opening of Tetralin on Nickel Supported Zirconium Doped.* **D. Eliche-Quesada, J. Mérida-Robles, P. Maireles-Torres, E. Rodríguez-Castellón, A. Jiménez-López.** s.l. : Langmuir, 2003, Vols. (19) 4985-4991.

30. *Activation of supported nickel oxide by platinum and palladium.* **E.J. Nowak, R.M. Koros.** s.l. : Journal of Catalysis, 1967, Vols. (7) 50-56.

31. *Influence of support calcination temperature on properties of Ni/TiO2 for catalytic hydrogenation of o-chloronitrobenzene to o-chloroaniline.* **N.Yao, J. Chen, J. Zhang, J. Zhang.** s.l. : Catalysis Communications, 2008, Vols. (9) 1510-1516.

32. *Investigation of Ni-based alumina-supported catalysts for the oxidative dehydrogenation of ethane to ethylene: structural characterization and reactivity studies.* **E. Heracleous, A.F. Lee, K. Wilson, A.A. Lemonidou.** s.l. : Journal of Catalysis, 2005, Vols. (231) 159-171.

33. *Effect of Thermal Treatment on the Nickel State and CO Hydrogenation Activity of Titania-Supported Nickel Catalysts.* **S.W. Ho, C.Y. Chu, S.G. Chen.** s.l. : Journal of Catalysis, 1998, Vols. (178) 34-48.

34. *Nickel supported on titania-silica: Preparation, characterisation and activity for liquid phase hydrogenation of acetophenone .* **Kumbhar, P.S.** s.l. : Applied Catalysis A: General, 1993, Vols. (96) 241-252.

35. *Bimetallic Ru/Ni supported catalysts for the gas phase hydrogenation of acetonitrile.* **P. Braos-García, C. García-Sancho, A. Infantes-Molina, E. Rodríguez-Castellón, A. Jiménez-López,.** s.l. : Applied Catalysis A: General, 2010, Vols. (381)132-144.

36. *Effective alkene epoxidation with dilute hydrogen peroxide on amorphous silica-supported titanium catalysts.* **M.C. Capel-Sanchez, J.M. Campos-Martin, J.L.G.**

Fierro, M.P. de Frutos, A. Padilla Polo. s.l. : Chemical Communications, 2000, Vols. 855-856.

37. *CoMo/Ti-SBA-15 catalysts for dibenzothiophene desulfurization .* **R. Nava, R.A. Ortega, G. Alonso, C. Ornelas, B. Pawelec, J.L.G. Fierro.** s.l. : Catalysis Today, 2007, Vols. (127) 70-84.

38. *Practical Surface Analysis. Auger and X-Ray Photoelectron Spectroscopy.* **D. Briggs, M.P. Seah.** New York, Salle and Sauerländer : Wiley, 1990.

39. *Supported gold catalysts in SBA-15 modified with TiO2 for oxidation of carbon monoxide.* **C.L. Peza-Ledesma, L. Escamilla-Perea, R. Nava, B. Pawelec, J.L.G. Fierro.** s.l. : Applied Catalysis A: General, 2010, Vols. (375) 37-48.

40. *Properties of Ni/Si02 catalysts: Relationship to ether formation from alcohols.* **L.S. Kraus, Herman Pines, J.B. Butt.** s.l. : Journal of Catalysis, 1991, Vols. (128) 337-351.

41. *New interpretations of XPS spectra of nickel metal and oxides.* **A.P. Grosvenor, M.C. Biesinger, R.S.C. Smart, N.S. McIntyre.** s.l. : Surface Science, 2006, Vols. (600) 1771-1779.

42. *Hydrogenation of oleic acid over ruthenium catalysts .* **M.J Mendes, O.A.A Santos, E Jordão, A.M Silva.** s.l. : Applied Catalysis A: General, 2001, Vols. (217) 253-262.

43. *Development of new catalytic systems for upgraded bio-fuels production from bio-crude-oil and biodiesel .* **V.A. Yakovlev, S.A. Khromova, O.V. Sherstyuk, V.O. Dundich, D.Yu. Ermakov, V.M. Novopashina, M.Yu. Lebedev, O. Bulavchenko, V.N. Parmon.** s.l. : Catalysis Today, 2009, Vols. (144) 362-366.

44. *Adsorption of activated ketones on platinum and their reactivity to hydrogenation: a DFT study.* **A. Vargas, T. Bürgi, A. Baiker.** s.l. : Journal of Catalysis, Vols. (222) 439-449.

45. *Deactivation of hydroprocessing catalysts .* **E. Furimsky, F.E. Massoth.** s.l. : Catalysis Today, 1999, Vols. (52) 381-495.

46. *Kinetic study of liquid-phase hydrogenation of citral over Ir/TiO2 catalysts.* **P. Reyes, H. Rojas, J.L.G Fierro.** s.l. : Applied Catalysis A: General, 2003, Vols. (248) 59-65.

47. *Hydrodeoxygenation of benzofuran over sulfided and reduced Ni–Mo/γ-Al2O3 catalysts: Effect of H2S.* **A.Y. Bunch, X. Wang, U.S. Ozkan.** s.l. : Journal of Molecular Catalysis, 2007, Vols. (270) 264-272.

48. *SMSI-like behavior and Ni promotion effect on NiZnAl catalysts in steam reforming of methanol.* **Y. Men, M. Yang.** s.l. : Catalysis Communications, 2012, Vols. (22) 68-73.

Chapter 7

HDO of phenol over zeolite-supported Pt and Ir catalysts

Chapter 7

HDO of phenol over zeolite-supported Pt and Ir catalysts

This chapter describes the effect of support (HY and ZSM-5) and metal phase (Pt, Ir, Pt+Ir) in the reaction of hydrodeoxygenation (HDO) of phenol, which is a typical compound present in bio-oils derived from fast pyrolysis of lignocelluloses' biomass. The oxide precursors, fresh reduced and spent catalysts were studied by several physical and chemical techniques (chemical analysis, N_2 sorption, time resolved XRD, TPR, TPD-NH_3, ^{29}Si and ^{27}Al NMR, XPS, HRTEM) and their catalytic response were evaluated in both batch and fixed-bed flow reactors under 30 bar of hydrogen pressure and temperatures of 200 °C and 310 °C, respectively. In general, all catalysts supported on the HY zeolite exhibited lager HDO activity than the ZSM-5-supported ones. This was linked with a larger S_{BET} and pore diameter of the HY zeolite favoring diffusion of the reactant and products within inner pore network. For all catalysts, the appearance of cyclohexanol suggests that the phenol transformation proceeds through the route of ring hydrogenation followed by hydrogenolysis. The Pt-Ir/HY catalyst demonstrated to be most active among the catalysts studied (selectivity to O-free products around 99%) including two

commercial catalysts (metallic 0.3Pt/Al_2O_3 and sulfided CoMo/Al_2O_3). The *in situ* reduction of this sample monitored by X-ray diffraction demonstrated that platinum was reduced almost entirely and only a small fraction of Ir (ca. 2%) became alloyed with Pt. The iridium phase induces a higher dispersion of platinum which enhances catalyst performance in the target reaction.

7.1. Introduction

Nowadays, the direct liquefaction of biomass followed by upgrading and refining is regarded as very promising alternative to fossil fuels. In the existing petroleum refining infrastructure, traditional hydrotreatment process can be employed for upgrading pyrolysis bio-oils by oxygen removal and by increasing of hydrogen content (1) (2). However, the conventional hydrotreating catalysts based on metal sulfides are not enough effective for hydrodeoxygenation (HDO) reaction because of their quick deactivation by water product and loss of the active phase by oxidation of the sulfide phases (3) (4) (5). Therefore, the challenge is to design new multifunctional catalysts capable of maintaining stability during hydrotreatment of bio-liquids.

It is well known that bifunctional catalysts having both acid and metal sites are needed for HDO reaction: the metal sites are needed for hydrogenation whereas H+ sites of the support are needed for dehydration (6). Since noble metals showed high hydrogenation ability at low temperatures and bio-liquids possess a very low amount of S-containing compounds capable to poison the metal sites, the noble metals appear as a good option for substitution of metal sulfides in the catalyst formulation (7) (8) (9). Considering the role of the support, zeolites are good alternatives to the alumina substrate. However, the zeolite needs to satisfy two

conditions: (i) the zeolite pore dimensions must be above the kinetic diameters of the hydrocarbon molecules in the bio-liquids and (ii) zeolite acidity must be optimized in order to minimize coke formation. Concerning the former condition, recent studies have shown that zeolites are better substrates than alumina or silica in hydrodeoxygenation of phenol due to their regular pore system and a strong acidity (6) (10).

Recently, hydrotreating of O-containing model compounds have been reported over various zeolite-supported noble metal catalysts in both flow and batch reactors (11) (12) (13) (14). The HDO of phenol reaction was carried out at high H_2 pressure (4 MPa). Upon the reaction conditions employed, the phenol transformation over Pt/Beta catalysts proceeds via hydrogenation-hydrogenolysis ring-coupling reactions producing monocyclic and useful bicyclic hydrocarbons (6). On the contrary, bifunctional transalkylation and hydrodeoxygenation of anisole was reported for Pt/HBeta catalyst (10). The effects of the substrate structure on HDO activity of Pd catalysts supported on H-Beta and ZSM-5 zeolites was by studied by Čejka *et al.* (15) (12). As expected, it was found that substrate structure has a determining effect on the catalyst activity being H-Beta zeolite more suitable as support than ZSM-5 one (15) (12). Similarly, Pt catalysts supported on mesoporous ZSM-5 showed better performance in dibenzofuran HDO than its counterpart supported on microporous ZSM-5 zeolite due to the diffusion limitation of dibenzofuran in the microporous structure of ZSM-5 (10).

Considering the stability of substrate, a particularly promising approach to the development of novel HDO catalysts lies in the use of highly acidic ultrastable HY zeolite substrate. This is because the ultrastable HY zeolite has the advantages of higher surface-to-volume ratio than alumina, variable framework compositions and high hydrothermal stability (16). Moreover, this zeolite showed interesting

textural properties because its structure comprises hexagonal prisms, sodalite cages and supercages with maximum openings of 0.26, 0.26 and 0.74 nm, respectively. Thus, this zeolite has an appropriate structure to allow diffusion of large molecules. However, a large deactivation of bifunctional zeolite-supported noble metal catalysts in the HDO of phenol was reported (17). Moreover, for zeolite-based catalysts the reaction temperature should be optimized because at high reaction temperature (350 to 450 ºC) oxygenates should be transformed to carbonaceous deposits and to a much lesser extent to alkanes (18) (19).

In line with the above, the present work focused on the effect of support (HY vs. ZSM-5) and the effect of Ir alloying with Pt on the yields to O-free products in the HDO of phenol. This model compound was used as representative of the compounds present in the pyrolysis oil.

7.2. Experimental

7.2.1. Preparation of supported Pt-Ir catalysts

Two commercial supports were employed to deposit Pt and/or Ir phases: (i) ultrastable HY (USY; Conteka, B.V., Sweden) Si/Al = 4.56, Na_2O content 0.14 wt.%, unit cell 2.454 nm, BET = 662 $m^2\ g^{-1}$ and (ii) ZSM-5 zeolites (Akzo Nobel, Sweden) Si/Al = 19, BET = 331 $m^2\ g^{-1}$.

Monometallic Pt- or Ir/HY and Pt or Ir/ZSM-5 catalysts were prepared by impregnating the proper weight of support with aqueous solutions of hydrogen hexachloroplatinate(IV) hydrate (Sigma, reagent grade) and iridium trichloride trihydrate (Johnson Matthey, Alfa), respectively.

Two binary Pt-Ir catalysts were prepared by simultaneous impregnation of HY and ZSM-5 substrates following the incipient wetness method using an aqueous solution containing $IrCl_3 \cdot H_2O$ and $H_2PtCl_6 \cdot 6H_2O$. Each support was loaded with 3 wt% of Pt, 3 wt% of Ir and 1.5 wt% of Ir - 1.5wt% of Pt, respectively. After impregnation, the catalysts were dried overnight in air at 110 °C and then calcined at 400 °C for 3 h.

7.2.2. HDO of phenol in a flow reactor

The gas-phase hydrodeoxygenation of phenol was performed in a high-pressure laboratory-scale set-up equipped with down-flow fixed bed catalytic reactor (see **Chapter 3, Figure 3.3**). The phenol was diluted in decaline to obtain a 2 wt.% solution. The reaction was carried out at 310 °C, 3 MPa of total pressure, H_2 flow rate = 7 L (STP) h^{-1}, WHSV = 3.83 h^{-1} and employing 0.10 g of the catalyst (particle size: 0.25- 0.30 mm) diluted up 0.5 cm^3 with SiC (particle size: 0.25 mm). Before activation, catalyst was dried at 160 °C for 1 h with a N_2 flow of 100 mL/min, then catalyst was reduced *in situ* at 350 °C for 3 h with a mixture H_2 : N_2 = 1:10 molar. Before running the reaction, the N_2 pressure increased to the desired value (3.0 MPa), and the catalyst bed was heated to reaction temperature of HDO (310 °C). After closing the flow of N_2, the liquid feed (2% by volume of phenol dissolved in decalin) injected by a high pressure pump Knauer HPLC (0.3 ml min^{-1}; WHSV = 3.9 h^{-1}) in a hydrogen stream (40 $mL.min^{-1}$) was fed to the reactor. The reactor effluents were condensed and liquid samples were analyzed using an Agilent 6890A GC equipped with a FID detector. Two commercial catalysts 0.3%Pt/Al_2O_3 (supplied by Johnson & Matthey) and $NiMo/\gamma\text{-}Al_2O_3$ (HR-348, supplied by Procatalyse) were also studied for comparison purposes.

7.2.3. HDO of phenol in a batch reactor

The catalyst activity was evaluated also in the HDO of phenol reaction carried out in a batch reactor with a volume of 300 mL (**see Chapter 2, Figure 3.3**). A batch type reaction is important because it allows to observe reaction intermediates and to determine the reaction path. The autoclave was equipped with a stirrer for maximum dispersion of gas in a liquid system (900 rpm).

The samples were collected through a tube of diameter 1/8″. The hydrogen is introduced into the reactor through a pressure regulator which maintains a constant pressure during the course of the experiment. Reagent (10.6 mmol of phenol) was dissolved in tetralin (80 mL) and using hexadecane as internal standard. 100 mg of catalyst previously reduced (350 °C, 3 h) were placed in the reactor. The system was heated to reaction temperature (200 °C) under N_2 atmosphere. Then N_2 was replaced by H_2 pressurizing the reactor to 3 MPa. This last step was considered time zero of the reaction.

Samples were taken periodically during the course of the reaction and analyzed on a Hewlett-Packard 5890A chromatogram (Fig. 4b.) provided with a FID detector and a DB-1 capillary column (30 m long x 0.450 mm x 2.55 μm thick) to a temperature of 250 °C. Response factors of reagent and products were measured from solutions of known concentrations.

7.3. Results and discussion

7.3.1. Characterization of the oxide precursors

7.3.1.1. Chemical analyses

The Pt and It loading was determined by X-ray fluorescence (XRF) spectrometry. The composition of the HY- and ZSM-5-based samples is presented in **Table 7.1** where nominal values of Pt and Ir loading are compared to the ones obtained from the experimental XRF analysis. As seen in this table, for all samples the metal content determined by XRF is lower than of the theoretical ones (3 wt.%). Noticeably, both binary Pt-Ir/HY and Pt-Ir/ZSM-5 samples show the same total (Pt+Ir) metal loading (2.0 wt.%). On the contrary to binary samples, the ZSM-supported monometallic samples show a larger metal loading than their HY-supported counterparts.

Table 7.1. Metal loading and XRD data of the oxide precursors

Catalyst	Pt	Ir	Pt	Ir	XRD	
	Nominal (%)		XRTF (%)		crystal size (nm)	Phase
Pt/ HY	3.0	0	1.6	0	59.4	Pt^0
Pt-Ir/ HY	1.5	1.5	1.0	1.0	32.9	Pt^0
Ir/ HY	0	3.0	0	1.9	-	-
Pt/ ZSM-5	3.0	0	2.7	0	44.5	Pt^0
Pt-Ir/ ZSM-5	1.5	1.5	1.1	0.9	35.1	Pt^0
Ir/ ZSM-5	0	3.0	0	2.3	-	-

7.3.1.2. Wide-angle XRD

Wide- angle X-ray diffraction patterns were recorded to investigate the presence of any crystallite species in the oxide precursors. **Figure 7.1** shows the XRD patterns of the HY- and ZSM-5-based samples. Considering, the reference patterns taken from the database included in the program used (X'Pert High Score), all ZSM-5-suported catalysts exhibited typical diffraction lines at 2θ angles of 7.9°, 8.8°, 14.7°, 15.5°, 23.3º and 23.7° (JCPDS 01-079-2401) whereas the HY-supported catalysts showed many narrow peaks at 2θ values of 6.3, 10.3°, 12.0°, 15.8°, 20.6° and 23.9° associated with the zeolite faujasite (JCPDS 01-077-1549).

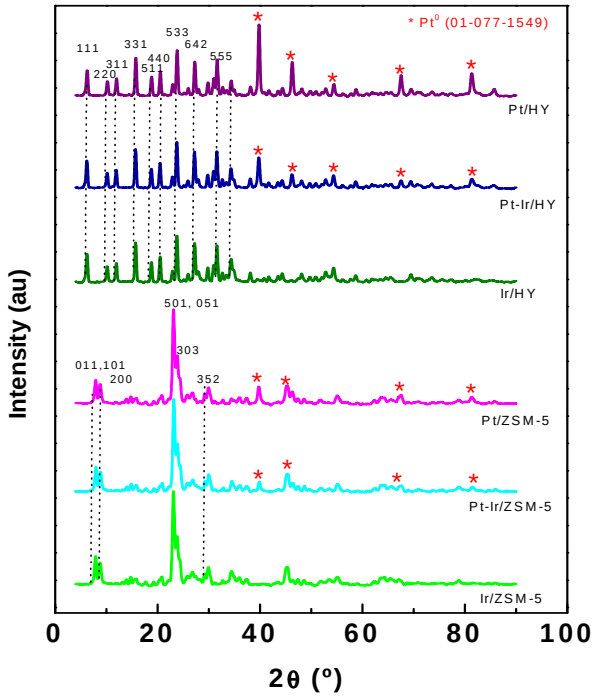

Figure 7.1. Wide-angle X-ray diffraction patterns of oxide precursors. The dashed vertical lines are the Bragg positions for pure zeolites.

For Pt and Pt-Ir samples supported on HY and ZSM-5 zeolites, the peaks at ca. 39.8°, 46.2°, 67.5°, 81.3° and 85.7° can be associated with metallic Pt phase having a cubic crystal structure (JCPDS 00-004-0802). Thus, the XRD patterns of the two binary samples present the main characteristic peaks of the crystalline of Pt phase (JCPDS card, number 00-004-0802), in particular, the planes (111), (200) and (220), showing that both alloy Pt-Ir catalysts mainly resemble the single-phase disordered structure (solid solution). The diffraction peaks in the Pt-Ir alloy oxide precursors are not shifted to 2θ higher values with respect to the corresponding peaks in the monometallic counterparts. The absence of this shift cannot to exclude possibility of the Ir atoms incorporation in the structure of Pt because of both Ir and Pt atoms showed very close atomic radii (Pt = 1.83 Å and Ir = 1.87 Å).

The mean size of the Pt crystallites was estimated from XRD using Scherrer's equation. The average Pt^0 crystallite sizes of Pt/HY and Pt/ZSM-5 samples, calculated from XRD line broadening of the most intense 2θ line of 39.8º are listed in Table 7.1. As seen in this table, the average Pt^0 crystallite sizes of monometallic Pt/HY and Pt/ZSM-5 samples were much larger (59.4 nm and 44.5 nm, respectively) than that of the binary Pt-Ir/HY and Pt-Ir/ZSM-5 catalyst (32.9 nm and 35.1, respectively). Thus, it can be concluded that Pt dispersion on the surface of binary precursors is enhanced with respect to its monometallic counterparts.

Finally, for Ir/HY and Ir/ZSM-5 catalysts, only the diffraction lines of the zeolite substrates were observed. Since the Ir crystallites were below the XRD detection limit, this may indicate either the formation of well-dispersed amorphous phases and/or the presence of Ir crystals smaller than 4 nm.

7.3.1.3. N_2 adsorption-desortion isotherms

The textural properties of bare supports before and after metal loading were evaluated from nitrogen adsorption–desorption isotherms at -196 ºC. As can be seen in **Figure 7.2**, the N_2 isotherms of HY- and ZSM-5-based catalysts are of Type I/II, which are typical for the micro- and macroporous structures. In such case, the formation of a monolayer at low relative pressure is the prevailing process whereas at high relative pressure a multilayer adsorption takes place (20). According to the IUPAC classification, all isotherms have type H3 hysteresis loop, which is indicative of solids having pores of non-uniform size and/or shape (20). For HY-based catalysts, the larger adsorbed volume observed in the high relative pressure region suggest the presence of macropores. This is rather surprising, although mixing this zeolite with alumina by the manufacturer is a common practice.

The Barret-Joyner-Halenda (BJH) formula was employed to determine pore size distribution (PSDs) of the oxide precursors in both meso- (2-50 nm) and macroporous (> 50 nm) regions. Unfortunately, the BJH method is imprecise in the region below 1 nm, where the supercages of the HY zeolite appear.

By considering the average pore diameter compiled in **Table 7.2**, both ZSM-5 and HY samples shows similar pore diameters (in the range 3.5-3.9 nm). Pt/HY, Pt-Ir/ZSM-5 and Ir/ZSM-5 catalysts show a little larger pore diameter than their respective unloaded supports. This could be explained in terms of the decrease of micropore volumes due to pore mouth blocking by the metal oxides particles.

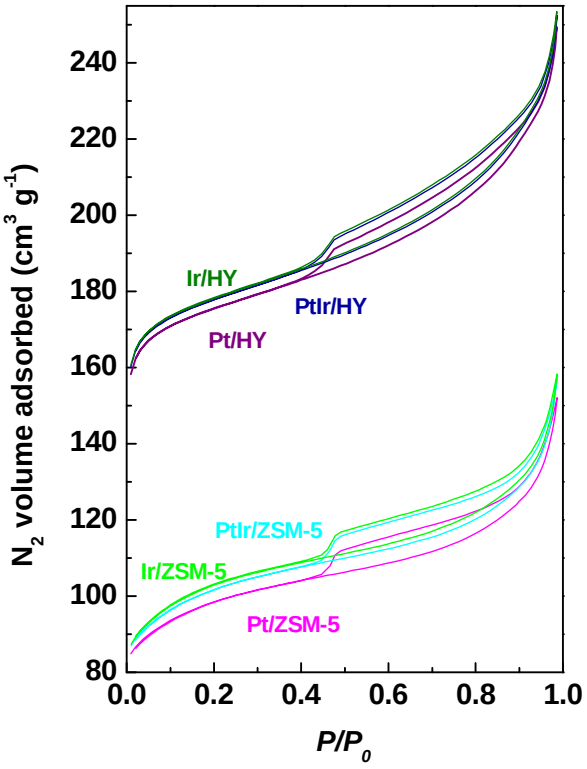

Figure 7.2. Nitrogen adsorption-desorption isotherms at -196°C of oxide precursors.

The specific BET surface area (S_{BET}) of bare HY substrate is two-fold larger than those of bare ZSM-5 (662 m^2/g vs. 326 m^2/g). Metal loading into the ZSM-5 substrate led to very small decrease of specific surface area (309-323 m^2/g). A very small decrease in the S_{BET} area after metal oxide loading into ZSM-5 substrate indicates that the main location of metals occurs on the exterior zeolite surface. On the contrary, a significant decrease in the specific surface area is observed after metal incorporation into HY zeolite (from 662 m^2/g to 540-548 m^2/g) suggesting the

possible location of metal phases within inner ore structure. To confirm this possibility, the normalized specific surface area (NS_{BET}) has been calculated.

Table 7.2. Textural properties of the oxide precursors[a].

Catalyst	NS_{BET}	S_{BET} (m^2/g)	d (nm)	$V_{micropores}$ (cm^3/g)	V_{total} (cm^3/g)
HY	-	537	1.9	0.24	0.40
Pt/ HY	1.02	540	5.0	0.23	0.37
Pt-Ir/ HY	1.04	547	5.0	0.23	0.37
Ir/ HY	1.04	548	5.2	0.23	0.38
ZSM-5	-	326	3.5		0.12
Pt/ ZSM-5	0.97	309	3.7		0.13
Pt-Ir/ ZSM-5	1.00	319	3.6		0.13
Ir/ ZSM-5	1.01	323	3.5		0.14

[a] As determined from N_2 adsorption-desorption isotherms at -196 °C; S_{BET}: BET surface area; V_{total}: adsorption total pore volume; $V_{micropores}$: *t*-plot micropore volume; *d*: BET adsorption average pore diameter; NS_{BET}: normalized BET surface area.

For all samples, the normalized BET surface area is close to 1.0 suggesting homogeneous metal species dispersion on the support surface as well as within the inner zeolite porous structure (in case of the HY, probably in the supercages).

7.3.1.4. Temperature-programmed reduction (TPR)

As temperature-programed reduction (TPR) provides information about the dispersion state of the metallic components as well as on the metal-support interactions, the reducibility of supported Pt and Ir species on the surface of HY and ZSM-5 zeolites was studied by temperature-programmed reduction (TPR). TPR profiles of monometallic Pt(Ir) and bimetallic Pt-Ir oxide precursors are shown in **Figure 7.3.** As seen in this figure, the TPR profile of both monometallic Pt/HY catalyst show unique, very strong peak with maxima at 452 °C. Considering the XRD information (*vide supra*) and literature data (21), this peak can be ascribed to the reduction of Pt^{2+} species located in supercages and/or sodalite units in the zeolite HY. For the Pt/HY sample, this peak is shifted from 503 to 452 °C with respect to the 0.72% Pt/HY sample prepared using the same platinum precursor but calcined at much lower temperature than those employed in this work (400 °C vs. 300 °C) (22). On the other hand, for Pt/ZSM-5 catalyst a broad peak with maximum around 784 °C could be attributed to the reduction of some Pt species located within the inner structure of ZSM-5. Thus, we can conclude that the calcination of Pt/ZSM-5 sample at 400 °C induced some migration of platinum oxides to sites having higher coordination degree.

It is known that the interaction between two metals as well as the metal-support interaction can affect the reduction temperature. In the case of weak interaction, the metal oxide species can be easy reduced at lower temperature than in the case of a strong metal-support interaction (SMSI). Regardless of the support, two monometallic Ir samples showed peaks at 149 °C, 217 °C (very strong) and 360 °C. The small broad peak at 149 °C comes likely from the reduction of small clusters of IrO_x deposited on the surface of both zeolites. The intermediate strong

peak around 217 °C could be attributed to iridium oxide species interacting strongly with the support. Finally, a small board peak with maxima around 360 °C is probably due to a reduction of Ir ions located at different exchange positions within the zeolite structure (23).

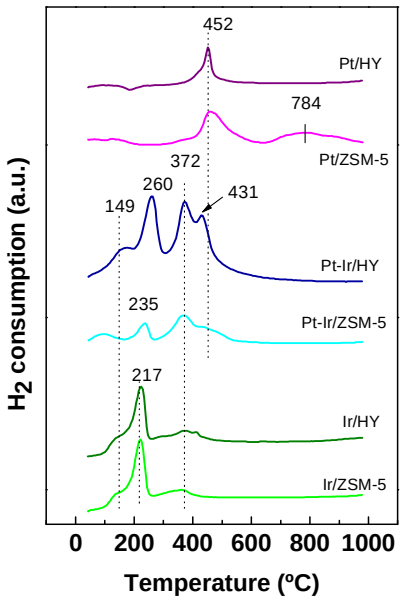

Figure 7.3. TPR profiles of oxide precursors.

The binary Pt-Ir/HY catalyst shows a higher exposure of metal species than its Pt-Ir/ZSM-5 counterpart, as it can be obtained by comparing H_2 consumptions of both catalysts (see **Figure 7.3**). However, their peak at 431 °C associated with the reduction of Pt^{2+} is upward shifted with respect to the same peaks of the monometallic Pt/HY and Pt/ZSM-5 samples (from 452 °C to 431 °C). Thus, in good agreement with the study on the wet-impregnated Pt-Ir/γ-Al_2O_3 catalysts by Huang et al. (24), the iridium addition promotes the reduction of platinum species in the bimetallic oxide precursors. Such interaction between both Pt and Ir metals

probably start already during the drying step at 120 °C (24). Indeed, considering the shape and peak location in the TPR profiles of binary samples, this interaction is possible because of the spatially well-distributed metal precursors in the substrate during the incipient wetness sample preparation (25).

Table 7.3. Temperature maxima (°C) of the TPR peaks

Catalyst	Ir $^{(IV)}$	Ir $^{(IV)}$	Ir $^{(IV)}$	Pt$^{(II)}$	Pt$^{(II)}$
Pt/ HY	-	-	-	452 (strong)*	-
Pt/ ZSM-5	-	-	-	452 (strong)*	784
Ir/ HY	149	217 (strong)*	372	-	-
Ir/ ZSM-5	149	217 (strong)*	372	-	-
Pt-Ir/ HY	149	260 (strong)*	372 (strong)*	431 (strong)*	-
Pt-Ir/ ZSM-5	-	235 (strong)*	372 (strong)*	431	-

*Intensity of the peak

Similarly to Pt species, the higher reduction temperature of Ir species on both binary samples with respect to their Ir/HY and Ir/ZSM-5 counterparts can be considered as a proof of a stronger metal-support interaction. This could be explaining considering the charge distribution and charge effects during preparation. It is known that hexachloroplatinic acid ($H_2PtCl_6{\cdot}6H_2O$) is easily dissolved in water whereas iridium trichloride ($IrCl_3{\cdot}3H_2O$) needs heating and vigorous stirring for its solubilization. The anion $PtCl_6^{2-}$ and polar $IrCl_3$ precursor species are hydrated and thus surrounded by water ligands held in place by ion–dipole and dipole–dipole interactions, respectively. Upon mixing the zeolite with the aqueous metal solution, a stronger interaction between zeolite and the $PtCl_6^{2-}$

anion occurs than with $Cl^{\delta-}$ in $IrCl_3$. As a consequence, the TPR peak is shifted towards a higher reduction temperature, which is generally considered as proof of a stronger metal-support interaction (26).

7.3.2. Characterization of fresh reduced catalysts

7.3.2.1. *In situ* reduction monitored by Time-Resolved High Resolution XRD

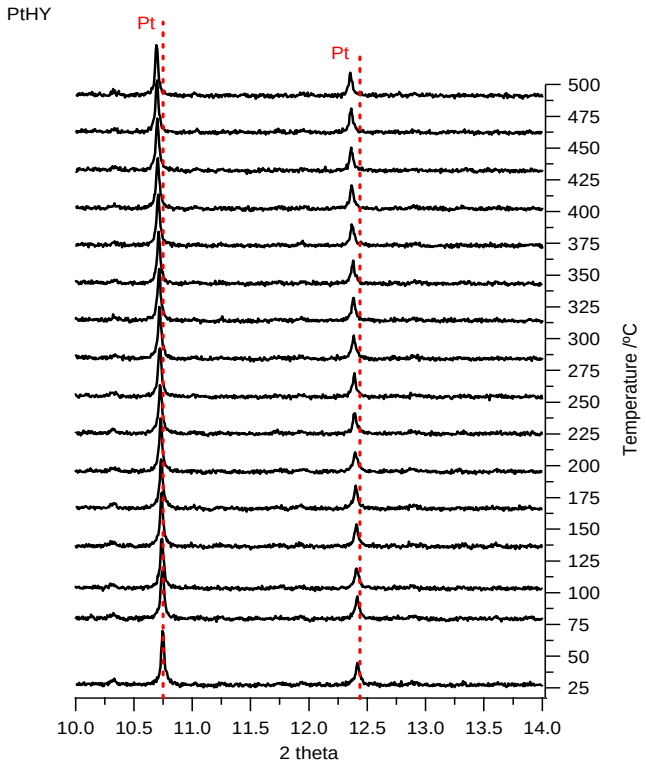

Figure 7.4. Time resolved XRD patterns of the in *situ* reduced Pt/HY.

The influence of temperature on the reduction of Pt/HY and Pt-Ir/HY catalysts was monitored by *in situ* time-resolved high resolution X-Ray diffraction by heating the sample from room temperature to 500 ºC under a 5%H_2/He flow (**Figures 7.4** and **7.5,** respectively**)**.

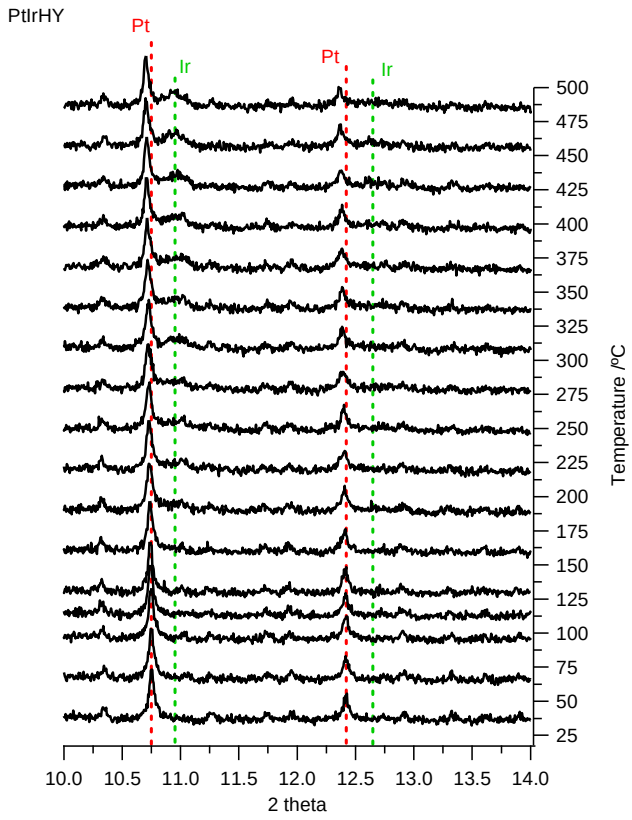

Figure 7.5. Time resolved XRD patterns of the *in situ* reduced Pt-Ir/HY

Table 7.4 shows the particle size for Pt and Ir in the monometallic and bimetallic catalysts. Platinum particle size of bimetallic sample is slightly smaller (35.8 nm) than the monometallic sample (46.4 nm). In spite their similar content and preparation method, Iridium is much better dispersed than the platinum.

The dimension of the Pt cell parameter of the bimetallic sample is slightly smaller than in the monometallic sample, suggesting a small degree of alloying. Taking into consideration the reference standards for the Pt (3.923) and Ir (3,839) metal from the ICSD, the shift observed in the samples (0.0017 Å, **Table 7.2**) corresponds approximately to 2% of Ir alloying degree. In other words, only a small fraction of the Ir incorporated is forming an alloy with Pt.

Table 7.4. Pt cell parameter and crystallite size (determined from Scherrer equation) for the Pt/HY and Pt-Ir/HY samples

Sample	Pt cell parameter (Å)	Particle size (/nm	
		Pt	Ir
Pt/HY	3.924103	46.4	-
Pt-Ir/HY	3.922404	35.8	18.1

Figure 7.6.A shows the evolution of cell dimension with temperature for both Pt/HY and PtIr/HY samples. No abrupt changes are observed in the lattice parameter of the bimetallic sample. The cell parameters expand linearly with temperature in a similar slope to the one obtained for the monometallic sample.

The evolution of iridium metallic phase with temperature is displayed in **Figure 7.6.B**. At low reduction temperature, there are no peaks ascribed to Ir, which reduction starts at 150 °C. Its weight fraction increases sharply up to 300 ºC and smoothly afterwards. At the end of the experiment iridium is completely reduced, as indicated by the stabilization of the fraction at the end of the reduction.

Another indication that the iridium reduction is complete is that Ir/Pt ratio is close to 50%, the nominal amount present in the samples.

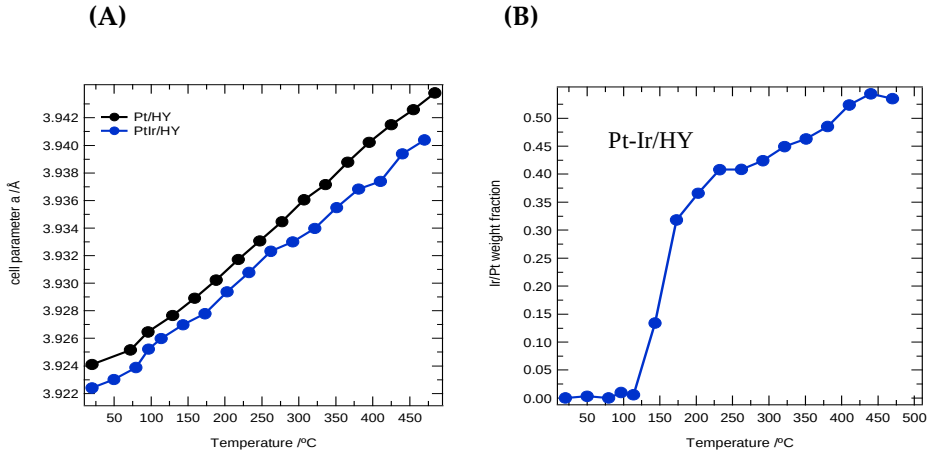

Figure 7.6. Influence of the reduction temperature on the Pt cell parameter for Pt/HY and Pt-Ir/HY (**A**); and on the Ir/Pt weight fraction of the Pt-Ir/HY sample (**B**), as determined by time-resolved high resolution XRD.

7.3.2.2. ^{29}Si NMR and ^{27}Al NMR

Si/Al ratio was also calculated from ^{29}Si NMR and ^{27}Al NMR techniques. As the number of electrons of Si and Al are identical it can't be distinguished by X-ray diffraction. Therefore, the catalysts were studied by ^{29}Si NMR magic angle spinning spectroscopy. **Figure 7.7** shows a set of bands corresponding to Si in a tetrahedral environment in which next neighbors are 4Al, 3Al 1Si, 2Al 2Si, 1Al 3Si, 4Si whereas ^{27}Al NMR spectra are shown in **Figure 7.8**. The chemical shift corresponding to Si and Al bonds are listed in **Table 7.5**.

An analysis of the intensities of these bands can provide information about replacing Si/Al. The Si/Al ratios of each catalyst can be calculated by Equation 7.1:

$$\text{Si/Al} = \frac{\sum I}{0.25 * \sum_{1}^{4} n * In} \quad \textbf{(Equation 7.1)}$$

Table 7.5 shows calculated values from the intensities of the bands of Si surrounded different numbers of Al, HY series has greater amount of Al around the silanol groups, which induces a strong electron density transfer OH groups and generates a large number of strong acid sites.

Table 7.5. ^{29}Si and ^{27}Al NMR data of reduced HY- and ZSM-5 supported samples

Catalyst	Si/Al ratio	**Chemical shift (ppm)**	
		^{29}Si	**^{27}Al**
Pt/ HY	6.0	-88.8 : Si(*3*Al) -94.54: Si(2Al) -100.7: Si(*1*Al) -105.7: Si(*0*Al) -111.0: Si(*0*Al) amorphe	59.0 -1.1
Pt-Ir/ HY	5.1	2.4 : Si(*3*Al) 10.9: Si(2Al) 42.9: Si(*1*Al) 56.4: Si(*0*Al)	58.3 33.8 -1.6
Ir/ HY	5.8	-88.4 : Si(*3*Al) -94.2: Si(2Al) -100.5: Si(*1*Al) -105.8: Si(*0*Al) -110:1: Si(*0*Al) amorphe	58.2 -1.5
Pt/ ZSM-5	22.9	-105.4: Si(*1*Al); -111.4: Si(*0*Al; -114.7: Si(*0*Al)	53.9 -2.1
Pt-Ir/ ZSM-5	23.0	-105.4: Si(*1*Al) -111.6: Si(*0*Al) -115.0: Si(*0*Al)	53.8 -1.8
Ir/ ZSM-5	25.8	-105.2: Si(*1*Al) -111.5: Si(*0*Al) -114.8: Si(*0*Al)	53.8 -1.6

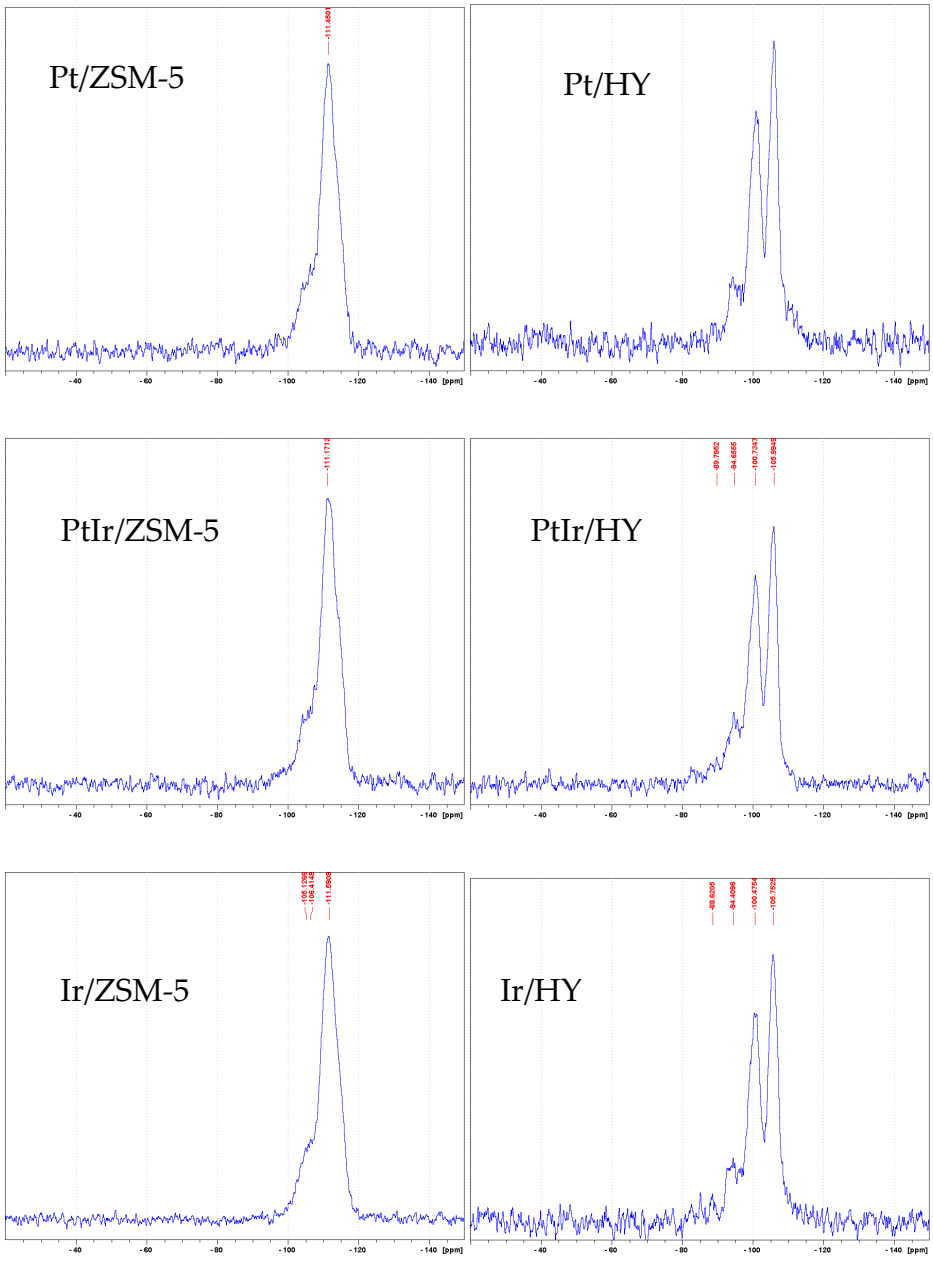

Figure 7.7. ^{29}Si NMR spectra of the calcined Pt-Ir catalysts.

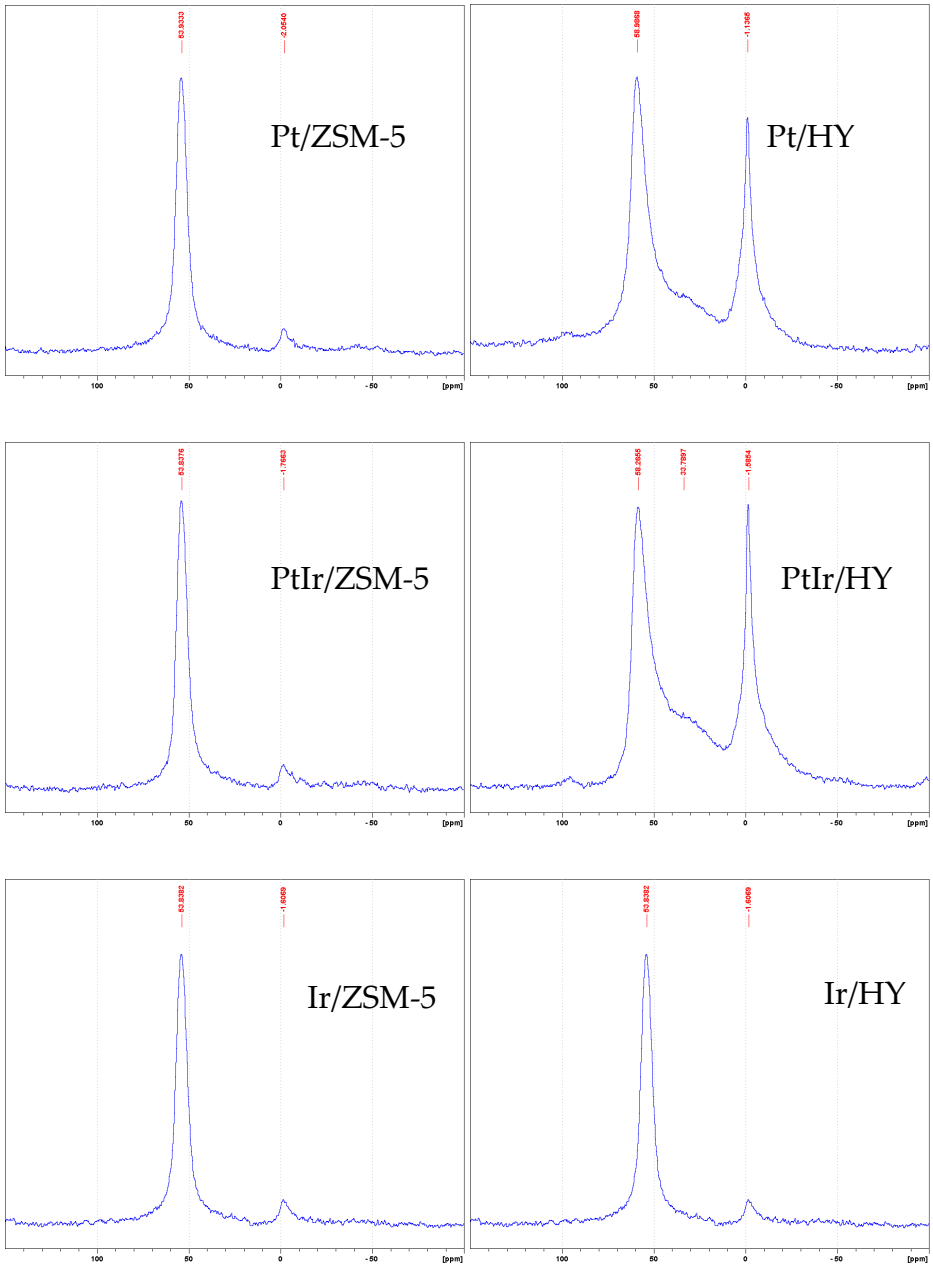

Figure 7.8. ^{27}Al NMR spectra of the reduced Pt-Ir catalysts.

Concerning ^{27}Al NMR spectra (**Figure 7.8**), the strongest peak is around 54 ppm for the series supported on the ZSM-5 zeolite, corresponding to tetrahedrally coordinated Al atoms in the environment of oxygen, forming part of the structure of the zeolite. The octahedrally coordinated Al atoms of the extra framework Al species (EFAL) are characterized by a signal close to 0 ppm. For the ZSM-5-supported catalysts, this peak exhibits a very low signal. In the series supported on HY there are two strong signals, the first about 58 ppm corresponding to the tetrahedrally coordinated Al atoms and another signal close to 0 ppm corresponding to the octahedrally coordinated Al atoms of EFAL Al species. Additionally, the HY-supported catalysts exhibit a shoulder between 50-30 ppm indicating the gradual formation of distorted tetra coordinated Al (50 ppm) and pentacoordinated Al (30 ppm) species (27).

7.3.3.3. Temperature-programmed desorption of NH_3 (TPD-NH_3)

The acid strength and the amount of acid sites were determined from NH_3-TPD measurements. Ammonia exhibits strong basicity and is a small molecule (cross-sectional area 0.141 nm^2), which allow for the detection of acid sites located in very narrow pores and to adsorb onto Brønsted and Lewis acid sites of HY and ZSM-5 substrates. Since NH_3-TPD represents a dynamic measurement of a thermodynamic property, the strength of acid sites is related to the corresponding desorption temperature. In order to avoid physical adsorption, ammonia adsorption was performed at 100 °C on the catalysts previously degassed at 350 °C. The ammonia desorption profiles of the oxide precursors are shown in **Figure 7.9**. **Table 7.6** compiles weak, medium and strong acidity data obtained after Gaussian deconvolution of the peaks. Considering the strength distribution depicted by the

maximum temperature, the acid strength was arbitrarily classified as weak, medium and strong.

For ZSM-5-supported samples, the peak centered at 400 °C is due to Al sites (28) the ammonia was desorbed in temperature ranges of 150–330 and 330–500 °C, which correspond to weak and strong acid sites, respectively. It has been suggested that the weaker acid sites are located closer to the surface, whereas the strong acid sites are located in the deepest part of the zeolitic structure (29). From the data compiled in **Table 7.6**, the following acidity trend can be established for weak-medium acid sites: Pt/HY ≈ Ir/HY ≈ Pt-Ir/HY > Pt-Ir/ ZSM-5 > Ir/ ZSM.5 > Pt/ZSM-5 and for strong acid sites: Pt/HY > Ir/HY ≈ Pt-Ir/HY > ZSM-5 series (none). From the total acid sites compiled in **Table 7.6**, the following acidity trend can be established for total acid sites: Pt/HY > Pt-Ir/HY ≈ Ir/HY >> Pt-Ir/ZSM-5 > Ir/ZSM-5 > Pt/ZSM-5.

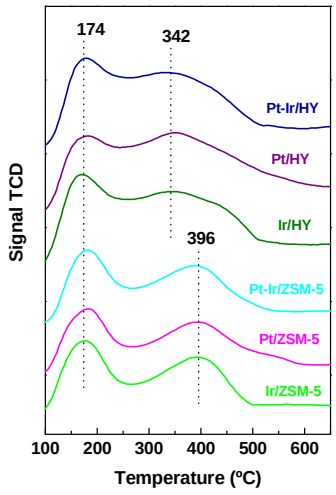

Figure 7.9. TPD profiles after NH_3 adsorption at 100 °C on reduced HY- and ZSM-5 -supported Pt and Ir catalysts.

Table 7.6. Acid properties of the calcined catalysts Pt-Ir/HY and Pt-Ir/ZSM-5 by TPD-NH_3

Catalyst	Amount of acid sites (mmol NH_3/g cat)			
	Weak <250 °C	**Medium 250-400 °C**	**Strong >400 °C**	**Total**
Pt-Ir/ZSM-5	2.4 (174 °C)	3.7 (396 °C)	0	6.1
Pt/ZSM-5	2.3 (174 °C)	2.2 (396 °C)	0	4.5
Ir/ZSM-5	2.0 (174 °C)	3.3 (396 °C)	0	5.3
Pt-Ir/HY	1.9 (174 °C)	6.9 (342 °C)	1.9	10.7
Pt/HY	1.6 (174 °C)	7.1 (342 °C)	3.0	11.7
Ir/HY	1.9 (174 °C)	7.2 (342 °C)	1.7	10.8

*(Maximum temperature of peak deconvolution)

7.3.3. Catalytic activity in phenol hydrotreating

7.3.3.1. HDO of phenol (continuous mode)

The HDO of phenol on HY- and ZSM-5-based catalysts was investigated in a continuous flow system at 30 bar hydrogen pressure and a temperature of 310 °C. The influence of support (HY versus ZSM-5) and type of active phase (Pt and/or Ir) on the catalytic behavior of the monometallic and bimetallic samples are summarized in **Table 7.8** where the phenol conversion, the specific reaction rates (expressed as mmoles of phenol per h and per g of catalyst) after 4 h of time on stream are reported.

Table 7.8. Phenol conversion and specific reaction rates of the HY- and ZSM-5-supported catalysts tested in the HDO reaction carried out in a flow reactor (P_{H2}=30 bar, T=310 °C,$WHSV$=3.9 h^{-1}).

Catalyst	Conversion (%)	rate (x 10^{-2} mol $_{phenol}$ h^{-1} g_{cat}^{-1})	Selectivity toward O-free products (at 20% of phenol conversion)
Ir/HY	8	0.32	98.0
Ir/ZSM5	9	0.35	75.0
Pt/HY	26	1.07	87.0
Pt/ZSM5	20	0.82	53.5
Pt-Ir/HY	**38**	**1.55**	**96.0**
Pt-Ir/ZSM5	25	1.04	89.0
0.3%Pt/Al_2O_3	19	0.78	98
NiMoS/Al_2O_3 HR348	34	0.90	100

The reaction rates for the catalysts are shown in **Figure 7.10**. As seen in this figure, after 4 h of on-stream reaction, the activity trend is: Pt-Ir/HY > Pt/HY > Pt-Ir/ZSM-5 > Pt/ZSM-5 >> Ir/ZSM-5 > Ir/HY. This trend suggests that HY zeolite is much more effective as support than ZSM-5 counterpart. For both supports, the activity follows the trend: Pt-Ir > Pt >> Ir. Thus, the alloying of Pt with Ir led to an

increase in catalyst activity and, regardless of the support employed, Pt-based catalysts are more active than their Ir-based counterparts.

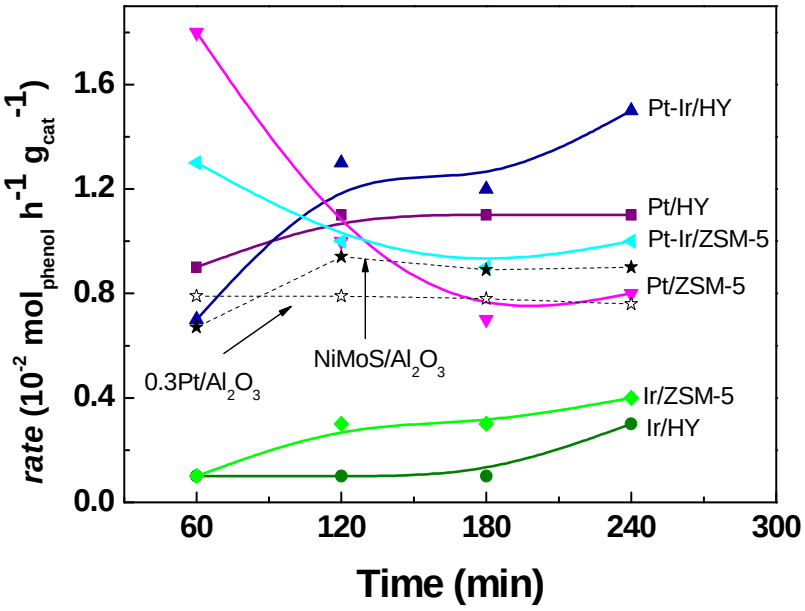

Figure 7.10. Time on stream behavior of reduced catalysts in the HDO of phenol at T = 310ºC, P_{H2} = 3 MPa and $WHSV$= 3.9 h^{-1}.

Under reaction conditions employed (T = 310 °C, P = 3 MPa, $WHSV$ = 3.9 h^{-1}), all catalysts show a high selectivity toward desirable products (> 90% except Ir/ZSM-5 ~ 75%). **Figure 7.11** shows the selectivity to O-free and O-containing products for the Pt-Ir / HY (ZSM-5). Regardless of the support and the active phase, the HDO of phenol reaction proceeds through route of hydrogenation followed hydrogenolysis, as deduced from the formation of cyclohexanol. With exception of the Pt-Ir/ZSM-5, benzene was detected for all catalysts. It was

obtained a higher catalytic activity for the reaction of phenol HDO with Pt-Ir/HY catalyst than the rest of the catalysts (**Figure 7.12**). The Pt-Ir/HY catalyst is the most active and effective toward O-free products among the catalysts studied, this is primarily linked to its large S_{BET} and the optimized total acidity (RMN and TPD-NH_3).

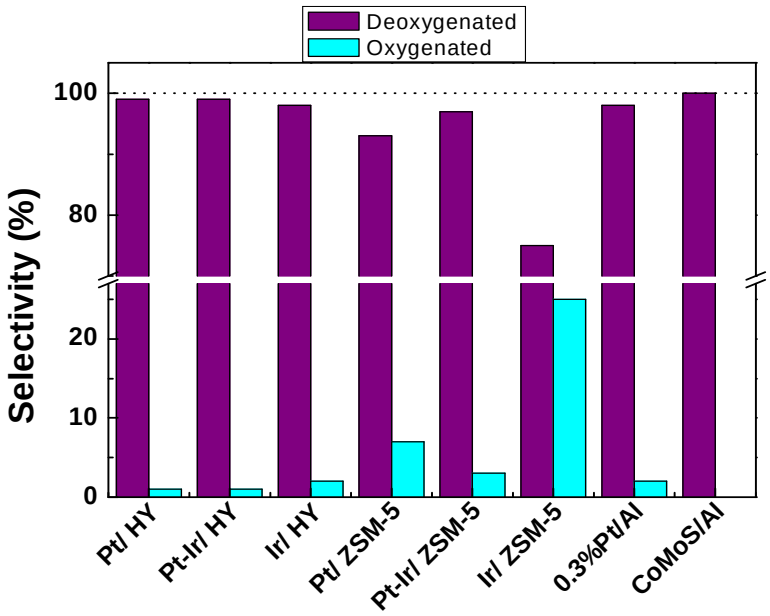

Figure 7.11. Selectivity toward O-free and O-containing products achieved in the HDO of phenol at *TOS* = 4 h over HY- and ZSM-5-based Pt-Ir catalysts and commercial samples (*T* = 310 °C, *P* = 3MPa, *WHSV*= 3.9 h^{-1}).

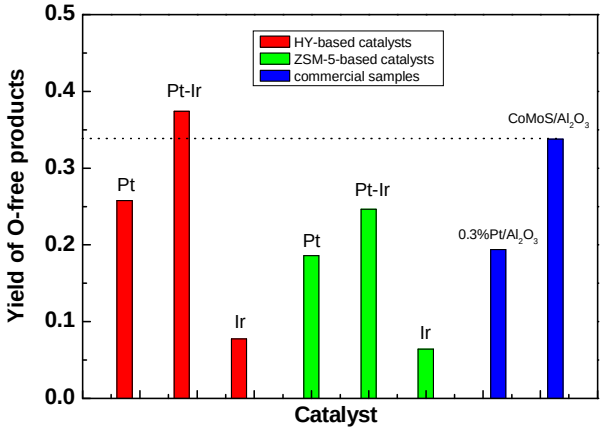

Figure 7.12. Yields of O-free products achieved in the HDO of phenol at *TOS* = 4 h over HY- and ZSM-5-based Pt-Ir catalysts and commercial samples (*T*=310 °C, *P*=3MPa, *WHSV*= 3.9 h^{-1}).

7.3.3.2. HDO of phenol (discontinues mode)

The catalyst activity was evaluated also in the phenol HDO in a batch reactor. This reaction at *T* = 200°C and *P*= 30 bar is important because it allow observe reaction intermediate and therefore to get some insight on the reaction path. **Table 7.9** shows the total phenol conversion HDO, respectively. A higher catalytic activity was obtained for the reaction of phenol with the HY than the ZSM-5-based series. In the case of the HDO reaction, a higher activity was observed for Pt-Ir/HY and Pt/HY catalysts than for the rest of the catalysts. **Figure 7.13** shows the selectivity against phenol conversion. Contrary to ZSM-5, the HY-based catalysts showed heavy products (two or more molecules of phenol), as deduced from 2D chromatography results. This is linked with the bigger pore size of HY zeolite with respect to ZSM-5.

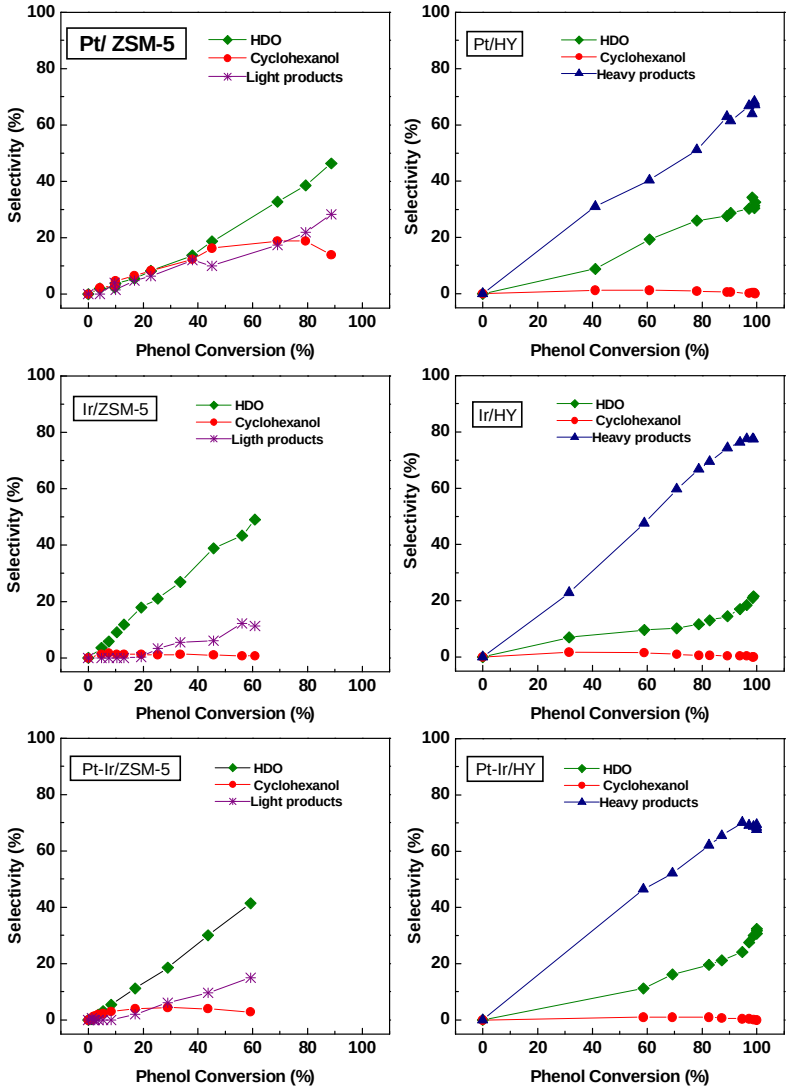

Figure 7.13. Selectivity against total phenol conversion for HDO of phenol on HY- and ZSM-5-supported catalysts. Light products: benzene, cyclohexane, cyclohexene and methylcyclopentane; heavy products: sum of products with molecular weight $\geq 2\ M_{phenol}$.

Table 7.9. Activity of HY- and ZSM-5-based catalysts in the HDO of phenol (batch reactor, T=200 ºC, P_{H2}= 3 MPa).

Sample	rate (x10^{-7} mol g^{-1} s^{-1})	HDO conv.* (%)
Ir/HY	213	29
Pt/HY	241	52
Pt-Ir/HY	260	67
Ir/ZSM-5	33	32
Pt/ZSM-5	74	23
Pt-Ir/ZSM-5	68	36

[a] Phenol conversion toward O-free products

Table 7.10. Selectivity (at 60 % of phenol conversion) for HDO of phenol[a] (batch reactor, T=200 ºC, P_{H2}= 30 bar) over HY- and ZSM-5-based catalysts

Catalyst	Selectivity (%)					
	Methyl-cyclo-pentane	Benzene	Cyclo-hexane	Cyclo-hexene	Methyl-cyclohexane	Cyclo-hexanol
Ir/ HY	0	0	100	0	0	0
Pt/ HY	0	11	36	14	36	3
Ir-Pt/ HY	0	11	84	0	0	5
Ir/ ZSM-5	4	0	96	0	0	0
Pt/ ZSM-5	2	6	60	0	0	32
Ir-Pt/ZSM-5	0	0	95	0	0	5

.

As shown in **Figure 7.14**, upon reaction conditions employed, the major product in the HDO of phenol over all catalysts was cyclohexane (selectivity in range 90%-100%). Other products, such as benzene, cyclohexene, methylcyclopentane and methylcyclohexane, were archived with much lower selectivity's.

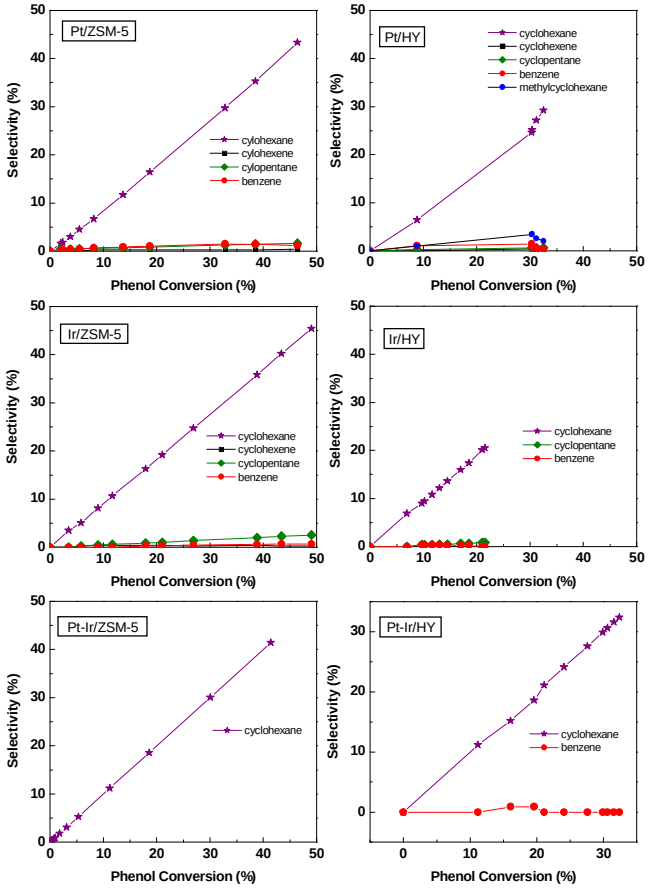

Figure 7.14. Distribution of the products in the HDO of phenol (T = 200°C, P = 3MPa, batch reactor).

General reaction scheme for HDO of reaction is shown in **Figure 7.15.** Regardless of the reaction conditions employed, the HDO reaction proceeds through route of hydrogenation followed hydrogenolysis, as deduced from the formation of cyclohexanol. With exception of the Pt-Ir/ZSM-5, the formation of benzene occurs in all catalytic tests.

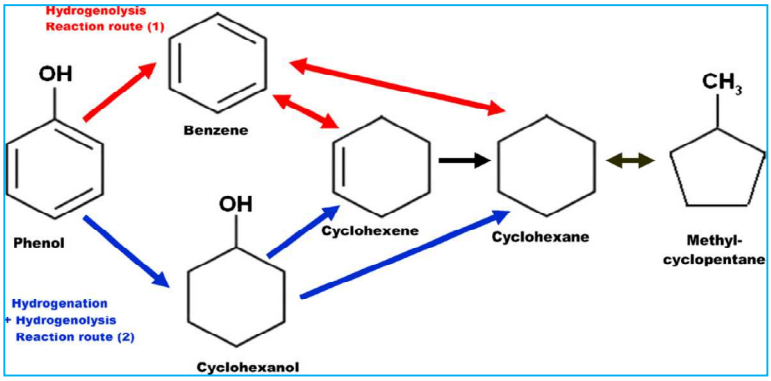

Figure 7.15. General scheme for HDO of phenol reaction over HY- and ZSM-5-supported Pt-Ir catalysts.

7.3.4. Characterization of spent catalysts

7.3.4.1. X-ray photoelectron spectroscopy (XPS)

Surface composition and oxidation state of the elements of catalysts were determined by XPS analysis. The binding energy (BE) of core electrons and surface atomic ratios are presented in **Tables 7.7 and 7.8**, respectively. As one might expect for aluminosilicates, all catalysts showed Si 2p and Al 2p peaks with BE at 103 ±0.1 eV and 75.0±0.1 eV, respectively. **Figure 7.16** shows the XPS spectra of Ir(Pt) 4f –Al 2p core levels of the Ir-containing oxide precursors. For four Ir-containing samples, binding energy (BE) of Ir $4f_{7/2}$ at 61.0 ± 0.1 eV According to the

literature, the BE values are close to at 60.9 eV corresponding to Ir^0 species (30). This BE values are close to that reported previously for fresh reduced Pt-Ir/Al_2O_3 (61.2 eV) (31). From **Table 7.7** it is clear that there is a downward shift in the position of the Ir $4f_{7/2}$ peak, going from 61.0 eV for Ir/ZSM-5 sample to 60.6 eV for the binary Pt-Ir/ZSM-5 catalyst. Because the peak at 62.0 eV indicative of IrO_2 species (32), this species is absent: Ir is entirely in its metallic state for all catalysts. Finally, one might note that all catalysts showed absence $IrCl_3$ species (BE at 62.7 eV) (33).

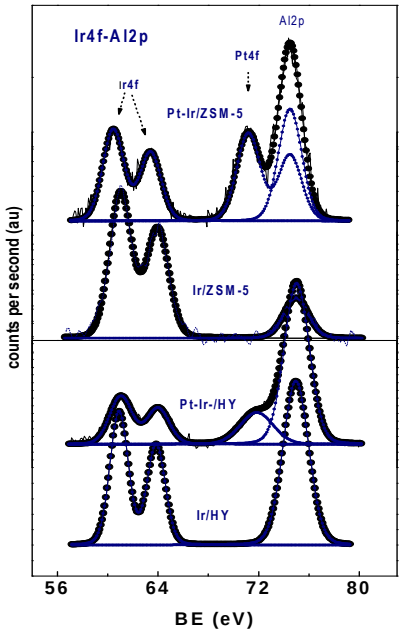

Figure 7.16. Ir 4f-Al 2p core level spectra of the fresh reduced Ir/HY, Ir/ZSM-5, Pt-Ir/HY and Pt-Ir/ZSM-5 catalysts.

Table 7.7. Binding energy (eV) of core electrons of the fresh reduced HY- and ZSM-5- based Pt and It catalysts.

Catalyst	Si 2p	Al 2p	Pt $4d_{5/2}$	Pt $4d_{7/2}$	Ir $4f_{7/2}$
Ir/HY	103.1	75.0	-	-	60.9
Ir/ZSM5	103.0	75.0	-	-	61.0
Pt/HY	103.1	75.1	314.7	-	-
Pt/ZSM5	103.1	75.0	314.7	-	-
Pt-Ir/HY	103.0	75.0	314.8	71.7	61.1
Pt-Ir/ZSM5	102.9	74.9	314.7	71.1	60.6

Evidently, the reduction temperature employed (400 °C) was enough to reduce iridium oxide species, in accordance with TPR results (*vide supra*). This reduction temperature was also appropriate for the complete reduction of Pt oxide species, as deduced from the BE value at 314.7 eV (Pt $4d_{5/2}$) consistent with the presence of Pt^0 species (34). As seen in **Figure 7.16**, the Pt $4f_{7/2}$ profiles of both binary samples displayed peaks at ca. 71.1 eV (Pt-Ir/ZSM-5) and 71.7 eV (Pt-Ir/HY) associated with Pt^0 (35).Concerning the binary samples, it should be mentioned that Pt-Ir alloy formation is hardly possible. According to the electronegativity of the elements, Ir (2.20) and Pt (2.28), the charge transfer from iridium to platinum is not expected.

Quantitative XPS data of the spent catalysts are presented in **Table 7.8**. From the comparison of Pt/Si atomic ratio for the monometallic and bimetallic samples it can be concluded that Pt surface exposure on the HY-supported catalysts is higher than on their ZSM-5 supported counterparts. The same trend is

observed for the iridium species. As a consequence, the surface exposure of both Pt and Ir on the HY zeolite is two-times higher for the Pt-Ir/ZSM-5.

Table 7.8 Surface atomic ratios of the spent Ir/HY, Ir/ZSM-5, Pt/HY, Pt/ZSM-5, Pt-Ir/HY and Pt-Ir/ZSM-5 catalysts.

Sample	Si/Al at	Ir/Si at	Pt/Si at	(Pt+Ir)/Si
Ir/HY	1.54	0.047	-	-
Ir/ZSM5	17.0	0.016	-	-
Pt/HY	1.63	-	0.0075	-
Pt/ZSM5	16.5	-	0.0066	-
Pt-Ir/HY	1.76	0.012	0.0032	0.044
Pt-Ir/ZSM5	16.9	0.006	0.0014	0.020

7.3.4.2. High Resolution Transmission Electronic Microscopy (HRTEM)

The morphology of phases formed in the spent Pt-Ir/HY and Pt-Ir/ZSM-5 catalysts tested in the HDO of phenol (batch reactor, T = 200 ºC, P_{H2} = 3 MPa) was examined by HRTEM. As seen in **Figure 7.17,** both TEM micrographs show nearly globular shaped particles of a size much larger than the pore diameter. The metal particles are better distributed on surface of Pt-Ir/HY than on the Pt-Ir/ZSM-5 catalyst. The local EDS analysis (not shown here) with electronic spot of 10 and 20 nm suggested a similar concentration of Pt and Ir, in good agreement with XRF data (*vide supra*). More information on the morphology of the phases formed was revealed by statistical evaluation (about 200 particles) from various HRTEM images. **Figure 7.18** shows the statistical analysis of the Pt(Ir) particle size distribution. Contrary to the Pt-Ir/ZSM-5, the Pt-Ir/HY sample shows narrow

particle size distribution. The mean particle size of the ZSM-5 supported sample is much larger sample than of HY-supported ones (9.1 nm vs. 3.3 nm).

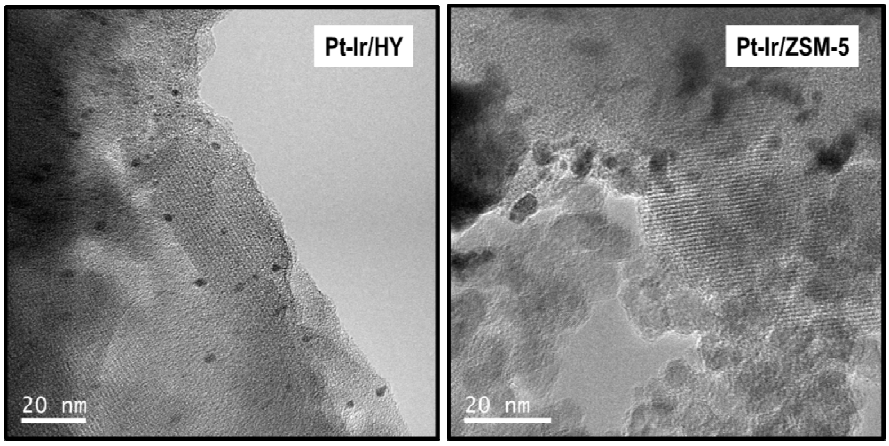

Figure 7.17. TEM micrograph of the spent Pt-Ir/HY (a) and Pt-Ir/ZSM-5 (b) samples tested in HDO of phenol (batch reactor, T=200 ºC, P_{H2}=3MPa).

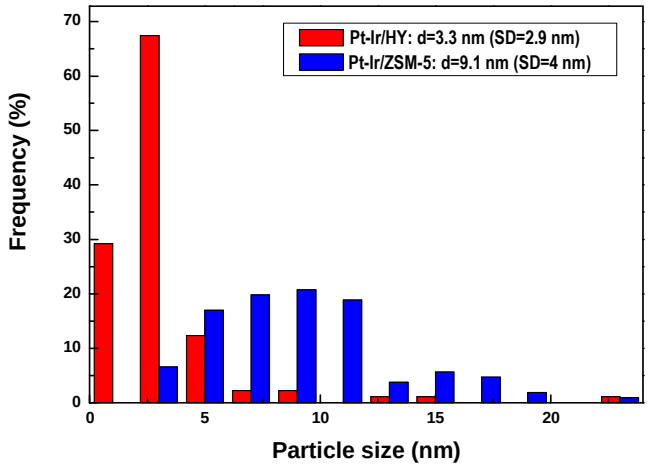

Figure 7.18. Pt/Ir particle size distribution for the spent catalysts tested in the HDO of phenol reaction (batch reactor, T = 200 ºC, P = 30 bar). SD: statistical deviation.

7.3.4. Catalyst activity- structure correlation

In general, the phenol conversion was much larger on the HY-supported samples than on the ZSM-5-supported ones being bimetallic (Pt-Ir) catalysts more active than monometallic (Pt, Ir) ones. The explanation of a larger activity achieved on the Pt-Ir/HY catalyst with respect to Pt-Ir/ZSM-5 counterpart is straightforward. From the catalyst characterization, this catalyst exhibits: (i) larger specific BET surface area and pore diameter (**Table 7.3**); (ii) larger amount of metal oxide species, as deduced from H_2 consumption (from TPR; Figure 7.3); (iii) larger acidity, as deduced from combined ^{29}Si NMR and TPD-NH_3 (**Tables 7.5** and **7.6**, respectively). In this sense, it was proposed that Brønsted acid sites might act as an electron acceptor and to decrease the electron density of the metal (36); (iv) larger metal surface exposure, as deduced from (Pt+Ir)/Si atomic ratio (see XPS results, **Table 7.**8); and (v) larger metal phase dispersion, as confirmed by TEM results (**Figure 7.17**). For the Pt-Ir/HY, high resolution XRD results suggested that only a small fraction of the Ir (2%) formed alloy with Pt. Thus, one might expect a larger increase in activity if the Pt-Ir alloy will be formed.

The selectivity results presented in this chapter clearly show that, regardless of the reaction conditions employed, the products formed depend on the characteristics of the support (HY vs. ZSM-5): more light products are obtained when shape selective ZSM-5 zeolite is used, whereas heavier hydrocarbons are produced on the HY-supported catalysts. Thus, as far as the fuel qualities of the upgraded bio-oils are concerned, the products obtained with the HY-supported catalysts turned out to be the more interesting than those obtained with ZSM-5-supported ones. Considering the textural properties of the catalysts (**Table 7.3.**), the product distribution could be explained considering easier diffusion of phenol

and products within parallel channels of HY zeolite whose openings are large enough (7.4 Å) to admit quite large molecules *(37)*. On the contrary, the ZSM-5 zeolite possesses a three-dimensional system of intersecting channels, characterized by intermediate pore size openings (5.5 Å), which restrict the access of branched and cyclic hydrocarbons but allow the straight-chain and light products to enter and be preferentially cracked to the lighter products (shape selectivity).

For all catalysts the possible contribution of Cl- ions to the largest phenol conversion on PtIr/HY catalyst cannot to be ruled out because chloride ions can polarize surface hydroxyl groups of support leading to an increase of acidity *(38)*. Thus, taking into account that the C-O bond cleavage is likely to be metal centered and the hydrogen dissociation occurs on the support and on the metal phase, the polarized surface hydroxyl groups of zeolite may enhance the effect of hydrogen spilled over the metal interface.

Finally, contrary to the HDO reaction carried out in a flow reactor, when HDO reaction was performed in a batch reactor, formation of heavy products occurs on the HY-supported catalysts. This formation confirms that flow conditions are needed in order to evaluate correctly the HDO activity of the synthetized catalysts.

7.4. Conclusions

The results presented in this chapter allow to outlining the factors influencing on the activity and selectivity of noble metals (Pt, Ir) supported on HY and ZSM-5 zeolites in the reaction of hydrodeoxygenation of phenol. From the catalyst-activity structure correlation, the main conclusions are:

(i) Regardless of the active phase and type of reactor employed, the higher HDO activity was achieved over HY-supported catalysts.

(ii) Under the reaction conditions employed, the bimetallic systems exhibited a larger activity than their monometallic counterparts.

(iii) In the reaction carried out in a batch reactor, the catalysts supported on the HY zeolite exhibited a large selectivity toward products having two or more aromatics rings.

(iv) The activity of the catalysts is strongly influenced by the textural properties and support acidity being HY zeolite more effective as support than ZSM-5.

7.5. References

1. *Catalytic hydrodeoxygenation.* **Furimsky, E.** s.l. : Applied Catalysis A: General , 2000, Vols. (199) 147-190.

2. *Historical deveopments in hydroprocessing bio-oils.* **Elliot, D.C.** s.l. : Fuels, 2007, Vols. (21) 1792-1815.

3. *Study of the hydrodeoxygenation of carbonyl, carylic and guaiacyl groups over sulfided CoMo/γ-Al2O3 and NiMo/γ-Al2O3 catalyst: II. Influence of water, ammonia and hydrogen sulfide.* **E. Laurent, B. Delmon.** s.l. : Applied Catalysis A: General, 1994, Vols. (109) 97-115.

4. *A review of catalytic hydrodeoxygenation of lignin-derived phenols from biomass pyrolysis.* **Q. Bu, H. Lei, A.H. Zacher, L. Wang, S. Ren, J. Liang, Y. Wei, Y. Liu, J. Tang, Q. Zhang, R. Ruan.** s.l. : Bioresource Technology, 2012, Vols. (124) 470-477.

5. *Stability of CoMo/Al2O3 catalysts: Effect of HDO cycles on HDS.* **T.R. Viljava, R.S. Komulainen, T. Selvam, A.O.I. Krause.** s.l. : Studies in Surface Science and Catalysis, 1999, Vols. (127) 145-152.

6. *Hydrodeoxygenation and coupling of aqueous phenolics over bifuncional zeolite-supported metal catalysts.* **D.Y. Hong, S.J. Miller, P.K. Agrawal, C.W. Jones.** s.l. : Chemical Communications, 2010, Vols. (46) 1038-1040.

7. *Superior performance in deep saturation of bulky aromatic pyrene over acidic mesoporous Beta zeolite-supported palladium catalyst.* **T. Tang, C. Yin, L. Wang, Y. Ji, F.S. Xiao.** s.l. : Journal of Catalysis , 2007, Vols. (249) 111-115.

8. *Hydrodesulfurization of 4,6-dimethyldibenzothiophene and dibenzothiophene over alumina-supported Pt, Pd, and Pt-Pd catalysts .* **N.R. Adeline, R. Prins.** s.l. : Journal of Catalysis , 2006, Vols. (242) 207-216.

9. *Active phases and sulfur tolerance of bimetallic Pd–Pt catalysts used for hydrotreatment.* **Y. Yoshimura, M. Toba, T. Matsui , M. Haradaa, Y. Ichihashia, K.K. Bandoa, H.**

Yasudaa, H. Ishiharab, Y. Moritab, T. Kameokab. s.l. : Applied Catalysis A: General, 2007, Vols. (322) 152-171.

10. *Bifunctional transalkylation and hydrodeoxygenation of anisole over a Pt/HBeta catalyst.* **X. Zhu, L.L. Lobban, R.G. Mallinson, D.E. Resasco.** s.l. : Journal of Catalysis, 2011, Vols. (281) 21-29.

11. *Hydrodeoxygenation of dibenzofuran over noble metal supported on mesoporous zeolite.* **Y. Wang, Y. Fang, T. He, H. Hu, J. Wu.** s.l. : Catalysis Communications, 2011, Vols. (12) 1201-1205.

12. *Hydrodeoxygenation of aldehydes catalyzed by supported palladium catalysts.* **D. Procházková, P. Zámostný, M. Bejblová, L. Červený, J. Čejka.** s.l. : Applied Catalysis A: General, 2007, Vols. (332) 56-64.

13. *From biomass to advanced bio-fuel by catalytic pyrolysis/hydro-processing: Hydrodeoxygenation of bio-oil derived from biomass catalytic pyrolysis.* **Y. Wang, T. He, K. Liu, J. Wu, Y. Fang.** s.l. : Bioresource Technology, 2012, Vols. (108) 280-284.

14. *Zeolite-Beta-supported platinum catalysts for hydrogenation/hydrodeoxygenation of pyrolysis oil model compounds.* **J. Horáček, G. Šťávová, V. Kelbichová, D. Kubička.** s.l. : Catalysis Today, 2013, Vols. (204) 38–45.

15. *Hydrodeoxygenation of benzophenone on Pd catalysts.* **M. Bejblová, P. Zámostný, L. Červený, J. Čejka.** s.l. : Applied Catalysis A: General , 2005, Vols. (296) 169-175.

16. *Hydrogenation of aromatics on sulfur-resistant PtPd bimetallic catalysts.* **R.M. Navarro, B. Pawelec, J.M. Trejo, R. Mariscal, J.L.G. Fierro.** s.l. : Journal of Catalysis, 2000, Vols. (189) 184-194.

17. *Hydrodeoxygenation of phenol over zeolite-supported metal catalysts.* **D.Y. Hong, P.K. Agrawal, S.J. Miller, C.W. Jones.** AIChE Annual Meeting : Catalysis and Reaction Engineering Division, 2009.

18. *Catalytic upgrading of pyrolytic oils to fuel over different zeolites.* **S. Vitolo, M. Seggiani, P. Frediani, G. Ambrosini, L. Politi.** s.l. : Fuel , 1999, Vols. (78) 1147-1159.

19. *Catalytic upgrading of pyrolytic oils over HZSM-5 zeolite: behaviour of the catalyst when used in repeated upgrading–regenerating cycles.* **S. Vitolo, B. Bresci, M. Seggiani, M.G. Gallo.** s.l. : Fuel, 2001, Vols. (80) 17-26.

20. *Surface area and pore texture of catalysts.* **G. Leofanti, M. Padovanb, G. Tozzolac, B. Venturellic.** s.l. : Catalysis Today, 1998, Vols. (41) 207–219.

21. *Characterization of bimetallic NaY-supported Pt-Pd catalyst by EXAFS, TEM and TPR.* **T. Rades, C. Pak, M. Polisset-Thfoin, R. Ryoo, J. Fraissard.** s.l. : Catalysis Letters, 1994, Vols. (29) 91-103.

22. *Aromatics reduction of pyrolysis gasolina (PyGas) over HY-supported transition metal catalysts.* **P. Castaño, B. Pawelec, J.L.G. Fierro, J.M. Arandes, J. Bilbao.** s.l. : Applied Catalysis A: Genera, 2006, Vols. (315) 101-113.

23. *Temperature programmed analysis and its applications in catalytic systems.* **S. Bhatia, J. Beltramini, D.D. Do.** s.l. : Catalysis Today, 1990, Vols. (7) 309-438.

24. *Pt-Ir/ Al2O3 catalysts—The effect of Pt–Ir interaction on Ir agglomeration and catalytic performance.* **Y.J. Huang, S.C. Fung, W.E. Gates, G.B. McVicker.** s.l. : Journal of Catalysis , 1989, Vols. (118) 192-202.

25. *Interaction between iridium and platinum precursors in the preparation of iridium—platinum catalysts .* **J. Xue, Y.J. Huang, J.A. Schwarz.** s.l. : Applied Catalysis, 1988, Vols. (42) 61-76.

26. *Catalytic ring opening of naphthenic structures: Part II. In-depth characterization of catalysts aimed at upgrading LCO into a high-quality diesel-blending component.* **U. Nylén, B. Pawelec, M. Boutonnet, J.l.G. Fierro.** s.l. : Applied Catalysis A: General , 2006, Vols. (299) 14-29.

27. *Steaming of Zeolite Y: Formation of Transient Al Species.* **B.H. Wouters, T. Chen, P.J. Grobet.** s.l. : The Journal of Physical Chemistry B, 2001, Vols. (105) 1135-1139.

28. *Methods for Characterizing Zeolite Acidity.* **W.E. Farneth, R.J. Gorte.** s.l. : Chemical Review, 1995, Vols. (95) 615-635.

29. *Concerning the aluminum distribution gradient in ZSM-5 zeolites.* **E.G. Derouane, J.P. Gilson, Z. Gabelica, C. Mousty-Desbuquoit, J. Verbist.** s.l. : Journal of Catalysis, 1981, Vols. (71) 447-448.

30. **J.F. Moulder, W.F. Stickle, P.E. Sobol, K.D. Bomben.** *Handbook of X-ray Photoelectron Spectroscopy.* Minnesota : Perkin-Elmer Corporation, 1992.

31. *Highlights from a development process of cetane-enhancing catalysts.* **[U. Nylén, J. Mazón Arechederra, B. Pawelec, J. Frontela Delgado, M. Pérez Pascual, J.L.G. Fierro.** s.l. : Energy & Fuels, 2008, Vols. (22) 2138-2148.

32. *XPS investigation of surface oxidation layers on a platinum electrode in alkaline solution .* **Peuckert, M.** s.l. : Electrochimica Acta, 1984, Vols. (29) 1315-1320.

33. *ESCA Studies on the charge distribution in some dinitrogen complexes of Rhenium, Iridium, Ruthenium and Osmium.* **Folkesson, B.** s.l. : Acta Chemica Scandinavica, 1973, Vols. (27) 287-302.

34. *XRS study of pumice-supported palladium and platinum catalysts.* **A.M. Venezia, D. Duca, M.a. Floriano, G. Deganello.** s.l. : Surface Interface Analysis, 1992, Vols. (9) 543-547.

35. *Factors influencing selectivity in naphthalene hydrogenation over Au- and Pt-Au-supported catalysts.* **B. Pawelec, A.M. Venezia, V. La Parola. S. Thomas, J.L.G. Fierro.** s.l. : Applied Catalysis A: General, 2005, Vols. (283) 165-175.

36. *Strong modification of Pt-CO interaction caused by alloying with chromium in Pt-Cr/HZSM-5 catalysts.* **O.P. Tkacheno, E.S. Shpiro, N.I. Jaeger, R. Lamber, G. Schulz-Ekloff, H. Landmesser.** s.l. : Catalysis Letters, 1994, Vol. (23) 251.

37. *Synthesis and manufacture of zeolites.* **Vaughan, D.E.W.** s.l. : Chemical Engineering Progress , 1988, Vols. (84) 25-31.

38. *Factors influencing selectivity in naphthalene hydrogenation over Au- and Pt-Au-supported catalysts.* **B. Pawelec, A.M. Venezia, V. La Parola, S. Thomas, J.L.G. Fierro.** s.l. : Applied catalysis A: General, 2005, Vols. (283) 165-175.

Chapter 8

Enhancement of phenol hydrodeoxygenation over Pd catalysts supported on mixed HY zeolite and Al_2O_3

Chapter 8

Enhancement of phenol hydrodeoxygenation over Pd catalysts supported on mixed HY zeolite and Al_2O_3

This chapter describes the effect of the support (zeolite ultrastable HY, alumina (Al) and mixed HY–Al carriers) on the catalytic activity of Pd catalysts in the phenol hydrodeoxygenation (HDO) reaction carried out in a flow fixed-bed reactor at T = 310 °C, P = 3 MPa and $WHSV$= 2.05 h^{-1}. The catalysts were characterized by N_2 physisorption, XRD, TPR, TPD-NH_3, DRIFT spectroscopy of adsorbed CO, HRTEM, X-ray photoelectron spectroscopy (XPS) and TPO/TGA techniques. From the catalyst activity-structure correlation, it can be concluded that the HDO of phenol is favoured on the bifunctional Pd/20%HY–Al catalyst which possesses moderate acidity and improved Pd dispersion on the support surface. The contributions of the acid sites to the catalyst activity and deactivation by coke are discussed.

8.1. Introduction

Mitigating greenhouse gases (GHGs) is one of the biggest challenges in the 21st century and requires long-term planning as well as social awareness. Renewable sources of energy can contribute significantly to the effort of mitigating GHGs. Among different renewable energy technologies, biomass-based technologies have high potential (1). Biomass has been proposed as a feedstock for liquid fuels and chemicals (2) (3). Many processes that transform biomass to liquid fuels start with the thermal breakdown of biomass feedstock producing the so-called bio-oils (4). The final bio-oils have higher energy density than the raw biomass precursor, which makes it more suitable for industrial applications (5).

Pyrolysis bio-oils obtained from the fast pyrolysis of biomass are complex mixtures of reactive chemical compounds (carboxylic acids, aldehydes, ketones, carbohydrates, degraded lignin), water (up to 25%), and some alkali and alkaline-earth metals (Na, K, Mg, Ca) (6). The high contents of oxygenated compounds (close to 40% oxygen) contribute to some deleterious properties, such as high viscosity, corrosiveness, poor heating value, immiscibility with hydrocarbon fuels, as well as to undesirable formation of carbon deposits in parts of the automotive engines upon combustion, especially in compression-ignition engines, i.e. diesel engines. In order to improve the thermostability of these bio-oils, the oxygen removal *via* hydrodeoxygenation (HDO), which is a similar process to hydrotreatment in a petroleum refinery, is a common practice (7).

Past efforts for HDO catalyst development were focused on alumina-supported hydroprocessing catalysts, intensively used in petroleum refining for several decades and therefore little attention has been paid to development of novel catalysts. Thus, the catalysts often studied for HDO were sulfided CoMo/γ-

Al_2O_3 and NiMo/γ-Al_2O_3 systems (8) (9) (10) (11) (12) (13). Unfortunately, in the absence of a sulfiding agent, the sulfided catalysts deactivated quickly in HDO reaction and the selectivity to different hydrocarbons changed with time on-stream due to oxidation of the active phases (11). Thus, great efforts have been devoted to enhance the stability of these catalysts, but the results are not yet satisfactory (7) (8) (9) (10) (11) (12) (13). Recent laboratory and commercial developments in the field of catalytic hydroprocessing of biomass-derived liquefaction conversion products are presented in a few excellent revisions (14) (15) (16) (17) (18) (19).

Recently, the use of noble metal catalysts as an alternative to sulfided catalysts for HDO reaction has been extensively studied (14) (15) (16) (17) (18) (19). As pioneering patent demonstrated that Pd catalysts are highly effective for hydrogenation of organic compounds typically found in bio-oils (20), more studies were developed on Pd-based catalysts than in other noble metals (14) (15) (16) (17) (18) (19). Thus, the HDO activity of Pd-based catalysts was investigated using acidic substrates such as ZrO_2 (21) (22) (23), Al_2O_3 (24) (25), SiO_2-Al_2O_3 (25), SiO_2 (26) (27), SBA-15 and Al-SBA-15 (28), $Al_2(SiO_3)_3$ (29), SAPO-31 (30), carbon (31) (32) (33) (34) (35) (36) (37) (38) (39), zeolites Beta and ZSM-5 (37) (38), MCM-41 (37), and super acid SO_4^{2-}/ZrO_2/SBA-15 (40) substrates. On the contrary, studies of the HDO reaction over Pd catalysts supported on basic carriers are scarce (41) (42). The reason for this lies in the fact that the HDO reaction over noble metals supported on acidic substrates requires both metal site and acid sites, being H_2 dissociated on metal sites while O-containing compounds are adsorbed and activated on either metal sites or on the cations/oxygen vacancies located at the metal-support interface (14) (15) (16) (17) (18) (19). Moreover, it is well known that the acidic sites

of supports might to catalyse dehydration, isomerisation, alkylation and condensation reactions (43).

The effects of the substrate structure (C, H-Beta, ZSM-5, MCM-41) and its acidity on activity of supported Pd catalysts in the transformation of benzophenone and benzaldehyde were investigated by Čejka *et al*. (37) (38) who found that the substrate structure has a determining effect on the course of HDO reaction being the most suitable one Pd catalysts supported on large pore zeolite Beta (37) (38). This was confirmed also for Pt catalysts supported on H-Beta (44) and HY (45) (46) zeolites**.** Similarly, Pt catalysts supported on mesoporous ZSM-5 showed better performance in dibenzofuran HDO than its counterpart supported on microporous ZSM-5 zeolite due to the diffusion limitation of dibenzofuran in the microporous structure of ZSM-5 (44). Considering the stability of substrate, a particularly promising approach to the development of novel HDO catalysts lies in the use of highly acidic ultrastable HY zeolite substrate. This is because the ultrastable HY zeolite has the advantages of higher surface-to-volume ratio than alumina, variable framework compositions and high hydrothermal stability (47). Zeolite acidity, however, drastically leads to fast deactivation rates and increases the amount of undesirable cracking products, which accelerates the rate of coke deposition and the yield of gases (48). In this sense, a large deactivation of bifunctional zeolite-supported noble metal catalysts in the HDO of phenol was reported (45).

To the best of our knowledge, the only study on HY-supported noble metal HDO catalysts was reported by Hong *et al.* (46) who showed that bifunctional HY zeolite supported Pt catalysts are effective for the aqueous phenol HDO using a fixed-bed reactor working under high H_2 pressure (4 MPa). It was found that phenol transformation over Pt/HY catalysts proceeds via hydrogenation-

hydrogenolysis ring-coupling reactions producing monocyclic and useful bicyclic hydrocarbons (46). The bare HY zeolite demonstrated to be not effective catalyst for HDO of phenol upon reaction conditions employed (T = 473-523 K and P_{H2} = 4 MPa) confirming that bifunctional catalysts are needed for HDO reaction: H^+ sites for dehydration and metal sites for hydrogenation are needed. Notwithstanding, it is emphasized that Pt/HY catalysts were activated at high temperature (500°C) (46), thus sintering of Pt crystallites is expected to occur on the surface of HY zeolite.

Taking into account that future commercial applications of lignin, its conversion will require catalysts with improved resistance to deactivation (44). In the present work, we aimed to exploit the advantage of the properties of the alumina and HY zeolite mixtures as support for Pd in order to develop stable and more selective catalysts toward the hydrogen-donor species. Indeed, revision of the literature on the use of Pd catalysts for HDO reaction (20-42) indicates that hybrid HY-Al substrate has not been used to prepare Pd HDO catalysts. Thus, we compare here the activity for phenol HDO reaction of Pd catalysts supported on alumina, mixed alumina-HY zeolite materials and alumina-free zeolite, trying to establish a relationship between activity and catalyst structure. Moreover, considering that the mechanism of hydrogenation over supported noble metal catalyst is still debated (14) (15) (16) (17) (18) (19), our selectivity results might contribute to clarify this point. The physicochemical properties of the catalysts have been evaluated by various techniques and their activity compared with those of a commercial zeolite-loaded alumina-supported NiMo sulfide hydrocracking catalyst to provide the catalyst with hydrocracking function arising from substrate acidity.

8.2. Experimental

8.2.1. Catalyst preparation

Four supported Pd catalysts were prepared using γ-Al_2O_3 (Girdler), HY zeolite (Conteka), and mixed 10%HY/γ-Al_2O_3 as supports. Two mixed HY-Al_2O_3 supports were prepared by physical mixture of different amounts (10 and 20 wt %) of ultrastable HY zeolite (Conteka) and γ-Al_2O_3 (Girdler) in excess of distilled water under vigorous stirring at room temperature for 2 h. The characteristics of the HY zeolite are as follows: SiO_2/Al_2O_3 mole ratio 5.6, Na_2O content 0.14 wt.% and unit cell 2.454 nm. After solid decantation, the solid was dried at 110 °C for 12 h and calcined at 250 °C for 1 h. Depending on the composition, the supports will be abbreviated here after as (x)HY-Al, where x is the nominal wt.% of HY (10 and 20%). Before Pd incorporation, all substrates were dried at 250 °C for 1 h. Supported palladium catalysts were prepared by wet impregnation of the respective substrate with aqueous solutions of H_2PdCl_6 (Sigma) with the appropriate concentration to achieve a metal content of 1 wt %. A known weight of carrier was contacted with a solution containing the required amount of palladium added to 100 mL of water, and the pH was fixed at a value close to 7. After the adsorption equilibrium was reached (contacting for 12 h at room temperature), the excess of water was removed in a rotary evaporator till dryness. Subsequently, the impregnate was dried at 110 °C in air for 12 h, and finally calcined at 300 °C for 4 h.

8.2.2. Catalytic activity measurements

The hydroconversion of the phenol was performed in a high-pressure laboratory-scale set-up equipped with a down-flow fixed bed catalytic reactor.

Each experiment used 0.20 g of catalyst (particle diameter: 0.25–0.30 mm) mixed with 0.30 g of SiC (diameter 0.5 mm). Before catalyst activation, the catalyst was dried under a N_2 flow of 100 mL min^{-1} at 150 °C for 0.5 h. The catalyst was then reduced in situ at 300 °C for 2 h at atmospheric pressure by a mixture flow of 55 mL of 10:1 of H_2:N_2. After reduction, the catalyst was purged under a N_2 flow of 100 mL min^{-1} at 300 °C for 0.5 h and then stored overnight under a N_2 flow. Before the experimental run, the N_2 pressure was increased to the desired value (3.0 MPa), and the catalytic bed was cooled down to the temperature of the HDO reaction (310 °C). After that, N_2 flow was shut down, the liquid feed (2 vol% of phenol dissolved in decaline) injected by a high-pressure HPLC Knauer pump (WHSV = 2.05h^{-1}) into a hydrogen stream was fed to the preheated reactor. Owing to the high boiling point of the reactant and the solvent, on-line analysis of the reaction products was not convenient. Consequently, the reactor effluents were condensed, and liquid samples were analyzed by a GC Agilent 6890A with a FID detector.

8.3. Results and discussion

8.3.1. Characterization of the oxide precursors

8.3.1.1. Chemical analysis

The morphology of four Pd oxide precursors was studied by SEM technique. SEM observations of the Pd/10%HY-Al and Pd/20%HY-Al samples revealed non-uniform distribution of HY zeolite on the alumina being Pd

deposited preferentially on the HY surface rather than on alumina, as confirmed by EDX/SEM elemental analysis (data not shown here). Pd/HY sample showed more uniform and smaller grains than its Pd/Al counterpart.

Table 8.1. Palladium content[a] and textural properties[b,c] of pure supports and oxide precursors

Catalyst	Pd[a] (wt%)	S_{BET} [b] ($m^2 \cdot g^{-1}$)	NS_{BET}[c]	V_{total} ($cm^3.g^{-1}$)	d[c] (nm)
Pd/Al	0.81	154 (163)	0.96	0.49 (0.33)	12.7 (7.5)
Pd/10%HY-Al	0.77	179 (185)	0.99	0.41 (0.44)	11.0 (11.4)
Pd/20%HY-Al	0.80	194 (216)	0.91	0.37 (0.46)	10.2 (12.0)
Pd/HY	0.77	476 (594)	0.81	0.35 (0.29)	8.9 (7.1)

[a] As determined by ICP-AES.

[b] As determined by N_2 adsorption-desorption isotherms at -196 °C. (Values in parentheses correspond to bare support); SBET: specific BET surface area; V_{total}: total pore volume, d: average pore diameter

[c] NS_{BET}: normalized S_{BET} calculated from equation NS_{BET}=(S_{BET} of oxide catalyst/[(1-y) x S_{BET} of support], where y is the Pd loading determined by ICP-AES

Table 8.1 summarizes the main physicochemical characteristics of all oxide precursors and bare supports. Regardless of the support, all oxide precursors showed similar palladium loading (0.77-0.81 wt.%) which is close to the nominal one (1.0 wt.%). The textural properties of oxide precursors were evaluated from nitrogen adsorption-desorption isotherms.

8.3.1.2. Nitrogen adsorption- desorption isotherms

Figures 8.1(A) and **8.1(B)** show the N_2 adsorption-desorption isotherms of the bare supports and oxide precursors, respectively. Bare HY and Pd/HY samples exhibited type I isotherm with a hysteresis loop which, according to

the IUPAC classification, belong to type H4 (49). The almost horizontal plateau of Pd/HY isotherm is characteristic of an ideal microporous solid, although some mesoporosity could be also observed. The latter is probably created during the hydrothermal treatment of the HY zeolite. Contrary to the Pd/HY, the N_2 adsorption-desorption isotherms of the Pd catalysts supported on both mixed HY-Al_2O_3 substrates are of type IV with H1 hysteresis loop. This means that both catalysts are mostly mesoporous. The hysteresis loop H1 has a narrow loop with two branches almost parallel and vertical. This type of hysteresis is usually found on solids consisting of agglomerates or aggregates of particles having a narrow pore size distribution. The N_2 adsorption-desorption isotherm of Pd/Al belong to type IV with H2-type hysteresis loop, characteristics of solids with "ink-bottle" pores (50).

The values of BET area, total pore volume and the average pore diameter are also summarized in **Table 8.1**. As it can be seen, the BET surface area follows the trend: Pd/HY >> Pd/20%HY-Al > Pd/10%HY-Al > Pd/Al whereas for the total pore volume the trend is different: Pd/Al > Pd/10%HY-Al > Pd/20%HY-Al > Pd/HY. The highest BET area and the lowest total pore volume of the Pd/HY catalyst is due to the large microporous region of HY zeolite (**Figure 8.1(A)**). As a consequence, this catalyst showed 3-fold higher BET surface area than its Pd/Al counterpart (476 vs. 154 $m^2 \cdot g^{-1}$). The increase in BET surface area when increasing the HY zeolite content in mixed HY-Al_2O_3 materials is due to a larger contribution of the HY zeolite microporosity system. Considering the relatively low zeolite content in the composite carriers, a relatively small increase in N_2 sorption capacity upon raising HY content was observed (**Table 8.1**). As expected, impregnation of the carriers with H_2PdCl_6 salt precursor leads to a decrease in BET area of the catalysts as compared to the bare

support indicating some pore blocking by palladium species. Additionally, one might expect that some dissolution of the support occurs during impregnation of carrier with an acidic aqueous solution of H_2PdCl_6, similar to what was observed previously for the preparation of the $RuCl_3/Al_2O_3$ catalysts (51) (52).

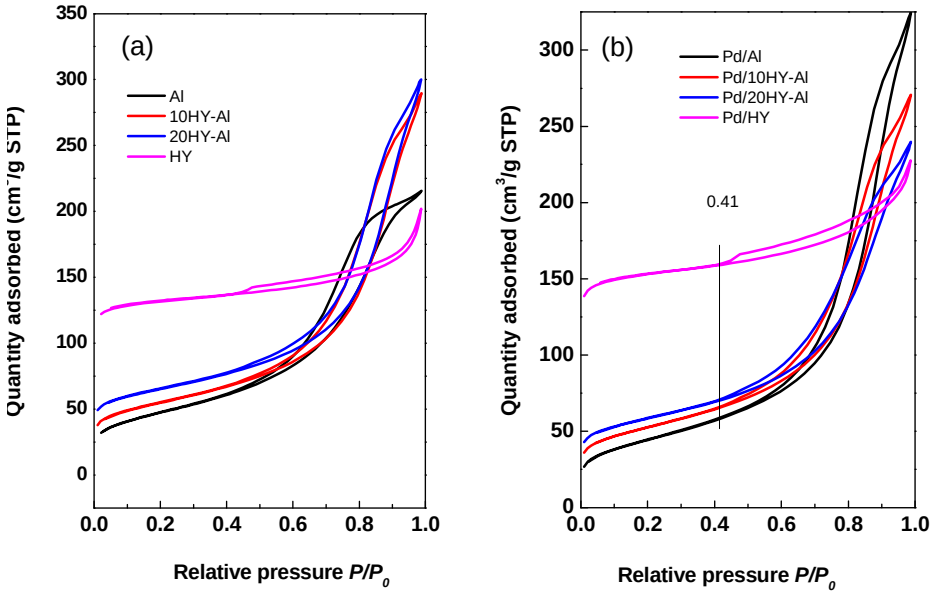

Figure 8.1. N_2 adsorption-desorption isotherms at -196 °C of pure supports **(A)** and oxide catalyst precursors **(B)**.

In order to ascertain the pore modification induced by the addition of HY zeolite to alumina, the Barret-Joyner-Halenda (BJH) formula was employed to determine pore size distribution (PSDs) of the oxide precursors in both meso- (2-50 nm) and macroporous (> 50 nm) regions. Unfortunately, the BJH method is imprecise in the region below 1 nm, where the supercages of the HY zeolite appear. The BJH pore size distribution of the oxide precursors is shown in Figure 2.

As expected, the pore size distribution changed going from Pd/Al to Pd/HY sample. The Pd/Al shows a very broad pore size distribution between 2 and 70 nm, with a maximum at 17 nm, however the PSD of Pd/HY catalyst is narrower (2-30 nm) and the maximum peaks at ca. 10.9 nm. For the Pd/10%HY-Al and Pd/20%HY-Al catalysts, PSD showed a bimodal distribution with maxima peaking at about 14.3 and 13.7 nm, respectively indicating that the average pore diameter decreased with an increase of HY content in mixed HY-Al_2O_3 substrates. Considering the average pore diameter compiled in Table 1, the pore diameter follows the trend: Pd/Al (12.7 nm) > Pd/10%HY-Al (11.0 nm) > Pd/20%HY-Al (10.2 nm) > Pd/HY (8.9 nm). This trend clearly indicates that loading HY zeolite into alumina leads to a decrease of the average pore diameter, as it could be expected.

To evaluate the influence of Pd loading on the location of Pd species within the support structure, the normalized S_{BET} (NS_{BET}) was calculated employing **Equation (8.1).** For the Pd/Al and both Pd catalysts supported on mixed HY-Al_2O_3 materials, NS_{BET} values in 0.91-0.99 range suggest the presence of Pd species on the support surface. For the Pd/HY sample, the NS_{BET} value of 0.8 suggests the presence of Pd species on the support surface as well as their location within the inner support's porous structure (probably in the supercages of the HY zeolite). Thus, the comparison of the normalized S_{BET} values indicates that, regardless of the support, most of the palladium species are accessible for reactant molecule (phenol).

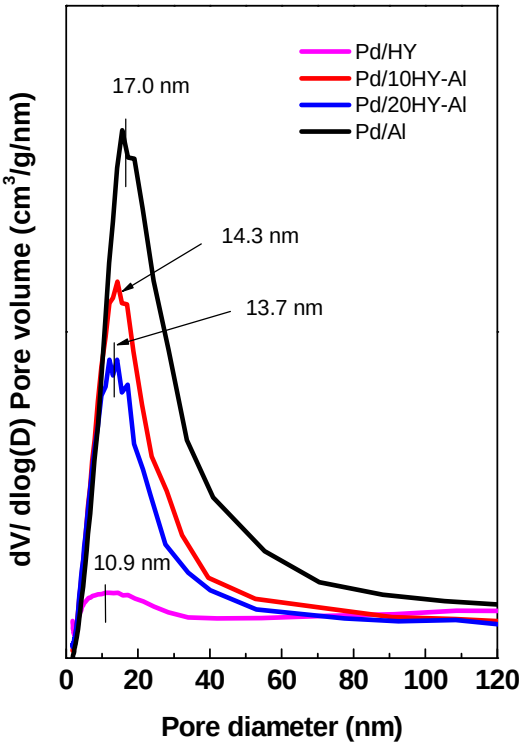

Figure 8.2. BJH pore size distribution of Pd-based oxide precursors (from adsorption branch) calculated by the Harkins and Jura equation.

8.3.1.3. X-Ray Diffraction (XRD)

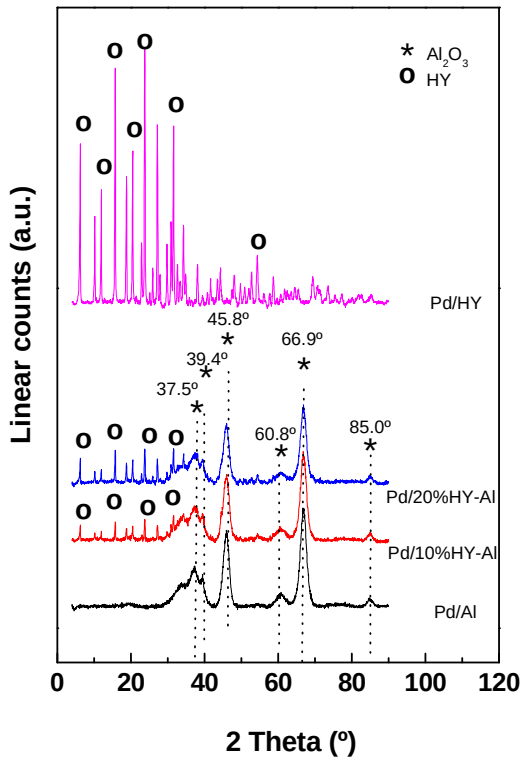

Figure 8.3. XRD diffraction patterns of Pd-based oxide precursors.

X-ray powder diffraction data of the calcined catalysts were used to identify crystalline palladium species formed on the support surfaces (**Figure 8.3**). Regardless of the support composition, no peaks of PdO or Pd^0 crystallites were observed indicating their amorphous character or that crystallite sizes are below the detection limit of the XRD technique (< 4 nm). The X-ray diffraction patterns of

the Pd/Al and Pd/HY catalysts were typical of the Al_2O_3 (JCPDS 00-001-1303) and faujasite (JCPDS 00-0111-0672) phases, respectively. As expected, both Pd/10%HY-Al and Pd/20%HY-Al catalysts showed both phases simultaneously. Thus, all Al-containing catalysts exhibited typical diffraction lines of Al_2O_3 material at 2θ values of 37.5°, 39.4°, 45.8°, 60.8°, 66.9° and 85.0° whereas the HY-containing catalysts showed many narrow peaks at 2θ values of 6.1°, 10.3°, 12.2°, 15.6°, 18.4°, 20.3°, 23.7°, 27.0°, 31.8°, 34.2°, 38.4° and 54.6°, which are typical of zeolite faujasite. As expected, comparison of XRD profiles of the zeolite peaks in the HY-containing catalysts revealed an increase of their intensity with an increase of HY content in the mixed HY-Al_2O_3 supports.

8.3.1.4. Temperature Programmed Reduction (TPR- H_2)

TPR profiles of bar supports and oxide precursors are shown in **Figure 8.4**. As expected, contrary to pure supports, Pd catalysts showed H_2-consumption in the temperature range 0-300 °C. Thus, the H_2-consumption peak at 16 °C observed for Pd/HY catalysts is due to reduction of highly dispersed PdO_x species (53) (54) whereas the negative H_2 consumption peak at 85 °C detected on Pd/Al and the two Pd(x)HY-Al catalysts is usually ascribed to the desorption of hydrogen from a bulk palladium hydride formed through hydrogen diffusion into Pd crystallites (55). This behaviour is typical for catalysts with low metal dispersion due to the high palladium concentration in the large particles. The quantification of H_2 consumption/evolution is listed in **Table 8.2**. From these data, the amount of hydrogen desorbed from bulk palladium hydride follows the trend: Pd/10%HY-Al ≈ Pd/Al > Pd/20%HY-Al >> Pd/HY (none). The absence of bulk β-$PdH_{0.6}$ species on the surface of Pd/HY catalyst is in agreement with TEM data which indicate the formation of smaller size Pd^0 particles on this sample.

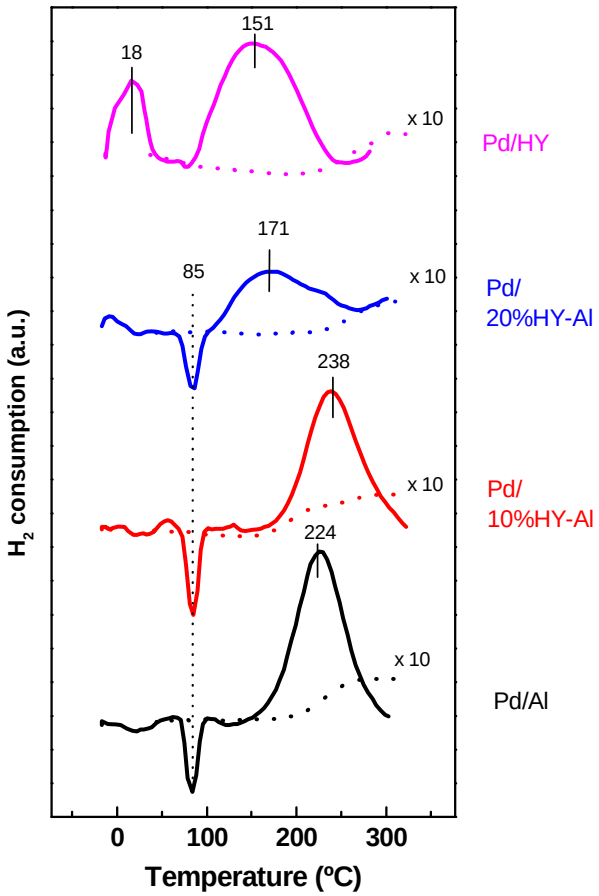

Figure 8.4. TPR profiles of bare supports (doted line) and Pd–based oxide precursors (solid line) Pd/Al, (b) Pd/10%HY-Al, (c) Pd/20%HY-Al, (d) Pd/HY.

The Pd catalysts exhibited two types of reduction peaks: one at low-temperature, which is due to reduction of easy reducible palladium oxide, and the other broad one located at somewhat higher temperature (200-300 °C) due to reduction of a more stable PdO species interacting strongly with the support (56)

(57). For the Pd/Al and Pd/10%HY-Al catalysts, the peak maxima appeared around 224 and 238 °C respectively, indicating similar crystallite sites. For the Pd/20%HY-Al and Pd/HY catalysts, this peak is very broad and shifted to lower temperature when compared with Pd/Al and Pd/10%HY-Al catalysts. Indeed, considering that reduced Pd/HY samples showed the lowest Pd^0 particle among the catalysts studied (HRTEM results *vide infra*) and that bulk Pd-hydride is not formed, the shift of its peak maxima toward lower temperature can be explained considering that PdO clusters are firstly reduced to form Pd atoms at lower temperature (H_2 consumption at 18 °C) and then H_2 is dissociated over these Pd atoms and then the H-atoms spilt over on the surface reduce the highly dispersed Pd^{2+} species (H_2 consumption at 151 °C). Finally, an enhanced reduction of Pd species on the Pd/HY can be explained considering the H_2 dissociation on reduced palladium particles and subsequent hydrogen migration to the carrier interface (spill-over effect).

Table 8.2. Hydrogen consumption during TPR of calcined Pd catalysts

Catalyst	Amount of H_2 (mmol/g_{cat})			
	16 °C	85 °C	200- 300 °C	Total
Pd/Al	-	-0.24	1.68	1.44
Pd/10%HY-Al	-	-0.26	1.82	1.56
Pd/20%HY-Al	-	-0.21	1.96	1.75
Pd/HY	0.89	-	2.44	3.33

8.3.2. Characterization of the reduced catalysts

8.3.2.1. Temperature Programmed Desorption of Ammonia (TPD- NH_3)

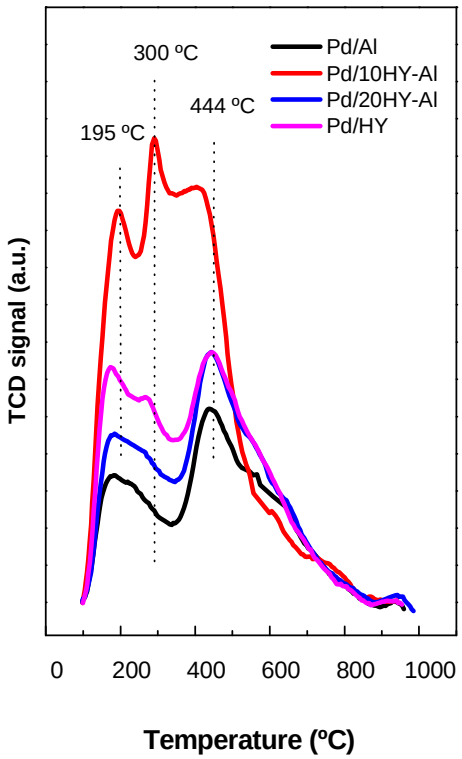

Figure 8.5. TPD-NH_3 profiles of reduced Pd-based catalysts: Pd/Al, Pd/10%HY-Al, Pd/20%HY-Al, Pd/HY.

In order to compare the acidity of samples before and after Pd incorporation, in **Figure 8.5** is shown the TPD-NH_3 profiles of the reduced Pd catalysts (H_2/Ar reduction at 300 °C for 1 h). These profiles were mathematically

fitted using Gaussian functions. Based on the desorption temperature, acid sites were identified to possess weak (T < 250 °C) and medium strength (250- 500 °C). Regardless of support, calcined Pd catalysts show weak and medium strength acid sites which could be identified as Brønsted and structural type, respectively (58). The concentration of acid sites (expressed as $mmol_{NH3}/g_{cat}$) is shown in **Table 8.3**. From these data, it is seen that Pd loading on acidic supports results in the loss of an important fraction of acid sites. This is due to the loss of -OH groups upon Pd^{2+} ions attachment to the support surface. The total acidity of the catalysts follows the trend: Pd/HY > Pd/20%HY-Al > Pd/10%HY-Al > Pd/Al. This trend clearly indicates that the incorporation of HY zeolite into alumina carrier led to an increase acidity.

Table 8.3. Acid properties of pure supports (in parenthesis) and reduced Pd/Al, Pd/HY-Al and Pd/HY catalysts as determined by TPD-NH_3.

Catalyst	Amount of acid sites (mmol $NH_3 \cdot g_{cat}^{-1}$)		
	Weak T < 250 °C	Moderate T= 250-500 °C	Total
Pd/Al	0.9 (0.9)	0.4 (1.1)	1.3 (2.0)
Pd/10%HY-Al	0.9 (1.8)	0.8 (1.9)	1.7 (3.7)
Pd/20%HY-Al	1.8 (1.8)	0.7 (3.6)	2.5 (5.4)
Pd/HY	1.8 (3.4)	3.0 (7.7)	4.8 (11.1)

8.3.2.2. High Resolution Transmission Electron Microscopy (HRTEM)

HRTEM was employed to reveal Pd distribution on the different supports. The HRTEM images of the fresh reduced catalysts are displayed in **Figure 8.6**. In general, Pd crystallites are heterogeneously distributed on the support surface but they become more homogeneous upon increasing zeolite content. The influence of

support on the Pd crystallite size distribution was determined by statistical analysis of various HRTEM images (see **Table 8.4**).

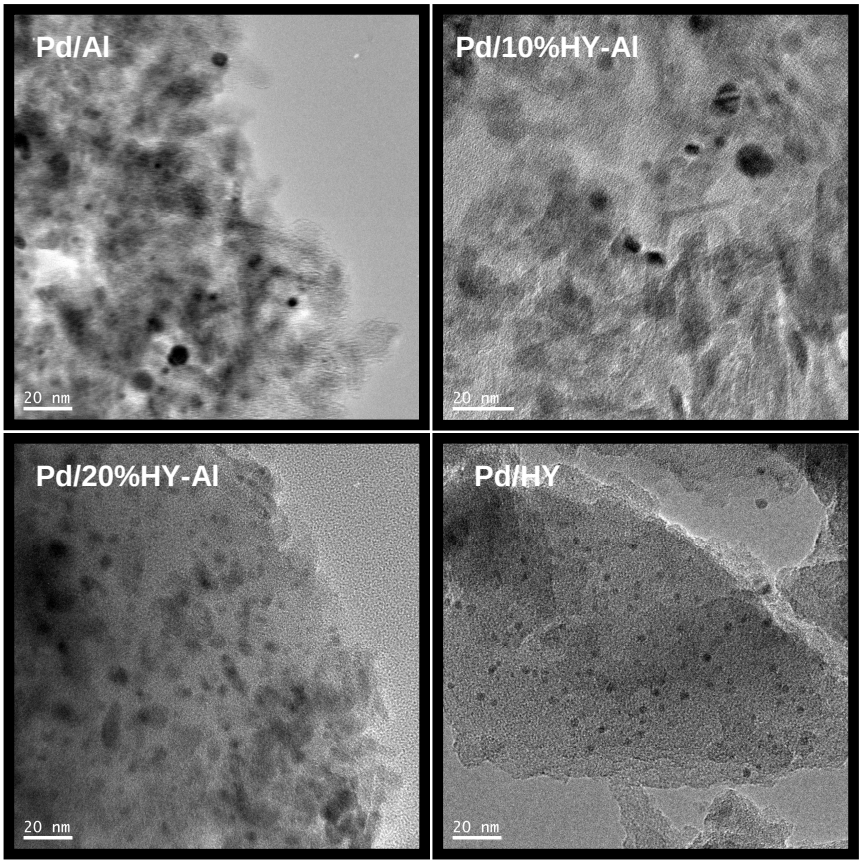

Figure 8.6. HRTEM of the pre-reduced Pd catalysts.

The influence of support on the Pd particle size distribution, determined by statistical analysis of various HRTEM images, is shown in **Figure 8.7**. Clusters size distribution was obtained by counting at least 300 particles on several micrographs per sample. For the Pd particle size, the observed trend is: Pd/HY (3.2 ± 0.7 nm) <

Pd/20%HY-Al (4.6 ± 1.2 nm) < Pd/10%HY-Al (5.0 ± 1.7 nm) < Pd/Al (5.7 ± 2.2 nm). In good agreement with TPR results (**Figure 8.6**), the Pd/HY catalyst shows the lowest Pd particle size among the catalysts studied. Finally, the surface density of the Pd^0 particles, expressed as Pd^0 particles per 50 nm^2, follows the trend: Pd/HY >> Pd/Al > Pd/20%HY-Al > Pd/10%HY-Al (**Table 8.4**). Unfortunately, the poor contrast between HY and alumina substrates does not allow to unambiguously discriminate the preferential location of palladium particles on either HY or alumina phase. In this sense, the EDX/SEM elemental analysis gave information that Pd is deposited preferentially on the HY surface rather than on alumina (data not shown).

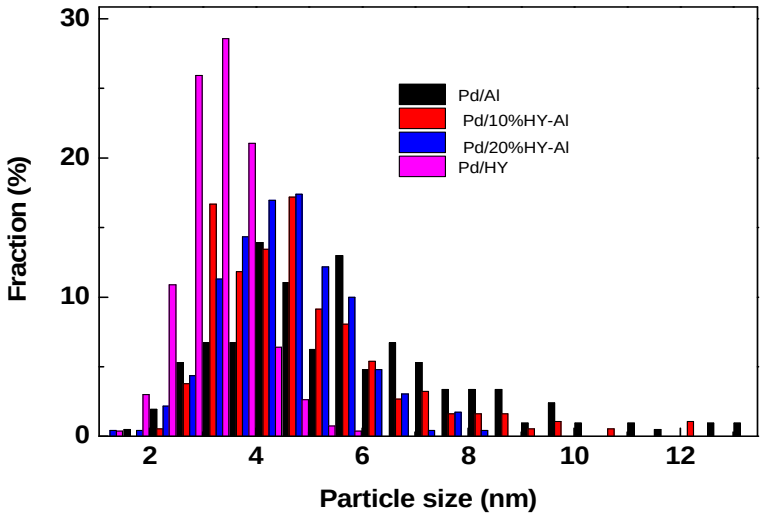

Figure 8.7. Influence of support on the particle size distribution as determined by statistical analysis of various HRTEM images of the pre-reduced Pd catalysts.

It is emphasized that Pd crystallite size determined by XRD and HRTEM is different. This is due to difference in the detection limit and associated error to XRD and TEM measurements. The XRD technique is not able detect regular crystal

particles with size lower than 4 nm whereas the TEM technique can do it. In addition, TEM technique does not allow distinguish very small particles (< 1 nm) from the zeolite background because of the lack of contrast. It is also emphasized that the catalyst area irradiated by the electron beam is several orders of magnitude than in case of the XRD analysis, therefore the Pd size calculated by statistical analysis may not be representative for the whole sample. We can say that the number of small Pd clusters is underestimated by TEM and that this leads to an overestimation of the average Pd crystallite size.

Table 8.4. HRTEM parameters (statistics analysis) of the reduced (300 °C) Pd/Al, Pd/HY-Al and Pd/HY catalysts

Catalyst	Particle size (nm)	Surface density of Pd^0 particles per 50 nm^2
Pd/Al	5.7 ± 2.2	26 ± 5
Pd/10%HY-Al	5.0 ± 1.7	11 ± 2
Pd/20%HY-Al	4.6 ± 1.2	20 ± 6
Pd/HY	3.2 ± 0.7	48 ± 6

8.3.2.3. X- Ray Photoelectron Spectroscopy (XPS)

Information on the Pd state and the surface composition of the reduced (300 °C, H_2) catalysts was obtained by XPS analysis. **Figure 8.7** shows the Pd 3d core-level spectra of all reduced catalysts and Table 4 summarizes the Pd $3d_{5/2}$ binding energies (BEs). For all zeolite-containing catalysts, the binding energy of Pd $3d_{5/2}$ core level at 334.9 eV (335.0 eV for Pd/HY) is due to metallic Pd (58) (59). The BE of the Pd$3d_{5/2}$ peak in Pd/Al catalyst was 0.5 eV lower than that measured for Pd/10%HY-Al and

Pd/20%HY-Al catalysts. This BE shift of Pd might involve Pd particle size effect. Considering the TPR results, the possible contribution of the metal-support interaction to the BE shift can be precluded. Quantitative XPS data of all catalysts are summarized in **Table 8.5**.

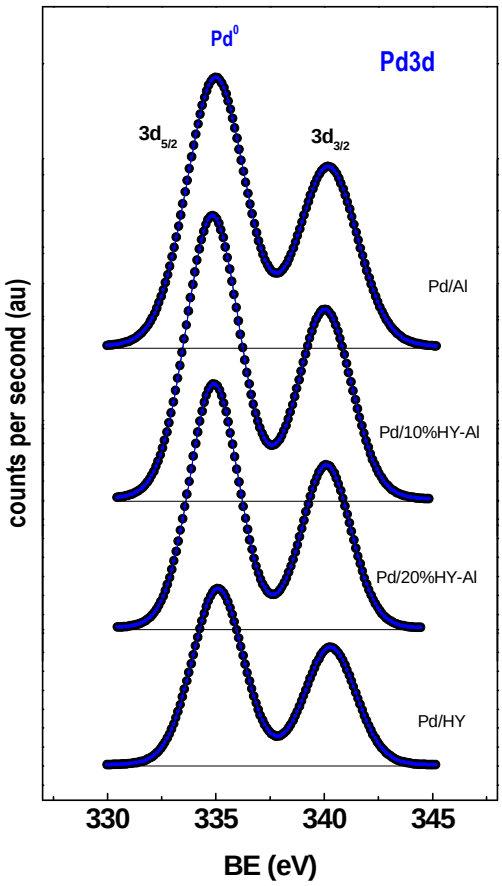

Figure 8.7. Pd $3d_{3/2}$ core-level spectra of *in-situ* pre-reduced (300 °C, H_2) Pd catalysts.

Table 8.5. Binding energy (eV) and surface atomic ratios (from XPS) of the reduced (300 °C) Pd/Al, Pd/HY-Al and Pd/HY catalysts

Catalyst	Pd $3d_{5/2}$ (eV)	Si/(Si+Al) at	Pd/(Si+Al) at
Pd/Al	334.5	-	0.0140
Pd/10%HY-Al	334.9	0.044	0.0139
Pd/20%HY-Al	334.9	0.092	0.0084
Pd/HY	335.0	0.654	0.0024

The surface exposure of Pd species was evaluated by the Pd/(Si+Al) atomic ratio follows the trend: Pd/Al ≈ Pd/10%HY-Al < Pd/20%HY-Al < Pd/HY. A linear correlation between palladium surface exposure and the location of palladium species on the surface, as derived from normalized specific surface area of the catalysts, was found (**Figure 8.8**). As expected, an increase of the Pd/(Si+Al) atomic ratio is accompanied by an increase of the normalized BET area indicating that both Pd/Al and Pd/10%HY-Al catalysts show the largest Pd exposure among the catalysts studied. Therefore, both Pd/HY and Pd/20%HY-Al catalysts exhibit a lower palladium surface exposure than Pd/Al and Pd/10%HY-Al ones. This difference can be also related to a higher amount of Pd species located within the pore structure of the HY zeolite. An additional evidence for this hypothesis comes from the linear correlation found between palladium surface exposure, determined by XPS, and the location of palladium species on the support surface, derived from the normalized BET area of catalysts (**Table 8.1**).

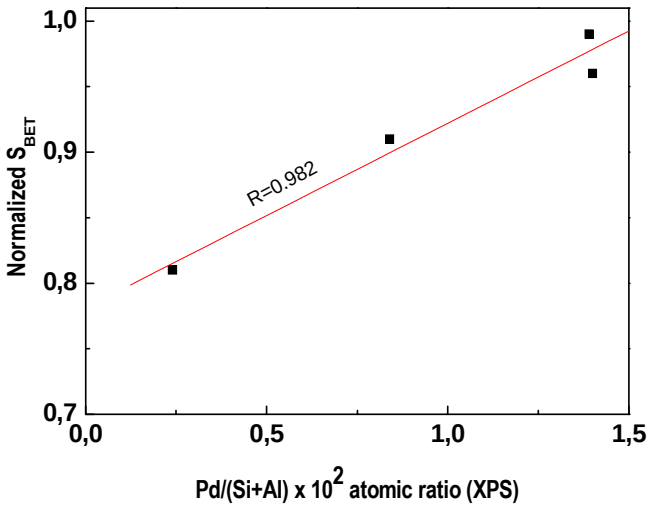

Figure 8.8. Correlation between palladium surface exposure, as determined by XPS (from **Table 8.5**), and the location of palladium on the outer catalyst surface, as determined normalized specific surface area of catalysts (from **Table 8.1**).

8.3.2.4. DRIFTs study of CO adsorption

In order to identify the nature of surfaces sites on the supported Pd catalysts after their activation in pure hydrogen at 300 °C was perfomed an CO adsorption followed by DRIFT spectroscopy. The DRIFT-CO spectra (irreversible CO adsorption at room temperature) are displayed in **Figure 8.8**. As compared with Al-containing samples, the Pd/HY catalyst showed significant differences in: (i) the frequency of the observed maxima, (ii) the total integrated intensity of the bands, and (iii) the ratio between different components.

Thus, three Pd/Al, Pd/10%HY-Al and Pd/20%HY-Al catalysts showed a narrow and intense band centered at 2091 cm^{-1} which should be ascribed to CO linearly bonded to metallic Pd (60). For the Pd/HY, this band is centered at 2108 cm^{-1}. Since the adsorption frequency depends on CO coverage, geometric effect, and the *d*-electron density of Pd (61) (62), for this catalyst the band shift toward higher frequency region (ca. 17 cm^{-1} blue shift) suggests that palladium would be in an electron-deficient state. Since TPR results indicated that the electronic effects associated with a strong metal-support interaction are not detected, the electronic state of Pd on HY zeolite may be related rather to changes in particle size (63).

All catalysts showed also a broad band in the 1900-2020 cm^{-1} frequency region. Based on the data found in literature, the bands centered at 1958 cm^{-1} (1984 cm^{-1} for Pd/HY) should be ascribed to multibonded CO species bridging over Pd^0 clusters (64) (65). The band tailing could be originated from heterogeneous particle dispersion (65). For all catalysts, the intensity of this band is significantly lower than the main band centered at 2091 cm^{-1}. The contribution of the total absorbance of the band due to the linear form was deduced from the ratio $R = I_{linear} / (I_{linear} + I_{bridged})$, where I_{linear} and $I_{bridged}$ are the integrated absorbance at the 2091 (2018 cm^{-1} for Pd/HY) and 1960 cm^{-1} bands normalized to one gram of palladium, respectively. For the *R* values, the observed trend is: Pd/20%HY-Al (0.92) > Pd/HY (0.86) >> Pd/10%HY-Al (0.49) > Pd/Al (0.29). Although the *R* value cannot be considered as the percentage of CO linearly bonded because the extinction coefficients were not determined (66), one might note that both catalysts with the largest HY content showed a largest contribution from CO linearly bonded to metallic Pd species.

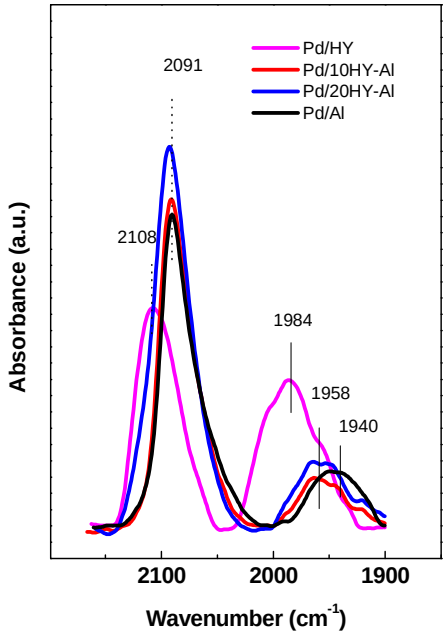

Figure 8.8. DRIFT spectra of chemisorbed CO on the *in situ* reduced (300 °C) palladium catalysts.

8.3.3. Oxygen removal from bio-liquid

Figure 8.9 shows the activities of the reduced Pd/Al, Pd/10%HY-Al, Pd/20%HY-Al and Pd/HY catalysts in the HDO of phenol at T = 310 ºC, P= 3MPa and WHSV = 1.61 h^{-1}. Conversion data are the average of the conversion achieved along 4 h of time on-stream (*TOS*) reaction at each temperature (during this time the conversion changes were < 4%).

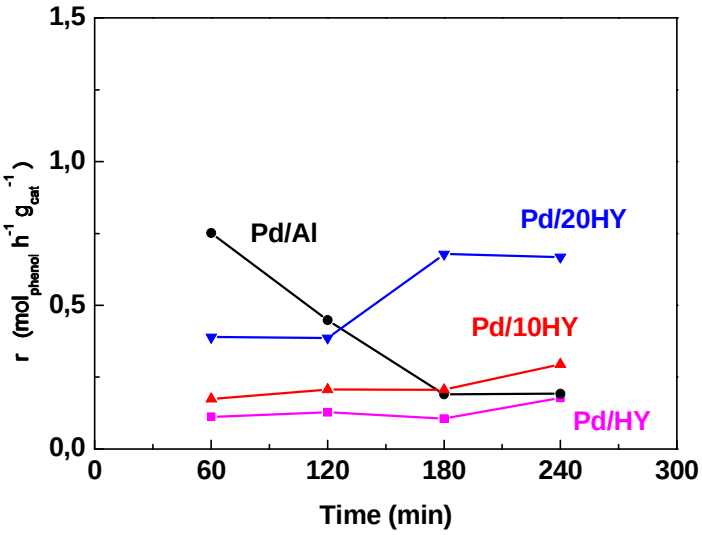

Figure 8.9. Time on-stream behavior of Pd catalysts in the HDO of phenol at T = 310 ºC, P= 3MPa and WHSV = 2.05 h^{-1}).

The highest phenol conversion was achieved for the Pd catalyst supported on the 20% HY/Al_2O_3 catalyst. Incorporation of a smaller amount of HY (10 wt.%) into alumina generated less active catalysts, and when pure HY zeolite was used as support activity was the lowest.

The only products detected in the HDO of phenol over all palladium catalysts in these conditions were two O-free compounds: cyclohexene and cyclohexane. Based on the selectivity data shown in **Figure 8.10** and **Table 8.6**, the proposed reaction scheme is based not only in product distributions but also in literature information (14) (15) (16) (17) (18) (19). For all catalysts, the HDO of

phenol might occur *via* two parallel pathways: a hydrogenation (HYD) with of phenol's aromatic ring followed by cleavage of the C-O σ bond leading to the formation of cyclohexane and a direct cleavage of the C-O σ bond leading to the formation of benzene (14) (15) (16) (17) (18) (19). This reaction scheme suggests that the use of hydrogen for phenol transformation over HY-containing Pd has two effects with respect to reaction mechanism: saturating double bonds and removing oxygen.

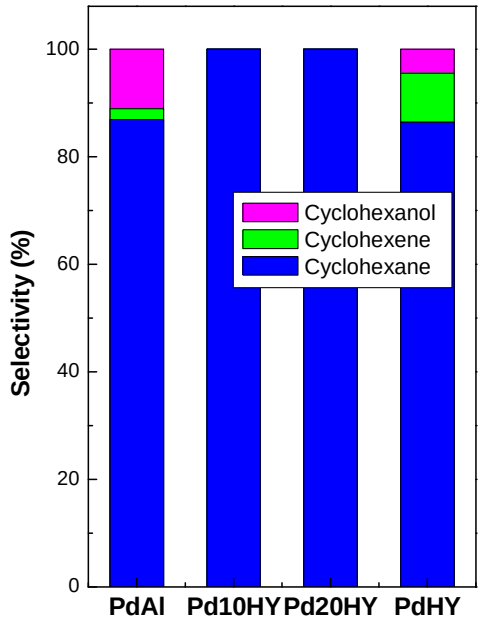

Figure 8.10. Selectivity toward O-free and O-containing products achived at *TOS* = 4 h.

Data collected in **Table 8.6** and **Figure 8.10** indicates that there is a strong effect of support (Al_2O_3, mixed HY-Al_2O_3 and HY zeolite) on product selectivity. In the HDO reaction at 310 °C, 3 MPa, *TOS* = 4 h, *WHSV* = 2.57 h^{-1} selectivity toward

cyclohexane follows the trend: Pd/20%HY-Al (100%) ≈ Pd/10%HY-Al (100%) > Pd/Al (87%) ≈ Pd/HY (86%) indicating that both Pd catalysts supported on hybrid substrates show larger hydrogen consumption for saturation of double bonds. While testing the Pd/HY and Pd/Al catalyst, relatively large quantity of cyclohexene and cyclohexanol were detected. Cyclohexanol suggest that preferential phenol transformation was via hydrogenation reaction route.

Table 8.6. Activity and selectivity data in the hydrotreating of phenol over supported Pd catalysts (T = 310 °C, P = 3 MPa, TOS = 4 h, $WHSV$ = 2.05 h^{-1}).

Catalyst	Conversion (%)	Cyclohexane	Cyclohexene	Cyclohexanol
Pd/HY	8.7	7.5 (86%)	0.8 (9%)	0.4 (5%)
Pd/Al	9.4	8.2 (87%)	0.2 (2%)	1.0 (11%)
Pd/10HY	14.4	14.4 (100%)	0	0
Pd/20HY	32.6	32.6 (100%)	0	0

Similarly to our study, direct hydrogenolysis of phenol to benzene was inhibited on acidic Pd/C catalysts having the combination of a hydrogenation catalyst and a strong acid, which were tested in aqueous-phase HDO of bio-derived phenols to cycloalkanes (31) (32).

8.3.4. Characterization of the spent catalysts

8.3.4.1. Catalyst deactivation by coke. Thermogravimetric analysis (TG/DTG)

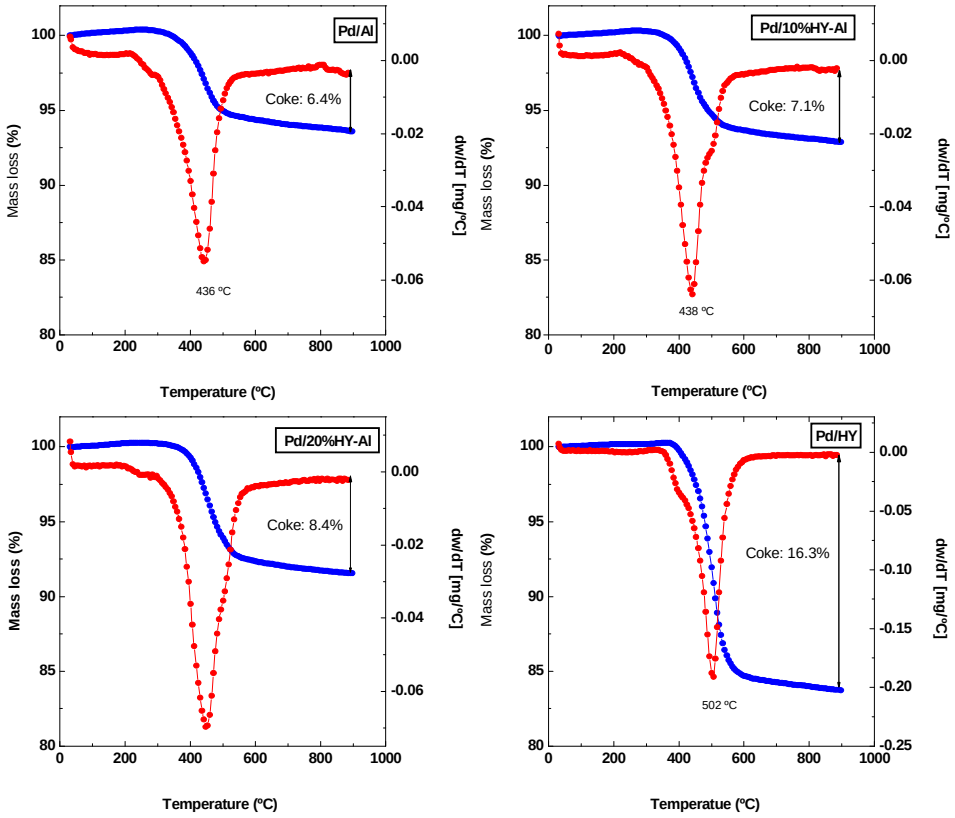

Figure 8.11. TPO/TGA profiles of spent palladium catalyst.

In order to shed light on the origin of catalyst deactivation during phenol HDO over reduced Pd catalysts, the quantity of coke deposited was evaluated by

TGA analysis. The amount of coke formed in the spent catalysts after 16 h on stream was evaluated by temperature-programmed oxidation in a 20% O_2/N_2 mixture. The weight change during oxidation together with DTG profiles are shown in **Figure 8.11**. Regardless of the support, all DTG profiles show one intense peak at temperatures below 500°C, which is due to burning of carbonaceous residues. For the Pd/10%HY-Al and Pd/20%HY-Al catalysts, this peak shows a shoulder located on the higher temperature region indicating the presence of more polymerized-type of coke species. On the contrary, the DTG peak of spent Pd/HY catalyst shows some shoulder at lower temperatures suggesting the formation of carbonaceous residues with higher degree of hydrogenation, which are easier to burn off. The percentages of total mass loss corresponding to all types of burnt coke species follows the trend: Pd/HY (16.3 %) >> Pd/20%HY-Al (8.4 %) > Pd/10%HY-Al (7.1 %) > Pd/Al (6.4 %).

8.3.5. Catalyst activity-structure correlation

In this study, mixed alumina-zeolite HY was successfully used as supports for the catalytic response of palladium catalysts in the phenol HDO reaction. Under the reaction conditions employed (T = 310 °C, P= 30 bar, $WHSV$ = 2.05 h^{-1}), the best catalytic response was archived on the Pd catalyst supported on mixed 20%HY-80%Al_2O_3 carrier.

Considering the catalyst's characterization data, several explanations can be advanced to explain the greater intrinsic activity of the Pd/20%HY-Al catalyst in the HDO of phenol at steady-state: (i), the optimized support acidity, as evidenced by TPD-NH_3 measurements, which led to an increase of the catalyst activity without excessive coking; (ii), an increase of specific BET surface area; (iii), additional activity

from acid sites (67) , and (iv) a large palladium dispersion, as evidenced by HRTEM and TPR results. The catalysts showing the best Pd dispersion, showed the largest activity per palladium surface atom. This suggests that the phenol HDO reaction could be a structure sensitive reaction, i.e. specific activity might to depend on the details of the surface structure of the palladium crystallites.

Contrary to the basic supports, H-spillover is a common feature observed on Pd catalysts supported on acidic substrates which contributes to enhance HDO activity (25)**.** This is a key requirement needed for the effective C-O bond cleavage of O-containing compounds. In this sense, a direct correlation between the support acidity and the HDO activity of Rh catalysts supported on different carriers was observed (25). Since Rh/ZrO_2 sample was found to be much less active than its counterparts supported on more acidic substrates (alumina, silica-alumina and nitric-acid treated carbon black), the authors concluded that bifunctional catalysts are needed for the effective O-removal from phenol.

It is generally accepted that the HDO reaction over noble metals supported on acidic substrates occurs on metal sites as well as on acid sites being H_2 dissociated on metal sites, while O-containing compounds are adsorbed and activated on either metal sites or on the cations/oxygen vacancies located at the metal-support interface (14) (15) (16) (17) (18) (19). In this chapter, the possible contribution of the H-spillover to the overall HDO activity should be obtained from a correlation between the catalyst acidity and HDO activity. Indeed, with exception of Pd/HY, the total acidity (**Table 8.3**) and HDO activity (**Table 8.6**) of the catalysts follows the same trend: Pd/20%HY-Al > Pd/10%HY-Al > Pd/Al. In good agreement with recent reports on the supported Pd HDO catalysts (14) (15) (16) (17) (18) (19), product distribution recorded in the present chapter suggests

that Pd metal sites can be responsible of phenol hydrogenation to cyclohexanol followed by its transformation into cyclohexane and cyclohexene.

Finally, TPO experiments (**Figure 8.11**) confirmed that the main catalyst deactivation in phenol HDO is deposition of carbonaceous residues/coke on the catalyst surface showing the Pd/HY catalyst the largest amount of coke among the catalysts studied. The amount of coke is directly proportional to the coke formation, as expected (68) (69). Thus, the larger extent of coke formed on the Pd/HY catalyst could be due to its larger surface concentration of acid sites. Thus, although the Pd/HY catalyst can be effective for the HDO reaction, it can be concluded that the density of its acid sites needs to be optimized; large enough to achieve high conversion of phenolic compounds, but not too high that would result in fast deactivation. The lowering of catalyst activity due to undesirable oxygenation function of residual chloride ions could be excluded since both XPS and EDX/SEM techniques did not detect the chloride impurity in the reduced catalysts.

8.4. Conclusions

The main conclusions in this chapter are:

(i) As a general conclusion, the use of mixed HY-Al_2O_3 (20 wt.% of HY) as support is beneficial for HDO reaction over palladium-based catalysts.

(ii) Conversion results showed that, upon reaction conditions employed (flow reactor, *T*= 310°C P= 3 MPa, solvent: decaline; *WHSV*= 1.61 h^{-1}), the HDO of phenol over Pd/20%HY-Al catalyst led to similar yields of O-free products as those obtained using the sulfided NiMo/Al_2O_3-zeolite hydrocracking catalyst.

(iii) The largest activity of Pd/20%HY-Al catalyst in the HDO of phenol was explained as due to the hydrogen spillover phenomenon and largest active phase dispersion on the carrier surface. Catalysts further developed from this one could be used in the final stage of bio-liquid transformation into high quality and O-free bio-oil.

(iv) A drastic decrease in activity going from Pd/20%HY-Al to Pd/HY sample indicated that the high catalyst acidity would result in fast catalyst deactivation.

8.5. References

1. *An overview of fast pyrolysis of biomass.* **A.V. Bridgwater, D. Meier, D. Radlein.** s.l. : Organic Geochemistry, 1999, Vols. (30) 1479-1493.

2. *Biomass resource facilities and biomass conversion processing for fuels and chemicals.* **Demirbaş, A.** s.l. : Energy Convers Manage , 2001, Vols. (42) 1357-1378.

3. *Large-scale biohydrogen production from bio-oil.* **S. Sarkar, A. Kumar.** s.l. : Bioresource Technology, 2010, Vols. (101) 7350-7361.

4. *Pyrolysis of wood/biomass for bio-oil: A critical review.* **D. Mohan, C.U. Pittman Jr, P.H. Steele.** s.l. : Energy & Fuels, 2006, Vols. (20) 848-889.

5. *Hydrotreatment of pyrolysis oils from biomass: reactivity of the various categories of oxygenated compounds and preliminary techno-economical study.* **P. Grange, E. Laurent, R. Maggi, A. Centeno, B. Delmon.** s.l. : Catalysis Today, 1996, Vols. (29) 297-301.

6. *Fast pyrolysis of forestry residue. 2. Physicochemical composition of product liquid.* **A. Oasmaa, E. Kuoppala, Y. Solantausta.** s.l. : Energy & Fuels, 2003, Vols. (17) 433-443.

7. *Catalytic hydrodeoxygenation.* **Furimsky, E.** s.l. : Applied Catalysis A: General , 2000, Vols. (199) 147-190.

8. *Hydrodeoxygenation of methyl esters on sulphided NiMo/gamma-Al2O3 and CoMo/gamma-Al2O3 catalysts.* **O.Í. Senol, T.R. Viljava, A.O.I. Krause.** s.l. : Catalysis Today, 2005, Vols. (106) 186-189.

9. *Study of the hydrodeoxygenation of carbonyl, carylic and guaiacyl groups over sulfided CoMo/γ-Al2O3 and NiMo/γ-Al2O3 catalyst: II. Influence of water, ammonia and hydrogen sulfide.* **E. Laurent, B. Delmon.** s.l. : Applied Catalysis A: General, 1994, Vols. (109) 97-115.

10. *CoMo/Carbon hydrodeoxygenation catalysts: influence of the hydrogen sulfide partial pressure and of the sulfidation temperature.* **M. Ferrari, S. Bosmans, R. Maggi, B. Delmon, P. Grange.** s.l. : Catalsis Today, 2001, Vols. (65) 257-264.

11. *Effect of sulphiding agents on the hydrodeoxygenation of aliphatic esters on sulphided catalysts.* **O.Í. Senol, T.R. Viljava, A.O.I. Krause.** s.l. : Applied Cataysis A: General, 2007, Vols. (26) 236-244.

12. *Stability of CoMo/Al_2O_3 catalysts: Effect of HDO cycles on HDS.* **T.R. Viljava, R.S. Komulainen, T. Selvam, A.O.I. Krause.** s.l. : Studies in Surface Science and Catalysis, 1999, Vols. (127) 145-152.

13. *Upgrading of bio-liquid on different mesoporous silica-supported CoMo catalysts.* **R.M. Navarro, B. Pawelec, P. Castaño, M.C.Álvarez-Galván, C.V. Loricera, J.L.G. Fierro.** s.l. : Applied Catalysis B2009; 92: 154-167, 2009, Vols. (92) 154-167.

14. *Synthesis of transportation fuels from biomass: chemistry, catalysts, and engineering.* **G.W. Huber, S. Iborra, A. Corma.** s.l. : Chemical Reviews, 2006, Vols. (106) 4044-4098.

15. *Historical developments in hydroprocessing bio-oils.* **Elliot, D.C.** s.l. : Energy & Fuels, 2007, Vols. (21) 1792-1815.

16. *A review of catalytic upgrading of bio-oil to engine fuels.* **P.M. Mortensen, J.D. Grunwldt, P.A. Jensen, K.G. Knudsen, A.D. Jensen.** s.l. : Applied Catalysis A: General, 2011, Vols. (407) 1-19.

17. *Hydrodeoxygenation of model compounds and catalytic systems for pyrolysis bio-oils upgrading.* **Z. He, X. Wang.** s.l. : Catalysis for Sustainable Energy, 2012, Vols. (1) 28-52.

18. *A review of recent laboratory research and commercial developments in fast pyrolysis and upgrading.* **E. Butler, G. Devlin, D. Meier, K. McDonnell.** s.l. : Renewable and Sustainable Energy Reviews, 2011, Vols. (15) 4171-4186.

19. *A review of catalytic hydrodeoxygenation of lignin-derived phenols from biomass pyrolysis.* **Q. Bu, H. Lei, A.H. Zacher, L. Wang, S. Ren, J. Liang, Y. Wei, Y. Liu, J. Tang, Q. Zhang, R. Ruan.** s.l. : Bioresource Technology, 2012, Vols. (124) 470-477.

20. **D.C. Elliott, J. Hu, T.R. Hart, G.G. Neuenschwander.** *Palladium catalyzed hydrogenation of bio-oils and organic compounds. WO2008151269 A2* US , 2008.

21. *Catalytic hydrodeoxygenation of guaiacol on Rh-based and sulfided CoMo and NiMo catalysts.* **Y.C. Lin, C.L Li, H.P. Wan, H.T. Lee, C.F. Liu.** s.l. : Energy & Fuels, 2011, Vols. (25) 890-895.

22. *Hydrodeoxygenation of guaiacol on noble metal catalysts.* **A. Gutierrez, R.K. Kaila, M.L. Honkela, R. Slioor, A.O.I. Krause.** s.l. : Catalysis Today, 2009, Vols. (147) 239-246.

23. *Hydrotreatment of wood-based pyrolisis oil using zirconia-supported mono- and bimetallic (Pt, Pd, Rh) catalysts.* **A.R. Ardiyanti, A. Gutierrez, M.L. Honkela, A.O.I. Krause, H.J. Heeres HJ.** s.l. : Applied Catalysis A: General, 2011, Vols. (407) 56-66.

24. *Production of renewable diesel by hydroprocessing of soybean oil: Effect of catalysts.* **B. Veriansyah, J.Y. Han, S. Kim SK, S.Ah. Hong, Y.J. Kim, J.S. Lim, Y.W. Shu, S.G. Oh, J. Kim.** s.l. : Fuel, 2012, Vols. (94) 578-585.

25. *Catalytic roles of metals and supports on hydrodeoxygenation of lignin monomer guaiacol.* **C.R. Lee, J.S. Yoon, Y.W. Suh, J.W. Choi, J.M. Ha, D.J. Suh, Y.K. Park.** s.l. : Catalysis Communications, 2012, Vols. (17) 54-58.

26. *Hydrogenation and Hydrodeoxygenation of 2-methyl-2-pentenal on Supported Metal Catalysts.* **T. Pham, L.L. Lobban, D.E. Resasco, R.G. Mallinson.** s.l. : Journal of Catalysis, 2009, Vols. (266) 9-14.

27. *Hydrodeoxygenation of furfural over supported metal catalysts: A comparative study of Cu, Pd and Ni.* **S. Sitthisa, D.E. Resasco.** s.l. : Catalysis Letters, 2011, Vols. (141)784-791.

28. *Bifunctional Pd/Al-SBA-15 catalyzed one-step hydrogenation-esterification of furfural and acetic acid: A model reaction for catalytic upgrading of bio-oil.* **W. Yu, Y. Tang, L. Mo, P. Chen, H. Lou, X. Zheng.** s.l. : Catalysis Communications, 2011, Vols. (13) 35-39.

29. *Conversion of furfural and 2-methylpentanal on Pd/SiO2 and Pd-Cu/SiO2 catalysts.* **S. Sitthisa, T. Pham, T. Prasomsri, T. Sooknoi, R.G. Mallinson, D.E. Resasco.** s.l. : Journal of Catalysis, 2011, Vols. (280) 17-27.

30. *Hydroconversion of sunflower oil on Pd/SAPO-31 catalyst.* **O.V. Kikhtyanin, A.E. Rubanov, A.B. Ayupov, G.V. Echevsky.** s.l. : Fuel , 2010, Vols. (89) 3085-3092.

31. *Highly selective catalytic conversion of phenolic bio-oil to alkanes.* **C. Zhao, Y. Kou, A.A. Lemonidou, X.B. Li, J.A. Lercher.** s.l. : Angewandte Chemie International Edition, 2009, Vols. (48) 3987-3990.

32. *Aqueous-phase hydrodeoxygenation of bio-derived phenols to cycloalkanes.* **C. Zhao, J. He, A.A. Lemonidou, X. Li, J.A. Lercher.** s.l. : Journal of Catalysis, 2011, Vols. (280) 8-16.

33. *Cleveage and hydrogenation (HDO) of C-O bonds relevant to lignin conversion using Pd/Zn synergetic catalysts.* **T.H. Parsell, B.C. Owen, I. Klein, T.M. Jarrell, C.L. Marcum, L.J. Haupert, L.M. Amundson, H.I. Kenttämaa, F. Ribeiro, J.T. Miller, M.M. Abu-Omar.** s.l. : Chemical Science, 2013, Vols. (4) 806-813.

34. *Hydrotreatment of fast pyrolysis oil using heterogeneous noble metal catalysts.* **J. Wildschut, F.H. Mahfud, R.H. Venderbosch, H.J. Heeres.** s.l. : Industrial Engineering Chemistry Research, 2009, Vols. (48) 10324-10334.

35. *Carbon-supported bimetallic Pd-Fe catalysts for vapor-phase hydrodeoxygenation of guaiacol.* **J. Sun, A.M. Karim, H. Zhang, L. Kovarik, X. Shari Li, A.J. Hensley, J.S. McEwen, Y. Wang.** s.l. : Journal of Catalysis, 2013, Vols. (306) 47-57.

36. *Catalytic deoxygenation of unsaturated renewable feedstocks for production of diesel hydrocarbons.* **M. Snåre, I. Kubičková, P. Mäki-Arvela, D. Chichova, K. Eränen, D. Yu Murzin.** s.l. : Fuel , 2008, Vols. (87) 933-945.

37. *Hydrodeoxygenation of benzophenone on Pd catalysts.* **M. Bejblová, P. Zámostný, L. Červený, J. Čejka.** s.l. : Applied Catalysis A: General, 2005, Vols. (296) 169-175.

38. *Hydrodeoxygenation of aldehydes catalyzed by supported palladium catalysts.* **D. Procházková, P. Zámostný, M. Bejblová, L. Červený, J. Čejka.** s.l. : Applied Catalysis A: General, 2007, Vols. (332) 56-64.

39. *Catalytic hydroprocessing of chemical models for bio-oil.* **D.C. Elliot, T.R. Hart.** s.l. : Energy & Fuels, 2009, Vols. (23) 631-637.

40. *One step bio-oil upgrading through hydrotreatment, esterification and cracking.* **Z. Tang, Q. Lu, Y. Zhang, X. Zhu, Q. Guo.** s.l. : Industrial Engineering Chemistry Research, 2009, Vols. (48) 6923-6929.

41. *Kinetics of phenol hydrogenation over supported palladium catalyst.* **N. Mahata, V. Vishwanathan.** s.l. : Journal of Molecular Catalysis A: Chemical, 1997, Vols. (120) 267-270.

42. *Hydrogenation of phenol over supported platinum and palladium catalysts.* **K. Talukdar, K.G.Bahattacharyya, S. Sivasanker.** s.l. : Applied Catalysis A: General, 1993, Vols. (96) 229-239.

43. *Cyclohexanone conversion catalyzed by Pt/gamma-alumina: Evidence of oxygen removal and coupling reactions.* **T. Nimmanwudipong, R.C. Runnebaum, D.E. Block, B.C. Gates.** s.l. : Catalysis Letters, 2011, Vols. (141) 1072-1078.

44. *Bifunctional transalkylation and hydrodeoxygenation of anisole over a Pt/HBeta catalyst.* **X. Zhu. L.L. Lobban, R.G. Mallinson, D.E. Resasco.** s.l. : Journal of Catalysis, 2011, Vols. (281) 21-29.

45. *Hydrodeoxygenation of phenol over zeolite-supported metal catalysts.* **D.Y. Hong, P.K. Agrawal, S.J. Miller, C.W. Jones.** s.l. : Catalysis and Reaction Engineering Division. AIChE Annual Meeting, 2009.

46. *Hydrodeoxygenation and coupling of aqueous phenolics over bifuncional zeolite-supported metal catalysts.* **D.Y. Hong, S.J. Miller, P.K. Agrawal, C.W. Jones.** s.l. : Chemical Communications, 2010, Vols. (46) 1038-1040.

47. *Hydrogenation of aromatics on sulfur-resistant PtPd bimetallic catalysts.* **R.M. Navarro, B. Pawelec, J.M. Trejo, R. Mariscal, J.L.G. Fierro.** s.l. : Journal of Catalysis , 2000, Vols. (189) 184-194.

48. *Hydrocracking activity of NiMo-USY zeolite hydrotreating catalysts.* **B. Egia, J.F. Cambra, B. Güemez, P.L. Arias, B. Pawelec, J.L.G. Fierro.** s.l. : Studies in Surface Science and Catalysis , 1997, Vols. (106) 567-571.

49. **S.J. Gregg, K.S.W. Sing.** *Adsorption, surface area and porosity.* London : Academic Press, 1982.

50. *Surface area and pore texture of catalysts.* **G. Leofanti, M. Padovan, G. Tozzola, B. Venturelli.** s.l. : Catalysis Today, 1998, Vols. (41) 207-219.

51. *Physicochemical characterization and H2-TPD study of alumina supported ruthenium catalysts.* **B. Lin, R. Wang, X. Yu, J. Lin, F. Xie, K. Wei.** s.l. : Catalysis Letters, 2008, Vols. (124) 178-184.

52. *Influence of catalyst pretreatments on propane oxidation over Ru/γ-Al2O3.* **J. Okal, M. Zawadzk.** s.l. : Catalysis Letters, 2009, Vols. (132) 225-234.

53. *Redox behaviour and catalytic properties of Ce0.5Zr0.5O2-supported palladium catalysts.* **M.F. Luo, X.M. Zheng.** s.l. : Applied Catalysis A: General, 1999, Vols. (189) 15-21.

54. *Temperature-programmed reduction and temperature-resolved sorption studies of strong metal-support interaction in supported palladium catalysts.* **T.C. Chang, J.J. Chen, C.T. Yeh.** s.l. : Journal of Catalysis , 1985, Vols. (96) 51-57.

55. *Benzene hydrogenation over supported and unsupported palladium: I. Kinetic behavior.* **M.A. Vannice, P. Chou.** s.l. : Journal of Catalysis, 1987, Vols. (107) 129-139.

56. *Palladium redispersion by spreading of palladium(II) oxide in oxygen treated palladium/alumina.* **H. Lieske H, J. Völter.** s.l. : Journal of Physical Chemistry , 1985, Vols. (89) 1841-1842.

57. *Influence of Pd precursor and method of preparation on hydrodechlorination activity of alumina supported palladium catalysts.* **R. Gopinath, N.S. Babu, J.V. Kumar, N. Lingaiah, P.S. Sai Prasad.** s.l. : Catalysis Letters, 2008, Vols. (120) 312-319.

58. *Enhancement of naphthalene hydrogenation over PtPd/SiO2–Al2O3 catalyst modified by gold.* **B. Pawelec, V. La Parola, S. Thomas, J.L.G. Fierro.** s.l. : Journal of Molecular Catalysis A: Chemical , 2006, Vols. (253) 30-43.

59. *Aromatics Hydrogenation on Pt-Pd metals supported on Zr-phosphate.* **S. Murcia-Mascarós, B. Pawelec, J.L.G. Fierro.** s.l. : Catalysis Communications, 2002, Vols. (3) 305-311.

60. *Deep hydrodesulfurization of DBT and diesel fuel on supported Pt and Ir catalysts.* **R.M. Navarro, B. Pawelec, J.L.G. Fierro, P.T. Vasudevan, J.F. Cambra, P.L. Arias.** s.l. : Applied Catalysis A: General, 1996, Vols. (137) 269-286.

61. *Chemisorption on surfaces - an historical look at a representative adsorbate: carbon monoxide.* **Jr, J.T. Yates.** s.l. : Surface Science, 1994, Vols. (299-300) 731-741.

62. *Infrared reflection-absorption spectroscopy of absorbed molecules.* **Hoffmann, F.M.** s.l. : Surface Science Reports, 1983, Vols. (3) 107-192.

63. *The origin of sulfur tolerance in supported platinum catalysts: The relationship between structural and catalytic properties in acidic and alkaline Pt/LTL.* **J.T. Miller, D.C. Koningsberger.** s.l. : Journal of Catalysis, 1996, Vols. (162) 209-219.

64. *The effect of chromium on sulfur resistance of Pd/HY–Al2O3 catalysts for aromatic hydrogenation .* **L. Hu, G. Xia, L. Qu, M. Li, C. Li, Q. Xin, D. Li.** s.l. : Journal of Catalysis, 2001, Vols. (202) 220-228.

65. *AuPd alloy formation in Au-Pd/Al2O3 catalysts and its role on aromatics hydrogenation.* **B. Pawelec, A.M. Venezia, V. La Parola, E. Cano-Serrano, J.M. Campos-Martin, J.L.G. Fierro.** s.l. : Applied Surface Science, 2005, Vols. (242) 380-391.

66. *Surface characterization of palladium-copper bimetallic catalysts by FTIR spectroscopy and test reactions.* **F. Skoda, M.P. Astier, G.M. Pajonk, M. Primet.** s.l. : Catalysis Letters , 1994, Vols. (29) 159-168.

67. *Hydrogenation of aromatics over supported Pt-Pd catalysts.* **B. Pawelec, R. Mariscal, R.M. Navarro, S. van Bokhorst, S. Rojas, J.L.G. Fierro.** s.l. : Applied Catalysis A: General , 2002, Vols. (225) 223-227.

68. *Hydrodesulfurization of diesel oil on Pt and NiW phases supported on alumina-zeolite mixtures.* **P.L. Arias, F. Zugazaga, B. Güemez, J.L. Cambra, B. Pawelec, J.L.G. Fierro.** s.l. : Symposium on recient advances in heteroatom removal presented before the Division of Petroleum Chemistry, Inc. 215th National meeting, Americam Chemical Society, Dallas, TX, March 29–April 3, 1998. ACS symposium series, 1998. (43) 63-67.

69. *Insights into the coke deposited on HZSM-5, Hβ and HY zeolites during the cracking of polyethylene.* **P. Castaño, G. Elordi, M. Olazar, A.T. Aguayo, B. Pawelec, J. Bilbao.** s.l. : Applied Catalysis B: Environmental , 2011, Vols. (104) 91-100.

Capítulo 9

Conclusiones

Capítulo 9

Conclusiones

A partir de los resultados obtenidos en la preparación, caracterización y estudio de la reactividad de los catalizadores en las reacciones de desoxigenación de moléculas modelo (fenol y anisol) y de la discusión de los mismos se han extraído las siguientes conclusiones:

Catalizadores CoMo soportados en diferentes materiales mesoporosos (SBA-15, SBA-16, DMS-1, HMS)

- Los catalizadores CoMo soportados sobre materiales mesoporosos son mucho más activos que el catalizador comercial NiMo/Al_2O_3.
- La actividad en desoxigenación de esta serie de catalizadores está fuertemente influenciada por la acidez del soporte y en menor medida del grado de sulfuración de las especies de Co. Durante la reacción, todos los catalizadores fueron estables con una desactivación por coque baja (1.5-2.4%).
- La selectividad hacia productos deseados está influenciada por la morfología del soporte. El catalizador CoMo/SBA-16 es el más apropiado hacia formación de parafinas y alcoholes y para eliminar oxígeno de

productos aromáticos oxigenados, siendo un buen candidato para producir combustibles de hidrocarburos a partir de biomasa.

Catalizadores CoMoW modificados con P soportados en diferentes materiales mesoporosos (SBA-15, SBA-16)

- La incorporación del fósforo (0.5% en peso) aumenta un 47% la actividad de hidrotratamiento sobre la molécula de anisol en el catalizador soportado sobre SBA-16, no así con el soportado sobre SBA-15, indicando que el efecto de la incorporación de fósforo depende de la morfología del soporte.
- Los catalizadores soportados sobre SBA-16 muestran un mayor rendimiento a benceno y mayor dispersión de las fases sulfuro que los soportados sobre SBA-15. Sin embargo, el rendimiento a producto deseado fue demasiado bajo para ser considerado en un posible uso en la eliminación de oxígeno a partir de biomasa.
- 0.5P-S16 fue el catalizador más activo en la transformación de anisol. Esta mejora está relacionada con el enriquecimiento superficial de la fase activa, una mayor acidez total y una mayor estabilidad durante el tiempo de reacción.
- La actividad de los catalizadores está fuertemente influenciada por la acidez del soporte y en menor medida por el grado de sulfuración de las especies de cobalto en la superficie. Se encontró una correlación entre el número de sitios ácidos fuertes y la actividad catalítica, que apunta a la participación de estos centros en el mecanismo de reacción.
- El mecanismo de reacción para la transformación de anisol de los catalizadores sulfurados de CoMoW soportados sobre SBA-15 (16) es

bifuncional, siendo mayor la implicación de centros metales ácidos, como se deduce de la participación y la isomerización sin hidrogenación del anillo aromático.

Catalizadores Zn-Ni soportados sobre diferentes materiales (SBA-15, SiO_2, $2SiO_2$-TiO_2, Ti-SBA-15)

- El catalizador de Zn-Ni bifuncional soportado sobre SBA-15 modificado con partículas de TiO_2 fue el catalizador más prometedor para la eliminación de oxígeno en bio-líquidos.
- Tanto el SBA-15 como el Ti-SBA-15 fueron materiales mucho más efectivos que TiO_2 o $2TiO_2$-SiO_2, debido a su mayor área específica BET y acidez.
- La actividad, la selectividad y la estabilidad del catalizador están estrechamente relacionadas con la cantidad accesible de Ni, NiO y sitios ácidos del catalizador. Un equilibrio entre ellas se necesita para diseñar un catalizador multifuncional capaz de tratar a los combustibles fósiles y renovables a la vez.

Catalizadores de Pt, Ir y Pt-Ir soportados sobre zeolitas (HY, ZSM-5)

- Independientemente de la fase activa y el tipo de reactor empleado, la mayor actividad de HDO se logró sobre catalizadores soportados-HY.
- En las condiciones de reacción empleadas, los sistemas bimetálicos mostraron una actividad mayor que los monometálicos.
- En la reacción llevada a cabo en un reactor discontinuo, los catalizadores soportados sobre la zeolita HY mostraron una gran selectividad hacia los productos que tienen dos o más anillos aromáticos.

- La actividad de los catalizadores está fuertemente influenciada por las propiedades de textura y la acidez del soporte utilizado siendo la zeolita HY más eficaz como soporte que ZSM-5.

Catalizadores de Pd soportados sobre HY, Al_2O_3, y mezcla de ambos (20HY, 10HY)

- Como conclusión general, el uso del soporte mezclado de HY-Al_2O_3 (20% HY) como soporte es beneficioso para la reacción de HDO sobre catalizadores basados en paladio.
- Los resultados de la conversión mostraron que, en las condiciones de reacción empleadas (reactor de flujo, T = 310°C, P = 3 MPa, disolvente: decalina; WHSV = 1,61 h^{-1}), la HDO de fenol sobre Pd/20%HY-Al llevó a rendimientos de productos desoxigenados similares a los obtenidos utilizando el catalizador sulfurado de hidrocraqueo NiMo/Al_2O_3-HY.
- La mayor actividad de Pd/20% HY-Al se explica al fenómeno de desbordamiento de hidrógeno y a una mayor dispersión de la fase activa en la superficie del soporte.
- Se produjo una disminución de la actividad del catalizador Pd/20% HY-Al al Pd / HY, indicando que una alta acidez del catalizador daría lugar a la desactivación del mismo.

From the results obtained in the preparation, characterization and study of the reactivity of the catalysts in hydrodeoxygenation reactions of model molecules (phenol and anisole) and the discussion of them have drawn the following conclusions:

CoMo catalyst supported on different mesoporous silicates (SBA-15, SBA-16, DMS-1, and HMS):

- All CoMo catalysts supported on mesoporous silicates are much more active than a commercial NiMo/Al_2O_3 catalyst.
- The HDO activity of the catalysts studied is strongly influenced by the support acidity and much less so by the sulfidation degree of surface cobalt species. All catalysts were stable during on-stream reaction, and deactivation by coke was relatively low (1.5–2.4%).
- The selectivity toward desired products is influenced by support morphology. The CoMo/SBA-16 catalyst is the most appropriate considering the formation of desirable products (paraffins and alcohols) and the removal of oxygen-containing products and polyaromatics (PAH). This sample is a good candidate for the first of a two-stage process to produce hydrocarbon fuels from biomass.

CoMoW catalysts modified with P supported on different mesoporous materials (SBA-15, SBA-16)

- In contrast to the catalyst 0.0P-S15, the steady-state activity of the catalyst supported on SBA-16 increased by 47% after modification with the

optimized amount of phosphorus (0.5 wt%), indicating the effect of the incorporation of phosphorus depends on the morphology of the support.

- Supported catalysts SBA -16 show a higher benzene yield and greater dispersion of the phases of their counterparts metal sulfide supported on SBA- 15. However, the product yield was too low to be considered for possible use in removing oxygen from biomass.
- The improvement of the catalyst activity 0.5P-S16 in the reaction is related to the surface enrichment of the active phase, the higher total acidity and higher stability during the reaction time.
- The activity of the catalysts is strongly influenced by the acidity of the support and to a lesser extent by the degree of sulfidation of cobalt species on the surface. We found a correlation between the number of strong acid sites and the catalytic activity, which points to the involvement of these centers in the reaction mechanism.
- The reaction mechanism for the transformation of anisole CoMoW sulphide catalysts supported on SBA -15 (16) is bifunctional , being greater involvement of acidic centers metal centers , as deduced from the participation and isomerization no hydrogenation of the aromatic ring.

Zn-Ni supported on different materials (SBA-15, SiO_2, $2SiO_2$-TiO_2, Ti-SBA-15)

- The bifunctional Zn-Ni catalyst supported on SBA-15 mesoporous silica material decorated with TiO_2 particles was found to be the most promising catalyst for O-removal from bio-liquids whereas the Zn-Ni catalyst supported on SBA-15 was found to be the most promising for hydrodearomatization of synthetic diesel.

- Both SBA-15 and Ti-SBA-15 substrates were much effective as supports than TiO_2 and $2TiO_2$-SiO_2 counterparts due to their much larger BET specific surface area and acidities.
- The catalyst activity, selectivity and stability were closely linked with the amount of accessible Ni, NiO and acid sites of the catalyst. A balance of these trees is required to design a multifunctional catalyst able to treat fossil and renewable fuels at once.

Pt, Ir and Pt-Ir catalysts supported over zeolitic materials (HY, ZSM-5)

- Regardless of the active phase and type of reactor employed, the higher HDO activity was achieved over HY-supported catalysts.
- Under the reaction conditions employed, the bimetallic systems exhibited a larger activity than their monometallic counterparts.
- In the reaction carried out in a batch reactor, the catalysts supported on the HY zeolite exhibited a large selectivity toward products having two or more aromatics rings.
- The activity of the catalysts is strongly influenced by the textural properties and support acidity being HY zeolite more effective as support than ZSM-5.

Pd catalysts supported over HY, Al_2O_3, and mixed (20HY-Al, 10HY-Al)

- As a general conclusion, the use of mixed HY-Al_2O_3 (20 wt.% of HY) as support is beneficial for HDO reaction over palladium-based catalysts.
- Conversion results showed that, upon reaction conditions employed (flow reactor, T= 310°C P= 3 MPa, solvent: decaline; $WHSV$= 1.61 h^{-1}), the HDO of

phenol over Pd/20%HY-Al catalyst led to similar yields of O-free products as those obtained using the sulfided NiMo/Al_2O_3-zeolite hydrocracking catalyst.

- The largest activity of Pd/20%HY-Al catalyst in the HDO of phenol was explained as due to the hydrogen spillover phenomenon and largest active phase dispersion on the carrier surface.
- A drastic decrease in activity going from Pd/20%HY-Al to Pd/HY sample indicated that the high catalyst acidity would result in fast catalyst deactivation.

Anexos

Anexo I. Lista de acrónimos

BE Energía de ligadura eV

BET *Brunauer-Emmett-Teller*

CG (GC) Cromatógrafo de gases (*Gas chromatograph*)

DMS-1 Silice mesoporosa desordenada (Disordered mesoporous silica)

DRIFT Espectroscopia infrarroja de reflectancia difusa por transformada de Fourier (*Diffuse Reflectance Infrared Fourier Transform*)

DTG Derivada del perfil del análisis termogravimétrico (*Differential Thermal Analysis)*

E_A Energía de activación

EDX Energía dispersiva de rayos X

FID Detector de ionización de llama

FTIR Espectroscopia infrarroja por transformada de Fourier (*Fourier Transform Infrared*)

GHSV *Gas hourly space velocity*

H_2-TPR Reducción a temperatura programada

HDN Hidrodesnitrogenación

HDO Hidrodesoxigenación

HDS Hidrodesulfuración

HMS Silice Mesoporosa Hexagonal (Hexagonal mesoporous silica)

ICP-AES Análisis elemental por espectrometría de emisión atómica con plasma acoplado (*Inductively Coupled Plasma Atomic Emission Spectroscopy)*

JCPDS *Joint Committee on Powder Diffraction Standards*

LHSV Velocidad espacial

MCM-41Material mesoporoso hexagonal

SBA-15 Material mesoporoso con estructura hexagonal bidimiensional

SBA-16 Material mesoporoso con estructura cúbica

SEM Microscopía electrónica de barrido (*Scanning Electron Microscopy*)

Tr Temperatura de reactividad

TCD Detector de conductividad térmica

TEM Microscopía electrónica de transmisión (*Transmission Electron Miscroscopy*)

TGA Análisis termogravimétrico (*Thermo Gravimetric Analysis*)

TPD Desorción a temperatura programada (*Temperature Proggramed Desorption*)

TPO Oxidación a temperatura programada (*Temperature Proggramed Oxydation*)

TPR Reducción a temperatura programada (*Temperature Programmed Reduction*)

TXRF Fluorescencia de rayos X por reflexión total (*Total reflection X-ray Fluorescence*)

WGS *Water-Gas Shift reaction*

WHGS *Weight hourly space velocity*

XPS Espectroscopia fotoelectrónica de rayos X (*X-Ray Photoelectron Spectroscopy*)

XRD Difracción de rayos X (*X-Ray Diffraction*)